University of Sussex

Ytterbium ion trapping and microfabrication of ion trap arrays

by

Robin C. Sterling

Submitted for the degree of Doctor of Philosophy

University of Sussex, Brighton, United kingdom

May 2011

Declaration

I hereby declare that this thesis has not been and will not be submitted in whole or in part to another University for the award of any other degree.

Signature:

Robin C. Sterling

UNIVERSITY OF SUSSEX

Robin C. Sterling, Doctor of Philosophy

Ytterbium ion trapping and microfabrication of ion trap arrays

Abstract

Over the past 15 years ion traps have demonstrated all the building blocks required of a quantum computer. Despite this success, trapping ions remains a challenging task, with the requirement for extensive laser systems and vacuum systems to perform operations on only a handful of qubits. To scale these proof of principle experiments into something that can outperform a classical computer requires an advancement in the trap technologies that will allow multiple trapping zones, junctions and utilize scalable fabrication technologies.

I will discuss the construction of an ion trapping experiment, focussing on my work towards the laser stabilization and ion trap design but also covering the experimental setup as a whole. The vacuum system that I designed allows the mounting and testing of a variety of ion trap chips, with versatile optical access and a fast turn around time.

I will also present the design and fabrication of a microfabricated Y junction and a 2-dimensional ion trap lattice. I achieve a suppression of barrier height and small variation of secular frequency through the Y junction, aiding to the junctions applicability to adiabatic shuttling operations. I also report the design and fabrication of a 2-D ion trap lattice. Such structures have been proposed as a means to implement quantum simulators and to my knowledge is the first microfabricated lattice trap.

Electrical testing of the trap structures was undertaken to investigate the breakdown voltage of microfabricated structures with both static and radio frequency voltages. The results from these tests negate the concern over reduced rf voltage breakdown and in fact demonstrates breakdown voltages significantly above that typically required for ion trapping. This may allow ion traps to be designed to operate with higher voltages and greater ion-electrode separations, reducing anomalous heating.

Lastly I present my work towards the implementation of magnetic fields gradients and microwaves on chip. This may allow coupling of the ions internal state to its motion using microwaves, thus reducing the requirements for the use of laser systems.

Acknowledgements

Some parts of my DPhil work focused on the assembly and operation of an ion trapping experiment. Due to the extent of this task this was done as part of a team. This thesis discusses the general experimental setup and results of trapping ions. Below I will outline my contributions to this work.

Chapter 3 - Experimental setup

In this chapter I describe the general experimental setup required for trapping ions. This includes a vacuum system designed to house microfabricated ion traps, this vacuum system was design and constructed by Altaf Nizamani with help from James McLoughlin, Philippa Young and myself.

Once ions were trapped several measurements were performed. Firstly the cooling laser wavelengths for each Yb isotope were measured, these measurements were carried out by myself, James McLoughlin, James Siverns and Altaf Nizamani, with the ionisation wavelengths being measured separately by Altaf Nizamani and James McLoughlin.

In order to characterise the ion trap a heating measurement was undertaken, this involved the implementation of computer control over the cooling laser and data collection, this was achieved by Altaf Nizamani and James McLoughlin. The heating measurement itself was performed by Altaf Nizamani, James mcLoughlin, James Siverns, Bjorn Lekitsch and myself.

Chapter 4 - Laser locking

In this chapter I discuss my work building a laser locking scheme to provide a reference laser with which to stabilise the cooling lasers. For this it was necessary to build a PI controller. The circuit design for this controller was provided by Dr Mattias Keller and soldered by Altaf Nizamani and James Siverns, I mounted the controller and implemented it into the locking scheme.

The design of the laser mount to house the 780 nm laser diode was based on a design provided by Prof. Hänsch and drawn by James McLoughlin. The construction and alignment of the mount, collimation lens and detraction grating was performed by myself with help from James McLoughlin.

Chapter 6 - Vacuum system

The final design of the vacuum system took many months and went through several iterations before the final design was settled upon. Significant contributions to this process was made by undergraduate project student James Sayers, who researched the optimal vacuum chambers and vacuum systems available. Additionally advice from Altaf Nizamani contributed towards the final design. The design of the custom parts were drawn by myself with contributions from James Sayers.

All other work, unless otherwise stated, is my own.

On a personal note I should first extend my full gratitude towards my supervisor, Winfried Hensinger. First for offering me the opportunity to undertake this DPhil but also for all the hours of physics discussions. His seemingly unlimited energy supply provided me with a supervisor who was always there to help and offer advice... instantaniously. I would also like to thank my second supervisor, Barry Garraway, for all the advice and guidance over the period of my degree.

However without my fellow students the accomplishments of the last few years would have been impossible, so a thank you must go to: James Siverns, James McLoughlin, Altaf Nizamani, Marcus Hughes, Bjorn Lekitsch, Seb Weidt and Kim Lake, as well as numerous undergraduates, but specifically: Tim Short, Pip Young and James Sayers. All of whom have challenged me and provided countless heated debates as well as offering much needed relief and good drinking friends.

I also want express my appreciativeness towards several members of Wolfgang Lange's lab, who despite being members of a separate group offered invaluable advice and were incredibly generous with both there time and patience, so I am indebted to: Peter Blythe, Anders Mortenson, Matthias Keller and Alex Wilson. My laser locking would have taken twice as long to work without them!

I also must thank my family, without whom I would never have had the motivation and support to complete such a challenging experience. Always there to offer advice and guidance through the many times where the reality of the undertaking seemed too great, and never complaining at my unending requirement for beer tokens and lifts. They have probably provided the most support, advice and guidance out of anybody over the course of my DPhil and I would have never managed it without them.

Importantly I want to thank all my friends, specifically: Peter Blake, Heather Mortlock, Kevin Bishop, Mark Bennett and Seb Stuart as well as many others[1] who over the many

[1] Alex, Ali, Claire, Clarence, Jenni, Jonny, Maria, Matt, Molly, Nai, Olivia, Pete n Tonic, Rosie, Sandy, Toby...

years, whether knowingly or not, have all offered huge support and a sane relief from physics when most needed. You have put up with hours of my complaining and kept me going through all the tough times.

Lastly a heartfelt thank you to Alison, who without, I might not have finished at all.

Contents

List of Tables

List of Figures

Well, of course the universe is gradually slowing down, isn't it. Huh. And, eh, and will eventually collapse inwardly on itself, according to the laws of entropy, ehm when all it's thermal and mechanical functions fail. Pheh. Thus rendering all human endeavour ultimately pointless... Just to get the ~~gig~~ thesis in some sort of context.

- Bill Bailey

Chapter 1

Introduction

Skip to the end.

- Tim Bisley - Spaced

Over the last 75 years since Alan Turing first published the idea of the Universal Turing Machine (UTM), computers have revolutionised the world we live in. Modern computers, utilizing nano-scale architectures with millions of components, can perform ever more detailed calculations and simulations of the physical world. However despite the advances in technology there still remains fundamental limitations to a classical computer's performance. No matter how much progress that can be made in hardware, the fundamental operation of a classical computer means that for some algorithms, we may never be able to solve them efficiently. An algorithm's is defined as being either efficient or inefficient depending on whether the time they take to solve a problem grows linearly with the size of the problem or exponentially. It is in this definition of efficiency that a quantum computer's power outstrips that of a classical machine.

In the early 1980's Richard Feynman and David Deutsch began to look at the idea of the quantum computer. Feynman showed that to truly simulate a quantum system you must use a quantum system to do so [6]. This introduces the idea of a quantum simulator, where a controlled quantum system is used to simulate a quantum system that is impractical to measure directly. Then in 1985 Deutsch extended Turing's idea of a UTM and formulated the idea of the Universal Quantum Computer [7], here he showed that a computer based on quantum mechanics was capable of solving certain problems efficiently where a UTM could not. This showed that a computer based on the laws of quantum mechanics has the potential to be more powerful than a classical computer can ever be. However it was not until 1994 before people began to pay much interest, this was sparked when Peter Shor published two quantum algorithms, most notably an algorithm

to efficiently find the primes factors of a number, offering an exponential improvement in computational time and known as Shor's algorithm [8]. Shor's algorithm generated significant interest because modern encryption, such as RSA, is reliant on the classical computer's inability to solve this problem efficiently. Shor's work was soon followed by Lov Grover in 1995, when Grover published a search algorithm. His algorithm reduces the number of searches required to return a specific answer from an unstructured database with N entries from an average N/2 searches to $\sqrt{N}/2$, now known as Grover's algorithm [9]. Whilst not showing the vast improvement in computational time that Shor did, the wide range of potential uses for Grover's algorithm generated considerable interest. It was only after these algorithms had been published that work truly began on building the first quantum computers.

Over the past 15 years tremendous advances have been made in the field of quantum computation, with many different approaches of implementation, with each showing varying degrees of success. The different technologies include (among others): superconducting qubits, optical photon qubits, optical lattices, nuclear magnetic resonance (NMR), cavity quantum electrodynamics (CQED) and trapped ion quantum computers. Out of these the ion trap quantum computer has shown the most promise and demonstrated all the necessary building blocks for a truly scalable quantum computer. These include: state preparation and detection [10, 11, 12, 13, 14], entanglement of many ions, performing quantum gate operations and error correction [15, 16, 17, 18, 19, 20, 21, 22, 23, 24] and ion transport through trap arrays [25, 26, 27, 28, 29, 30, 31].

The idea of a scalable ion trap quantum computer was first introduced in 2000 by J. I. Cirac and P. Zoller [32], their idea was then extended in 2002 by D. Kielpinski *et al.* [33] who introduced the idea of an ion trap array where ions are transported between regions, shuttled between interaction and storage areas. This approach offers a scalable architecture, with the potential for the control and manipulation of thousands of ions.

The first steps towards realising these scalable trap architectures were taken in 2005 with the first demonstration of trapping ions in a microfabricated semiconductor ion trap [34] and shuttling ions around a T-junction [28]. Since these initial experiments near adiabatic shuttling through X junctions has been demonstrated [30], demonstrating another fundamental requirement for a scalable ion trap quantum computers based on large ion trap arrays. Also significant advances in ion trap design and fabrication, aided by the advent of surface electrode ion traps, have produced the first generation of ion trap arrays [35, 36, 37, 38, 39, 40]. These traps have demonstrated some of the first steps towards a

truly scalable ion trap quantum computer. Despite these advances many problems still remain with microfabricated ion traps arrays. These include anomalous heating, low trap depth, rf barriers and exposed dielectrics to name a few. These technical challenges need to be overcome before a quantum computer, capable of more than the basic operations, can be built. These challenges can be divided into two categories: ion state manipulation and ion transport efficiency. This thesis focuses on the latter of the two problems: how to build ion traps with the ability to, with high precision, trap and store many ions and perform shuttling procedures. The focus of chapters 8-10 is to work towards the next generation of microfabricated ion traps, where hopefully these problems can be mitigated. However before testing of microtraps can begin it is important to first trap ions, this is the focus of chapters 3-6. This covers my work over the first few years, where along with other DPhil students and undergraduates we worked to build an ion trapping experiment up from an empty lab. In Chap. 2 I will introduce the basic operation of ion traps and the tools used to simulate the ion's behaviour inside these traps.

Chapter 2

Ion trap equations of motion and simulations

up up down down left right left right B A Start

2.1 Equations of motion

Earnshaw's theorem states that a point charge cannot be held in stable equilibrium with static electric fields. From Gauss's law, the divergence of any electric force is zero in free space; it must satisfy Laplace's equation. This means that only saddle shaped static potentials can be generated, like that shown in Fig. 2.1. If however, the saddle potential is rotated then this leads to a net force on the charged particle that always pointing towards the center of the trap.

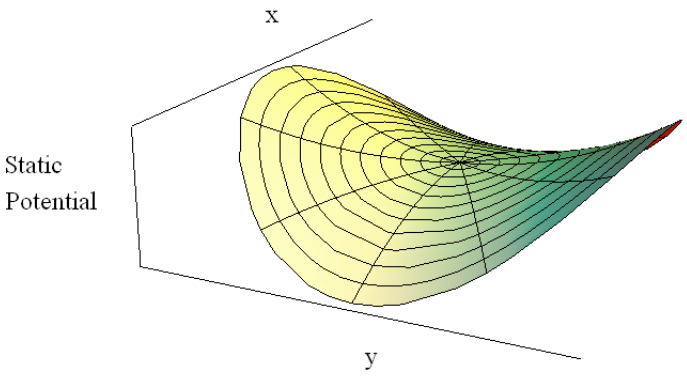

Figure 2.1: Static saddle shaped potential.

To understand how an ion trap confines charged particles it is necessary to look at the equations of motion that govern the ion inside a quadrupole ion trap. There are two primary ways we can derive the behavior of the ion. First by looking at the ponderomotive

pseudopotential. Then a more complete model involving the Mathieu equations.

2.1.1 Ponderomotive psuedopotential

We wish to derive the ponderomotive psuedopotential resultant from an inhomogeneous rf field. Following the discussion by H. G. Dehmelt [41] we can briefly outline the derivation of this potential. First we consider a particle with a charge e and a mass m in a homogeneous electric rf field, such as that produced between the parallel plates of a capacitor, shown in Fig. 2.2(a). The equation of motion of the particle in such a field is given by [41]

$$m\ddot{z} = F_z(z,t) = eE_0(z)\cos(\Omega t) \tag{2.1}$$

where $E_0(z) = V_0/(2z_0)$. We wish to find an equation which describes the particle displacement along z as a function of time. To achieve this we integrate Equ. 2.1 twice

$$z(t) = \frac{eE_0(z)}{m}\int\int \cos(\Omega_T t)dt$$

$$z(t) = -\frac{eE_0(z)}{m\Omega_T^2}\cos(\Omega_T t) + z_0 \tag{2.2}$$

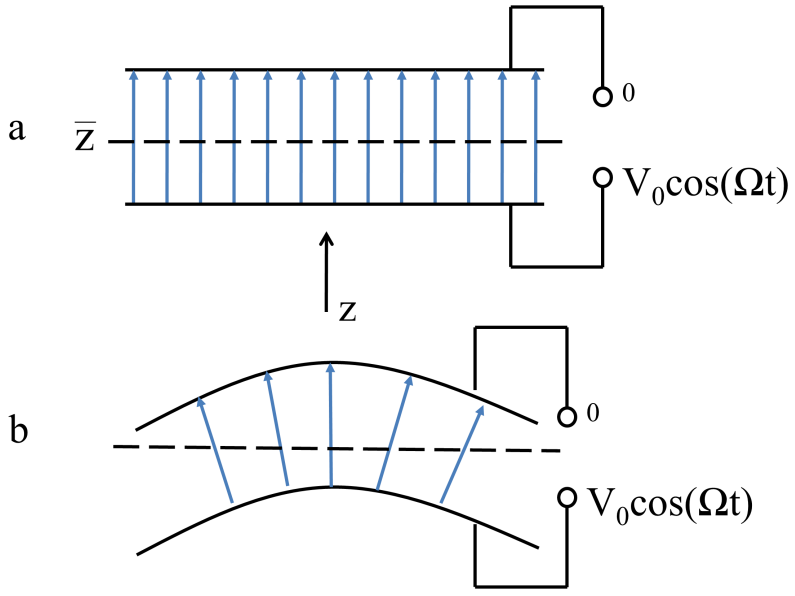

Figure 2.2: A) A homogenous field from a parallel plate capacitor. B) An inhomogeneous field from a bent parallel plate capacitor.

We can see that over one oscillation the average of force on the ion from Equ. 2.1 is zero, and therefore useless for trapping ions. If now, we make the field inhomogeneous by bending the capacitor plates as shown in Fig. 2.2(b), this inhomogeneity will slightly alter the ions orbit and the force felt by the particle. The result of this perturbation has the effect of making the time averaged force acting on the ion, finite. Making the approximation that when Ω_T is large the micromotion, which is the high frequency oscillation of the ion about the trap center, is zero. We then use the Taylor series and expand the electric field around z.

$$E_0(z) = E_0(z_0) + \frac{\partial E_0(z_0)}{\partial z}(z - z_0) + ...$$

Ignoring all higher order terms, we now substitute $z(t)$, and using the approximation that $z_0 \approx 0$ we are left with

$$E_0(z) \approx E_0(z_0) - \frac{\partial E_0(z_0)}{\partial z}\left(\frac{eE_0(z)}{m\Omega_T^2}\cos(\Omega_T t)\right). \tag{2.3}$$

Now substituting Equ. 2.3 into Equ. 2.1, we get an equation for the force on the ion in the inhomogeneous electric field.

$$F_z(z,t) = eE_0(z_0)\cos(\Omega_T t) - e\cos(\Omega_T t)\left(\frac{\partial E_0(z_0)}{\partial z}\frac{eE_0(z)}{m\Omega_T^2}\cos(\Omega_T t)\right)$$

$$F_z(z,t) = eE_0(z_0)\cos(\Omega_T t) - \frac{\partial E_0(z)}{\partial z}\frac{e^2E_0(z)}{m\Omega_T^2}\cos^2(\Omega_T t) \tag{2.4}$$

By averaging Equ. 2.4 over one oscillation, we know that the $\cos(\Omega_T t)$ term averages to zero, whilst the $\cos^2(\Omega_T t)$ averages to be a half, this now leaves

$$\langle F(z)\rangle = -\frac{e^2E_0^2}{2m\Omega_T^2}\frac{\partial E_0(z)}{\partial z}. \tag{2.5}$$

By making the substitution $\psi(z) = \frac{eE_0^2(z)}{4m\Omega_T^2}$ we get

$$\langle F(z)\rangle = -e\frac{\partial \psi(z)}{\partial z}. \tag{2.6}$$

This can be generalized to three dimensions, and is given by [41]

$$\langle F(x,y,z)\rangle = -e\nabla\psi(x,y,z). \tag{2.7}$$

Where $\psi(x,y,z) = \frac{eE_0^2(x,y,z)}{4m\Omega_T^2}$. Equation 2.7 gives the force felt by the ion from an oscillating inhomogeneous rf field. The ion motion in the ponderomotive pseudopotential can be approximated as secular harmonic motion [42], by using this approximation the ion secular frequency is given by [43]

$$\omega_p^2 = \frac{e^2}{4m\Omega_T^2}\frac{\partial^2}{\partial x^2}(|\nabla E_0(x,y,z)|^2). \tag{2.8}$$

We see that the ion will oscillate in the pseudopotential with a frequency given by Equ. 2.8. The above derivation has shown that it is possible to confine an ion in an oscillating inhomogeneous electric field, which results in an effective harmonic potential.

Numerical simulations can be used to extract the electrostatic field generated by a set of electrodes, by using these numerical results and equations 2.7 and 2.8 we can model the trap depth and ion secular frequencies from a proposed ion trap geometries.

2.1.2 Mathieu Equations

Whilst the ponderomotive pseudopotential gives an approximation a full description can be found; one that includes both the secular and micromotion of the ion. A quadrupole potential in three dimensions is given by Equ. 2.9 [44], where ϕ_0 is the applied potential, r_0 is the ion-electrode separation and λ, σ and γ are constants set by the geometry of the trap.

$$\phi = \frac{\phi_0}{2r_0^2}(\lambda x^2 + \sigma y^2 + \gamma z^2) \tag{2.9}$$

As we know the potential must satisfy Laplace's equation, $\nabla^2\phi = \frac{\phi_0}{2r_0^2}(2\lambda+2\sigma+2\gamma) = 0$ and for $\phi_0 \neq 0$, it is required that $\lambda + \sigma + \gamma = 0$. In a 2D structure a simple solution is $\lambda = 1$, $\sigma = -1$ and $\gamma = 0$, this geometry can be realised by using four hyperbolic electrodes, with opposite pairs of electrodes having potentials of $\pm\phi_0/2$, this geometry can been seen in Fig. 2.3. The 2D potential resulting for this electrode geometry is given by

$$\phi(x,y) = \frac{\phi_0(x^2 - y^2)}{2r_0^2}. \tag{2.10}$$

Now if an alternating potential of the form $\phi_{(t)} = \pm(U - V\cos(\Omega_T t))$ is applied, the potential at a point (x,y) in the ion trap is expressed as

$$\phi_{(x,y,t)} = (U - V\cos(\Omega_T t))\frac{x^2 - y^2}{2r_0^2}. \tag{2.11}$$

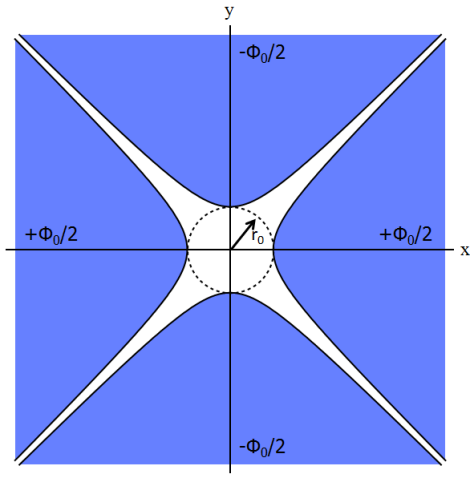

Figure 2.3: A hyperbolic electrode geometry.

We can find the force felt by an ion in this potential by calculating the gradient of the potential:

$$F_x = -e\nabla\phi_x = -e\frac{\partial}{\partial x}\Big[\frac{\phi_0(x^2-y^2)}{2r_0^2}\Big]$$

$$= -e\frac{\phi_0 x}{r_0^2}$$

substituting the force on the ion into $F_x = m\ddot{x}$ and putting in ϕ_0, we get the equations of motion for the ion in the x- and y-axes.

$$\ddot{x} + \frac{e}{mr_0^2}(U - V\cos(\Omega_T t))x = 0$$

$$\ddot{y} - \frac{e}{mr_0^2}(U - V\cos(\Omega_T t))y = 0$$

Now by using the substitutions $a = \frac{4eU}{mr_0^2\Omega_T^2}$, $q = \frac{2eV}{mr_0^2\Omega_T^2}$ and $\Omega_T t = 2\zeta$, then we obtain the Mathieu differential equations:

$$\frac{d^2x}{d\zeta^2} + (a_x - 2q_x\cos(2\zeta))x = 0 \tag{2.12}$$

$$\frac{d^2y}{d\zeta^2} - (a_y - 2q_y\cos(2\zeta))y = 0. \tag{2.13}$$

The Mathieu equations have stable or unstable solutions dependant on the values of the a and q parameters. These stable regions can be mapped out on a stability diagram, the stability diagram for our linear hyperbolic geometry is shown in Fig. 2.4. The shaded regions correspond to values of a and q that result in stable ion motion. If we imagine the ion is free to travel in the z direction, then for it to remain bound in the x- and y-axes the a and q parameters must result in stable motion in both these directions. Due to the symmetry of the trap the x and y stability diagrams are symmetric about the q-axis.

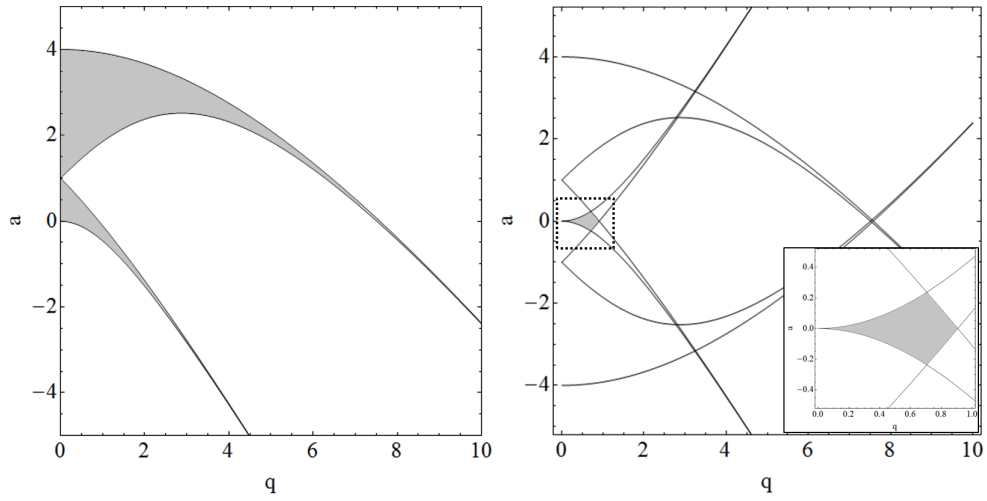

(a) (b)

Figure 2.4: a) x-axis stability diagram. b) x and y stability diagrams, inset shows the lowest stability region.

Figure 2.4(a) shows the x stability diagram with the $x-y$ stability diagram shown in Fig. 2.4(b). The lowest stability region is formed by a roughly diamond shaped section marked in grey.

Solutions to the Mathieu equations have been shown in numerous sources with detailed derivations given in [45, 46]. The solution to the Mathieu equations is given by [42]

$$u(t) = A\Big(\cos(\omega t+\phi_i)\Big[1+\frac{q}{2}\cos(\Omega_T t)+\frac{q^2}{32}\cos(2\Omega_T t)\Big]+\beta\frac{q}{2}\sin(\omega t+\phi)\sin(\Omega_T t)\Big) \quad (2.14)$$

Where $u(t)$ equals either x or y, A depends on the initial conditions and $\omega = \beta\frac{\Omega}{2}$, where $\beta \simeq \left(a+\frac{q^2}{2}\right)^{0.5}$. Equation 2.14 shows that the ion motion comprises of two distinct frequencies. Firstly the secular frequency given by $\cos(\omega_x t)$ but this is superimposed on the micromotion given by $\cos(\Omega_T t)$ which is at the rf drive frequency. The ion motion is shown in Fig. 2.5, as the ion moves away from the trap center the amplitude of the higher frequency Ω_T micromotion increases and is superimposed on top of the slower secular frequency. Typically the amplitude of the micromotion is small as a well cooled ion remains close to the trap center. However in a trap were static offset fields shift the ion equilibrium position, this micromotion can have a greater amplitude than the secular frequency. These offset fields can be compensated for and it is possible to reduce the motion of the ion well below the wavelength of incident cooling light.

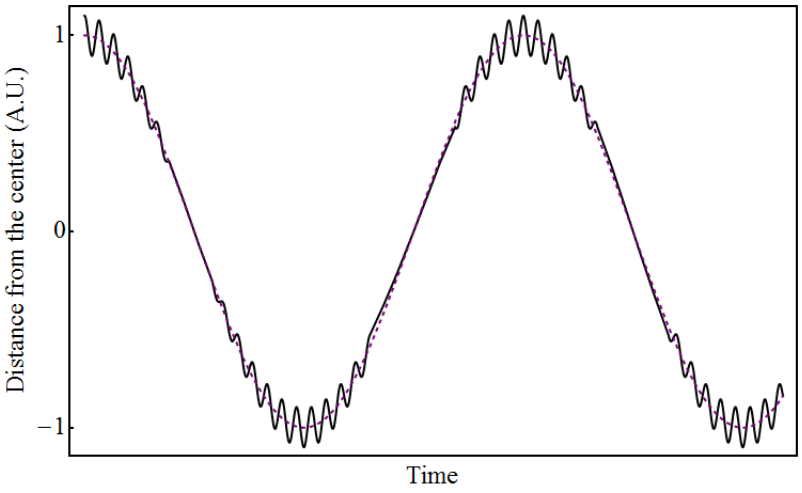

Figure 2.5: The full ion motion, the slower secular frequency with micromotion oscillation at the rf drive frequency superimposed on top. The amplitude of the micromotion increases as the ion moves away from the trap center.

2.2 Analytical model

Unfortunately the majority of ion trap modeling requires numerical methods, brute force simulations of the electrode structures. This results in large overheads in both time and computation power. Fortunately M. G. House [47] has shown an analytic model for the electrostatic fields from surface electrode ion traps. This model first defines a function that describe the electrostatic potential from an arbitrary rectangle in the y plane and given by Equ. 2.15. Using the basis function technique [48], explained is Sec. 2.4, these rectangular electrodes can be linearly summed to form the electrostatic potential of the entire trap geometry [47].

$$\begin{aligned}\phi(x,y,z) = \frac{V}{2\pi}\Bigg\{ &\arctan\left[\frac{(x_2-x)(z_2-z)}{y\sqrt{y^2+(x_2-x)^2+(z_2-z)^2}}\right] \\ &-\arctan\left[\frac{(x_1-x)(z_2-z)}{y\sqrt{y^2+(x_1-x)^2+(z_2-z)^2}}\right] \\ &-\arctan\left[\frac{(x_2-x)(z_1-z)}{y\sqrt{y^2+(x_2-x)^2+(z_1-z)^2}}\right] \\ &+\arctan\left[\frac{(x_1-x)(z_1-z)}{y\sqrt{y^2+(x_1-x)^2+(z_1-z)^2}}\right]\Bigg\}\end{aligned} \tag{2.15}$$

The model makes the assumptions that the electrostatic field is generated by a set of conducting electrodes that all lie in the $y = 0$ plane and occupy the entire plane, extending to infinity in both x- and z-axes and with infinitely small gaps between electrodes. This is the gapless plane approximation. House shows that a model to include gaps and their

electrostatic effect only slightly perturbs the potential at the ion, even for relatively large gaps. So for most simple geometries it is sufficient to assume that there is no gap. However in junction regions, where the electrode structure becomes significantly more complicated, simulations using both gaps and no gaps differ by up to a factor of two, and so this approximation should be used with caution.

Using the expression for a single electrode House then goes on to develop a model for confining ions above the electrode surface. He assumes a geometry similar to the one show in Fig. 2.6. With the rf electrodes having edges at $x = -c$ and $x = 0$ and the second with edges at $x = a$ and $x = a + b$ and the electrodes having voltages of $V_{rf}cos(\Omega t)$ at both $-c < x < 0$ and $a < x < a + b$ and 0 everywhere else, where V_{rf} is the peak rf voltage and Ω is the rf angular frequency. The 2D potential field is then given by Equ. 2.16 [47] and can been seen in Fig. 2.7. With the electric field defined the ion position above the surface is now given by $x_0 = \frac{ac}{b+c}$ and $y_0 = \frac{\sqrt{abc(a+b+c)}}{b+c}$ [47] and the trap minimum, or escape point, is given by $x_E = \frac{a}{2}$ and $y_E = \sqrt{2ab + a^2 + 2(a+b)\sqrt{2ab + a^2/2}}$ [47]. These are also marked in Fig. 2.7.

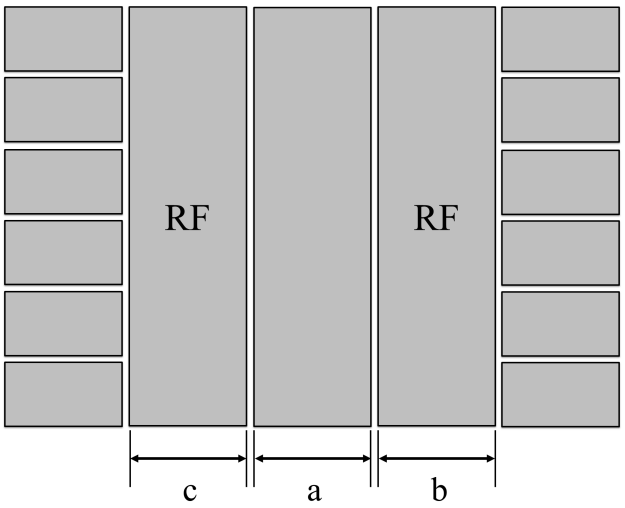

Figure 2.6: A typical surface electrode geometry, with the electrode extending to infinity in the z direction.

$$\phi(x, y, t) =$$

$$\frac{V_{rf}}{\pi}\left[\arctan\left(\frac{a+b-x}{y}\right) - \arctan\left(\frac{a-x}{y}\right) - \arctan\left(\frac{x}{y}\right) + \arctan\left(\frac{c+x}{y}\right)\right]\cos(\Omega t) \tag{2.16}$$

This analytical model can be used for simulating the basic linear rf structure of a surface electrode ion trap. It is also possible to include static voltage control electrodes

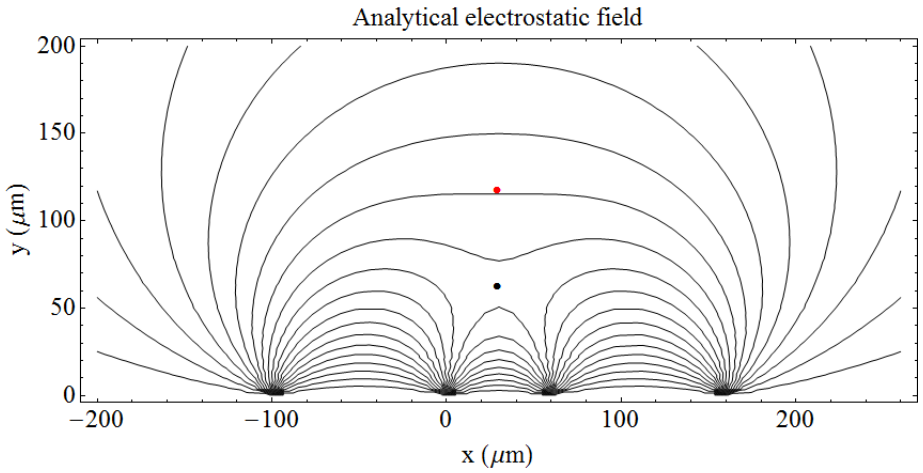

Figure 2.7: The electrostatic field produced by Equ. 2.16, where $a = 60\mu$m, $b = 100$ μm and $c = 100$ μm. The rf nil and ion escape point calculated using House's equations are marked by a black and red circle.

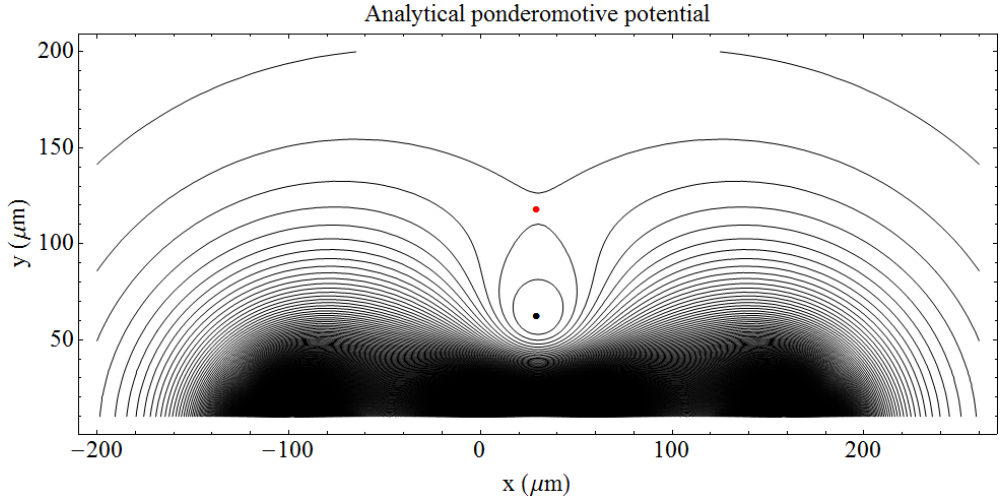

Figure 2.8: The ponderomotive potential generated by the above electrostatic field.

so that confinement along the z-axis is possible, as well as linear shuttling operations and ion combination and separation operations can all be simulated from these analytical electrostatic fields. Unfortunately the model in its current form provides only limited usefulness for more complicated electrode structures where electrode shapes are not always formed from simple rectangles and where the gapless plane approximation becomes less valid, such as junctions. In these situations it is necessary to use numerical methods to find the electrostatic potential.

2.3 Principal axis rotation

In sections 2.1.1 and 2.1.2 I showed that the ion motion is described as a 3D uncoupled harmonic oscillator. To ensure efficient laser cooling of the ion the laser's $\vec{k}$ vector must have a component along all three axes of ion motion. This is easily accomplished by ensuring that the trap axes and incoming lasers have a non zero angle between them.

For trap simulation it is simply enough to know that no axis of motion lays perpendicular to a cooling laser. Unfortunately the symmetry of many ion trap designs results in an axis of motion that lays perpendicular to the laser propagation direction. To ensure the ion is cooled in the case of 2 and 3 layer ion traps static voltages can be applied to trap electrodes, rotating the ion's principal axes of motion. For surface geometries it is possible to rotate the axes by breaking the symmetry of the rf electrodes.

At the center of the ion trap the ponderomotive potential is a quadratic of the form $F(x, y) = ax^2 + bxy + cy^2$, where a, b and c are constants and in the case were the axes of motion lay along x and y, $b = 0$. When $b \neq 0$, then we want to find the angle x and y have been rotated through. For this we can use the Hessian matrix, which for two dimensions is given by

$$\mathbf{H}f(x, y) = \begin{pmatrix} \frac{\partial^2 f}{\partial x^2} & \frac{\partial^2 f}{\partial x \partial y} \\ \frac{\partial^2 f}{\partial y \partial x} & \frac{\partial^2 f}{\partial y^2} \end{pmatrix}. \tag{2.17}$$

The Hessian matrix describes the local curvature of a function with the eigenvectors of the Hessian matrix giving the directions of pure curvature, where there is no mixed partial derivative, when $b = 0$, these eigenvectors correspond to the trap principal axes [49]. When the eigenvectors of a matrix are perpendicular and lay along the principal axis, as they do for the Hessian matrix, then we can say that they are equal to the rotation matrix [50].

So for a pseudopotential of the form $F(x, y) = x^2 + 0.5xy + y^2$, then the Hessian matrix is equal to

$$\begin{pmatrix} 2 & 0.5 \\ 0.5 & 2 \end{pmatrix}$$

Calculating the eigenvectors of this matrix will give

$$\begin{pmatrix} \frac{1}{\sqrt{2}} & \frac{1}{\sqrt{2}} \\ -\frac{1}{\sqrt{2}} & \frac{1}{\sqrt{2}} \end{pmatrix}.$$

So now by equating similar terms with the rotation matrix the angle through which the axis have been rotated is simply given by $\theta = \arccos \frac{1}{\sqrt{2}} = 45°$. When simulating ion traps we do not know the quadratic at the center of the trap, however we can find the Hessian matrix of our simulated pseudopotential at the trap center, then calculate the

corresponding eigenvectors and allowing the axis rotation to be found. Figure 2.9 shows the rf ponderomotive potential in black from a 2 layer trap. This is then rotated by applying a voltage to the static electrodes and the new potential and principal axes are shown in blue.

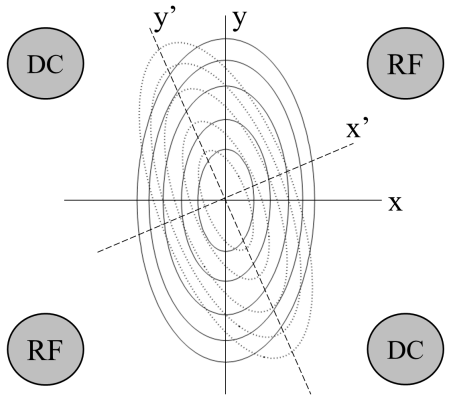

Figure 2.9: The axes of motion before rotation are shown in black, after a small voltage is applied to the static electrodes this through an angle and the new axes of motion are shown in blue.

Calculating the Hessian matrix and eigenvectors of the blue potential and comparing with the rotation matrix we find that the axes have been rotated $\approx 30°$.

2.4 Basis functions

The basis function technique is where the electrostatic field of the ion trap array can be described as a linear sum of each electrodes potential, when set to 1 volt with all the other electrodes held at ground. The justification of this is given by D. Hucul *et al.* [48], and will briefly be repeated here. The electric potential of a charge configuration with Dirichlet boundary conditions can be expressed as [51],

$$\Phi(x) = \frac{1}{4\pi\epsilon_0}\int_V \rho(x')G(x,x')d^3x' - \frac{1}{4\pi}\oint_S \Phi(x')\frac{\partial G(x,x')}{\partial n'}da'. \tag{2.18}$$

The first term in Equ. 2.18 is an integral over the internal volume of the ion trap with the appropriate Green function, $G(x,x')$, inside an empty ion trap though, $\rho(x') = 0$, leaving only the second term. This term is a surface integral over the boundary, which in our case is the surface of the electrodes multiplied by the normal derivative of the Green function with respect to the surface n'. The total trap potential can be written as a sum of the

individual electrode potentials like such [48]

$$\Phi(x') = \sum_i \Phi_i(x') \tag{2.19}$$

Now by substituting Equ. 2.19 into Equ. 2.18 we get the total trap potential [48]

$$\Phi(x) = -\frac{1}{4\pi} \sum_i \oint_{Si} \Phi_i(x') \frac{\partial G_i(x,x')}{\partial n_i'} da' \tag{2.20}$$

As the voltage is constant over the entire of the electrode surface we can now write Equ. 2.20 as a sum of voltages multiplied by the surface integral for the ith electrode [48].

$$\Phi(x) = \sum_i V_i \Theta_i \tag{2.21}$$

Where

$$\Theta_i = -\frac{1}{4\pi} \oint_{S_i} \frac{\partial G(x,x')}{\partial n'} da'$$

What this shows is that it is possible to calculate the electric potential of individual electrodes numerically, with all other electrodes held at ground, then by linearly summing these basis functions the full trap electrostatic field can be generated. Suitable electrode voltages can be applied by simply multiplying each electrode basis function by the desired voltage, or voltages can be changed to simulate ion shuttling procedures. These equations are strictly only valid for static voltages but with trap dimensions typically much smaller than the rf wavelength we can make the assumption that all voltage changes happen across the electrodes uniformly.

This allows us now to generate a simulation of an ion trap and have control over individual electrode voltages after numerical data has been collected. Basis functions for each electrode can be numerically calculated and then using Mathematica, these basis functions can be summed to generate the full ion trap potential, with totally arbitrary electrode voltages.

2.5 Numerical methods

Two primary forms of numerical simulation methods are commonly used for simulating physical systems. The most common and diverse is that of finite element method (FEM). This has been utilised to solve a huge range of problems from electrostatic fields to EM wave propagation, heat transfer, mechanical stress etc. In all these cases the basic method of simulation remains the same. The system to be simulated is drawn in the computer, nodes are spread through out the model and connected to form a mesh. This mesh contains the relevant material properties: dielectric constant, electrical conductivity, Youngs modulus, thermal conductivity etc. Then finally the computer iteratively evaluates each node giving an answer at this position. A function is then interpolated between all the nodal points. As an ion trap increases in size so does the number of required nodes, which grows as n^3, quickly making large junction regions extremely computationally costly. An alternative to FEM simulations is boundary element method (BEM), here the relevant differential equations (in our case Laplace's equation), which have been formulated as integral equations are solved. In the case where there is no charge in the trap region then only the surface integrals on the electrodes are non zero, the trap potential is purely defined by the potential surface values on the electrodes and the free space Green's function for Laplace's equation [48]. This means that the problem of finding the electrostatic potential within a trap region can be found by solving surface integrals on the electrodes. The electrode surfaces themselves are divided up into smaller bounded surfaces. This reduces the dimensionality of the problem from 3D, solving for the entire trapping volume to 2D, electrode surfaces only. This has obvious advantages when we wish to scale trap architectures up to more complicated junction regions and allows detailed simulations to take place in a matter of hours on standard lab desktop computers.

2.5.1 BEM simulation software

Initial BEM simulations where carried out using the commercial software 3D Charged Particle Optics (CPO-3D) produced by CPO Ltd. In CPO-3D the electrodes can be constructed from flat surfaces and are input by using dialog boxes. Each surface is assigned a voltage tag and is broken up into segments. The size of these segments sets the accuracy limit of the simulation.

Once the electrode structure has been constructed the surface integrals can be evaluated. Depending on the complexity of the geometry and number of segments used this could take from minutes to several hours. Once the equations have been evaluated electric

potential data can be extracted. By choosing a region inside the ion trap a mesh of data points can be taken. At each point in this 3D mesh the electric potential is calculated. This results in a data file listing the x, y, z position and the corresponding electric potential. A detailed explanation of how a simulation is performed using CPO-3D is given in App. A, this offers a step-by-step guide to electrode input and data acquisition.

Alternatively to using CPO-3D there is the bemsolver [52], which is a C++ program written for the open source Root compiler. This too uses boundary element method to generate the electrostatic potentials but has the advantage of reading .dxf file formats. This allows ion trap geometries to be drawn in computer aided design software such as AutoCAD or TurboCAD. The CAD file can then be read by the program and the electrode geometry simulated. This has a major advantage over CPO-3D as the complexity of the electrode geometry at junction regions is often nearly impossible to generate with the standard CPO-3D electrode library. For the optimisation of the SOI Y junction, iterative modifications to the junction rf geometry were made to reduce the rf barrier height. This would have proved extremely difficult and very time consuming if this had been attempting using CPO-3D.

First the trap geometry must be drawn. An initial drawing for the ion trap already existed but had been drawn using Solidworks. The traps simulated using the bemsolver were surface electrode arrays so to convert the Solidworks part to a .dxf the part was imported into a drawing and saved as a .dxf. This though is not sufficient as the individual voltage tags for electrodes are assigned by selecting appropriate electrodes and giving them a unique layer. Additionally the solver only produces accurate results when the electrode line boundary is a four sides polygon. This requires the Solidworks .dxf to be traced using 3D Polylines, then for each individual electrode a unique layer assigned. This was performed using TurboCAD. Once the initial drawing had be made further adjustments to the electrodes could be made directly in TurboCAD. Figure 2.10 shows an early TurboCAD drawing of a Y junction. Red lines correspond to the rf geometry whilst the green lines correspond to the ground electrodes.

In this simulation the rf and static electrodes are touching, using the gapless plane approximation. Figure 2.11 shows a later electrode geometry this time including realistic trenches. This simulation includes both trench walls and trench bottoms, this inclusion was found to make a significant difference to the rf potential barrier.

Using a text editor a C++ program can be edited to read our .dxf file and extract data in a similar format to that extracted via CPO-3D. This allows us to use the same

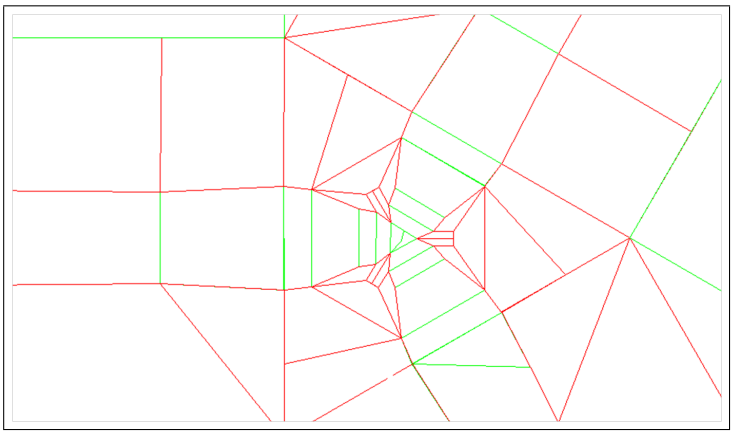

Figure 2.10: Early junction design using the gapless plane approximation. RF electrodes are red with static electrodes in green.

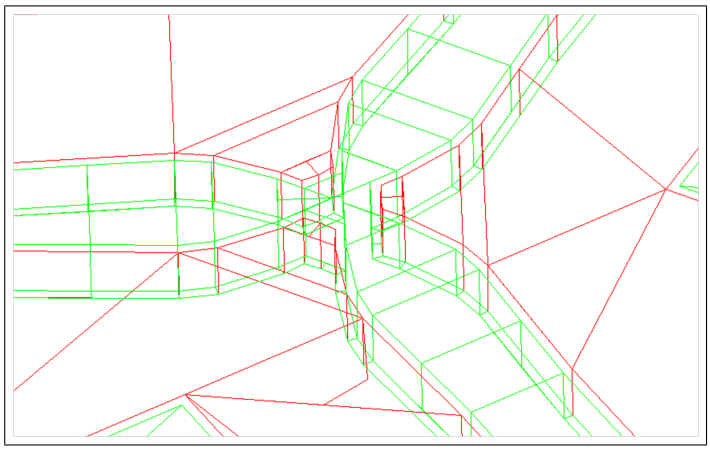

Figure 2.11: A more complete simulation including trenchs.

Mathematica notebooks.

2.6 Mathematica

After extracting electrode basis functions, either from CPO-3D or Root, the raw data files are then processed using Mathematica. Mathematica offers all the mathematical tools required for processing the electrode data as well as having a large range of symbolic processing capability.

Figures 2.12, 2.13 and 2.14 show a demo Mathematica notebook with the basic steps required to process the raw data. The beginning of the notebook starts by defining the constants for the simulation. These include the electron charge, ^{171}Yb mass, rf drive frequency and ψ, which is the product of all the constants from Equ. 2.7. Next the data is read into the notebook via the `Import` function. The data from both CPO and bemsolver

Constants

```
e =  1.6 10^-19;
my =  171 × 1.66 10^-27;
Ω =  2 Pi 45 10^6;
ψ =  e^2 / (4 my Ω^2);
```

Data input

```
dataRF =
  Import["C:\\Users\\Robin\\my documents\\physics\\ROOT\\my Y\\Y redraw\\MASK\\MASK
     2\\mask2 model\\southampton_mask_confirmation.dat", "Table"];
```

Conversion to meters

```
For[i = 1, i < Length[dataRF] + 1,
     For[j = 1, j < 4,
  {dataRF[[i, j]] = dataRF[[i, j]] / 1000}
   j++];
 i++]
```

Interpolation of the data

```
RF = Interpolation[dataRF]
```

```
InterpolatingFunction[{{-0.001, 0.00005}, {-0.0001, 0.0001}, {0., 0.0002}}, <>]
```

```
InterpolatingFunction[{{-0.001`, 0.00005`}, {-0.0001`, 0.0001`}, {0.`, 0.0002`}}, "<>"]
```

Evaluation of the ponderomotive pseudopotential

```
RFbase[x_, y_, z_] = 280 RF[x, y, z];
pondpotential[x_, y_, z_] =
  ((D[RFbase[x, y, z], x])^2 + (D[RFbase[x, y, z], y])^2 + (D[RFbase[x, y, z], z])^2);
Totalpotential[x_, y_, z_] = ψ pondpotential[x, y, z];
ContourPlot[Totalpotential[x / 10^6, y / 10^6] / e^2, {x, -200 , 300},
 {y, 5 , 350 }, Contours → 150, ContourShading → False, AspectRatio → Automatic,
 FrameLabel → {"x (μm)", "y (μm)"}, FrameStyle → Small, ContourLabels → Automatic]
```

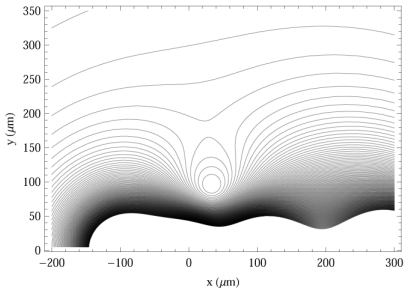

Figure 2.12: Mathematica demo notebook, showing the import and analysis of the raw data to calculate the rf ponderomotive potential.

have the format of four columns, corresponding to the x, y, z position and the electric potential at that position. The position data is given in millimeters so first this must be converted to meters. This is done by using two `For` loops, simply dividing the x, y, z positions by 1000, shown in "Conversion to meters" in Fig. 2.12.

Now the data is in the correct units a function can be generated to represent this data. This is done by using the `Interpolation` function, Mathematica fits a polynomial curve between each successive data point. This results in a smooth curve which passes through all the data points.

Under the heading of "Evaluation of the ponderomotive potential" in Fig. 2.12, the

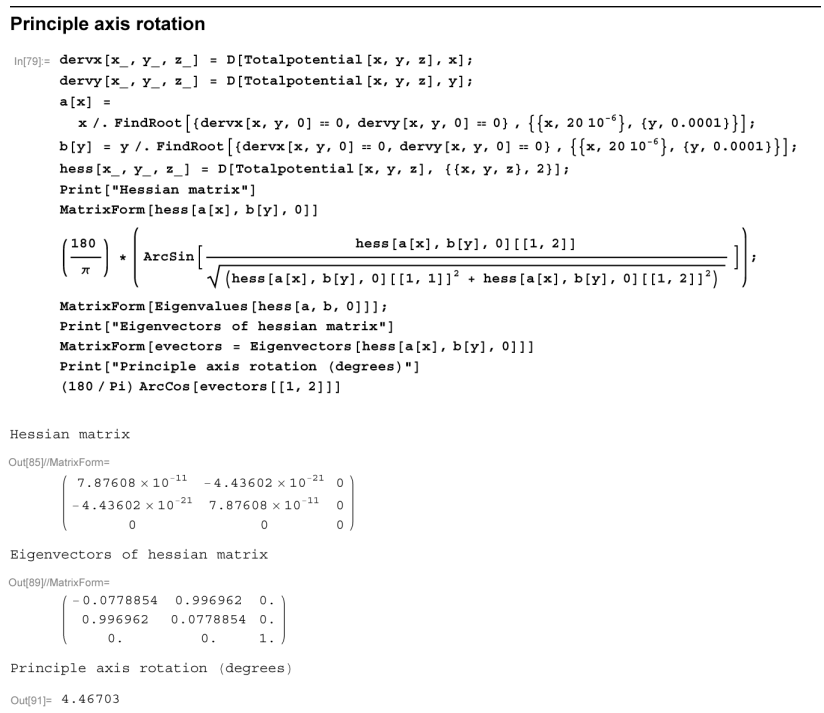

Figure 2.13: Mathematica demo notebook, calculating the angle through which the principal axis have been rotated.

interpolated function representing the rf basis function is first multipied by the peak rf voltage, 280 V. This is then differentiated with respect to x, y and z and squared, finally this function is multiplied by ψ yeilding the ponderomotive potential for, in this case, a drive frequency of $\Omega = 2\pi\times45$ MHz and peak rf voltage $\mathrm{V}_{RF} = 280$ V. A contour plot of the ponderomotive potential is show below this.

To calculate the trap depth and the secular frequency it is first necessary to find the angle through which the principal axes have been rotated. Figure 2.13 shows the code used to calculate the axis rotation using the Hessian matrix, as discussed in Sec. 2.3. This starts by finding the rf nil of the ion trap. Defining two functions `dervx` and `dervy`, which is the ponderomotive potential differentiated with respect to x and y respectively, then using the `FindRoot` function, lines 3 and 4 of Fig. 2.13, Mathematica can search for roots close to an initial guess given by the user. Since the rf nil and ion escape point are turning points of the ponderomotive potential, `dervx` and `dervy` will have a zero crossing at these positions. Using `FindRoot` to find the position where both `dervx` and `dervy` are equal to zero will yeild the position of the rf nil or ion escape point, which one will depend on the position of the initial guess.

Following this the Hessian matrix is defined and using the `Eigenvectors` function the eigenvectors of the Hessian matrix are found at the rf nil. Looking at the outputs in Fig.

Trap depth and secular frequencies

```
In[228]:= θ = -evectors[[1, 1]];
          derivxrot[x_, y_, z_] = D[Totalpotential[x Cos[θ] - y Sin[θ], x Sin[θ] + y Cos[θ], z], x];
          derivyrot[x_, y_, z_] = D[Totalpotential[x Cos[θ] - y Sin[θ], x Sin[θ] + y Cos[θ], z], y];
          an = x /.
             FindRoot[{derivxrot[x, y, 0] == 0, derivyrot[x, y, 0] == 0}, {{x, 20 10^-6}, {y, 90 10^-6}}];
          bn = y /. FindRoot[{derivxrot[x, y, 0] == 0, derivyrot[x, y, 0] == 0},
               {{x, 20 10^-6}, {y, 90 10^-6}}];
          at = x /. FindRoot[{derivxrot[x, y, 0] == 0, derivyrot[x, y, 0] == 0},
               {{x, 20 10^-6}, {y, 170 10^-6}}];
          bt = y /. FindRoot[{derivxrot[x, y, 0] == 0, derivyrot[x, y, 0] == 0},
               {{x, 20 10^-6}, {y, 170 10^-6}}];
          secx[x_, y_, z_] = (1 / my) * (D[Totalpotential[x Cos[θ] - y Sin[θ],
                x Sin[θ] + y Cos[θ], z], {x, 2}]);
          secy[x_, y_, z_] = (1 / my) * (D[Totalpotential[x Cos[θ] - y Sin[θ],
                x Sin[θ] + y Cos[θ], z], {y, 2}]);
          Print["Trap depth (eV)"]
          (Totalpotential[at, bt , 0] - Totalpotential[an, bn , 0]) / e
          Print["x' secular frequency (MHz)"]
          Sqrt[secx[an, bn, 0]] / (2 π 10^6)
          xyzhey[x_, y_, z_] =
            (1 / my) * (D[Totalpotential[x Cos[θ] - y Sin[θ], x Sin[θ] + y Cos[θ], z], {x, 2}]);
          Print["y' secular frequency (MHz)"]
          Sqrt[secy[an, bn, 0]] / (2 π 10^6)
          ContourPlot[Totalpotential[(x Cos[θ] - y Sin[θ]) / 10^6, (x Sin[θ] + y Cos[θ]) / 10^6, 0] / e ,
           {x, -200 , 200}, {y, 20 , 400 }, Contours → 100, ContourShading → False,
           AspectRatio → Automatic, FrameLabel → {"x (μm)", "y (μm)"},
           FrameStyle → Small, ContourLabels → Automatic]

Trap depth (eV)

Out[238]= 0.156015

x' secular frequency (MHz)

Out[240]= 2.65108

y' secular frequency (MHz)

Out[243]= 2.65108

Out[244]=
```

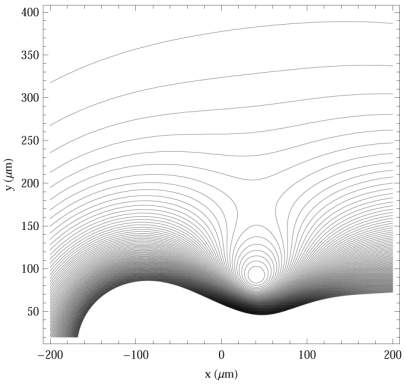

Figure 2.14: Mathematica demo notebook, calculating the trap depth and ion secular frequencies.

2.13 it can be seen that only the first four matrix elements of the Hessian matrix are non zero. This is because the ponderomotive potential is a linear Paul trap so there is no confinement, hence no curvature, along the z axis.

Figure 2.14 shows the code used to calculate both the ion secular frequencies and ion trap depth. By using the rotation matrix we can substitute the x and y coordinates for our rotated principal axes x' and y', where $x' = x\cos\theta - y\sin\theta$ and $y' = x\sin\theta + y\cos\theta$. It is then necessary to calculate both the rf nil and ion escape point in the rotated frame,

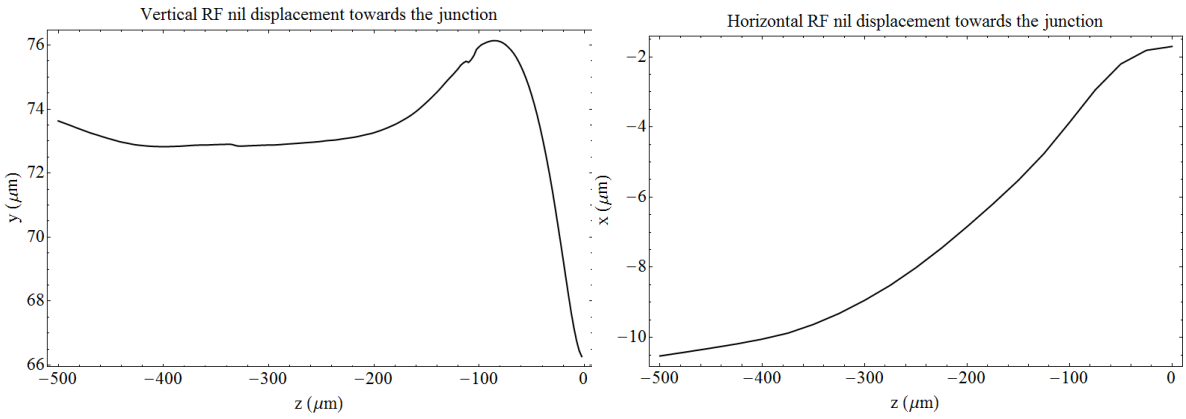

(a) (b)

Figure 2.15: a) is the vertical displacement towards the junction, b) the horizontal displacement parallel to the trap surface, where x = 0 μm corresponds to the mid point between to two rf electrodes.

this is be done in the same way as previous discussed. With the positions of the rf nil and escape point known it is now possible to calculate the secular frequencies and trap depth. To calculate the secular frequencies two functions are defined, `secx` and `secy`, these take the ponderomotive potential and substitute it into Equ. 2.8. Then the trap depth is calculated by finding the potential difference between the escape point and rf nil. The trap depth and secular frequencies are output at the bottom of Fig. 2.14, with the depth given in eV and secular frequencies in MHz.

2.6.1 RF barrier

It is possible to extend the `Findroot` function to not only find the rf minimum at one specific z position, but along the length of the trap. This is crucial as the rf minimum position relative to the trap electrodes moves as the ion approaches a junction. To calculate the rf minimum line a `For` loop calculates the rf minimum position at n positions along the z-axis and records the position in an array. The potential can now be calculated by evaluating the potential at each n position.

Figure 2.15 shows the rf minimum position as the ion approaches the Y junction. After evaluating each position the rf potential barrier can be found. Figure 2.16 shows the potential barrier when the data from Fig. 2.15 is evaluated. This shows the potential barrier the ion has to overcome when approaching a junction. By making alterations to the trap electrodes it is possible to reduce this barrier and aid adiabatic ion shuttling.

These methods were used when simulating the microfabricated ion trap geometries

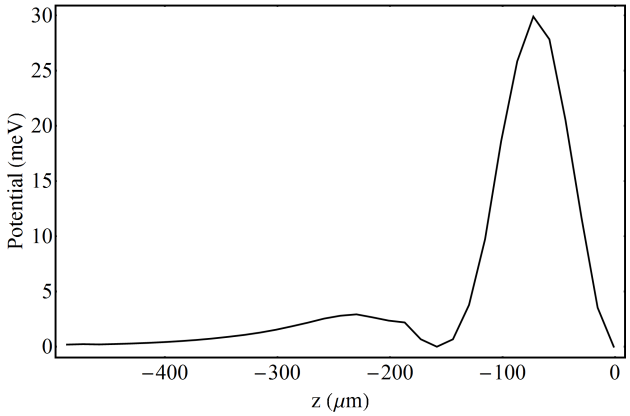

Figure 2.16: The ponderomotive potential potential barrier towards the Y junction.

presented later in this thesis. With the exact potentials and rf barriers corresponding to the trap designs being described in more detail.

Chapter 3

Experimental setup

...they mostly come at night... mostly.

- Newt - Aliens

3.1 Introduction

There are many aspects to successfully trapping and storing ions. With a wide range of technologies required to successfully build an experiment, it poses a difficult set of challenges. These include ultra high vacuum systems, capable of maintaining vacuum pressures of 10^{-12} Torr. Inductively coupling high voltage radio frequency supplies to the vacuum system using a helical resonator. Laser systems and laser stabilization to provide frequency stabilized sources of electromagnetic radiation, necessary for the creation of ions, as well as Doppler and ground state cooling and to perform quantum information processing (QIP). The experimental setup constructed to trap ytterbium ions is described below and discusses the main aspects relevant to trapping our first ions.

3.2 Ytterbium

Electrodynamically trapped ions have long been used for the study of quantum mechanics. Experiments have demonstrated unparalleled levels of quantum control over both the ions internal and motional degrees of freedom [10, 11, 13, 12, 14, 16, 18, 15, 21, 23]. To date many different species of ion are being investigated, these include Ba^+ [53], Be^+ [54], Ca^+ [55, 56, 57, 58, 59], Cd^+ [60], Mg^+ [61], Sr^+ [39, 62] and Yb^+ [63, 64, 65, 66]. Each species of ion offers a unique quantum system with each offering there own range of benefits and drawbacks. However ytterbium in particular offers several attractive features. These include optical transitions that all lay in or close to the optical spectrum, between

Isotope	$^1S_0 \leftrightarrow ^1P_1$ transition wavelength [nm]	$^2S_{1/2} \leftrightarrow ^2P_{1/2}$ transition wavelength [nm]	$^2D_{3/2} \leftrightarrow ^3D[3/2]_{1/2}$ transition wavelength [nm]
$^{170}Yb^+$	398.91051(6)	369.52364(6)	935.19751(19)
$^{171}Yb^+$	398.91070(6)	369.52604(6)	935.18768(19)
$^{172}Yb^+$	398.91083(6)	369.52435(6)	935.18736(19)
$^{174}Yb^+$	398.91114(6)	369.52494(6)	935.17976(19)
$^{176}Yb^+$	398.91144(6)	369.52550(6)	935.17252(19)

Table 3.1: Ytterbium ion transition wavelengths in vacuum. The ionisation $^1S_0 \leftrightarrow ^1P_1$ wavelengths correspond to our setup with a 63° angle between the ion and laser beam.

369 nm and 935 nm. This is beneficial as it removes the need for expensive custom optics and all wavelengths are achievable with diode laser systems. Additionally $^{171}Yb^+$ has a spin half nucleus, which allows for straight forward and efficient preparation and detection of the hyperfine ground state levels.

The energy level scheme for $^{171}Yb^+$ is show in Fig. 3.1, with the two ground state hyperfine levels $^2S_{1/2}|F = 0, m_f = 0\rangle$ and $^2S_{1/2}|F = 1, m_f = 0\rangle$ serving as the $|0\rangle$ and $|1\rangle$ qubit states respectively. Laser cooling and ion detection is achieved by driving the $^2S_{1/2}(F = 1) \rightarrow^2 P_{1/2}(F = 0)$ transition with a laser at ≈ 369.5 nm, the exact wavelengths are given in Tab. 3.1. However the $^2P_{1/2}$ state will also decay into the metastable $^2D_{3/2}$ level with a probability of 0.005, therefore a second laser at ≈ 935.2 nm is required [64]. The 935.2 nm laser excites the $^2D_{3/2}(F = 1) \rightarrow^3 D[3/2]_{1/2}(F = 0)$ transition where it then decays back to the ground state. Additionally there is a finite probability that the 369 mn laser will off resonantly excite the $^2P_{1/2}(F = 1)$ state where it will either decay to the $^2D_{3/2}(F = 1)$ or $^2D_{3/2}(F = 2)$ state where it will then be repumped with the 935 nm laser back to the $^2S_{1/2}(F = 0)$ level [67]. To ensure that the ion is pumped out of either of these states additional sidebands are added to both the 369 nm and 935 nm lasers at 14.7 GHz and 3.08 GHz respectively.

A final repump laser is required due to inelastic collisions between the ion and the residual background gas, this can result in the ion being knocked into the $^2D_{5/2}$ state where it subsequently decays to the $^2F_{7/2}$ state which has a lifetime of ≈ 6 years [68]. To bring the ion back to the ground state a third laser scanning between 638.610 nm and 638.616 nm excites the $^2F_{7/2}(F = 3\&4) \rightarrow^1 D[5/2]_{5/2}(F = 2\&3)$ transition where it subsequently decays back to the $^2D_{3/2}$ state.

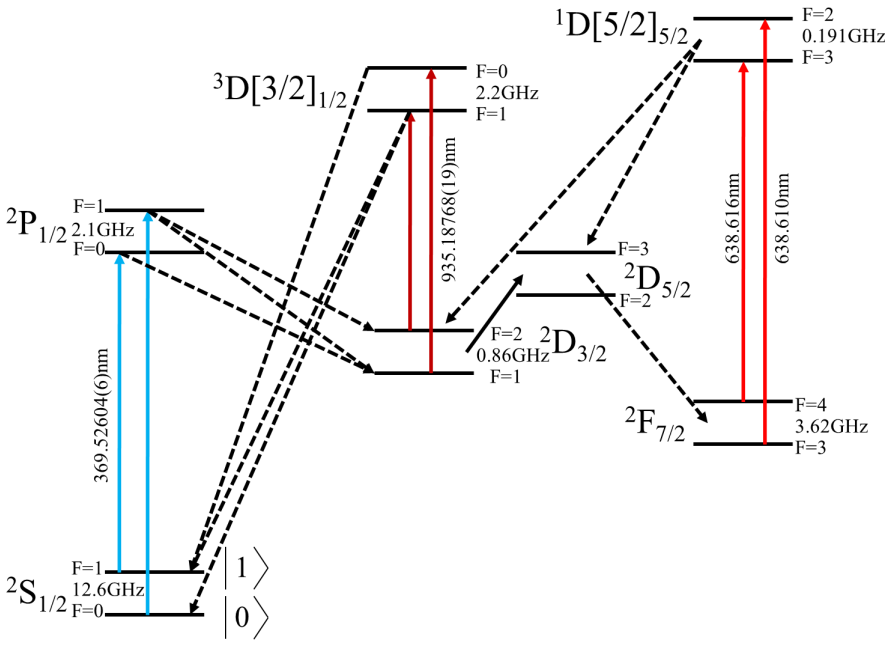

Figure 3.1: Energy level diagram for $^{171}Yb^{+}$.

Lastly a fourth laser is used for photoionisation. A neutral flux of ytterbium passes through the trapping region from an ohmically heated atomic oven. A laser at $\approx$ 398.91 nm is focused at the trap center along with the three other lasers. The 398 nm laser excites the neutral Yb $^1S_0 \leftrightarrow ^1P_1$ transition and the atom is then ionised by a second photon at 369 nm, which excites the electron from the $^1P_1$ state into the continuum. This is known as two colour photoionisation and allows isotope selective loading by tuning the ionisation laser frequency.

3.3 Doppler cooling

The simplest and most common form of laser cooling for trapping and storing ions is that of Doppler cooling. By red detuning the laser from the resonant atomic electric dipole transition, the laser, in the ions reference frame, will be Doppler shifted to be resonant when the ion is moving towards the laser and suppressed when moving away from the laser. Momentum imparted from resonant photons slow the ions motion, cooling the ion.

When the ion is trapped such that the natural linewidth is much larger than the secular frequency of the ion, $\Gamma \gg \omega_{sec}$, known as weak binding [69], the scattering events will take place in a time much faster than the ion oscillation. While the ion moves towards the laser beam, its velocity will increase until the incident laser frequency is Doppler shifted to be resonant with the dipole transition. At this point the ion absorbs and scatters photons,

for each absorption the ion receives a momentum kick of $p_a = \hbar\vec{k}$, slowing its motion, where $\vec{k}$ is the laser wavevector. After absorbtion the ion will quickly decay back into the ground state by releasing another photon. This spontaneous emission results in a second recoil momentum kick but this time in a random direction. By averaging over a large number of spontaneous decays then the net recoil momentum imparted to the ion is zero, resulting in an overall damping force. When the ion begins to move in the opposite direction, away from the laser, then the Doppler shift experienced by the ion moves the laser frequency further from resonance, suppressing photon absorbtion and preventing the laser from heating the ion.

The average momentum imparted to the ion from spontaneous photon emissions is zero, but the ion will undergo a random walk in momentum space. This is because of the finite transfer of momentum from each photon emission. For optimum cooling the laser should have a detuning of $\Gamma/2$, this puts a limit on the lowest kinetic energy of the ion given by [69]

$$k_B T = \frac{\hbar\Gamma}{2}. \tag{3.1}$$

Where k_B is the Boltzmann constant and T is temperature. For $^{171}Yb^{+}$ with a natural linewidth of $\Gamma/2\pi = 19.6$ MHz, the lowest temperature achievable with Doppler cooling is 470 μK.

For cooling below this requires more advanced cooling methods such as sideband cooling and electromagnetically induced transparency (EIT) however for initial ion trapping and ion heating measurements Doppler cooling is sufficient, and these methods will not be discussed here.

3.4 Vacuum system

To house the ion trap experiment an ultra high vacuum (UHV) system needed to be constructed. To reduce collisions between the trapped ion and background gases, which can destroy the quantum state of the ion and knock the ion out of the trap, it is desirable to achieve a pressure of $\approx 10^{-12}$ Torr. This is possible with modern systems and by using careful and thorough cleaning and assembly procedures.

The ion trap and atomic ovens are all housed in a Kimball Physics octagon and hemisphere, (part numbers MCF450-MH10204/8-A and MCF450-SO20008-C respectively).

These were chosen as they provide both, rear side laser access for symmetric traps but also parallel access to the trap surface for surface electrode ion traps.

To evacuate the system several different pumps are employed, first a turbomolecular pump brings the pressure down to $\approx 10^{-6}$ Torr. Then the whole vacuum assembly is baked in an oven at 200°C. During baking the system is pumped by two ion pumps, the first is attached to the turbo pump outside the oven and the second is attached to the vacuum system inside the oven. After two weeks the vacuum system is removed from the oven and mounted on the optical table with only the vacuum system ion pump running. At this point the vacuum system now has a pressure of $\approx 10^{-10}$ Torr. A titanium sublimation pump, also attached to the vacuum system, then deposits a layer of titanium on the inside of the vacuum system. Stray atoms and molecules react with the titanium sticking to it, (this does not work for noble gases). The titanium pump runs several times until the pressure reaches 10^{-12} Torr.

As well as the pumps and hemisphere a residual gas analyser (RGA) is attached to the system. This allows leak testing of the vacuum flanges. By passing helium over the flanges it is possible to measure an increase in the helium partial pressure inside the system and fix any leaks before the system is baked. The whole vacuum system can be seen in Fig. 3.2. This shows the hemisphere, RGA, ion pump, titanium sublimation pump and D-type connectors.

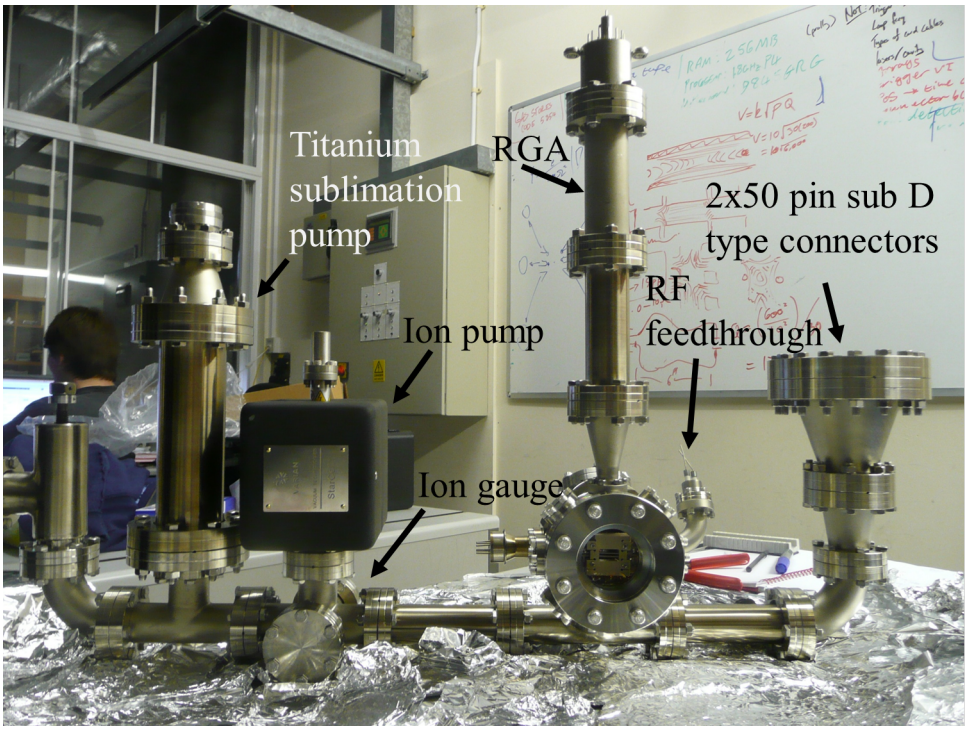

Figure 3.2: The whole vacuum system.

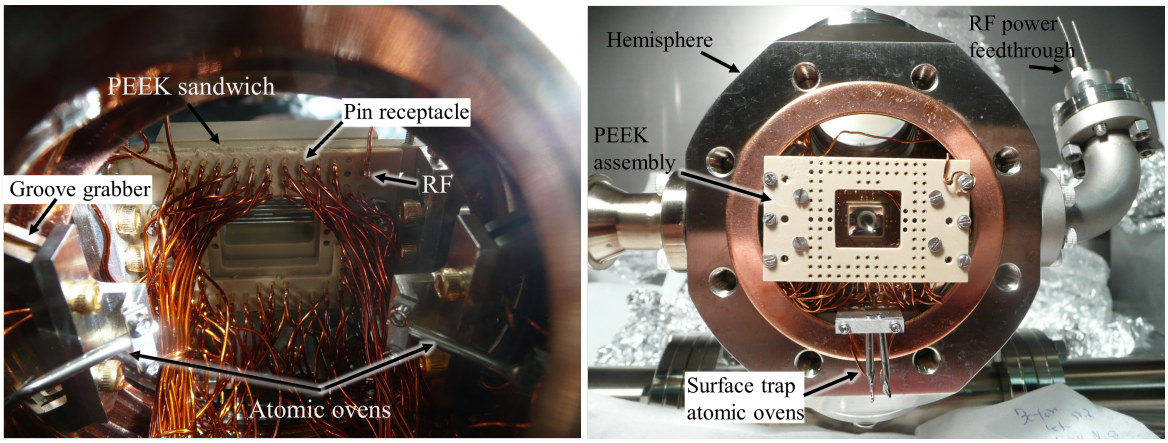

(a) (b)

Figure 3.3: Left shows the inside of the hemisphere from behind. It shows the Kapton coated wires connected to the pin receptacles, the atomic ovens and the groove grabbers. Right shows the front of the PEEK assembly before the hexagon has been attached. The chip carrier connects into the pin receptacles with atomic ovens beneath for surface trap loading.

The ion trap mount and electrical assembly is designed for chip carrier mounted traps, specifically the 101-pin ceramic pin grid array (CPGA) chip carrier, (Global Chip Materials, part number PGA10047002). The chip mounting bracket is made from UHV compatible PEEK, 90 gold coated pin receptacles, (Mill-Max, part number: 0672-1-15-15-30-27-10-0), are sandwiched between two PEEK plates, the chip bracket assemble can be seen in Fig. 3.3. Kapton insulated wires are crimped into the back of these receptacles and connect to a 2×50 pin sub D-type feedthrough connectors mounted on a 6" blank flange. Two more receptacles are used for rf and ground. These are connected by short thick bare copper wires to a 2 pin power feedthrough. To prevent shorting these wires are insulated with ceramic beads. The whole assemble is held in place by groove grabbers, these screw onto the PEEK mounts and then grab onto grooves machined in the hemisphere and octagon.

Atomic ovens containing both natural ytterbium and enriched ^{171}Yb are positioned behind the trap for backside loading and at the bottom in front of the trap for front side loading of surface traps. The ovens are constructed from a stainless steel tubes and are ohmically heated by passing current through them. Power is supplied to the ovens via an eight pin power feedthrough. The ytterbium leaves the oven in a diverging spray, which at the center of the trap is $\approx 60°$ to the ionization laser for symmetric traps and at $90°$

for surface traps.

Laser access is via eight $1\frac{1}{3}$" CF mounted fused quartz silica windows, these are mounted around the system to allow optical access for any type of trap. The windows are all anti reflection coated for all the wavelengths and incident angles, the reflection curves for the AR coatings are given in Fig. 3.5(a). A custom $4\frac{1}{2}$" CF mounted re-entrant window is attached on the front on the chamber and allows access of a microscope objective close to the trap center, with a window to ion distance of 4 mm, the dimensions of the window are given in Fig. 3.4. Figure 3.5(b) shows the anti reflection coating for the imaging window, optimised for 369 nm at both zero degrees and 40°, the angle of the exiting beam.

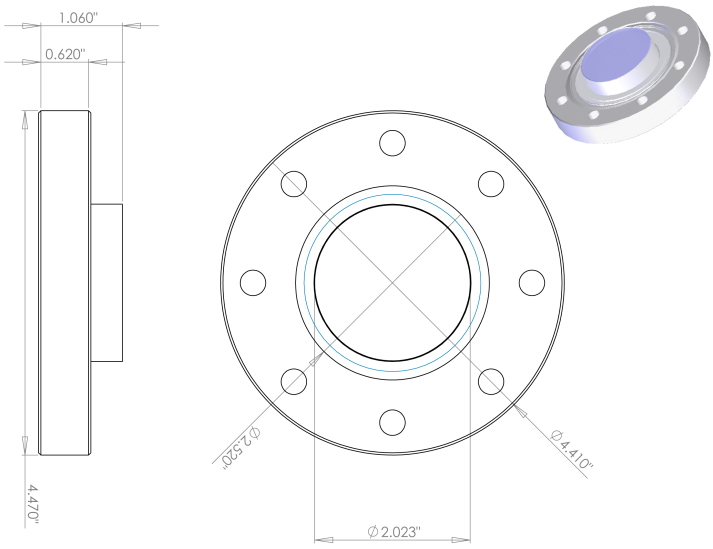

Figure 3.4: The design for the custom imaging window. This was designed by fellow DPhil student Altaf Nizamani.

3.5 Helical resonator

To impedance match our rf amplifier (NP Technologies, model #NP-541, serial #3282) to the ion trap a helical quarter wave resonator is used to inductively coupled the two. The design of a resonator is an antenna coil and helical coil inside of a grounded copper shield. The helical coil is electrically connected to the ion trap through a high power vacuum feedthrough. By adjusting the mutual inductance between the antenna and helical coil it is possible to match the impedance of the source, with an impedance of 50 Ω, to the impedance of the ion trap. Impedance matching ensures that there are no dangerous reflections that can be harmful to equipment and that the maximum power is delivered

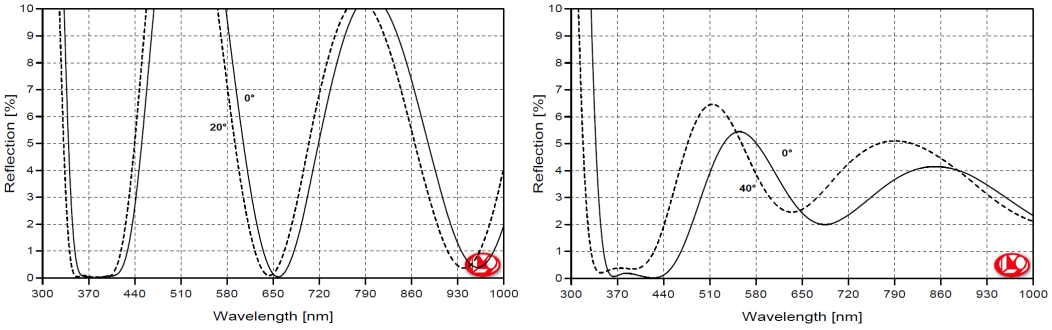

(a) (b)

Figure 3.5: a) Reflection curves for the laser access windows showing the reflection for zero degrees and 20°. b) Reflection curves for the imaging window, this has been optimised for 369 nm at both 0° and 40°.

to the trap. The resonant frequency of a resonator and the Q of the resonance are given by equations 3.2 and 3.3 respectively

$$f_0 = \frac{1}{2\pi\sqrt{LC}} \tag{3.2}$$

$$Q = \frac{1}{2\pi f_0 CR} \tag{3.3}$$

where L is the inductance, C is the capacitance and R is the resistance of the circuit. A high Q value is important for two reasons, firstly a high Q acts as a filter, reducing the power at unwanted frequencies, specifically frequencies close to the ions secular motion which would lead to increased ion heating. Secondly the peak rf voltage is a function of the resonator Q and is given by

$$V_{peak} = \kappa\sqrt{2PQ} \tag{3.4}$$

where P is power and κ is a unitless scaling factor given by the dimensions of the resonator.

An equivalent circuit diagram of a resonator connected to a load is shown in Fig. 3.6. The load resistance and capacitance, which are contributions from the ion trap as well as the vacuum system and other resistances and capacitances have a detrimental effect on the resonator Q and reduces the resonant frequency f_0. A full explanation on the operation of resonators with ion traps is given by J. D. Siverns *et al.* [70].

The resonator used for our experiment has a Q = 574 ± 46 without the ion trap attached and resonant frequency of 87.46 ± 0.30 MHz. The capacitance and resistance of the blade

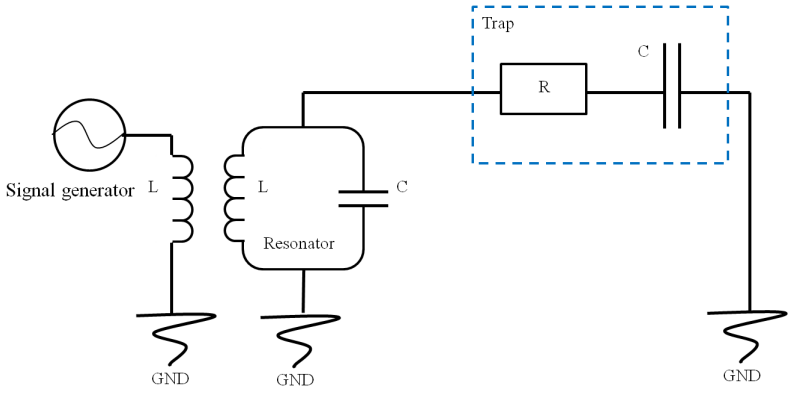

Figure 3.6: Equivalent circuit diagram for a resonator connected to an ion trap.

ion trap were measured to be $C_{trap} = 17 \pm 2$ pF and $R_{trap} \approx 0.1\ \Omega$. This resulted in a $Q_{trap} = 113 \pm 13$ when attached to the ion trap, and with a resonant frequency of $f_{trap} = 21.49 \pm 0.30$ MHz.

By measuring ω_x and ω_y secular frequencies of a single trapped $^{174}Yb^{+}$ ion and comparing with numerically simulated secular frequencies it is possible to infer a peak rf voltage. This yielded an rf electrode voltage of 930 ± 10 V, with an applied power of ≈ 13 W, which from Equ. 3.4 gives a $\kappa = 16.96 \pm 1.40$.

3.6 Lasers and imaging

All the lasers required for cooling and repumping are external cavity diode lasers, and with the exception of the 369 nm frequency doubled system were built in house, this is discussed further in Chap. 4.

Imaging of the trapped ions is achieved by using a triplet objective lens, (Special Optics, part number: 54-17-29-369), followed by a doublet. This is capable of imaging a diffraction limited ion onto either an electron multiplied CCD array (EMCCD), (Andor, part number: iXon885) or photon multiplier tube (PMT), (Hamamatsu, part number: H8259-01), the choice of which is determined by the experiment taking place. The imaging tube is constructed from Thorlabs lens tubes and held in place by a xyz translation stage. Alignment of the imaging triplet and focusing on the ion is achieved by adjusting the translation stages micrometers. A schematic of the imaging setup is given in Fig. 3.7. The PMT is housed in a light tight metal box, a flipper mirror also in this box is used to either reflect the light towards the PMT or when in the down position allows the light to be focused onto the camera.

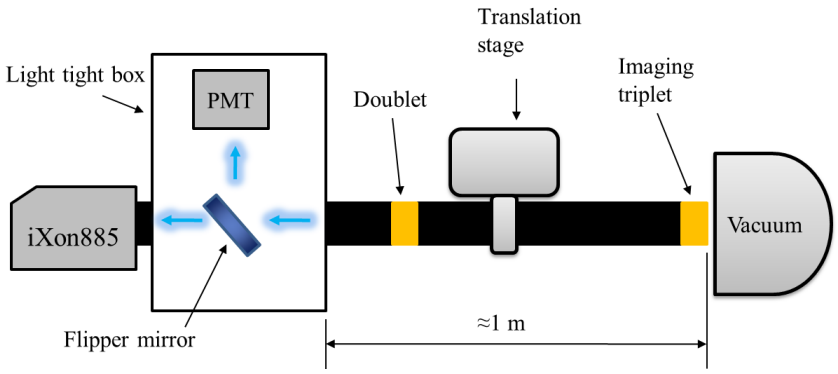

Figure 3.7: A schematic of the imaging setup.

3.7 Ion trap

The ion trap is a linear rf Paul trap, with segmented end cap electrodes. This was fabricated using gold coated stainless steel and PEEK and has an electrode-ion separation of 310 ± 10 μm. The design and assembly of this trap is discussed in Chap. 5.

3.8 Experimental setup

The experiment is placed on a vibration isolated optical table. Figure 3.8 shows a schematic of the experimental setup. A 780 nm laser frequency stabilized to a rubidium hyperfine transition provides a frequency reference and is used to stabilize the main experiment lasers via a transverse cavity locking scheme, this is further described in Chap. 4. The lasers are then aligned into single mode fibers. This separates beam alignment between the trap and the laser, allowing adjustments to be made to the lasers prior to the fibres without the need to re image the ion trap. After the fiber the 369 nm laser passes through an acoustic optic modulator (AOM), (Isomet, part number: 1212-2-949). The AOM allows fast switching of the cooling laser, with a rise time of $\approx$ 100 ns. Fast switching is required for stroboscopic ion-light interactions, used to perform quantum gates and algorithms, as well as ion heating measurements. A LabVIEW program is used to accurately time the AOM switching, the program triggers a digital pulse output from a field-programmable gate array (FPGA) card, (National Instruments, part number: NI-PXI-7842R), connected to the AOM amplifier, switching it either on or off. This can be fully automated and was used to perform ion heating measurements, discussed in Sec. 3.9.

The 369 nm and 399 nm lasers are combined on a bandpass filter, (Semrock, part number: FF01-370/10-25), this transmits 369 nm light and reflects the 398 nm laser. The combined UV beam is then combined with the 638 nm laser on a long wave pass dichroic

mirror, (CVI, part number: LWP-R369-T399-45-1037-C). The composite beam is then aligned into the trap.

To trap ions it is imperative that all the lasers are accurately aligned through the rf nil and that the imaging triplet is centered and focused on the trap center. To ensure laser and imaging alignment a process for positioning them relative to the electrode's positions was used. From numerical simulations the rf nil position with respect to the electrodes can be calculated. To align a laser through the nil, the laser was positioned and focused on each of the four end caps, recording the xyz translation stage micrometer positions for the laser at each end cap. From these positions the mid point along the rf electrode can be found. Moving the laser to this mid point and focusing the laser on the front and back rf electrodes we now have the micrometer positions for six points in the ion trap around the rf nil. Using this information it is then possible to align the laser through the rf nil. This process is repeated for each of the lasers, with chromatic abberations being accounted for in the combined 369 nm, 398 nm and 638 nm beam by individual lenses mounted on translation stages. The imaging triplet can be aligned in the same manner, the translation stage positions for the end caps and rf mid points are used to position the lens tube so that it is imaging the rf nil. Finally a band pass filter centered around 369 nm is placed in front of the camera, (Semrock, part number: FF01-370/10-25). This is to prevent scattered light from the other lasers that would swamp the ion fluorescence in noise.

Once the lasers are aligned the 369 nm and 398 nm beams have a focused beam waist of 30 ± 5 μm with powers of 500 μW and 1 mW respectively. The 638 nm and 935 nm lasers both have beam waists of 60 ± 5 μm and powers of ≈ 7 mW. The beam polarizations are orientated to be at 45° to an externally applied magnetic field, this is generated by three perpendicular sets of Helmholtz coils carrying 2.1 amps. This generates a magnetic field at the ion of 0.5 mT and couples all the Zeeman hyperfine levels to the cooling cycle.

To trap ions a current of ≈ 7 amps is passed through an atomic oven containing either natural ytterbium or 171 isotope enriched ytterbium. The oven is run while monitoring the vacuum pressure ensuring it does not increase above 10^{-10} Torr. It is important to note that ytterbium sticks to the vacuum system, trap and windows so the pressure measured on the ion gauge is the pressure of out gassing materials from the hot oven and wires, most likely absorbed water, and not the ytterbium from the oven. Once an ion is detected an iris in the 398 nm laser beam is closed and the ovens are switch off. It is now possible to adjust the optical alignment of the lasers and imaging, as well as the laser frequencies

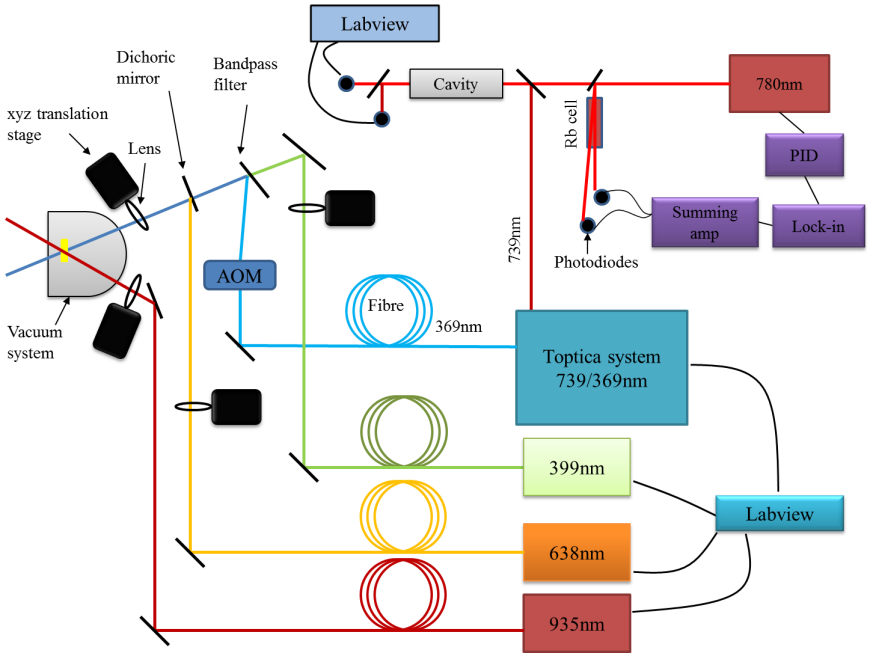

Figure 3.8: The experimental setup.

to optimise the ion fluorescence.

3.9 Ion heating measurement

Once ions were trapped it was important to measure the ion heating rate when the cooling laser is blocked. Resolved sideband spectroscopy is typically used to characterise the ion heating rate [71], however the ability to perform this was not available in the lab at the time. A simplified method to measure the ion heating rate has been developed and demonstrated by J. H. Wesenburg *et al.* [72]. This scheme uses the existing Doppler cooling laser to measure the cooling profile from an initially hot ion. The ion is allowed to heat for a period of time, during this time the Doppler cooling laser is switched off. After a sufficient delay time the cooling light is switch back on and the ion fluorescence is measured by a PMT. This technique requires that the ion heating is dominated along only one principle axis, as the ion heats its velocity along the weakly confined axis increases. This affects the instantaneous Doppler shift seen by the ion, with the scatter rate being a function of both the instantaneous Doppler shift and the power broadened transition linewidth, L.

The instantaneous Doppler shift during an ion oscillation is $\Delta_D = -kv$, where k is the laser wave vector and we can define Δ_{max} as the maximum instantaneous Doppler shift. The likelihood of an ion transition being driven is dependant on the probability that

it sees a Doppler shift resonant with the atomic transition. Therefore the fluorescence is a function of the overlap between the instantaneous Doppler shift probability density function $P_D(\Delta_D)$ and the broadened FWHM transition linewidth, L.

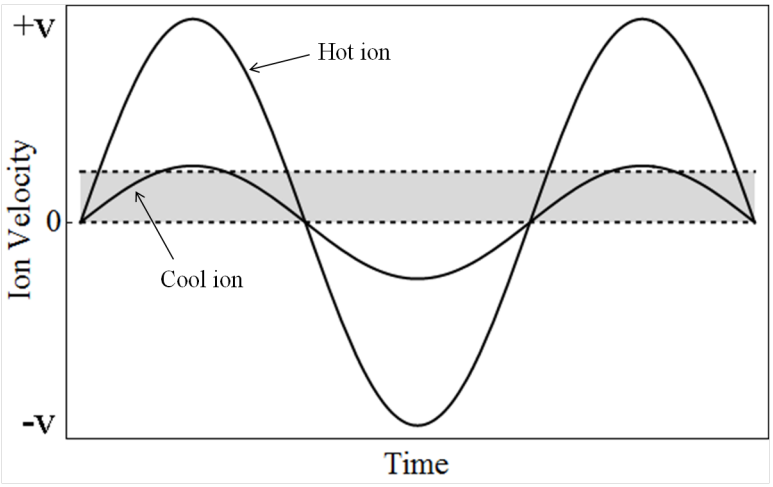

Figure 3.9: The velocity of both a hot and cold ion, the gray area between the two dashed lines correspond to the ion being resonant with the cooling light.

The reason for this can be understood by thinking about how the ion is moving inside the trap. It is weakly confined along one axis relative to the other two. When the ion is hot it will oscillate primarily along this axis, as it gets hotter the velocity during the oscillation period will increase, however the range of velocities where the ion sees a resonant Doppler shifted photon remains the same. The amount of time the ion spends at resonant speeds reduces as the ion increases in temperature, spending more time at faster velocities and Doppler shifted out of the ion's transition frequency. This is shown in Fig. 3.9, this shows the ion velocity as a function of time for both a hot and cool ion. Between the two dashed lines is a shaded gray region corresponding to when the ion is resonant with the cooling laser. For a hot ion, with fast motion we can see that it spends most of its time outside of this region, however for a cool ion the time it spends within this grey area is significantly longer resulting in a higher fluorescence rate.

This is however a rather simplistic way to understand the problem with actual fluorescence rate depending on the overlap between the instantaneous Doppler shift probability function and the broadened transition linewidth. Figure 3.10 [73] shows two cases, (a) shows a hot ion where the instantaneous Doppler shift is $\Delta_{max} \gg |L| + |\Delta|$, where Δ is the laser detuning from resonance. It can be seen that L and probability density function of the Doppler shift overlap poorly, meaning that there is a reduced probability of exciting the ion and therefore a reduced ion fluorescence. Looking at Fig. 3.10(b) we can see that

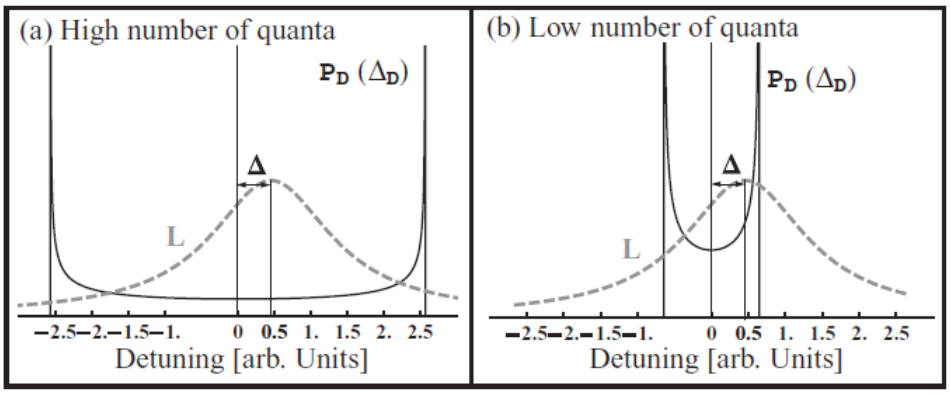

Figure 3.10: The overlap of the instantaneous Doppler shift probability density function, $P_D(\Delta_D)$, (solid) and the broadened transition line width L (dashed). (a) For a hot ion, where the maximum Doppler shift is great than the transition line width. (b) For a cold ion where there is good overlap between the probability density function and L.

for a cold ion there is good overlap of the probability density function and L meaning that the ion spends more of the time in the velocity range where it sees resonant photons. From these two cases it is easy to see how the fluorescence of the ion is temperature dependant. A hot ion will see less resonant photons and therefore scatter less than a cold ion. By measuring the change of fluorescence from an initially hot ion it is possible to calculate the original energy of the ion and therefore its initial temperature.

A full description of how to relate the ions fluorescence to the initial ion energy is given in references [71, 73], but will be briefly repeated here. To find how the ions fluorescence is related to the initial energy of the ion we can average the scatter rate over one oscillation. We can do this because the change of energy over one oscillation is small compared to the total energy change in recooling the ion, therefore we can average the energy and hence the scatter rate over one oscillation. The averaged scatter rate $\langle \frac{dN}{dt} \rangle$ is given by [73]

$$\left\langle \frac{dN}{dt} \right\rangle = \int \frac{dN}{dt} P_D(\Delta_D) d\Delta_D \tag{3.5}$$

where dN/dt is the instantaneous scatter rate. From of Fig. 3.10(a) we can see that the probability density function of the Doppler shift is effectively uniform over the transition linewidth allowing us to factor out the probability density function and allows the average scatter rate to be re-expressed in terms of ion energy [73]

$$\left\langle \frac{dN}{dt} \right\rangle (E(E_0, t)) = \frac{1}{\sqrt{E(E_0, t)}} \frac{sL^2}{2\sqrt{\frac{2}{m}} k_z (1+s)^{3/2}} \tag{3.6}$$

where $E(E_0, t)$ is the ion energy at time t, E_0 is the ion energy just before recooling, m is the ion mass, k_z is the z component of the laser wave vector and s is the saturation

intensity parameter. Now using a 1D Maxwell-Boltzmann distribution to describe the thermal distribution of the ion energy just before recooling, E_0, the average scatter rate for an ion at time t is given by [73]

$$\left\langle \frac{dN}{dt} \right\rangle_{E_0} = \int_0^\infty P_B(E_0) \left\langle \frac{dN}{dt} \right\rangle (E(E_0, t)) dE_0 \tag{3.7}$$

where $P_B(E_0)$ is the 1D Maxwell-Boltzmann distribution. From Equ. 3.7 we can now measure the scatter rate from our hot ion as it is recooled, by fitting Equ. 3.7 to our observed scatter rate we can measure the ion energy, E_0, just before recooling, telling us the initial temperature of the ion and therefore our heating rate.

This was implemented and used to measure a heating rate for our ion trap. It is necessary that the heating is dominant along one principle axis. By lowering the end cap potentials the z-axis secular frequency could be reduced so that $\omega_z \ll \omega_{radial}$, with frequencies of $(\omega_x, \omega_y, \omega_z)/2\pi = (2.069, 2.110, 0.178) \pm 0.001$ MHz, and assuming the ion heating rate has a $1/\omega^2$ dependance [74] the heating will be dominated along the z-trap axis. Switching off the Doppler cooling 369 nm laser was achieved using the AOM and controlled by a LabVIEW program. The program controls an FPGA card, this card sends a TTL pulse to switch the AOM on and off. The AOM was switched off for several different delay times: 1, 3, 5 and 7 seconds then the FPGA sends a second TTL pulse to the AOM amplifier to switch it back on, simultaneously the PMT count rate is measured by the same FPGA card. The LabVIEW program records the PMT count rate in 50 μs time bins for a total time of 4 ms. The initial energy E_0 of the ion has a thermal distribution so for each delay time the measurement was repeated 500 times and averaged. This whole process was automated with LabVIEW programs controlling the laser frequencies, AMO switching and recording the PMT count rate.

Equation 3.7 was then fitted to the fluorescence curve and the initial energy of the ion found. For all the data the laser detuning was kept at $\Delta = 6 \pm 2$ MHz, a saturation parameter of $s = 1.0 \pm 0.2$ and the observed transition linewidth was $L = 40 \pm 5$ MHz. This broadening is a result of power broadening and micromotion.

Figure 3.11 [73] shows the change in the ion energy in terms of motional quanta, n, for each of our four delay times. The insert shows the fluorescence curve measured for the 5 s delay time after all 500 runs are averaged. The experiment was repeated at 2 more secular frequencies, $\omega_z/2\pi = 287 \pm 1$ kHz and $\omega_z/2\pi = 355 \pm 1$ kHz. The heating rates for each secular frequency can be seen in Fig. 3.12 [73]. This shows that the heating rate follows the expected $1/\omega^2$ dependency.

The cause of the ion heating is a result of fluctuating electric potentials on the electrode

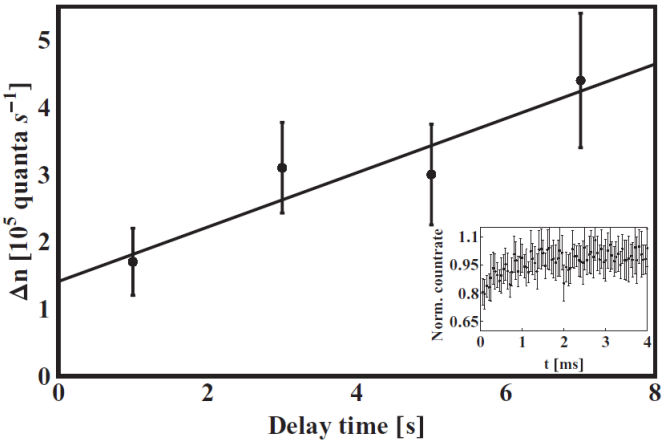

Figure 3.11: The energy gained by the ion for four delay times, with the ion energy being expressed as motional quanta, n. The insert shows the averaged fluorescence curve for a 5 second delay time.

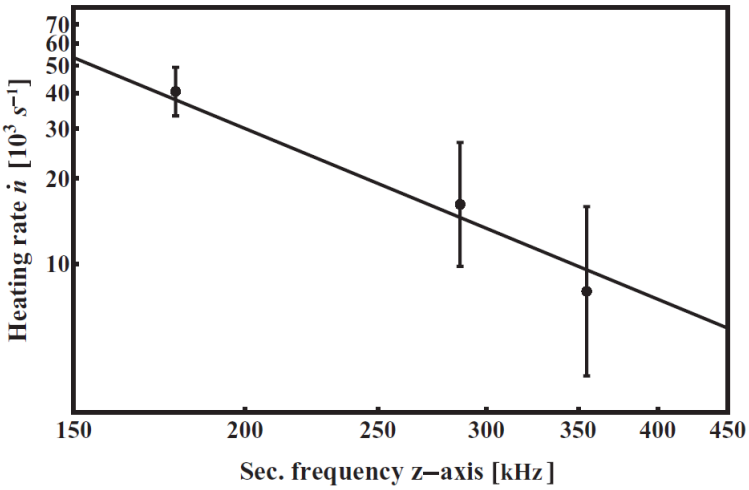

Figure 3.12: The heating rate for three different z axis secular frequencies. This shows that the heating follows the expected $1/\omega^2$ dependance.

surfaces. This is a combination of Johnson noise and fluctuating patch potentials [74]. Equ. 3.8 relates the electric-field noise density, $S_E(\omega_z)$, to the heating rate in motional quanta $\langle \dot{n} \rangle$.

$$\langle \dot{n} \rangle = \frac{q^2}{4m\hbar\omega_z} S_E(\omega_z) \tag{3.8}$$

From this the heating rate for our ion trap was calculated to be $S_E(1\text{ MHz}) = 3.6(9) \times 10^{-11}$ $\text{V}^2\text{m}^{-2}\text{Hz}^{-1}$. For an ion-electrode spacing of 310 μm this is consistent with previously measured ion traps at room temperature [75].

Chapter 4

Laser locking

Is that bit as clean as it could be? No it isn't, so let's improve it.

- James May

4.1 Introduction

Laser diodes provide a cheap and effective method for producing spectroscopic single mode lasers. Modern diodes are able to reach ultra violet wavelengths and with the availability of custom frequency doubling systems they provide the best source of laser light for a wide range of wavelengths.

An off the shelf diode will exhibit strong temperature and current dependence. This will cause the laser's frequency when free running to drift significantly beyond the cooling linewidth of ytterbium. To successfully trap ions it is necessary to provide continuous Doppler cooling light to prevent ion heating. Various electrical and optical methods to improve the frequency stability of laser diodes have been developed and implemented. Optical feedback processes, utilizing narrow frequency reflections from diffraction gratings extending the lasing cavity beyond the semiconductor and allowing careful adjustment of the resonator length and stimulated emission frequency. This simple optical feedback significantly improves the laser's linewidth down to <1 MHz [76] and offers the ability through use of a piezo to fine tune the laser's wavelength. This also offers the opportunity to apply electronic feedback to the piezo to compensate for thermal and random laser drift with high frequency, $>$ 1 kHz, compensation for acoustic and mechanical vibrations applied directly onto the laser current.

With a combination of methods using current and piezo error correction, it has been shown that a standard laser diode's frequency drift can be significantly reduced to 30 Hz

from free running of many MHz [77]. With various techniques demonstrated for both optical and electronic feedback, a compromise between complexity and laser control needs to be established. For Doppler cooling and ion trapping the laser frequency drift needs only to be small compared to 19.6 MHz, the atomic linewidth of ytterbium. For laser cooling and trapping a stability of <1 MHz over an hour is sufficient.

A major problem in stabilizing lasers is the existence of truly constant and highly accurate references with which to stabilize them. Fabry-Perot cavities offer high precision in frequency discrimination but lack an absolute reference and are susceptible to thermal drift as well as acoustic and mechanical vibrations. However an atomic source, without the presence of changing magnetic fields, offers a truly constant reference with which to lock a laser's frequency. Unfortunately there is only a limited number of suitable elements for this type of spectroscopic laser stabilization and hyperfine absorption lines often do not always lay close to a desired frequency. As with Yb there are no obvious elements suitable with close atomic transitions to directly use this to stabilize the cooling or repumping lasers. However rubidium does have transitions near 780 nm which is close to the supply of the doubled 369 nm laser at 739 nm, so this does provide a good starting point.

Modern stabilization systems utilize both atomic references and Fabry-Perot etalons to provide extremely stable and precise laser frequencies from laser diodes. These methods have been demonstrated to reduce diode laser linewidths to tens of Hz. In a proposed setup for drift stabilization below 1 MHz a far less sophisticated method is needed. Stabilization of a 780 nm laser by rubidium absorption spectroscopy can reduce laser drift below $\pm$ 1 MHz, and being stabilized to an atomic transition this should provide a stable and constant frequency with which a comparison between the lasers can be drawn.

To transfer the stability of the rubidium locked 780 nm laser a method to compare both lasers must be used. By aligning both the reference laser and experiment laser into a scanning confocal cavity a comparison between the resonant peaks of the 780 nm reference laser and an unlocked experiment laser can be drawn. By using LabView software an appropriate error signal can be derived. Such computer control has been demonstrated as a solution to laser stability and was used to provide long term feedback to several lasers [78].

4.2 Error Signal and Lock-in Technique

4.2.1 Lock-in

To use the absorption spectroscopy as a laser stabilization reference an error signal must be derived from the photodiode signal. This is done by using a phase sensitive lock-in amplifier. A lock-in amplifier is used for two reasons, firstly it is an extremely good filter, removing all signals other than the one we are interested in and secondly it can be used to generate an error signal. The principle of lock-in detection is that a small modulation is applied to the signal being detected, this in turn is multiplied with a reference signal of the same frequency. The product of the noisy signal multiplied with the reference signal is then averaged over a time much longer than the period of the reference frequency. The result of this is that now the output signal from the lock-in amplifier is DC and has an amplitude dependent on the relative phase between the measured signal and the reference signal. This makes the lock-in amplifier a band pass filter with an extremely sharp roll-off, as any noise with a frequency different to that of the modulation reference is heavily attenuated.

How a lock-in amplifier works as a very narrow band filter is better understood by looking at the maths describing its behavior. If we imagine we have a noisy signal $V_s = E_s$ and apply an oscillating modulation, the signal is now given by $V_s = E_s \sin(f_{mod}t + \phi_1)$, where f_{mod} is the modulation frequency, t is time and ϕ_1 is the phase. We then multiply the measured signal by a reference signal of the form $V_{ref} = \sin(f_{ref}t + \phi_2)$, where f_{ref} is the reference frequency and ϕ_2 is the reference signal phase. Using the trigonometric identity $\sin(A)\sin(B) = \frac{1}{2}[\cos(A-B) - \cos(A+B)]$ we get

$$V_{out} = E_s \sin(f_{mod}t + \phi_1)\sin(f_{ref}t + \phi_2)$$

$$= \frac{E_s}{2}[\cos((f_{mod} - f_{ref})t + \phi_1 - \phi_2) - \cos((f_{mod} + f_{ref})t + \phi_1 + \phi_2)]. \qquad (4.1)$$

For our Rb spectroscopy the laser modulation and reference modulation will have the same frequency, $f_{mod} - f_{ref} = 0$, substituting this into the equation for V_{out} and averaging over one period

$$V_{out} = \frac{E_s}{2}\left(\int_0^{2\pi} \cos(\phi_1 - \phi_2)dt - \int_0^{2\pi} \cos(2ft + \phi_1 + \phi_2)dt\right)$$

we are left with

$$V_{out} = \pi E_s \cos(\phi_1 - \phi_2). \tag{4.2}$$

From Equ. 4.2 we can see that the output from the lock-in amplifier is proportional to the relative phase between the measured signal and the local oscillator. So the output of the lock-in amplifier now only depends on the phase between the detected signal on the photodiode and the phase of the reference modulation at the lock-in amplifier. Now if we look at the case of any noise detected by the photodiode, the frequency of the noise will be such that $f_{noise} - f_{ref} \neq 0$, substituting this into Equ. 4.1 and averaging over one period we now get

$$V_{out} = \frac{E_s}{2}\Big(\int_0^{2\pi} \cos((\Delta f)t + \phi_1 - \phi_2)dt - \int_0^{2\pi} \cos((\Delta f)t + \phi_1 + \phi_2)dt \Big)$$

$$V_{out} = \frac{E_s}{2}\Big[\frac{1}{\Delta f} \sin((\Delta f)t + \phi_1 - \phi_2) \Big]_0^{2\pi} - \Big[\frac{1}{\Delta f} \sin((\Delta f)t + \phi_1 + \phi_2) \Big]_0^{2\pi} = 0 \tag{4.3}$$

where $\Delta f = f_{noise} - f_{ref}$. It is clear from Equ. 4.3 that for all non zero values of Δf the output from the lock-in amplifier is $V_{out} = 0$. This shows that for all noise on the signal which has a frequency other than the modulation frequency will be attenuated by the amplifier.

However to be useful as an error signal the output from the lock-in amplifier must be the differential of the input signal. Without differentiating the absorbtion peak it is impossible to know which side of resonance the lasers frequency is. However by measuring the gradient of the absorbtion peak, which will be positive on the rising slop, zero at resonance and negative on the falling slop, it is possible to know which side of resonance the laser is and feedback accordingly.

The intensity on the photodiode is a function of both the laser frequency, ω_l, and the modulation around this frequency. The modulation tunes the laser wavelength between ω_l and $\omega_l + \Delta\omega_l$, the lock-in amplifier then detects the difference in intensity between the two laser frequencies, $I(\omega_l) - I(\omega_l + \Delta\omega_l)$. Provided the modulation depth, $\Delta\omega_l$, is small, the output is dominated by the first two terms in the Taylor expansion [79]. Modulating the laser with a sinusoidal modulation at a frequency of Ω (where $\Omega = f_{mod}$), so that ω_l is given by

$$\omega_l(t) = \omega_0 + a\sin(\Omega t)$$

then we find the intensity on the photodiode is given by [79]

$$I(\omega_l) = I(\omega_0) + \sum_n \frac{a^n}{n!} \sin^n(\Omega t) \left(\frac{d^n I}{d\omega^n} \right)_{\omega_0}.$$

For a small modulation depth we can approximate $I(\omega_l)$ to be equal to the first two terms and ignore all higher orders. Now if we take this signal and pass it through the lock-in amplifier in the same manner as before we get

$$V_{out} \approx a \frac{dI}{d\omega} \cos(\phi_1 - \phi_2).$$

So when there is a small modulation on the laser, then the output from the lock-in amplifier is proportional to the derivative of the absorption signal. This can intuitively understood by looking at Fig. 4.1, this shows for when the laser is modulated both close to resonance and far from it. It is clear that when the laser is far from resonance the intensity change on the photodiode is small, when the laser is close to resonance the intensity change is large. Additionally if the laser is tuned past resonance there will be a phase change in the signal reaching the diode, this phase change is responsible for changing the polarity of the lock-in amplifier output signal.

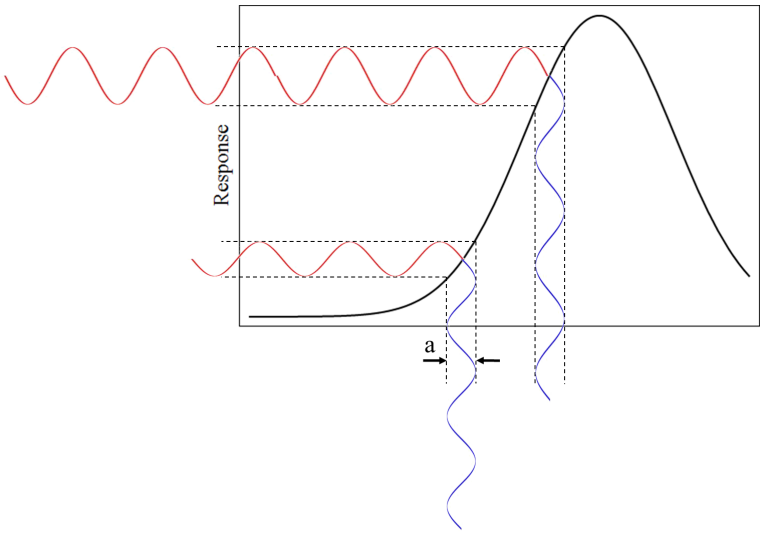

Figure 4.1: When the laser is modulated away from resonance the change of intensity at the photosdiode is small, however when the laser is cloase to resonance there is a large change in intensity. From this it is obvious why for small modulations the lock-in amplifier's output is the derivative.

Now if we consider when a is large, we can no longer ignore the high order terms in our Taylor expansion and the lock-in amplifier output will be some convolution of the curve over the modulation depth.

Electronically a lock-in amplifier consists of a frequency mixer, phase shifter and a low pass filter with a cut-off frequency: $f = \frac{1}{2\pi RC} \ll f_{ref}$, where R is resistance and C is capacitance. A basic circuit diagram for a lock-in amplifier is shown in Fig.4.2. A commercial amplifier will have a significantly more complicated design but the basic operation remains the same.

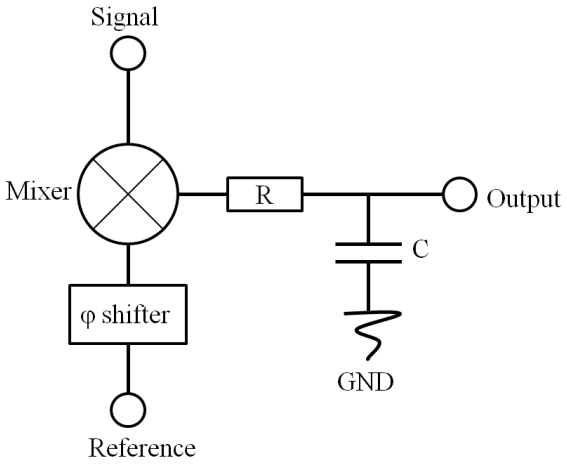

Figure 4.2: Diagram of the electronic principle of a Lock-in amplifier.

Lock-in amplifiers can be bought commercially, with a wide range of built in feature and frequency ranges. They are widely used for both frequency stabilization and for extracting signals from noisy sources.

4.3 Transfer Cavity Locking Scheme

The principle of a transfer cavity locking scheme is that with a stable reference laser it is possible to drift stabilize further lasers using a confocal cavity and computer controlled feedback [78].

With a rubidium stabilized laser with a drift of < 1 MHz over an hour providing a reference, a second beam at 739 nm is combined on a polarizing beamsplitter. This combined beam is then aligned into a confocal cavity. The cavity length is scanned by applying a sawtooth function to the cavity piezo, the output from the cavity is then split into the component parts using a second polarizing beamspitter and the intensity measured using photodiodes. The position of resonant peaks with respect to the ramp potential for the stable laser in principle should remain constant as there is little frequency drift. This is not the case as thermal drift of the cavity length will result in the peaks moving relative to the ramp potential. In order to provide a more accurate reference, the free spectral range (FSR) of the 780 nm laser is measured. This is compared with the time between the first

780 nm peak and a 739 nm resonance. If we call the FSR a and the separation between 780 nm and 739 nm peaks b, then a ratio given by $\frac{a}{b} = \Xi$, can be measured. Drift in the 739 nm laser will correspond to a change in Ξ, so by monitoring the change in the ratio a suitable error signal can be generated and fed back onto the laser piezo. A cavity scan across a FSR for both the 780 nm and 739 nm lasers is shown in Fig. 4.3, the separations a and b are labeled. This method of frequency stabilization has been demonstrated using a HeNe reference with a drift of $\pm$ 1 MHz over 1 hour and stabilizing a laser diode and Ti:Sapphire laser's frequencies to $\pm$ 1.2 MHz for many hours [78].

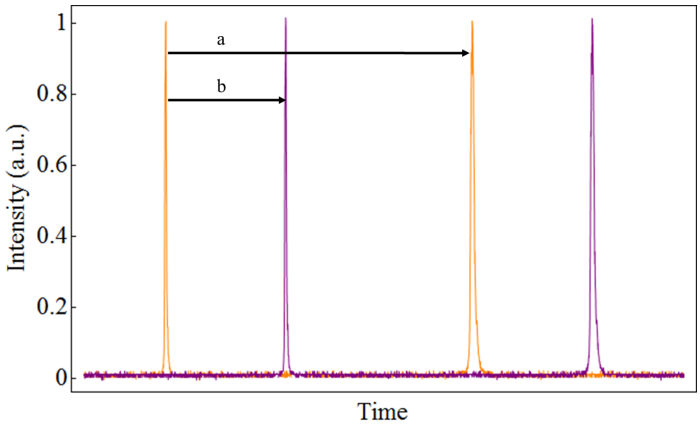

Figure 4.3: This shows the output of both photodiodes, the 780 nm laser shown in orange and the 739 nm laser in purple. A LabView program measures the time for a and b and calculates the ratio of the two.

To apply this to our experiment a LabView Realtime program was written to automatically measure both a and b and provide feedback to all the lasers. The intensity as measured by the photodiodes after the cavity is read into a computer using an analog input card, (National Instruments, part number: NI PCI-6143 S). Here a peak detection algorithm detects the laser peaks and automatically measures the time between subsequent 780 nm peaks and between user specified 780 nm and 739 nm peaks. The 739 nm laser is locked by manually adjusting the laser to the desired frequency, then using a PID controller in our LabView program the ratio set point Ξ, feedback gain and time constant can be set. The error signal is output via an analog output card, (National Instruments, part number: NI PCI-6722), which is sent to the laser's piezo amplifier. Thermal drift of the cavity can lead to peaks leaving and entering the length of the scan, this can result in the program measuring the incorrect peaks and losing the lock. To avoid this feedback to compensation for thermal drift on the cavity measures the position of the first 780 nm laser peak and keeps its position with respect to the ramp potential the same.

4.4 780 nm Diode Laser Construction

The construction of a laser diode system has many design considerations: laser diode, diffraction grating, thermal stabilization, piezo actuator, collimation lens and mechanical stability. One of the first considerations is the optical feedback used to narrow the laser linewidth and allows frequency corrections to be made. The following subsection will discuss the optical feedback setup used.

4.4.1 Optical feedback configuration

There are two main laser designs which utilize optical feedback from a diffraction grating, these are the Littrow [76, 80] and Littman-Metcalf configurations [81].

In the Littrow design the diffraction grating is placed in front of the diode and angled so that the 1st order diffraction beam is sent back into the diode with the zeroth order reflected as the main beam Fig. 4.4. Sending the first order back into the laser diode

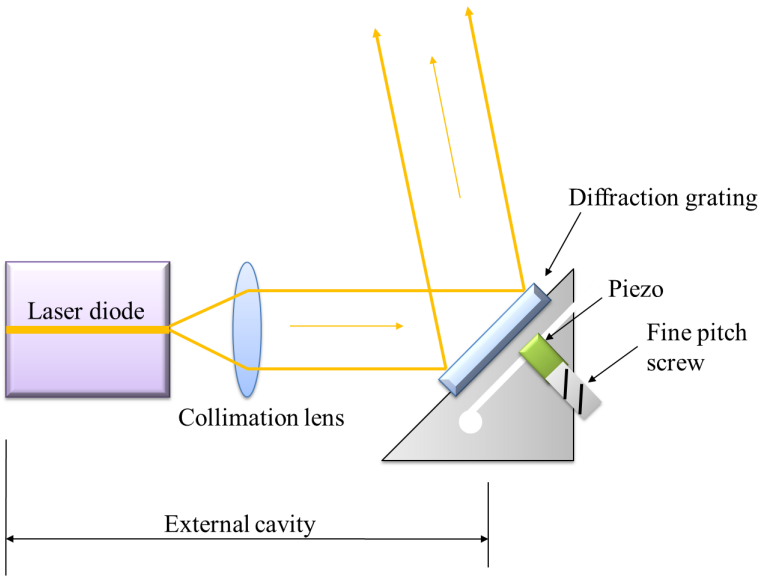

Figure 4.4: Littrow Configuration

overrides the diode cavity, extending the laser cavity between the rear facet of the diode and the diffraction grating. The resonant frequency of the new external cavity can now be controlled by adjusting the angle of the grating.

The grating is mounted on a triangular metal block that has a slot machined away parallel to the grating, shown in Fig. 4.4. A fine pitch screw and piezo apply pressure to the rear of the mounted grating allowing very precise changes in the grating angle to be made. The wavelength of light reflected into the diode is governed by the grating equation given by

$$n\lambda = d(\sin\theta + \sin\theta')$$

where n is the order of diffraction ($n = 1$), λ is the wavelength, d is the grating groove separation, θ is the angle of incidence and θ' is the angle of diffraction measured from the normal. By making small changes to the incident angle, θ, it is possible to drag the lasing frequency of the laser. However this change in angle also changes the angle that the zeroth order is reflected, this can be problematic in experiments where beam stability is critical. To avoid this problem the Littman-Metcalf configuration fixes the grating angle with tuning achieved via a mirror attached to a piezo. This design ensures that there is no angular displacement, but due to multiple reflections from the diffraction grating this configuration has significantly less output power efficiency, further information regarding the Littman-Metcalf configuration can be found in [81]. For this reason the Littrow configuration was used.

4.4.2 Laser Diode

When choosing a suitable laser diode it must be single mode, have the correct wavelength or a wavelength near the desired wavelength and a sufficient output power. In modern optical data storage devices such as CD-R's and CD-RW players high power ≈780 nm laser diodes are common; a Sharp 784 nm, 120 mW, single mode laser diode was selected for its high power and price, (Thorlabs, part number: GH0781JA2C).

The diode operational characteristics are given by tables 4.1 and 4.2. They show the temperature range and current over which the diode will operate. It also shows that the diode will lase between 780 nm and 787 nm. By controlling the diode temperature, current, and grating angle it is possible to drag the laser frequency to lase at the desired 780 nm.

These specifications allow the correct current controller, temperature controller and collimation lens to be bought.

4.4.3 Diode current controller

The wavelength emitted by a laser is highly dependant on the current across the diode. With a change of frequency of several GHz with a change of just a few tenths of a mA it is important that a stable current supply is used. A low noise current controller was used and has specifications as shown in Tab. 4.3, (Thorlabs, part number: LDC201CU). Laser

Characteristic	Symbol	Rating
Optical output power (CW)	P_0	120 mW
Optical output power (pulsed)	P_0	180 mW
Reverse voltage	V_{rl}	2 V
Operating temperature (CW)	T_{opc}	-10°C → 65°C
Operating temperature (pulsed)	T_{opp}	-10°C → 75°C
Storage temperature	T_{stg}	-40°C → 85°C

Table 4.1: The 780 nm laser diode's absolute maximum operational ratings.

Characteristic	Symbol	Minimum	Typical	Maximum
Threshold current	I_{th}	-	30 mA	40 mA
Operation current	I_{op}	-	141 mA	167 mA
Operation voltage	V_{op}	-	2.1 V	2.5 V
Peak wavelength	λ_p	780 nm	784 nm	787 nm
Beam divergence (//)	$\theta //$	7.8 °	8.7 °	9.6 °
Beam divergence ($\perp$)	$\theta \perp$	14.5 °	16 °	17.5 °

Table 4.2: Optical-electrical characteristics of the 780 nm laser diode.

Current control	**LDC201CU**
Control range	0→100 mA
Compliance voltage	5 V
Resolution	10 μA
Accuracy (full scale)	$\pm$ 50 μA
Typical noise without ripple (10 Hz to 10 MHz, RMS)	$<$ 0.2 μA
Typical ripple (50/60 Hz, RMS)	$<$ 0.5 μA
Transients (typical)	$<$ 10 μA
Typical drift in 24 hours (0-10 Hz at constant ambient temperature)	$<$ 2 μA
Current limit (constant current mode)	**-**
Setting range (20-turn trim pot)	0→100 mA
Resolution	10 μA
Accuracy	$\pm$ μA
Analog modulation input	**-**
Input resistance	10 kΩ
3 dB bandwidth	DC-0.2 kHz
Modulation coefficient	10 mA/V $\pm$ 5%

Table 4.3: Thorlabs LDC201CU low noise current controller specifications.

current modulation was achieved by applying a modulating current to a bias-T attached to the laser diode. This allowed a 100 kHz modulation to be added onto the dc drive current from the laser current supply.

4.4.4 Diode Temperature controller

The laser diode is also susceptible to temperature change and it is important to maintain a stable temperature across the diode. For this a Thorlabs TED200C 12W laser diode temperature controller monitors the laser diode temperature via a thermistor and using a PID controller feeds back to a peltier device. Additionally the laser diode mount is packed in a foam box to further isolate it from thermal fluctuations in the lab.

4.4.5 Collimation Lens

A diode laser will display large dispersion due to the small size of the lasing facet. To compensate for this it is necessary to use a collimation lens directly after the diode. When considering suitable lenses the numerical aperture (NA) and focal length are the important features of a lens. The focal length needs to be short as there is limited space on a mount and the closer to the diode the more light it will be able to capture. The NA refers to the range of angles a lens can operate over, this must be matched to ensure the dispersion from the diode is within the numerical aperture of the lens. The numerical aperture is related to the divergence of the laser diode by

$$NA = n \sin(\theta) \tag{4.4}$$

Where n is the refractive index of the medium surrounding the lens and θ is the lasers divergence angle. For our 780 nm laser diode the beam divergence is a maximum of 17° and in air with a refractive index of $n = 1$, this yields a numerical aperture of $NA = 0.3$. To ensure the lens captures most of the light emitted from the diode it is import to ensure the NA of the lens is greater than 0.3. An aspheric lens with a focal length of 2 mm and NA of 0.50 was found to be suitable for the diode, (Thorlabs, part no C150TM-B). This gives a collimated beam diameter of ≈ 1.3 mm.

4.4.6 Diffraction Grating

A diffraction grating must be carefully selected to ensure a suitable efficiency, this should be sufficiently high as to provide enough feedback to the laser diode, but not so high that it significantly reduces the laser output power. An efficiency of ≈ 50 %, usually provides sufficient feedback whilst only reducing the laser output by half.

There are two types of grating, ruled and holographic. A ruled grating is made by mechanically machining parallel lines onto the surface. Holographic gratings are manufactured using a laser interference pattern and photolithography, this removes ghosting effects from periodic flaws. The efficiency of a holographic grating is typically much less than that of ruled gratings, for this reason a holographic grating with 1800 grooves/mm and an efficiency of 45 % was selected, (Thorlabs, part number GH13-18V).

4.4.7 Construction

The final constructed laser is shown in Fig. 4.5, this shows a top view of the laser and the placement of the components, and a side drawing. A peltier cooler is sandwiched

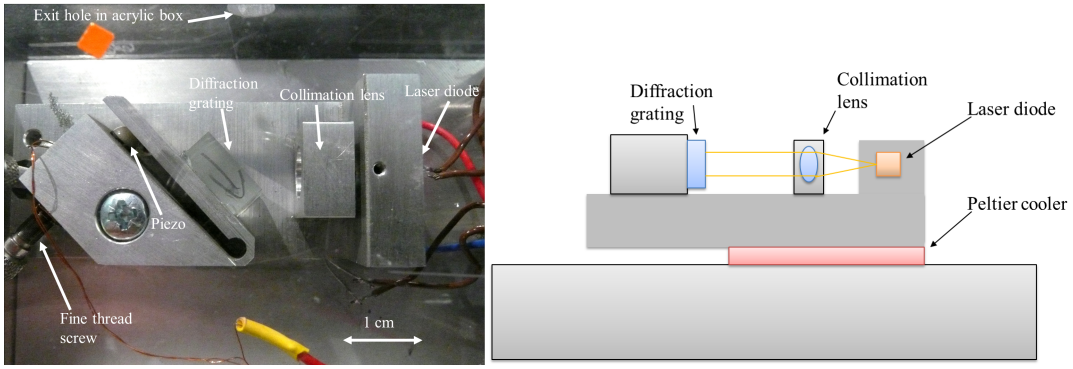

(a) (b)

Figure 4.5: a) A photo of the constructed laser. b) Side view drawing of the placement of all the components.

between the laser diode mount and the main body. This is used to maintain a constant diode temperature. A translation stage was used to align the aspheric lens to collimate the beam. By viewing the beam spot close to the diode then in the far field it is possible to collimate the beam. Once the beam is collimated the lens is glued into position. The grating was then aligned to optimize feedback into the diode using the fine adjustment screw. With further adjustments made to the drive current and temperature the emitted wavelength was brought to 780 nm.

The laser diode, lens and grating are all housed inside a transparent acrylic box, a small hole drilled in the plastic allows the beam to exit. This helps protect the laser diode and optics from dust and moving air that would change the diode temperature. To further isolate the diode the whole assembly is wrapped in a 3 inch thick layer of foam. This provides both additional thermal insulation as well as some acoustic isolation. The laser is screwed directly to the optical table, making the laser sensitive to any vibrations induced in the table. This could prove problematic however the rubidium lock is suitably robust to cope with the majority of knocks, even maintaining the laser frequency after substantial hits from ball drivers and spanners.

4.5 Fabry-Perot Confocal Cavity

To drift lock the other lasers to the 780 nm laser one needs a method of comparing the different frequencies. This can be done by aligning several lasers into a scanning Fabry-Perot cavity. Inside the cavity there are an infinite number of longitudinal cavity modes each with a distinctive frequency, a mode is resonant when the length of the light path inside the cavity is an exact multiple of half wavelengths of the light [82]. By scanning

the length of the cavity the cavity will pass over lengths L, such the $L = \frac{\lambda/2}{m}$, where m in an integer and λ is the specific laser wavelength. At these resonant lengths the cavity will transmit the resonant laser light, and reflect it at all other times.

There are various cavity designs, but the most straight forward is the confocal cavity. This has two concave mirror separated by a distance equal to their radius' of curvature. This has the advantage over other cavity designs in that the configuration is stable, meaning the beam does not walk out of the cavity and that all transverse modes are degenerate.

Two quantities can be defined to characterize a confocal cavity, the free spectral range (FSR) and the finesse. The light follows a figure of eight configuration between the mirrors shown by Fig. 4.6, giving a cavity FSR of

$$fsr = \frac{c}{4L} \tag{4.5}$$

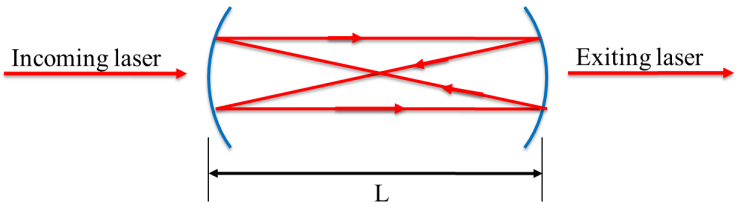

Figure 4.6: The light path through a confocal cavity, laser light enters from the right and follows a figure of eight path between the mirrors before exiting through the left mirror.

where c is the speed of light. The free spectral range is the frequency separation between successive cavity resonances and is dependant on the length of the cavity.

The finesse is used as a measure of cavity loss, it is a ratio between the FSR and the full width half maximum (FWHM) of a resonant peak and is given by

$$f = \frac{FSR}{FWHM}. \tag{4.6}$$

For the transverse cavity locking scheme two separate confocal cavities were built, the design drawings are given in App. B. The first was built to be resonant with both the 780 nm and the 739 nm lasers. This used broadband dielectric coated mirrors centered around 750 nm, with high reflectivity at both wavelengths, specified by the manufacturer to be R $>$ 99 %, (CVI, part number: TLM2-750-0-0537-0.075CC). They each have a radius of

curvature of 75 mm, giving a FSR of 1 GHz. For the second cavity custom coated mirrors were bought. These are highly reflective $> 99.3 \pm 0.2$ % at 369 nm, 399 nm, 638 nm, 780 nm and 935 nm, and have a radius of curvature of 100 mm giving a FSR of 750 MHz, (CVI, part number. TLM1-369/399/780/935-0-0537-UV-0.010CC).

The cavities were constructed from stainless steel and consist of a male and female part, as shown in Fig. 4.7. The male part has a fine pitch screw thread that threads into the female section. They are closely fitted to ensure stability. A ring piezo with an attached thread adapter, (Piezomechanik, part numbers: HPSt 150/14-10/12 and HAg respectively), is glued to the female section, a custom built brass holder holds a mirror and screws to the piezo. A second mirror is glued directly to the male part.

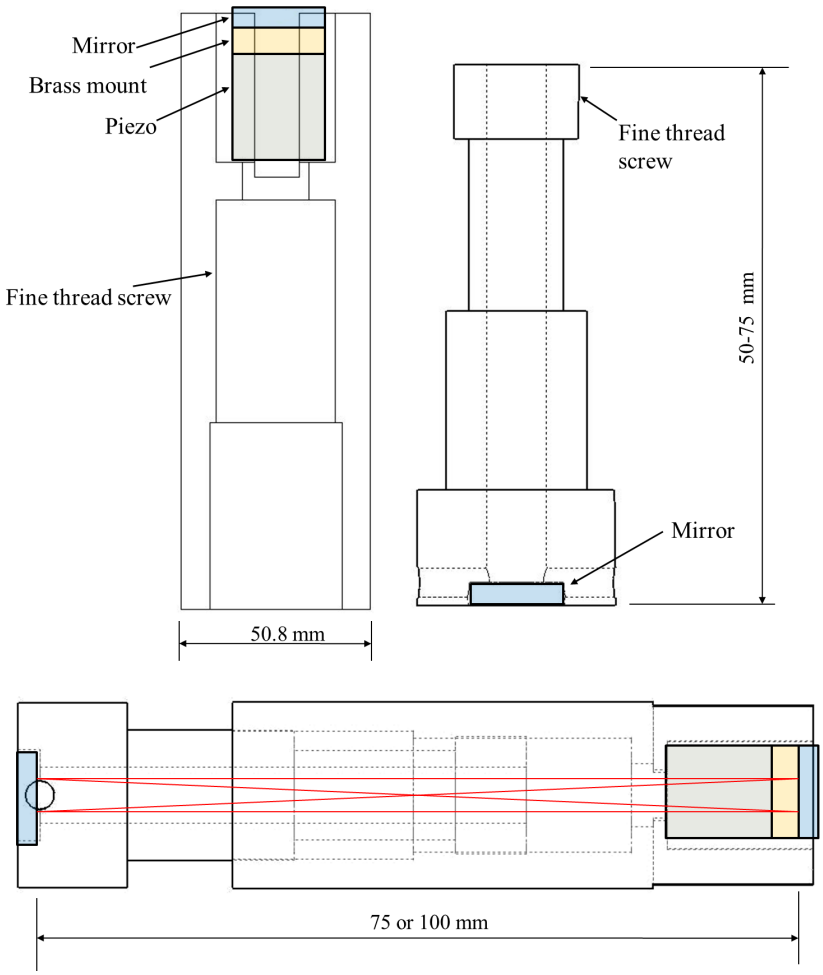

Figure 4.7: Top: Left, female cavity section with a piezo, brass mount and mirror attached. Right, male cavity section with mirror attached. Bottom shows the assembled trap when the male and female parts are screwed together.

The cavity is brought to be approximately confocal in length, then a laser is aligned into it. Scanning the piezo the output from the cavity is measured using a photodiode.

The cavity length can then be adjusted to bring it to be confocal and the optical alignment optimized. Figure 4.8 shows a scan of the 780 nm laser, the measured finesse is 134 ± 5. The design drawings for the cavities are given in App. B.

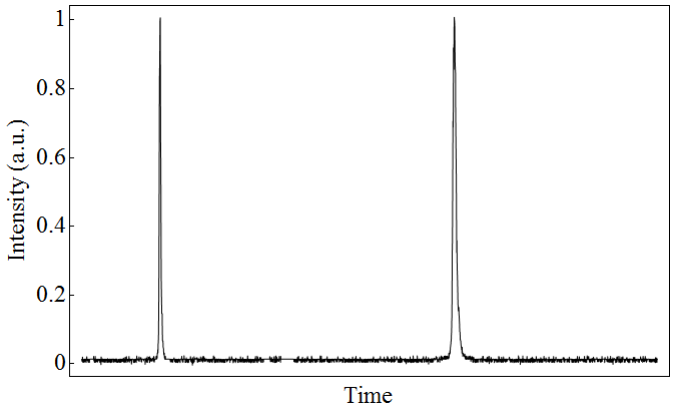

Figure 4.8: A scan over two 780 nm resonant peaks, with a FSR of 1 GHz and finesse of 134 ± 5.

4.6 Experiment electronics

4.6.1 PID Controller

After the lock-in amplifier an error signal that can be sent to the laser piezo needs to be generated. This is achieved via a PID controller, this uses three separate processes to output an appropriate error signal to maintain the laser at a predetermined set point. The operations used to generate the error signal are a proportional, integral and differential signals which are summed to produce a final error signal. The proportional output is dependent on the instantaneous error input from the lock-in amplifier, the integral output is dependent on a sum of recent errors and the differential output is dependant on the rate of change of the error signal. For the laser system only a PI controller was used as a sufficient error signal can be generated without the differentiator and for simplicity it can be neglected. This combination means fast laser movement is compensated by the proportional output and laser drift from resonance is compensated for by the integrator.

The proportional output from the PI controller is given by

$$P_{out} = K_p e(t) \tag{4.7}$$

where K_p is the proportional gain constant and e is the error signal from the lock-in amplifier. This simply multiplies the instantaneous error signal by a gain constant, usually with opposite sign to provide an instantaneous negative error signal. This compensates for

fast laser movement but will not maintain the laser at a set point. For this the integrator is required, the integral is given by

$$I_{out} = K_I \int_0^T e(t)dt \tag{4.8}$$

where K_I in the integral gain constant. By fixing a set point the integral will provide a feedback signal proportional to the distant from this set point. This prevents laser drift due to slower processes such as thermal fluctuations, and can maintain a fixed laser frequency. The total output from the PI controller is now given by

$$PI_{out} = K_p e(t) + K_I \int_0^T e(t)dt. \tag{4.9}$$

Operational amplifiers (op-amps) can provide fast electronic feedback, there simple application makes them especially useful when building circuits to amplify, integrate and differentiate.

The PI controller was built in house using a printed circuit board and surface mount components, the circuit diagram for the PI controller is shown in Fig. 4.9. The four op amps are contained within one IC, (Texas Instruments, part number: OPA 4277). The input from the lock-in amplifier is connected to a three way switch, this allows the polarity of the input to be switched, ensuring there is always negative feedback. The signal then passes to a proportional amplifier and integral amplifier in parallel with each other. The output from the proportional and integral amplifiers is then summed and output. An additional modulation input is included. This allows a voltage to be applied directly to the piezo without interfering with the locking loop. This means the laser frequency can be scanned, useful for observing the Rb spectrum and optimising optical alignment, with the PI controller and lock-in amplifier still connected to the piezo amplifier.

To configure the controller it is necessary to set the output offset on the PI controller. This is achieved by disconnecting any input into the the PI controller and viewing the output on an oscilloscope, then adjusting the proportional offset, P1, to equal zero. Next the input offset must be adjusted correctly. Connecting the PI controller to the lock-in amplifier and viewing the error signal as it scans across the Rb transition the locking crossing point can be set to zero by adjusting the input offset control, P2. When the controller has been correctly set the laser scan can be stopped, bringing the laser close to a hyperfine transition and first turning on the proportional then the integral the PI controller will begin to hold the laser frequency close to the set point. By adjusting the individual gains, P3 and P4, and integral time constant but placing different value

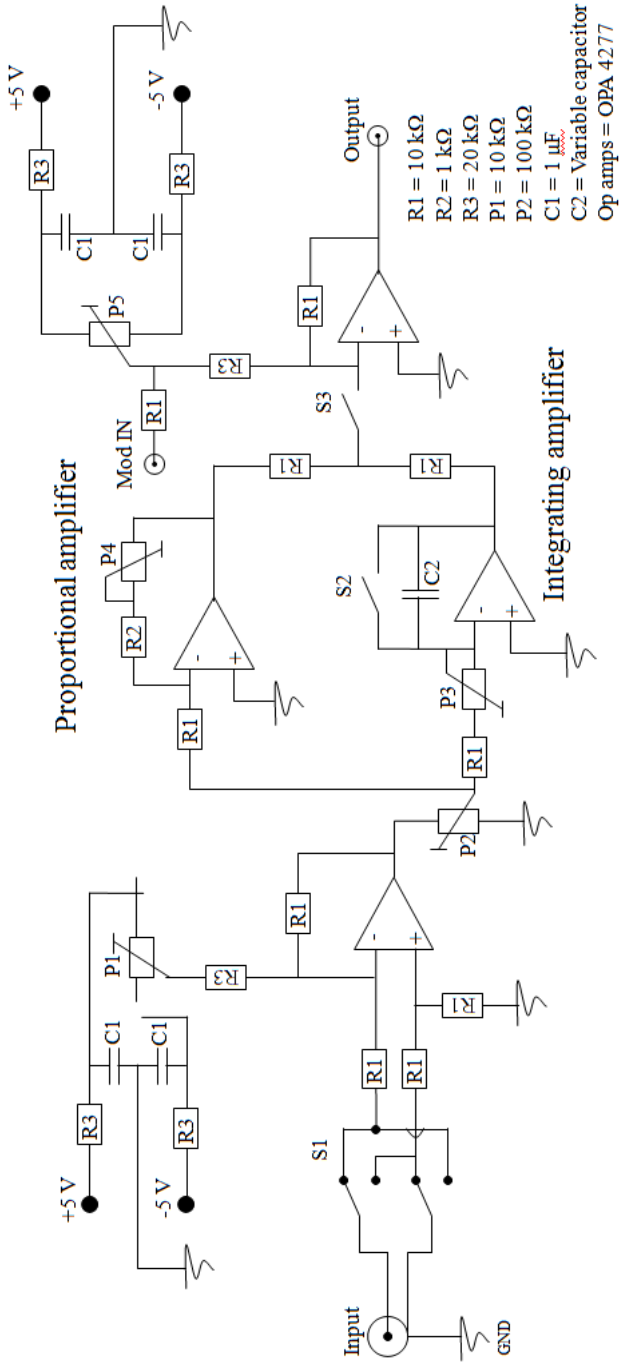

Figure 4.9: Circuit diagram for the PI controller.

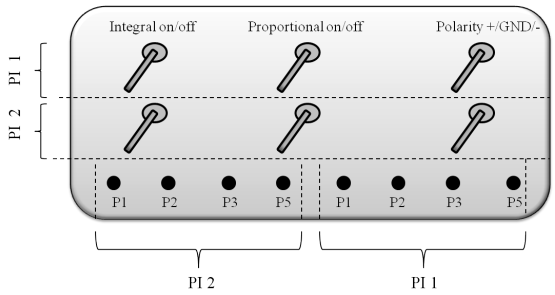

Figure 4.10: Drawing of the PI controllers front panel, showing how the controls for the two controllers are split. The top row of switches control PI 1 with the bottom row controlling PI 2. Left switch turns the integral on, with the switch positing down for on and up for off. The center switch turns the proportional control on, with up for on and down for off. The right switch controls the polarity of the error signal, this is a three way switch, with the up and down positions having opposite polarities and the central position at ground. The polarity of the error signal feedback is dependant on the signal phase at the lock-in amplifier. The pots are labeled corresponding to the pot labels in Fig. 4.9

capacitors for C2, the speed of feedback and the stability of the laser can be optimized. Figure 4.10 shows a drawing of the PI controller front panel.

4.6.2 Lock-in Amplifier

When buying a lock-in amplifier the most important consideration is the frequency range it is designed to operate over. As shown earlier the output of the lock-in amplifier needs to be effectively static in comparison to the modulation frequency. This requires a modulation frequency several orders of magnitude greater than the desired feedback. A single phase analogue lock-in amplifier was bought, (Scitec Instruments, part number: Model 410). This has an operational frequency range of 10 Hz$\rightarrow$100 kHz, when modulating the laser with a 100 kHz modulation this allows feedback at several hundred Hz.

4.6.3 Photodiodes

To measure the laser intensity photodiodes and photodiode circuits needed to be built. First suitable photodiodes were selected for there frequency response and wavelength sensitivity. Typical photodiodes show the strongest sensitivity in the NIR wavelength range with affectivity no sensitivity in the UV at 369 nm. Therefore photodiodes that are sensitive across the range of experimental lasers were found. Hamamatsu silicon S5972 diodes are sensitive between $\approx$ 350 nm$\rightarrow$1000 nm, with a peak response at 760 nm, the pho-

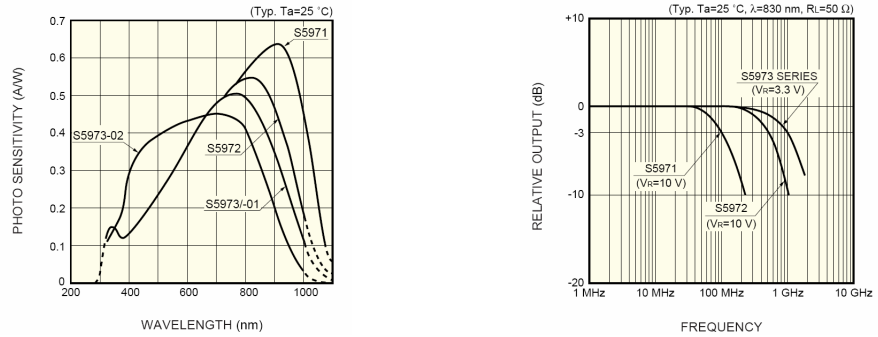

(a) (b)

Figure 4.11: a) Wavelength sensitivity of the Hamamatsu S597X photodiodes. b) Frequency response of the Hamamatsu S597X photodiodes.

todiode wavelength sensitivity is shown in Fig. 4.11(a) [83]. Additionally they have a frequency response of 500 MHz, this ensures that they will respond quickly to any changes in laser intensity. The relative output with frequency is shown in Fig. 4.11(b).

4.6.4 Photodiode circuits

For the majority of stand alone photodiodes used on the optical table a standard inverting op-amp circuit was used, these can provide large gain with moderate speed; rise times of $\approx$ 200 nS. The circuit diagram for this circuit is given in Fig. 4.12, the values of R_1 and R_2 depend on the wavelength being used. The gain from this circuit is given by $V_{out} = -\frac{R_2}{R_1}V_{in}$, with typical gains ranging from 50-1000, or up to 100,000+ for UV diodes. These were made by using stripboard and soldering the components on. More recent circuits have been made using a PCB printer using surface mount components. This helps reduce noise in the circuit and allows more compact circuits to be built.

For the Rb absorption spectroscopy it was necessary to build a balanced photodiode pair. A PCB was designed to include amplifiers for two photodiodes and an instrumentation amplifier to subtract the signals, the circuit diagram is show in Fig. 4.13. This takes both photodiode signals and using inverting amplifiers, amplifiers the signals with a gain of 1000. The signals then pass to the instrumentation amplifier which subtracts one from the other, these can be bought as ICs but for this circuit it was built using three op-amps. By including three potential dividers the amplitude of the individual photodiodes and the overall amplifier gain can be varied. The benefits of this circuit is that it rejects large values of common mode noise improving the signal to noise ratio. Figure 4.14 shows the PCB design for the Rb balanced photodiode circuit.

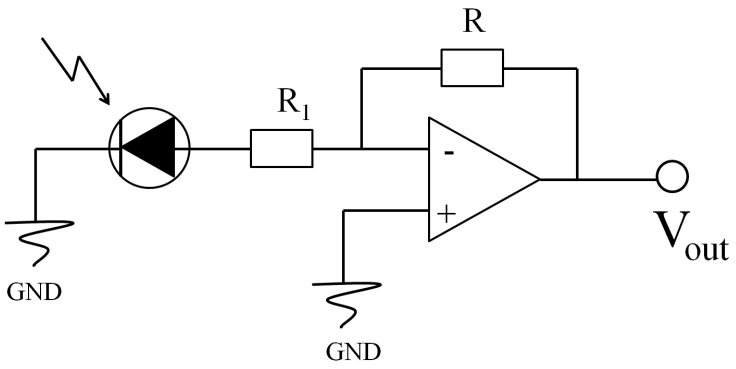

Figure 4.12: Circuit diagram for a basic PD circuit, the values of R_1 and R_2 depend on the wavelength being used, typical values are $R_1 = 1$ kΩ, $R_2 = 1$ MΩ, the op-amps used are LF411.

4.7 Doppler Free Absorption Spectroscopy of Rubidium and laser stabilization

Rubidium offers a good choice as a reference for an atomic source, with a hyperfine structure near to our pre doubled cooling laser wavelength of 739 nm, and with a wide range of accessible single mode 780 nm laser diodes, it is cheap to build. As the laser is tuned over the resonant transitions of rubidium, absorption of laser light will vary the intensity incident on a photodiode. Absorptions appear over a broad range of frequencies due to Doppler shifted resonant transitions of the gas, atoms moving towards and away from the beam will absorb photons when the laser is near resonance due to the laser being Doppler shifted in the atoms reference frame. This broadened background has a width on order of 500 MHz and hides any hyperfine definition in the absorption spectrum.

To observe the rubidium hyperfine structure within the broadened absorption region a pump and probe beam must be used. First a high intensity pump beam passes through the gas cell, a probe beam is then passed in the opposite direction overlapping the pump beam and is collected on a photodiode. When the laser is tuned over the resonances, sharp peaks corresponding to the hyperfine transitions are now visible in the Doppler background. This is because the co-propagating beams are each absorbed by an opposite velocity class of atoms. When the laser is at a resonant wavelength, the atoms with zero velocity with respect to the laser beams absorb the incident light. The pump beam saturates most of the zero velocity rubidium atoms, reducing the absorption of the probe beam at these frequencies. However when the laser is not at resonance the pump beam has little effect on the probe beams absorbtion.

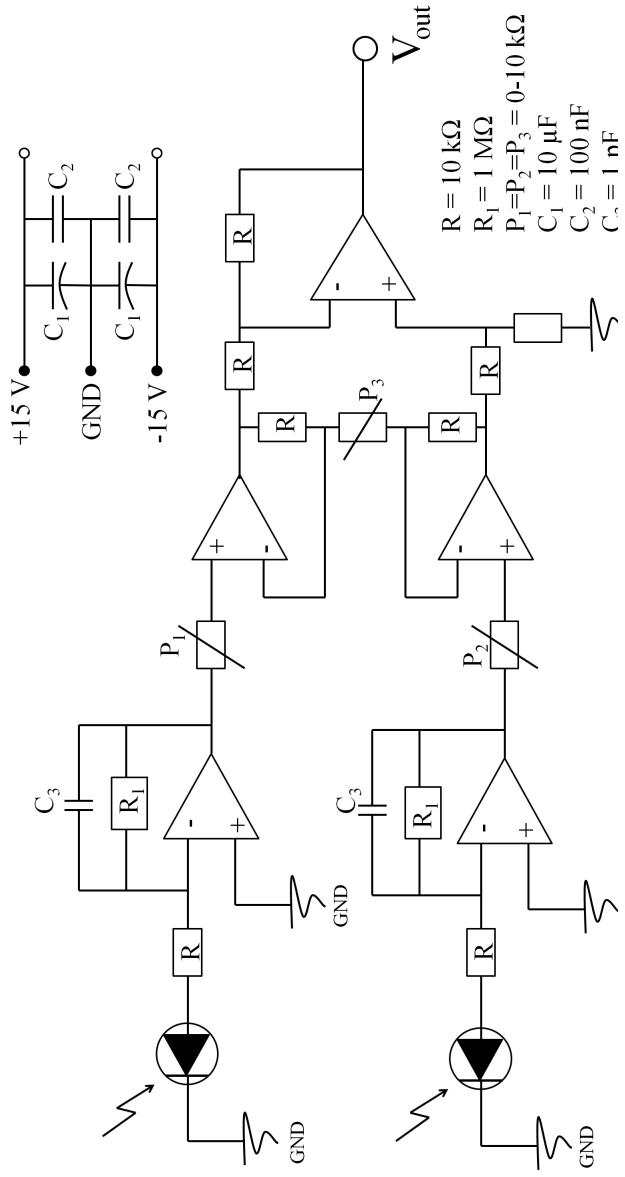

Figure 4.13: Circuit diagram for balanced PD pair.

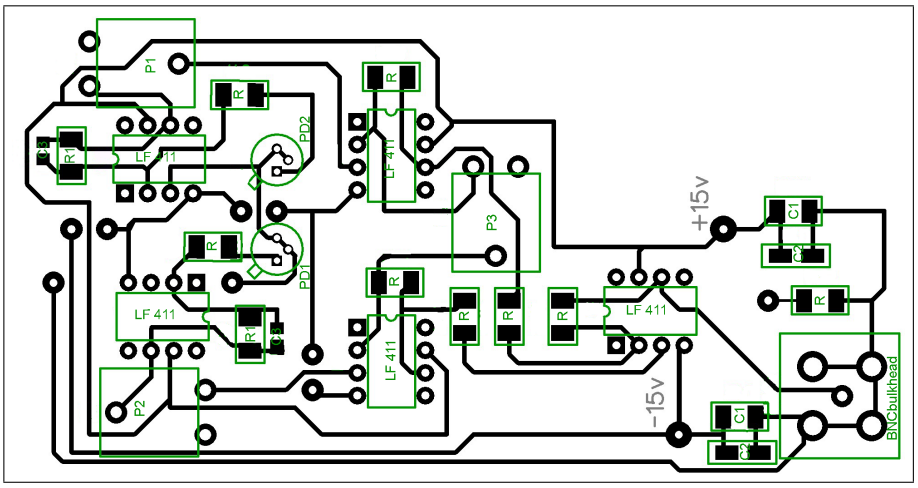

Figure 4.14: PCB layout for balanced PD pair.

Both ^{85}Rb and ^{87}Rb have transitions close to 780 nm, with energy levels for ^{87}Rb being shown in Fig. 4.15. This shows three allowed transitions from the groundstate, F = 2 hyperfine state. When the laser is scanned over these frequencies, three additional peaks will be observed, making a total of six absorbtion peaks. The addition absorption peaks are a result of crossover resonances. A crossover resonance occurs when the laser is tuned exactly half way between two transitions. At this position the laser will interact with a non zero velocity class of atoms, the pump beam will drive one transition while the probe beam drives the second transition, because both transitions share a common ground level the pump beam still effects the absorption of the probe beam, resulting in reduced absorbtion and additional peaks in the spectrum [84].

The optical setup for the 780 nm laser is shown in Fig. 4.16. The 780 nm laser passes through an optical isolator, this prevents back reflections into the diode that would otherwise prevent laser stabilization. It then passes through a $\lambda/2$ waveplate, this rotates the laser polarization to ensure transmission through the polarising beamsplitters (PBS). Next a beamsplitter removes two beams that are then used for the rubidium absorption spectroscopy. The beamsplitter is a high reflectivity custom coated mirror, with high reflectivity at 369 nm, 399 nm, 638 nm and 935 nm, (LaserOptik, part number: B-02436). By changing the incident angle, the reflectivity at 780 nm can be varied between R $\approx$ 1% - 74%. A second weak reflection from the rear surface provides a probe beam, with the rest of the beam being transmitted and sent to the cavities. These two beams then pass through a neutral density (ND) filter, (Melles Griot, part number: 03 FSB 005), and a second beamslitter. This picks 180 μW from the pump beam and is used as the Doppler background beam. The resulting pump beam has an intensity of 135 μW and a probe

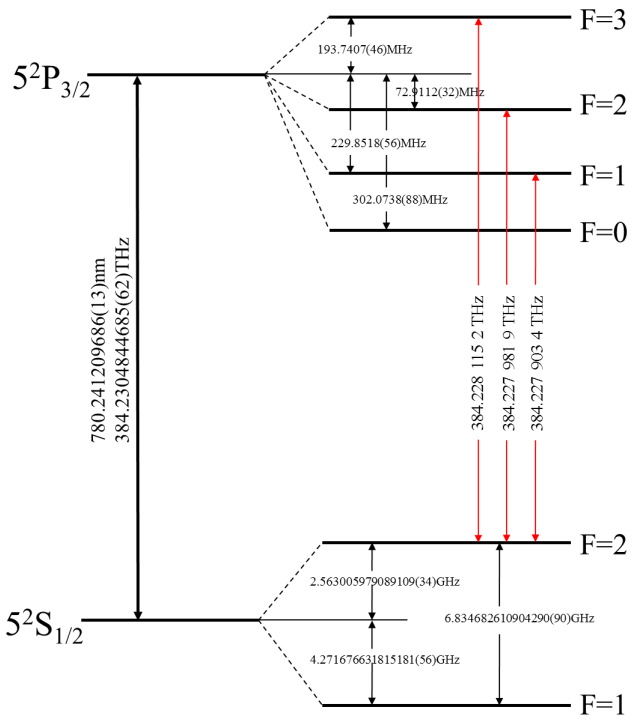

Figure 4.15: Hyperfine structure of ^{87}Rb D_2 transitions, transition frequencies taken from Ref. [5].

beam of 3 μW. The pump and probe beams are closely overlapped and both the probe and Doppler background beams are detected on photodiodes.

The rest of the beam is split between two confocal cavities and the wavemeter, with each receiving $\approx$ 4 mW of power. The 780 nm laser is aligned into the cavities through a PBS. The 780 nm polarization is aligned to transmit through the beamsplitter whilst both the 935 nm and 739 nm lasers reflect. All the lasers are detected on individual photodiodes after the cavities.

By scanning the laser piezo the 780 nm lasers frequency can be scanned over both ^{85}Rb and ^{87}Rb D_2 transitions and is shown in Fig. 4.17. This shows the broadened Doppler background, with a width of $\approx$ 500 MHz, showing sharp hyperfine transitions close to the center of each dip. By subtracting the Doppler background we are left with just the hyperfine intensity peaks, a scan over the ^{87}Rb D_2 transitions can be seen in Fig. 4.18.

A 100 kHz modulation is applied directly to the laser drive current. A signal generator sends a triangle wave to both the laser diode current controller and lock-in amplifier. By adjusting the voltage output the modulation depth can be altered. Scanning the laser frequency using the piezo at 10 Hz and viewing both the absorbtion signal and lock-in output the error signal can be viewed and is shown in Fig. 4.19.

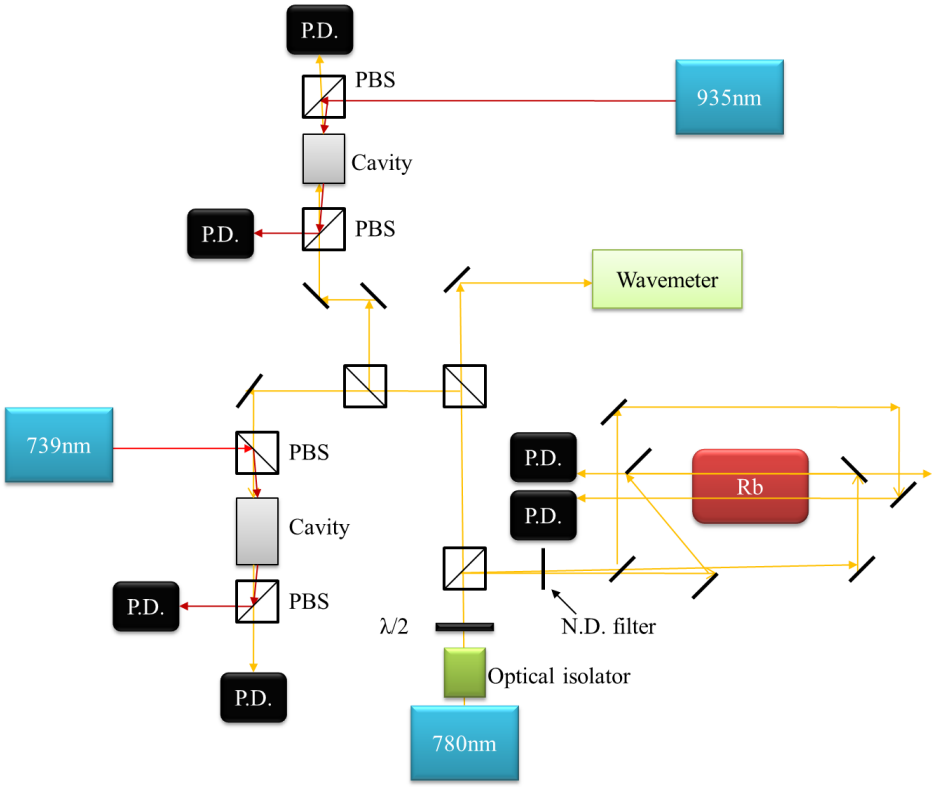

Figure 4.16: Rb absorption optical set-up

The output from the lock-in amplifier is then sent to the PI controller. Adjusting the input offset, the lock set point of the error signal are set. By stopping the laser scan and manually adjusting the piezo, the laser frequency can be brought close to a hyperfine transition. Once close, the proportional control is switched on, then followed by the integral. If the controller is set correctly this should begin to feedback to the laser piezo and maintain the laser frequency close to the set point.

By adjusting the gain on the proportional as well as the gain and time constant of the integral it is possible to optimize the laser feedback, and improve frequency stability.

4.8 Laser stability and noise measurements

Several measurements of the laser stability were taken to assess the long and short term frequency stability of the laser. As a measure of frequency noise on the laser the output from the photodiode circuit was recorded. This was decomposed into its frequency components by taking the Fourier transform of the data, which was performed in Mathematica. Secondly the Allen variance of the laser was measured, this describes the stability of the laser over several integration times. Lastly and most crudely wavemeter measurements of the frequency was monitored over several hours.

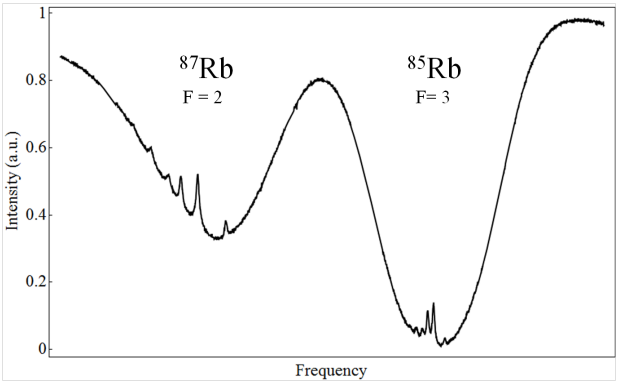

Figure 4.17: Hyperfine structure of ^{87}Rb F=2 and ^{85}Rb F=3 lines.

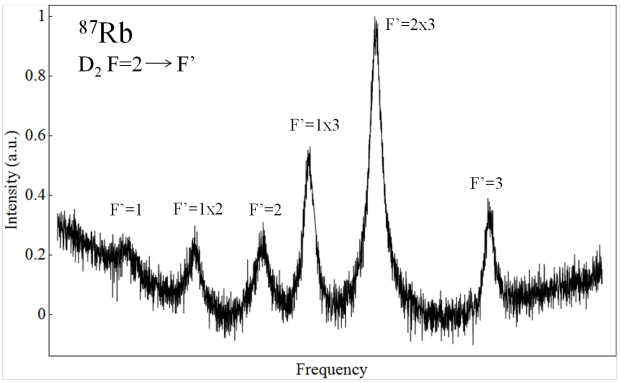

Figure 4.18: Hyperfine structure of ^{87}Rb F=2 transitions, the crossover resonances are labeled with an x.

An initial frequency spectrum was taken from the photodiode circuit unilluminated to give a base line. This shows any potential frequency spikes due to oscillations in the electronics and that are independent of the laser itself. Figure 4.20 shows the Fourier transform of the photodiode circuit alone. This shows a predominantly flat spectrum other than the DC component and two sharp peaks at approximately 22 kHz and 102.5 kHz, the exact cause of these peaks is not known, but these spikes do not hinder the laser measurements so are ignored.

Now by locking the laser to the rubidium cell the same measurement can be taken. This time the FT will show the frequencies at which the laser oscillates. The Fourier transform for low frequency and high frequency laser oscillations are show in figures 4.21 and 4.22. The black line corresponds to the laser with red line showing the PD noise. It is also possible to use this to investigate different forms of noise on the laser. The primary source of noise is from HEPA filters above the optical table. These provide a continuous supply of filtered air to help keep the optics clean, however they produce a large amount of acoustic noise. Figure 4.23 shows two Fourier transforms, in black is the 780 nm laser

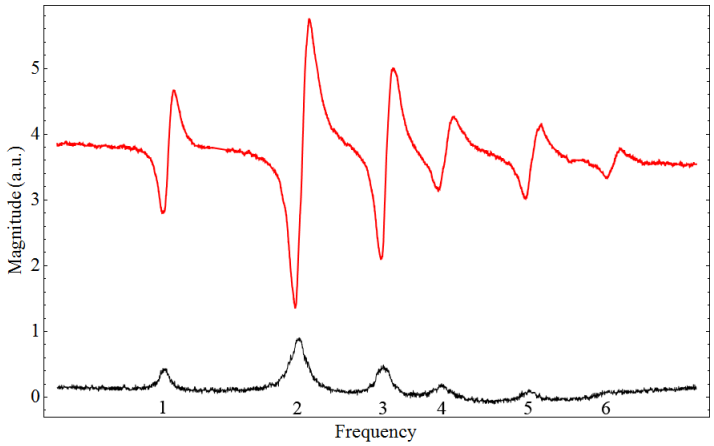

Figure 4.19: A scan over the ^{87}Rb hyperfine transition, showing the photodiode signal and the lock-in amplifier output.

locking with the HEPA filters running, the red line shows the Fourier transform with the filters off.

It can be seen that the HEPA filters introduce a large amplitude of low frequency noise, specifically bellow 30 Hz, but with further peaks at 50 Hz and between 80-100 Hz. When plotting the same data upto 125 kHz on a log-log scale, as show in Fig. 4.24, it can be seen that the filters have negligible effect above $\approx$ 200 Hz.

It is also useful to measure the spectral noise density of the laser. To measure this the error signal from the lock-in amplifier is recorded. The error signal is proportional to the rubidium transition linewidth, with the peak to peak error signal amplitude corresponding to the FWHM of the transition peak, it is now possible to convert the error signal voltage into a laser frequency.

The Rb transition linewidth will be subject to broadening so first a measurement of the experimental linewidth must be taken. This was achieved by scanning the laser frequency oven approximately 1.5 GHz and observing both the rubidium absorption signal and the transmission through a confocal cavity. The cavity has a known FSR of 1 GHz, so by measuring the time between adjacent peaks this calibrates the time scale into laser frequency. The measured FWHM of the ^{87}Rb F = 2 $\rightarrow$ F = 2$\times$3 crossover transition was $\gamma = 35.7 \pm 0.2$ MHz, the dominant broadening mechanism is power broadening, due to the laser being significantly above saturation intensity, though others will contribute eg collisional broadening. This can be used as a calibration of the error signal, which from peak to peak corresponds to the transition FWHM. This now translates a voltage into a laser frequency, with a sensitivity of 97 MHzV^{-1}. Recording 50 ms of the error signal a spectral density plot of the laser was calculated and is shown in Fig. 4.25.

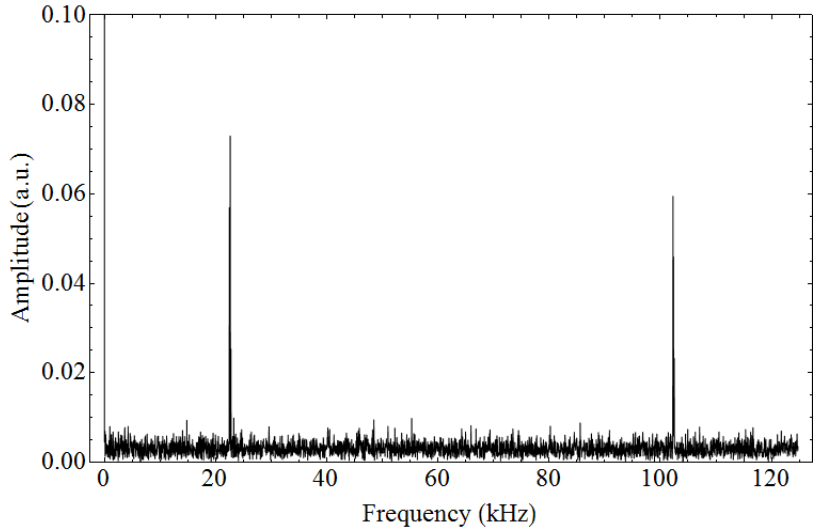

Figure 4.20: The Fourier transform of the photodiode dark noise. Sample time was 200 ms with a sampling rate of 500 000 data points. This shows two large frequency components at $\approx$ 22 kHz and $\approx$ 102.5 kHz.

4.8.1 Allan variance

In order to characterise the frequency stability of an oscillator it is possible to use the Allan variance $\sigma_y(\tau)$. This is used alternatively to the standard deviation, as the Allan variance has been showed to always converge to a well defined value, something the standard deviation does not [85]. The Allan variance is given by

$$\sigma_y^2(\tau) = \sum_{k=1}^{M-1} \frac{(y_{k+1} - y_k)^2}{2(M-1)}. \tag{4.10}$$

Where M is the number of recorded data points and y_k is the number of data points divided by the time at the kth point. Using the Allan variance it is possible to use the same data and calculate the variance for different measurement times, 2τ, 4τ... This is done by repeatedly pairing adjacent measurements and finding the average. This then gives the Allan variance of the laser frequency over a range of integration times. Figure 4.26 shows the Allan variance given by the data used for the spectral density plot.

The value of the Allan variance corresponds to the root mean square of the change in frequency between two measurements taken with a set time delay. From Fig. 4.26 we can see that for two measurements taken 10 seconds apart they will have an RMS frequency difference of 0.11 MHz. This shows the laser stability for different integration times, the value of the Allan this improves up to 1 second then increases up to approximately 1MHz for an integration time of $>$ 2 minutes.

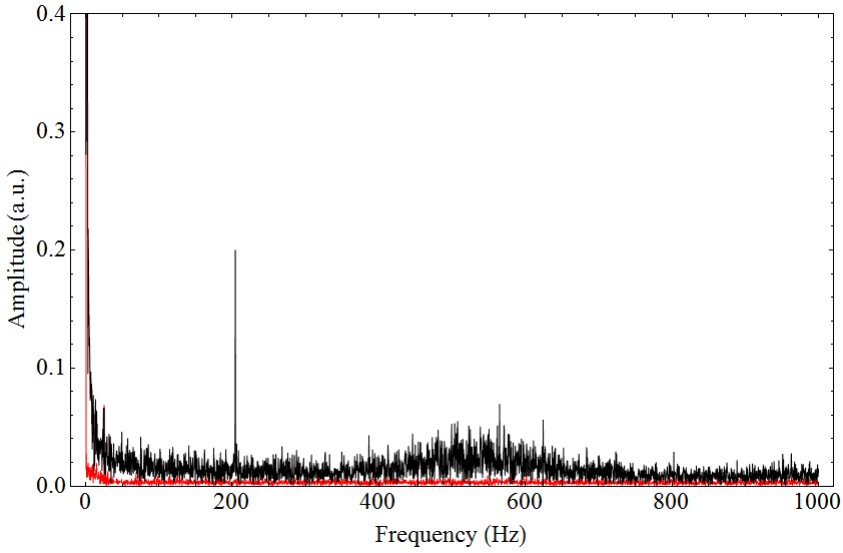

Figure 4.21: The Fourier transform of the photodiode signal with the laser locking, shown in black. The photodiode noise is shown in red. Sample time was 200 ms with a sampling rate of 500 000 data points. This shows a large frequency components at $\approx$ 200 Hz and further noise between 400-700 Hz.

4.9 Wavemeter measurement and calibration

To gauge long term stability the laser's frequency was monitored over several hours on the wavemeter. This is specified to an absolute accuracy of 60 MHz, but for shorter times gives a measurement of relative accuracy of several MHz. Monitoring the laser frequency over several hours showed that the laser drifted no more than $\pm$ 5 MHz and over times of several minutes $<$ 1 MHz. Though the true stability is likely to be greater than this.

To provide continuous measurement of the laser wavelengths a High Finesse WS7 Super Precision wavemeter is fiber coupled to all the experiment lasers. This measures laser wavelength over a range between 350-1120 nm, covering all our lasers, with an accuracy of $\pm$ 60 MHz. To ensure the highest level of accuracy the wavemeter is calibrated regularly to a known source, this can be either a stabilize HeNe laser. This has a built in stabilising system and can provide a reference frequency with an accuracy $<$ 5 MHz. Alternatively the rubidium locked 780 nm laser is used. By locking the 780 nm laser to the peak of the F $= 2 \rightarrow 2$ & 3 crossover transition, with a transition frequency measured to be 384.2279929 THz $\pm$ 2.4 MHz [5] as a reference frequency.

To ensure the wavemeter is calibrated correctly the laser is first scanned over the hyperfine transition. The zero volt crossing is the peak of the transition, the position of this crossing is marked on the scope. The laser is then locked to this transition. Adjusting

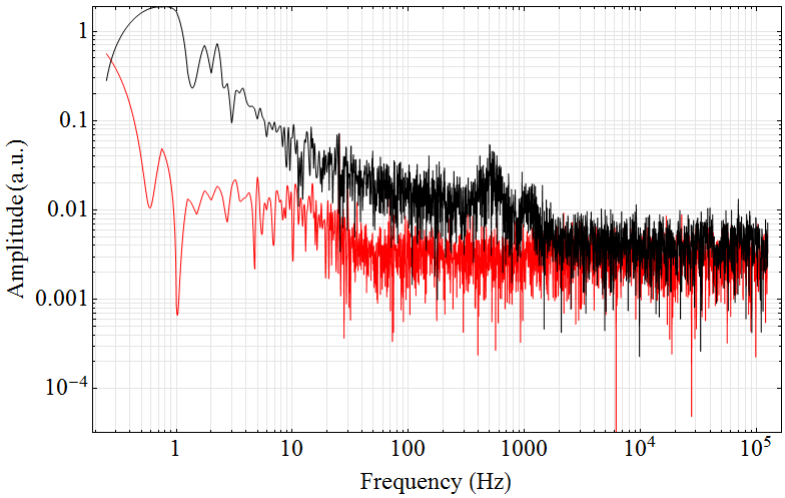

Figure 4.22: A log-log plot of the Fourier transform of the photodiode signal with the laser locking, shown in black. The photodiode noise is shown in red. Sample time was 200 ms with a sampling rate of 500 000 data points. This shows a large frequency components at $\approx$ 200 Hz and further noise between 400-700 Hz, with noise amplitude decreasing upto $\approx$ 1 kHz after which it remains constant.

the offsets on the PI controller it is possible to move where on the error signal slop the laser locks. Carefully adjusting this offset while the laser is locked, the laser frequency can be brought onto resonance. Once the laser is frequency stabilised on the crossover resonance the wavemeter can be calibrated to the value given in Ref. [5].

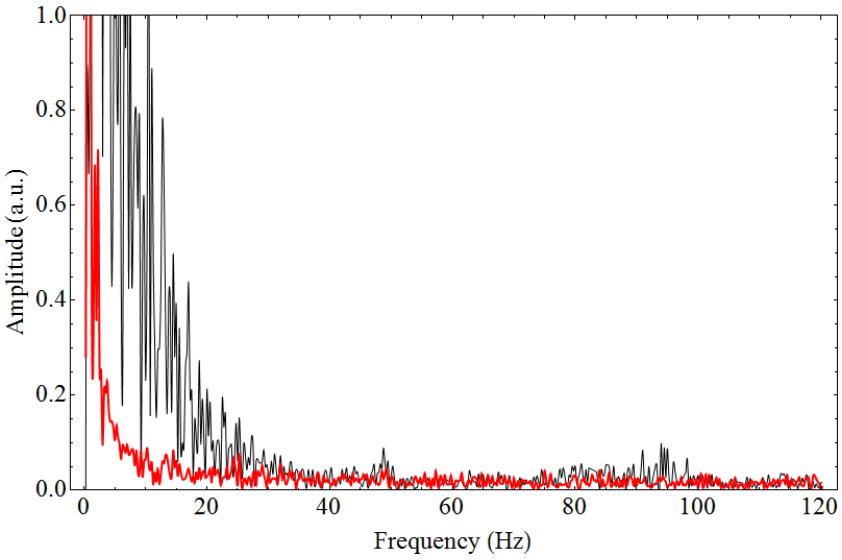

Figure 4.23: The Fourier transform of the photodiode signal when the laser is locking with both the HEPA filters on (black line) and off (red line). Sample time was 200 ms with a sampling rate of 500 000 data points. It can be seen that the HEPA filters introduce a large amplitude of low frequency noise, specifically below 30 Hz, though there are additional peeks at 50 Hz and between 80 and 100 Hz.

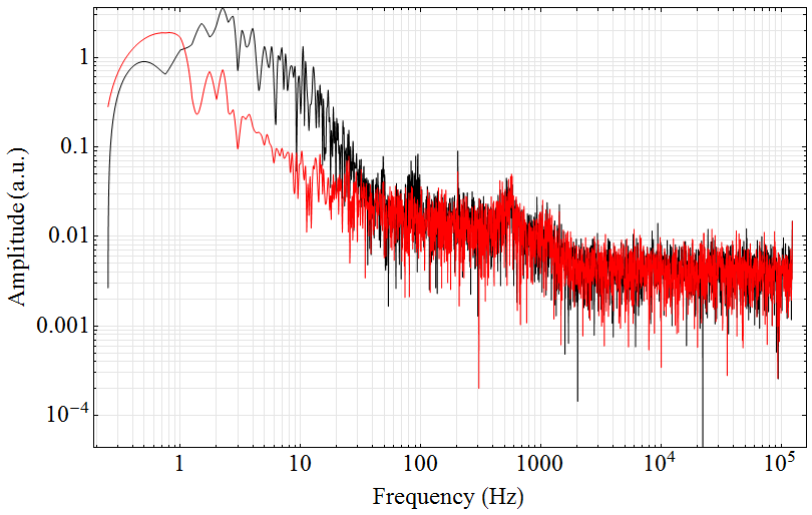

Figure 4.24: A log-log plot of the high frequency Fourier transform for when the laser is locked with both the HEPA filters on (black line) and off (red line). This shows that the HEPA filter has negligible effect above $\approx$ 200 Hz.

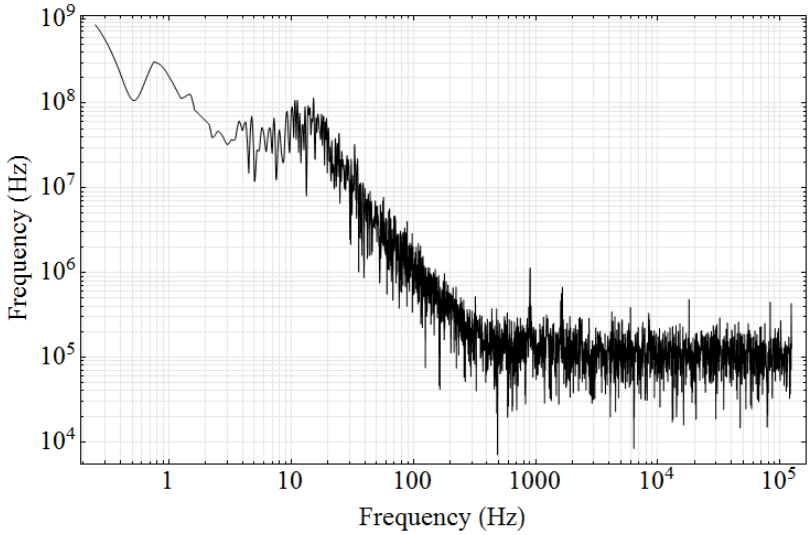

Figure 4.25: The spectral density of the laser taken from the error signal output from the lock-in amplifier. The sample time was 50 ms with a sample rate of 500 000 points. The x-axis corresponds to the noise frequency while the y-axis corresponds to the laser frequency change.

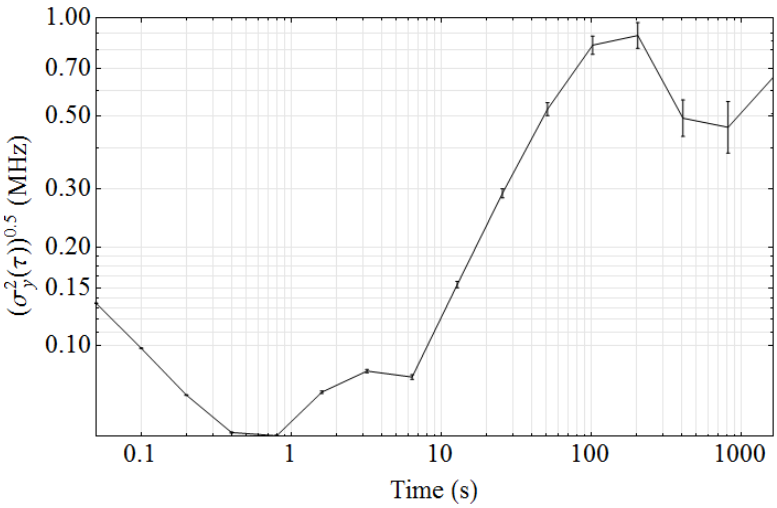

Figure 4.26: The Allan variance give from the laser error signal. The sample time was 50 ms with a sample rate of 500 000 points.

Chapter 5

Blade Ion Trap

Experience is the name so many people give to their mistakes.

- Oscar Wilde

5.1 Introduction

For initial ion trapping experiments a large, manually assembled ion trap was built. It was designed to be compatible with the vacuum system chip bracket and to have > 1 MHz secular frequencies in all three axes, > 1 eV trap depth and micromotion compensation for all three axes. Micromotion electrodes are require to compensate for static offset electric fields generated by background sources. These displace the ion from the rf nill and result in excess micromotion on the ion.

The trap was simulated using CPO and Mathematica and designed using SolidWorks. The trap itself was fabricated on site in the university workshop, and assembled in the lab. It was successfully used to trap Yb+ ions.

5.2 3 Layer PEEK trap

Initially a 3 layer ion trap was built and used to attempt trapping of our first ions. This consisted of six, 1 mm diameter, tungsten rods mounted in a PEEK block. RF power was applied to the middle two electrodes with the outer four electrodes providing micromotion compensation and principle axis rotation. Confinement along the z-axis was provided by two end cap electrodes at either end of the trap. The trap design can be seen in Fig. 5.1.

Electrical contact between the trap electrodes and the vacuum chip bracket was made by 0.3 mm tungsten wires, these passed through the PEEK mount and into the chip bracket pin receptacles. Electrical connection between the thin tungsten wires and the

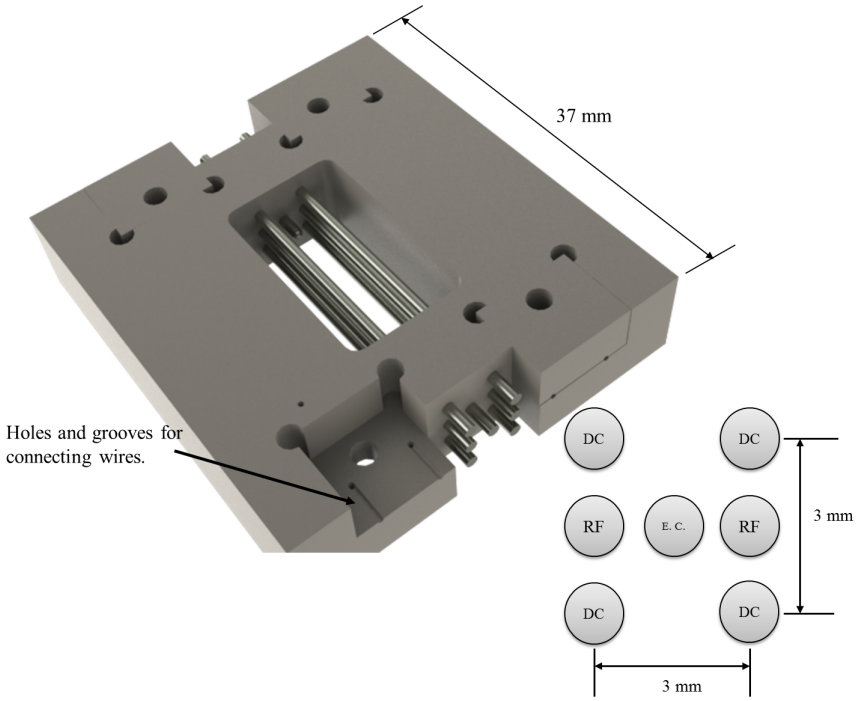

Figure 5.1: A SolidWorks drawing of the trap and the electrode layout.

trap electrodes was made by spot welding constantan foil between the two. To prevent the connecting wires becoming loose they were bent and clamped in position with PEEK blocks screwed into the main trap body. The trap was mounted and used to attempt trapping for several months. Figure 5.2 shows the trap after it was removed from the vacuum system.

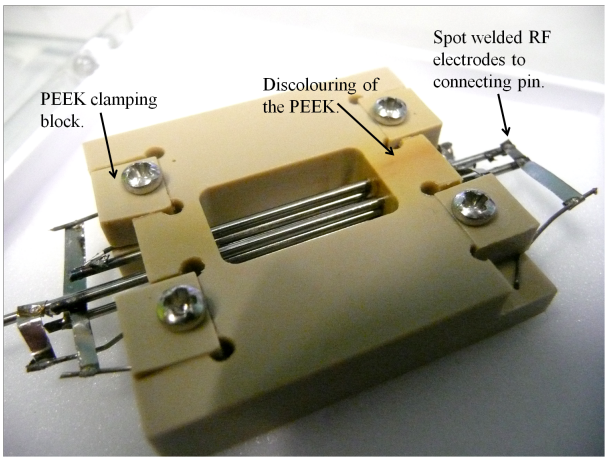

Figure 5.2: The PEEK ion trap after it was removed from the vacuum system after several months of attempting to trap. Discolouring of the PEEK mount can be seen, it is thought that this was caused by the 369 nm and 399 nm lasers. This discolouring is also likely to have resulted in large charging of the dielectric.

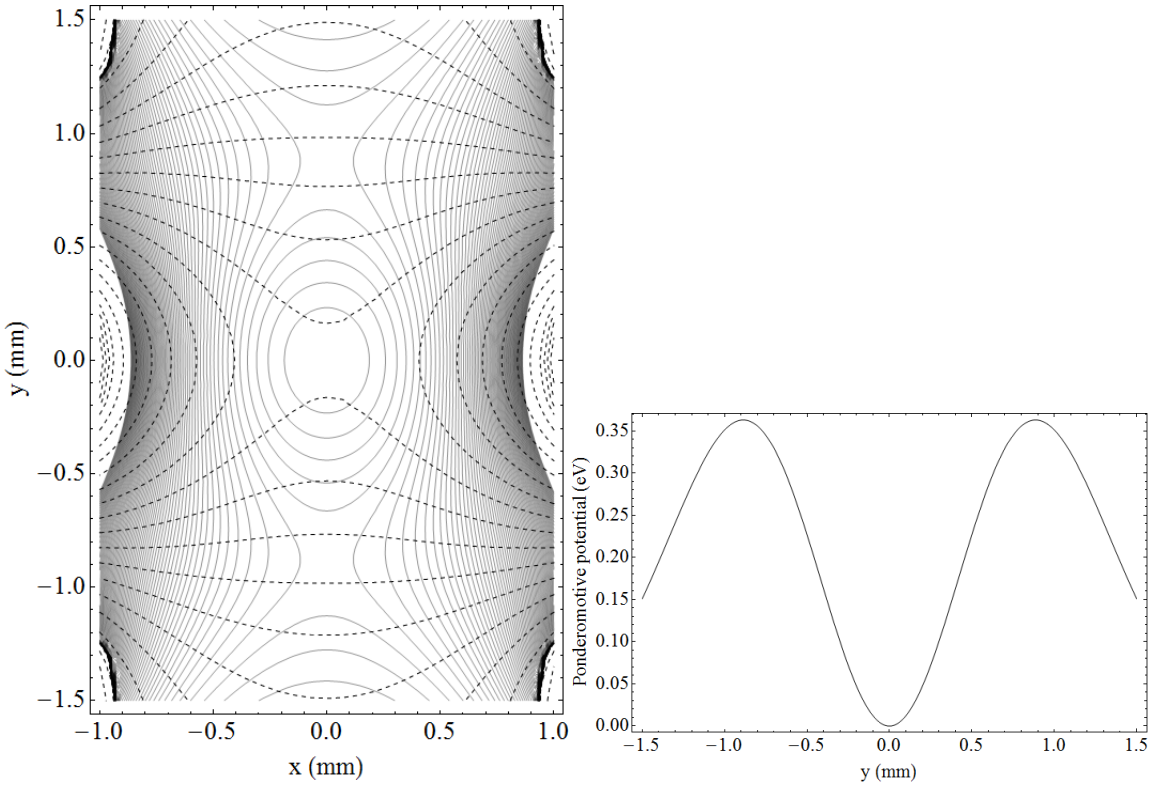

(a) (b)

Figure 5.3: a) Contour plot of both the electrostatic potential (dashed) and ponderomotive potential (solid) of the three layer PEEK trap. b) Plot of the PEEK traps ponderomotive potential along the y-axis at $x = 0$.

The trap was removed for several reasons, firstly numerical simulations showed that the trap depth was significantly lower than that expected from the equivalent 2 layer geometry. Simulations of the electrode geometry show that the trap depth at a frequency of $\Omega/2\pi = 21.48$ MHz and a peak rf voltage of $V_{RF} = 1000$ V, approximately equal to the trap parameters used to trap our first Yb ions, is only ≈ 0.35 eV compared with a two layer geometry with the same ion-electrode separation has a trap depth of ≈ 2 eV. Figure 5.3(a) shows a contour plot of both the electrostatic potential (dashed) and the ponderomotive potential (solid), Fig. 5.3(b) shows the potential along the y-axis at $x = 0$.

Additionally it was noticed that after extended exposure to the UV laser beams the PEEK became significantly discoloured. This discolouring, which can be seen in Fig. 5.2, is likely to have caused charging of the dielectric material. This uncontrolled charging could severally disrupt the trap stability and make the trap difficult to successfully load. Furthermore due to the large distance between the electrodes, effective imaging of the trap region was extremely difficult. For these reasons it was decided that the vacuum system

would be opened and a new trap designed and built.

5.3 Blade Trap

To replace the PEEK ion trap I designed a two layer linear Paul trap, the geometry of which can be seen in Fig. 5.4. This shows first an xy cross section through the trap center, with an electrode-electrode separation of 300 μm, and ion-electrode separation of 212 μm. Radial confinement of the ion is generated by two radio frequency electrodes, with laser and imaging access along the x-axis at $y = 0$. Confinement along the z-axis is achieved by segmenting the static electrodes and applying end cap potentials. The segmentation can be seen in the bottom of Fig. 5.4 which shows the top level of the trap.

Micromotion compensation is achieved by using three parallel wires that run the length of the trap. They are labeled C1 and C2 in Fig. 5.4. Compensation along the x-axis is achieved by C1 which has been split into two wires to allow laser access. Both wires are electrically connected so that their respective y components cancel leaving only a potential along the x-axis.

5.4 Trap simulations

The electrodes electrostatic basis functions were simulated in CPO, with the ponderomotive potential, trap depth and secular frequencies being calculated in Mathematica. To draw the blade electrodes first a narrow cylindrical electrode was input as the electrode tip and from this two rectangle faces extend back to create the top and bottom faces of the electrode. The cylinder diameter was estimated to be on the order of the curvature at the tip of the electrode, of approximately 0.1 mm. Additional cylinders were included for the compensation electrodes, with a diameter of 1 mm.

Simulations of the trap geometry are shown in Fig. 5.5, this shows a contour plot of the ponderomotive potential and a plot of the potential along the x-axis at $y = 0$. The trap uses an rf drive frequency of $\Omega/2\pi = 21.48$ MHz and peak rf voltage of $V_{rf} = 280$ V. The corresponding trap depth is 2.35 eV with radial secular frequencies of $\omega_x/2\pi = \omega_y/2\pi = 1.64$ MHz. Numerical noise close to the electrodes result in irregular contours but the simulation is still accurate[1] close to the trap center.

To ensure efficient laser cooling along all three trap principal axes the x- and y-axes of motion can be rotated by applying voltages to the two central electrodes. A voltage of

[1] Simulations of the electrode configurations given in Ref.[**?**] show agreement to >99%.

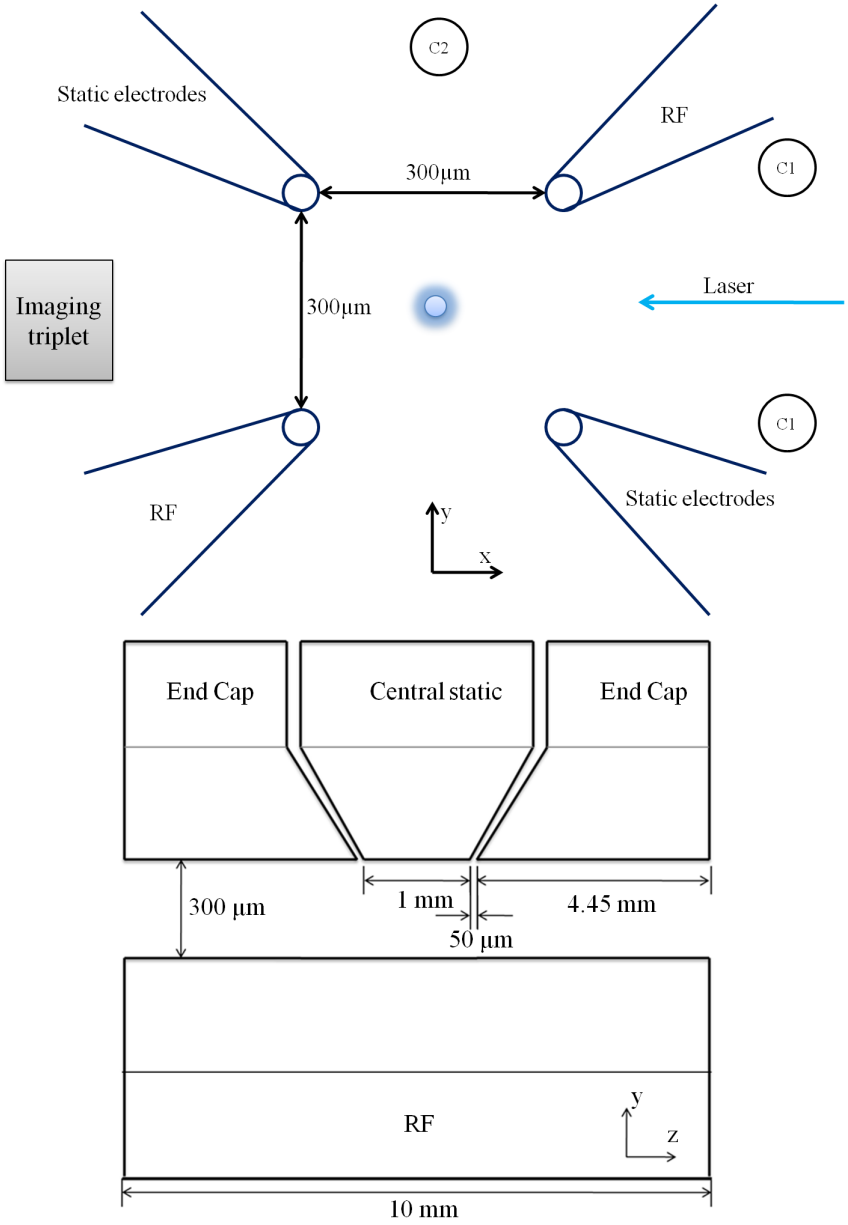

Figure 5.4: The top figure shows a cross section through the trapping region. The upper right and lower left electrodes are at rf and provide the radial confinement. With laser access from behind. The bottom shows a view from the top of the trap, the static electrode has been segmented to provide end cap potentials.

approximately 1 V on the central static electrodes rotate the axes by 45°, this rotation can be seen in Fig. 5.6.

5.4.1 Residual ponderomotive potential

In the ideal linear Paul trap there is zero ponderomotive potential along the z-axis. In reality because there is a gap between the segmented electrodes a small residual ponde-

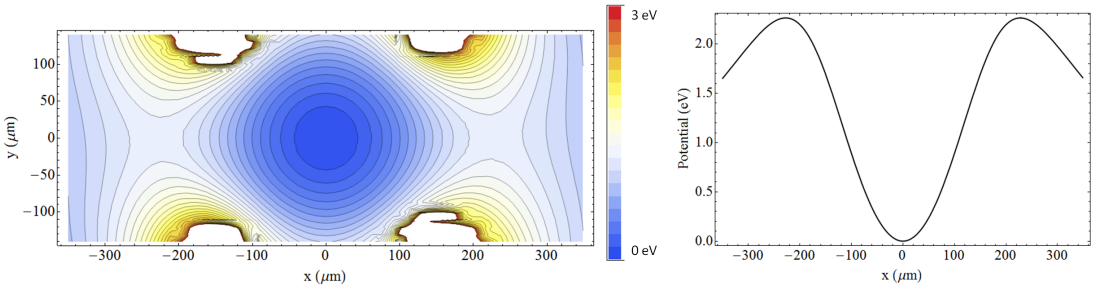

Figure 5.5: CPO model of the blade electrodes. Left shows the ponderomotive potential, right shows the ponderomotive potential along the x axis at y = 0.

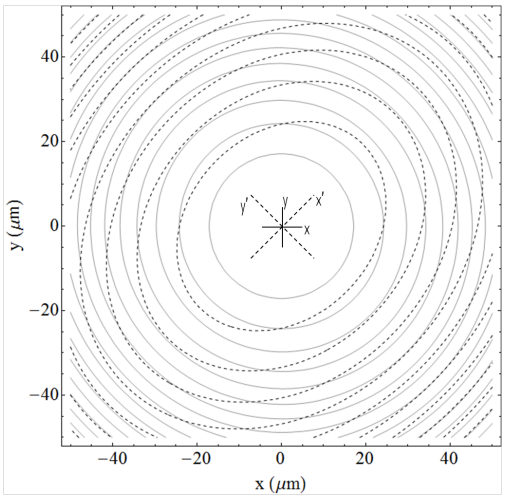

Figure 5.6: Contour plot showing the rf ponderomotive potential, solid, and the potential after a rotation voltage has been applied, dashed. This shows that the principal axes of motion have been rotated by 45°, ensuring the laser has a component along all three axis of ion motion.

romotive potential along the z-axis is generated. By reducing the width of these notches the residual potential can be reduced [43].

The ponderomotive potential along the z-axis is shown in Fig. 5.7. This corresponds to an rf voltage of $V_{RF} = 280$ V, it can be seen that the potential at the static electrode notches is on the order of meV and results in a secular frequency along the z-axis of $\omega_z/2\pi \approx 4$ kHz, which is $\approx 0.4\%$ that of the radial secular frequency.

5.5 Solidworks design

When designing the trap there were several constraints that needed to be taken into consideration. Firstly the whole trap needed to fit in the space allotted for a microfabricated

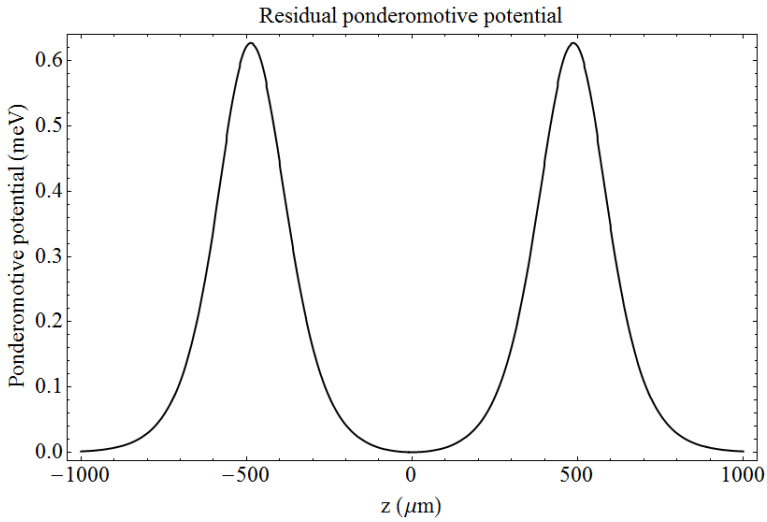

Figure 5.7: The potential along the z-axis at the rf nil. In the ideal linear Paul trap the potential would be zero but gaps between static electrodes introduce a residual rf ponderomotive potential along the z-axis.

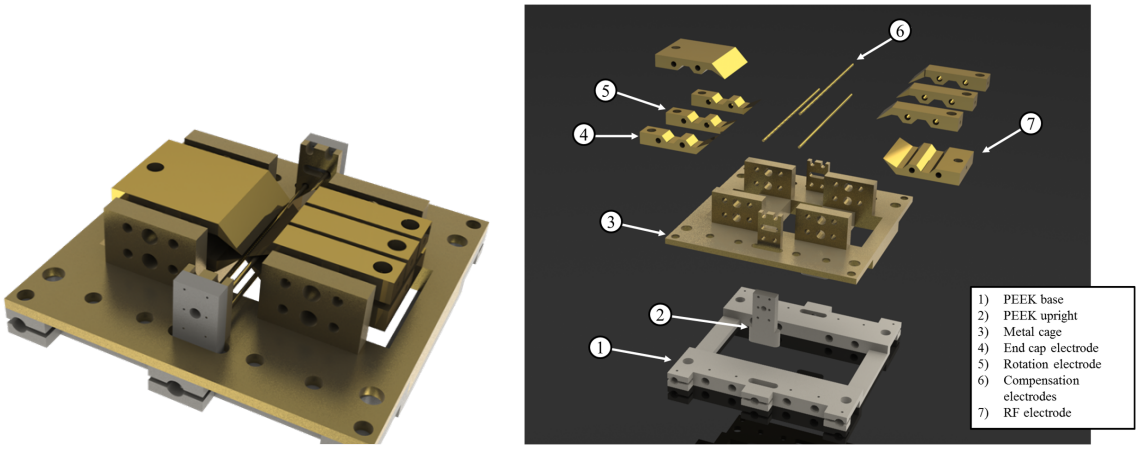

(a) (b)

Figure 5.8: a) Solidworks drawing of the assembled blade trap. b) Exploded view of the blade trap.

chip trap mounted on a chip carrier. This meant a space of $\sim 3 \times 3$ cm and 1 cm high. It needed to shield all dielectric insulating surfaces from the ion and finally that it needed to be possible for the university workshop to fabricate it.

Figure 5.8 shows two SolidWorks drawings of the blade ion trap. Figure 5.8(b) shows an exploded view of the trap, showing all the main components. The ion trap is constructed so that the electrodes are suspended from ceramic rods held by a metal cage. The electrodes are clamped into position via grub screws and insulated by PEEK spacers, the electrodes themselves hide these spacers from the ion. The metal cage is then mounted on top of a

PEEK base that provides electrical insulation from the vacuum pin receptacles and holds connecting wires that connect each electrode with the corresponding pin.

The following sections describe the design of the individual components from Fig. 5.8(b) used to construct the blade trap. All the technical drawings for the trap are in App. C.

PEEK base (1)

Figure 5.9 shows the PEEK base. Small holes tightly fit gold coated stainless steel wires which pass through these holes from the vacuum system pin receptacles up through the metal cage and connect to the electrodes. These holes were carefully positioned to make sure that they correctly line up to the correct pin receptacles in the vacuum system chip bracket. To ensure these wires are firmly held in place threaded holes perpendicular allow a grub screw to be screwed into the base and clamp these wires in place, though it was found not to be necessary. The tapped grub screw holes pass all the way through the PEEK base to ensure that there are no trapped volumes which can result in a virtual leak. Four larger holes in each corner are through holes for screws that will hold the whole assembly together. On the bottom the PEEK is recessed around these larger holes, this allows a nut to be fastened onto the screw and lay flush with the back of the mount. A slot is machined either end of the base. This is to allow a vertical PEEK piece, Fig. 5.8b (2), to be mounted in the base. This PEEK upright is required to hold the compensation electrodes and can be seen in Fig. 5.10.

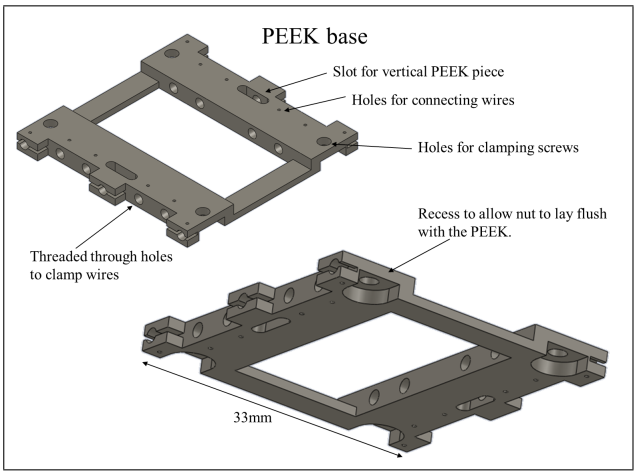

Figure 5.9: SolidWorks drawing of the PEEK base.

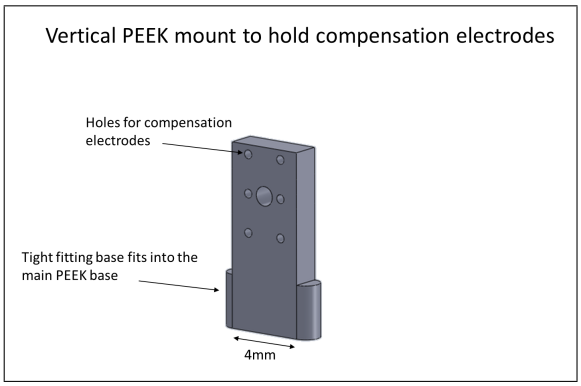

Figure 5.10: Solidworks drawing of the PEEK upright which holds the compensation electrodes.

Stainless steel cage (3)

Figure 5.11 shows the stainless steel cage that holds the electrodes. It covers the entirety of the PEEK base to ensure that all dielectrics are well hidden from the ion. PEEK discolouring was observed after exposure to laser radiation, it is suspected that in vacuum this can lead to uncontrolled charging of the dielectric material and disrupt trap operation. Holes in the metal base are positioned to match similar holes in the PEEK base, though they are larger as to avoid making contact with the connecting wires and inadvertently grounding the electrode. There are three rectangular square holes in the base, the central hole is to allow laser and atomic oven access to the trapping region. The two outer holes allow access to grub screws mounted in the bottom four electrodes.

There are four larger central uprights, these provide the supports from which the electrodes are suspended. Ceramic rods pass through these upright and hold the electrodes in the correct positions. Larger central taped holes allow grub screws to clap the electrodes in place. PEEK spaces between the electrodes and grub screws prevent electrical shorting.

The two smaller uprights are to provide shielding of the PEEK uprights that hold the compensation electrodes, they also provide mechanical stability for the PEEK pieces.

Electrodes (4,5,6,7)

Figure 5.12 shows the rf and segmented static electrodes. The two end caps taper in towards the center of the trap. The central electrode has a length at the tip of 1 mm and is separated from the end caps by approximately 50 μm, this gap increases as the electrodes get further from the trap center. PEEK spacers fit into a gap machined behind the electrode faces, keeping them electrically isolated. Electrical connection is made via a hole in the back of the electrode, the wire is clamped in position using a grub screw that

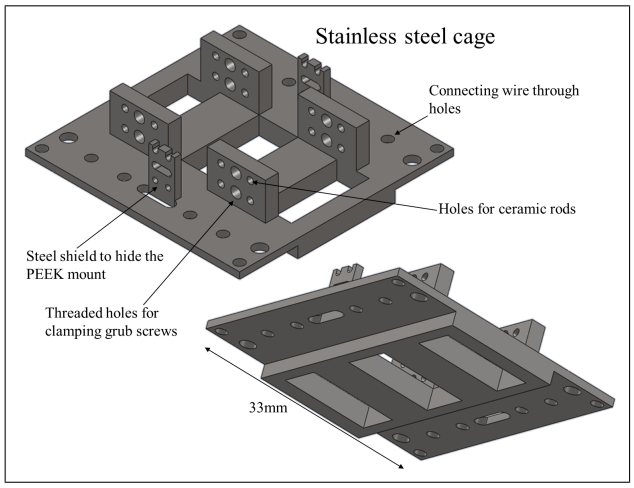

Figure 5.11: SolidWorks drawing of the steel cage.

screws through a large tapped hole, also at the rear of the electrode. The underside of each electrode has a machined trench in the center. This is to reduce the surface area that is close to the rf electrode in an attempt to minimize capacitance. The electrodes were all machined from stainless steel and gold plated with 5 μm of gold. This is to improve surface quality and reduce rf resistance. For precision they were machined using a wire eroder. A wire eroding machine passes a large current through a fine wire, the wire scrolls past the metal to be machined arching between the wire and the metal surface. This erodes the metal and can cut very precise shapes, with a machine tolerance on the order of 10 μm. This does however leave a pitted surface structure on the metal, therefore before the electrodes were gold coated the blade edge were carefully lap polished, resulting in a very smooth surface finish. Viewing the blade edge under the ion imaging camera shows that it has deviations of no more than 5 μm.

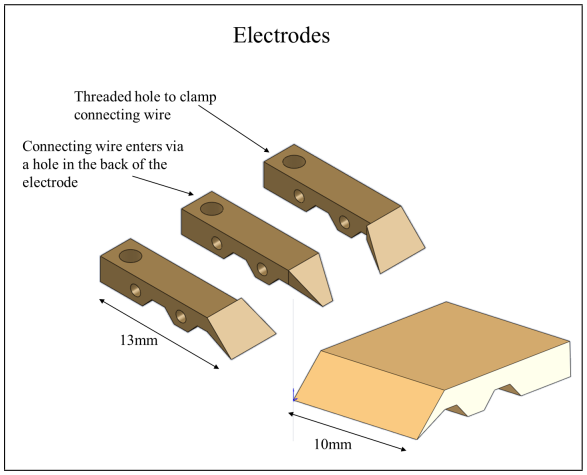

Figure 5.12: SolidWorks drawing of the electrodes.

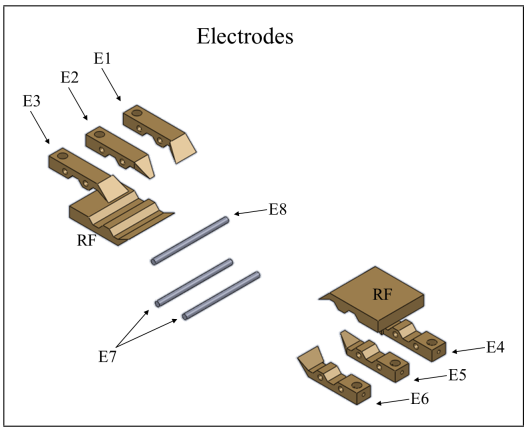

Figure 5.13: An exploded view of the trap electrodes with there appropriate voltage tag.

Figure 5.13 shows the electrode numbering used to assign electrode voltages.

Assembled trap

The trap was initially assembled using ceramic rods to align the electrodes but after examining the electrodes under a microscope it became clear that the machining tolerances of the electrodes was not sufficient. This resulted in several electrodes requiring to be remachined. Ultimately the ceramic rods were abandoned and the electrodes were maneuvered into position using translation stages whilst being viewed under a microscope. Once the electrodes were in the correct position the grub screws were fastened, clamping the electrodes to the metal cage. This is reasonably simple when mounting an rf electrode but becomes significantly more difficult when mounting the three static electrodes and the PEEK spacers. As a result, a large amount of time went into the trap assembly and the final electrode positions where not that of the intended design. The final electrode-electrode spacings are 343 $\pm$ 14 μm in the x-axis and 554 $\pm$ 14 μm in the y-axis, this gives an ion-electrode spacing of 310 $\pm$ 10 μm. After careful imaging of the rf and static electrodes the trap was resimulated to find the new trap depth and secular frequencies, discussed in the following section.

Figure 5.14 shows the assembled trap when using the ceramic rods and all compensation electrodes. After this the trap had to be disassembled and was rebuilt to improve electrode positioning.

After mounting the trap in the vacuum system and pumped down it was found that end cap corresponding to E4 had become electrically grounded. This is most likely due to the connecting wires moving during bake out and touching the metal cage as they pass through the bottom. Despite this it is possible to apply voltages to the remaining

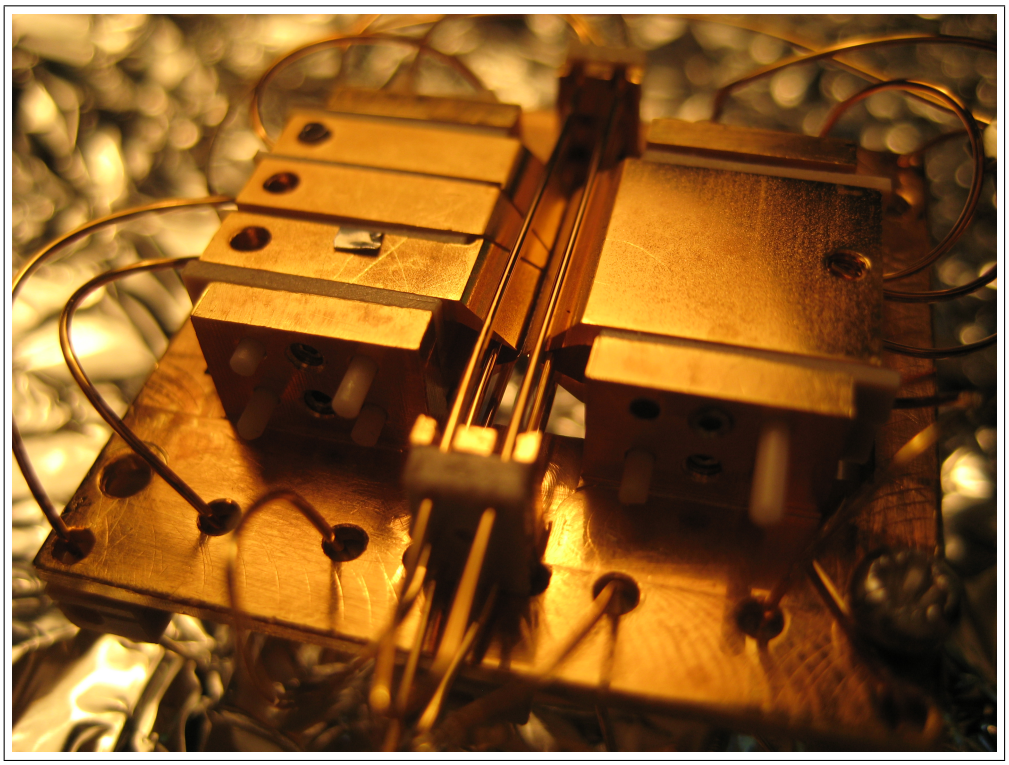

Figure 5.14: The assembled trap.

electrodes to trap the ion at the rf nil.

5.6 Corrected simulations and operation

After the vacuum system was baked and mounted on the optical table the trap was imaged using a microscope objective and CCD camera. Using this the electrode positions could be accurately measured in their final position. These new positions were then entered into the CPO model of the trap and a new more accurate simulation of the trap was taken. Figure 5.15 shows the ponderomotive potential of the trap when modeled with the corrected electrode positions.

It is possible to see that as a result of non symmetric electrode positions the ponderomotive potential is also asymmetric, with the shallowest point of escape close to $x = 330$ μm, $y = 70$ μm. The potential corresponds to a peak rf voltage of $V_{RF} = 680$ V and a drive frequency of $\Omega/2\pi = 21.48$ MHz, giving a q = 0.44. It was also found that during baking wires connecting electrodes E4 and E5 had moved and were now shorting the electrodes directly to ground. This prevented using E4 as an end cap electrode and so a combination electrode voltages on the remaining electrodes needed to be found to

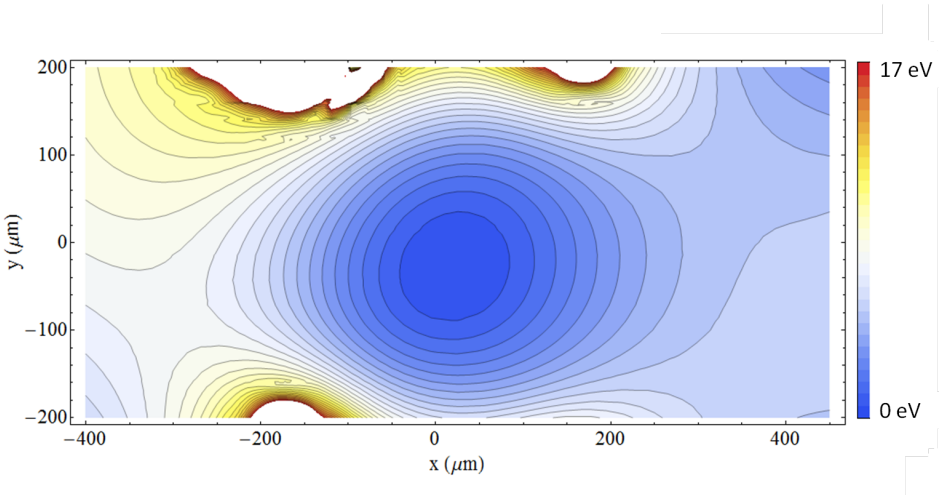

Figure 5.15: The ponderomotive potential of the trap after the final electrode positions were modeled. The potential corresponds to the trap electrodes with the voltages given in Tab. 5.1.

provide suitable stable trapping. The electrode voltages used are given in Tab. 5.1.

To load the ion trap a current is passed through an atomic oven leading to a flux of neutral ytterbium atoms to pass through the center of the trap. All the lasers are aligned to focus at the rf nil so that once an atom is ionised and feels the electric field it will becomes trapped. At this point the ionisation laser is blocked by an iris. Figure 5.16 shows a zigzag crystal of $^{174}Yb^{+}$ ions. The dark gaps correspond to dark ions of a different isotopes, off resonant with the cooling laser's frequency. Once loading is optimised it is possible to load the trap at a rate of approximately 10 ions per minute. Due to the depth of the trap the ions will remain trapped in the event of a collision with background gas, in the absence of cooling light and even if the laser is accidentally blue detuned, heating the ion.

To measure the ion secular frequency a signal generator was capacitively coupled to electrode E2. A low amplitude tickle frequency was scanned while observing a single ion on the camera. Once the tickle frequency matches one of the three secular frequencies this resonantly excites the ions motion and is seen as the ion goes from a white dot to a large fuzzy area. The secular frequencies were measured to be $\omega_x/2\pi = 2.069 \pm 0.001$ MHz, $\omega_y/2\pi = 2.110 \pm 0.001$ MHz and $\omega_z/2\pi = 1.030 \pm 0.001$ MHz, which shows a simulation accuracy of $\approx 95\%$ for ω_x and ω_y and $\approx 99\%$ for ω_z. Trap depth was found by matching measured secular frequencies to numerically calculated secular frequencies which gives a trap depth of 4.9 ± 0.2 eV.

Electrode voltages		
Electrode	Voltage (V)	Error ± (V)
RF	680	10
E1	148.88	0.01
E2	7.36	0.01
E3	25.03	0.01
E4	0.00	0.01
E5	0.00	0.01
E6	167.76	0.01
E7	169.22	0.01
E8	-2.70	0.01

Table 5.1: Typical trap operation electrode voltages. Depending on the operation of the trap and micromotion compensation these voltages will change. As a result of electrodes shorting the voltages have to be simulated as stable trapping voltages do not follow the traps symmetry.

By manually adjusting the compensation electrode E7 and E8 it should be possible to minimise ion micromotion, however in practice varying the static electrodes is necessary. By scanning the Doppler cooling laser frequency over the ion transition frequency and measuring the ion fluorescence we measure the transition linewidth. This is broadened by the laser intensity and excess micromotion. By reducing the laser power to remove power broadening and iteratively changing the electrode voltages while measuring the transition linewidth it is possible to minimise the ion trap micromotion. Performing this procedure it was possible to reduce the broadened transition linewidth to $\approx$ 30 MHz, still greater than the natural linewidth of 19.6 MHz. The trap is now being used to perform our first quantum information processes.

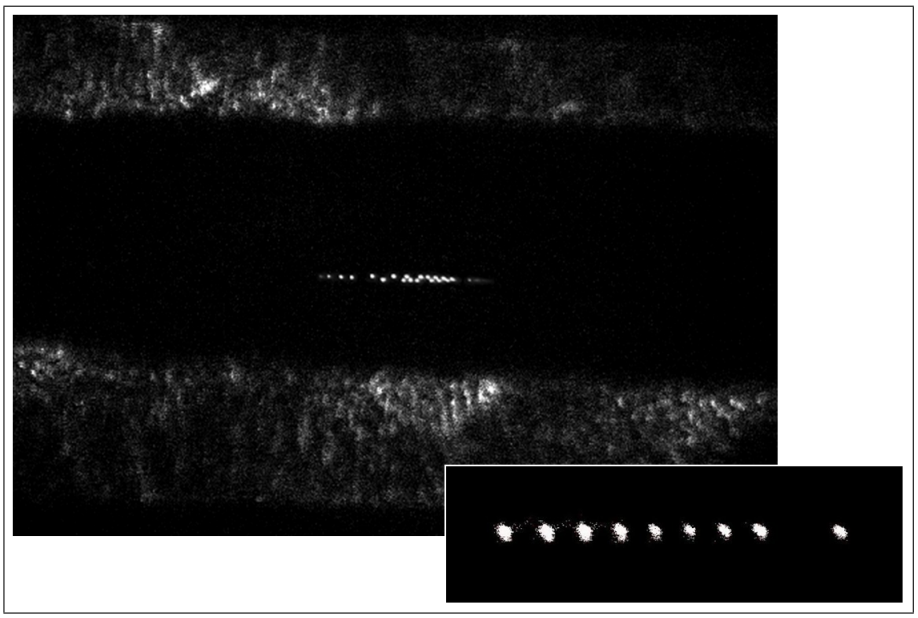

Figure 5.16: A zigzag crystal of trapped ions, large dark spaces are off resonant ytterbium isotopes. The scatter at the top and bottom are from the trap electrodes. The insert shows a close up of a linear chain of Yb ions.

Chapter 6

Vacuum system

If less is more, then just think how much more "more" will be.

- Dr Frasier Crane - Frasier

6.1 Introduction

To allow faster testing of microfabricated ion traps a second vacuum system was designed and built. This too had to be compatible with chip carrier mounted traps and to allow both surface traps, which require laser access and atomic ovens parallel to the trap surface and symmetric trap arrays which need laser and atomic oven access from the rear. Additionally it needed to improve on several drawbacks of the first vacuum system. It was found that due to the layout and small size of the original system that optical alignment could prove difficult. Vacuum pumps, nipples and flanges all obstruct the placement of translation stages and optic mounts, for the new vacuum system it was an important consideration that all vacuum windows were unobstructed. Another drawback of the first system was that aligning laser beams to exit the vacuum system without back reflections could prove extremely difficult. The lasers tend to clip the metal of a recessed window causing reflections back into the vacuum chamber and the imaging triplet. To avoid this the new vacuum system recessed window needed to be carefully designed and modelled to ensure that the lasers can leave the vacuum system unhampered. Other modifications included additional flexibility for potential traps; allowing a much greater volume for large traps to be mounted, and additional feedthroughs for microwave sources and optical fibres.

All the requirements of the new vacuum system are summarised bellow.

6.1.1 Vacuum system requirements

- Capable of achieving 10^{-12} Torr.
- Compatible with surface and multi layer ion traps.
- Optical access for any type of trap and guaranteed beam exit.
- Additional feedthroughs for optical fibres and microwaves.
- Greater trap housing volume for large ion traps.
- Improved external access for imaging and beam alignment optics.
- The trap center should be at the beam height of 5".
- Atomic ovens for both natural ytterbium and enriched ^{171}Yb, for both surface and symmetric traps.

6.2 Vacuum chamber

For the new vacuum system a new vacuum chamber needed to be found. One that was larger than the previous system to allow better optical access and more flexibility for ion traps. For this a combination of a Kimball Physics spherical octagon, (part no. MCF600-SphOct-F2C8), shown in Fig. 6.1(a)[1] and weldable cluster (part no. MCF450-WeldClstr-E1C4), shown in Fig. 6.1(b) could be used. These two parts were welded by Kimball to form one part and combined with a recessed window would form the vacuum chamber.

Figure 6.2 shows two SolidWorks drawings of the main vacuum chamber. Ion trap imaging takes place through a custom recessed window, discussed in Sec. 6.8, that is mounted onto the front of the spherical octagon, labeled in Fig. 6.2(a). Laser access for surface ion traps is achieved via six $2\frac{3}{4}$" CF mounted windows, (Kurt J. Lesker (KJL), part no: VPZL-275Q). These are mounted around the octagon, with two more windows mounted at 45° on the weldable cluster. Finally an additional $4\frac{1}{2}$" CF mounted window, (KJL, part no: VPZL-450Q), is mounted directly behind the trap on the weldable cluster, labeled in Fig. 6.2(b).

A 2 pin power feedthrough, (KJL, part no: EFT0523093), is mounted on the top octagon flange directly above the chip brachet. This is the RF feedthrough and connects the helical resonator to the trap. It is specified for operation up to 5000 V and 30 amps, well beyond any power potentially applied to the trap.

[1]Taken from the Kimball Physics website: www.kimballphysics.com

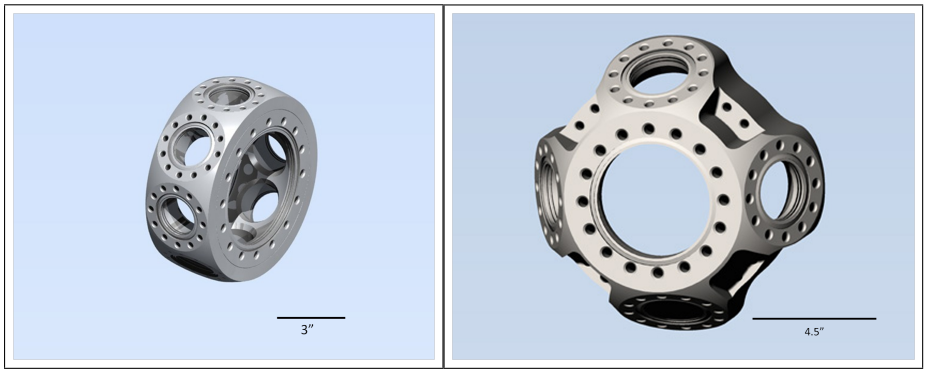

(a) (b)

Figure 6.1: a) Drawing of the spherical octagon. b) Drawing of the weldable cluster, taken from the Kimball physics website.

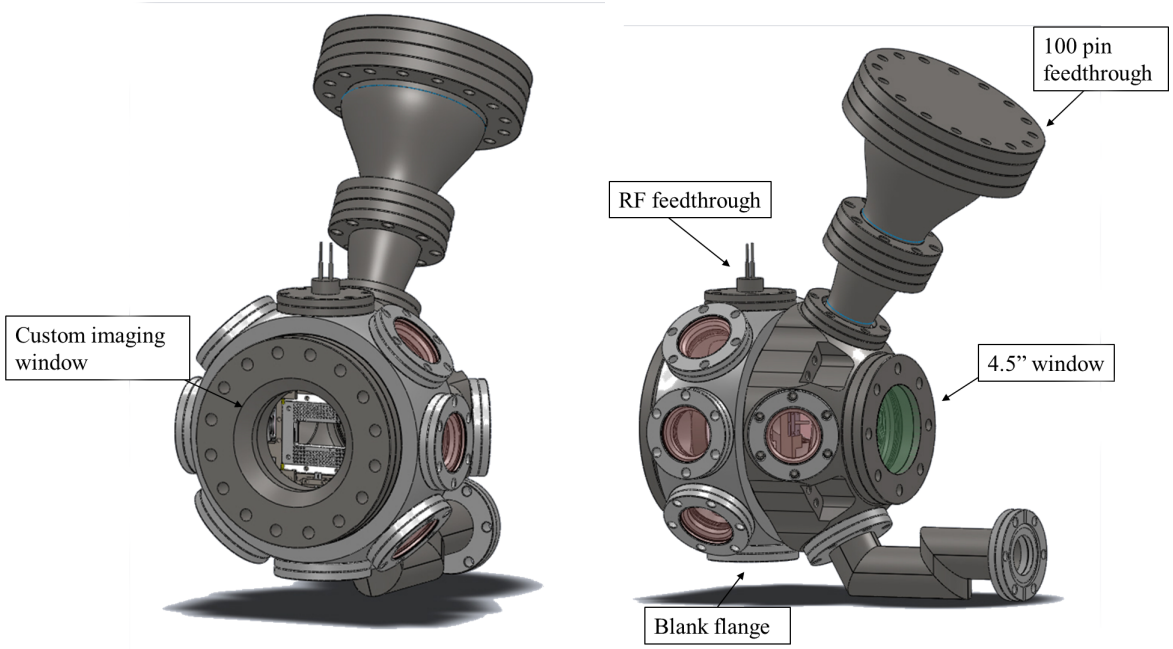

(a) (b)

Figure 6.2: Drawings of the vacuum chamber with all the windows and feedthroughs attached, the assembly was made in SolidWorks.

To provide the 100 electrical connections to the chip bracket a 6" flange with two 50 pin D type connectors is mounted to the top flange on the weldable cluster. This is connected via two conical reducers, first a 6" to $3\frac{1}{3}$" CF reducer connects to the 6" flange, (KJL, part no: CRN600X337), then a second conical reduces from $3\frac{1}{3}$" to the weldable clusters $2\frac{3}{4}$" CF flange (KJL, part no: CRN337X275), shown in Fig. 6.2.

The chamber is connected to the rest of the vacuum system via a custom elbow, seen at the bottom of Fig. 6.2(b). This is designed to hold the chamber so that the center of the ion trap is at the laser height of 5".

Finally the system is sealed by a blank $2\frac{3}{4}$" CF flange on the bottom of the spherical octagon, (KJL, part no: F0275X000N), seen at the bottom of Fig. 6.2(b). A mount will be placed under this flange to provide additional support for the chamber.

6.3 Custom Elbow

To ensure that the center of the trap, which is mounted in the center of the spherical octagon, is at the laser height of five inches, a custom elbow was made to support the chamber and to connect to the rest of the vacuum system. Because of the chamber's size it was not possible to use a standard part. For the first system this connection had been made via a custom tee piece. This connected the chamber at a right angle to the rest of the vacuum system, requiring the CF flange to be connected to the tee piece with a precise angle to ensure the chamber is perpendicular to the table. This design however requires all the pumps, gauges and feedthoughs to be placed either side of the chamber, this layout inhibits the ability to closely align optics with the chamber. For the new vacuum system it was required that this problem should be avoided.

The new chamber is mounted using the custom elbow, with the vacuum system set directly behind the chamber allowing free access to both rear 45° windows.

Figure 6.3 shows a SolidWorks[2] drawing of the custom elbow. Both CF flanges are rotatable to allow easy adjustment of the chamber alignment. The lower section of the elbow will rest on the optical table, providing support for the chamber. Because of the weight of the chamber there is a possibility that the welded joints of the elbow would not be able support the system alone. Additional support will be provided directly beneath the chamber to carry the majority of the weight. The technical drawings for this part, and all subsequent custom parts are given in App. D.

[2]SolidWorks drawing rendered in PhotoView 360.

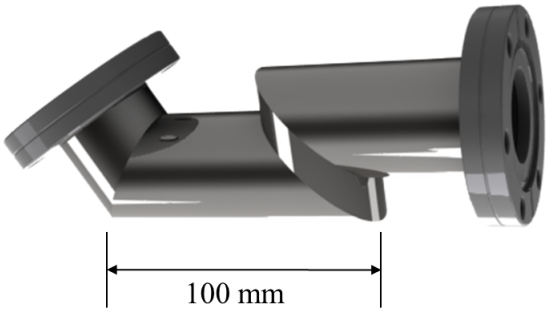

Figure 6.3: Solidworks drawing of the custom elbow.

6.4 Chip carrier

For the new vacuum system another requirement was to find a chip carrier that allowed improved optical access. The current chip carriers used are the Global Chip Materials 100 pin ceramic pin grad array (CPGA), (part number: PGA10047002). This connects to 2× 50 pin feedthroughs allowing connection to 88 individual static electrodes, (after some pins are lost for rf, ground and removed to reduce rf capacitance).

Optical access for surface electrode ion traps requires the laser beam to be brought in parallel to the trap surface, with a separation between the beam and the trap of ≈ 40 - 100 μm. This requires a clear path from the vacuum window across the trap and again exiting the vacuum system. To make use of all 88 electrodes in the current chip carriers requires making wire bonds between the trap and the chip carrier all around the edge of the trap, this results in no clear path for the laser as it would be interrupted by bond wires. This problem is shown in Fig. 6.4.

For the new system it was decided that a chip carrier that still allowed up to a hundred connections but also allowed for optical access from the side. For this a 208 pin CPGA was found, (Global Chip Materials, part number: PGA20855101).

This chip carrier has 208 pins, with 52 bond pads along each side. This allows all 100 connections to be made to the top and bottom rows of bond pads, leaving the sides free for optical access. This however also required a new design of chip bracket to mount these

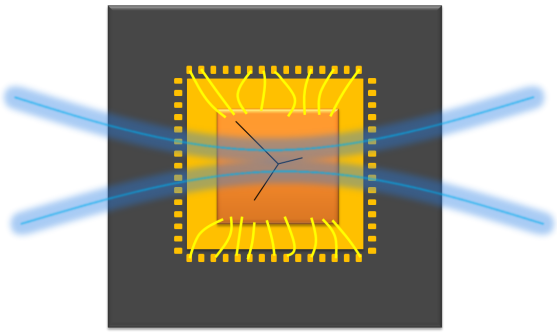

Figure 6.4: Drawing of how laser access limits the area for making wire bonds.

chip carriers.

6.5 Adjustable chip bracket

A requirement of the new system is to be compatible with both microfabricated ion traps as well as large macro ion traps. This proved difficult in the old system as a small volume limited the macro ion traps that could be constructed. In the first vacuum system the available volume to place an ion trap is a footprint of 3 × 3 cm with a 1 cm height. This could prove limiting for chip designs that incorporate advanced on chip features such as digital signal processing and fibre optics, that may require greater space.

Figures 6.5, 6.6(a) and 6.6(b) show SolidWorks drawings of the chip bracket. To increase the flexibility of the system and to allow both large and small microfabricated ion traps to be mounted and imaged an adjustable chip bracket was designed, the chip bracket consists of the combined parts 2, 3 and 4 from Fig. 6.5. Instead of the chip bracket being fixed to the vacuum system a metal chip rail is mounted to the chamber. The chip bracket is then free to move back and forth along the rails changing the distance between the chip bracket and the imagining window allowing for a wide range of chips to be mounted.

The chip bracket is held in the correct position with four screws, the screws pass through threaded holes in the chip carrier and are fixed to the chip rail by a small clamping screw positioned in a groove machined in the base of the alignment screw, the mechanism for the screw drive is shown in Fig. 6.7. By turning the screws the chip bracket position can be carefully aligned, then once the chip bracket is in place the clamping screws are tightened preventing any further movement.

This flexibility means that it is possible to diffraction limit image trapped ions on both microfabricated surface traps as well as larger machined multilayered structures. This would overcome many of the design problems faced when trying to build a large

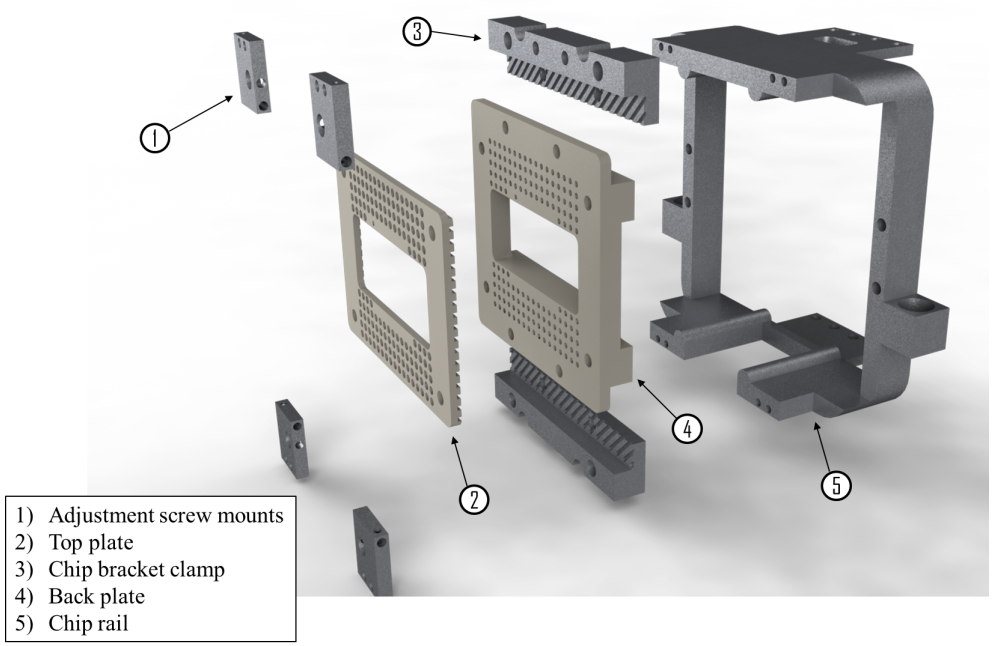

Figure 6.5: SolidWorks exploded view of the chip rail assembly. Four adjustment screw mounts, labeled (1), hold the adjustment screws that thread through the top and bottom chip bracket clamps, labeled (3). These hold the top and back chip plates, labeled (2) and (4). The top plate holds the male pin receptacles whilst the female receptacles plug into the back of the back plate. Grooves on the chip bracket clamps then slot onto raised rails on the chip rail (5).

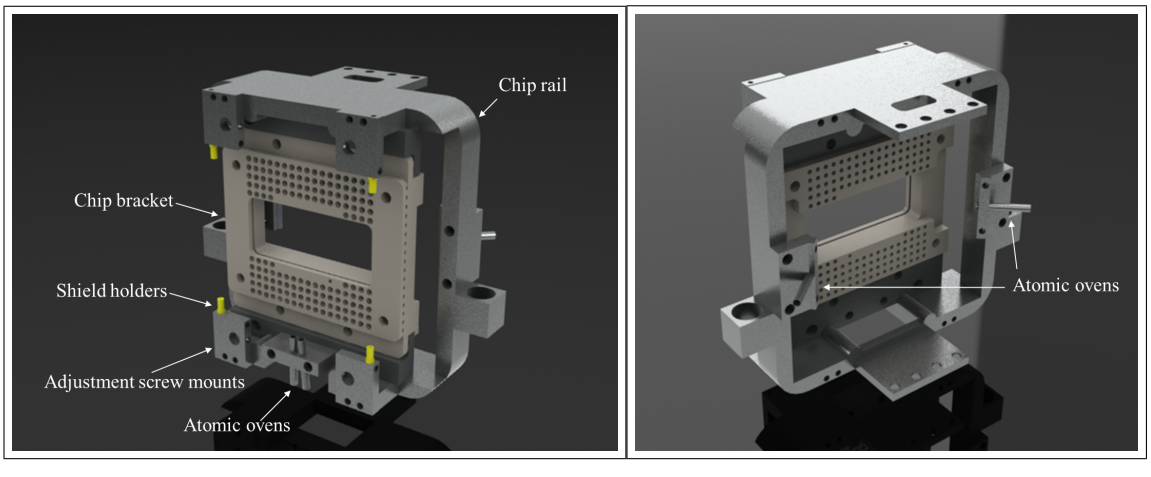

(a) (b)

Figure 6.6: a) Front view of the chip rail with mounted chip bracket. The yellow pin receptacles in the four corners allow grounded shielding to be suspended in front of the trap. b) Rear view of the chip rail with mounted chip bracket.

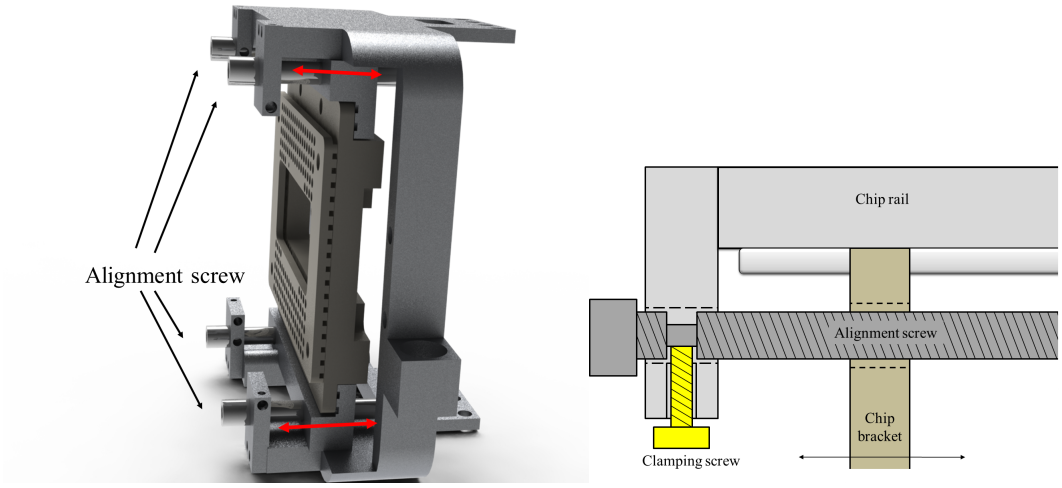

(a) (b)

Figure 6.7: a) Solidworks side view of the assembled chip bracket, by turning the adjustment screws this drives the chip bracket back and forth. b) Drawing of how the adjustment screw works and how it is held in place.

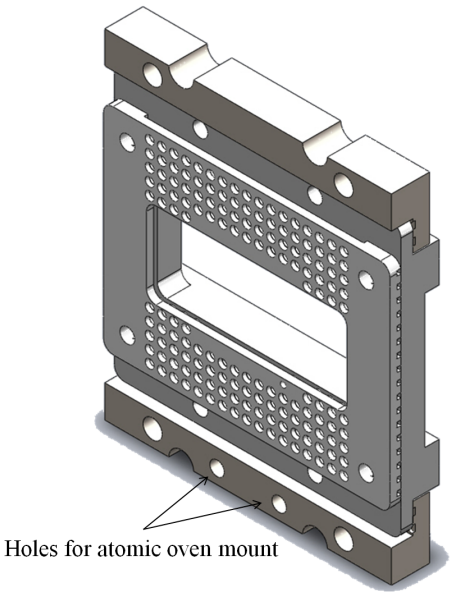

Figure 6.8: Solidworks drawing of the two PEEK plates and clamps.

linear Paul trap for the first system, described in Chap. 5.

6.5.1 Chip bracket

The chip bracket is made from two plates of PEEK sandwiched together and held by two metal clamps, the chip bracket is shown in Fig. 6.8. In the first vacuum system it was found that the pin receptacles used would crack and the electrical connection between the receptacle and the connecting wire was no longer reliable. To try and prevent this from

happening a receptacle would be crimped onto the wire, this means that the end of the wire now had a female connector that can now be plugged into a male receptacle mounted in the chip bracket, Fig. 6.9 shows a schematic of the assembly. This should both allow easy replacement of damaged receptacles and reduce the stress to the receptacles. The receptacles used are from Mill-Max, part numbers: 0133-0-15-15-30-27-04-0 and 0672-4-15-15-30-27-10-0. The dimensions are show in figures 6.10(a) and 6.10(b)[3].

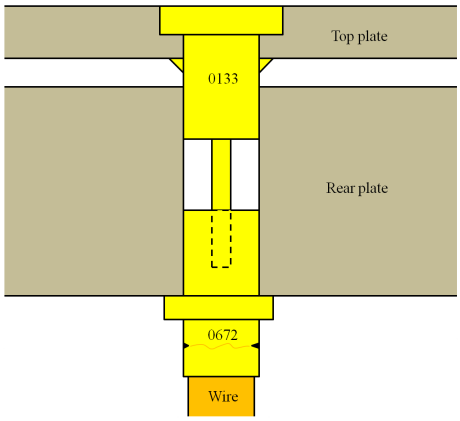

Figure 6.9: Drawing of how the pin receptacles and PEEK plates match. The thin top plate holds the 0133 press fit male pin receptacle and extends into the rear plate. The 0672 female receptacle is then crimped onto the wire and plugged into the back of the chip bracket.

The top plate receptacle holes are counter sunk with a wider hole allowing the wide top of the male 0133 receptacle to lay flush with the top of the plate. The receptacles are press fit mounted, a small barb prevents the receptacle from falling out once it has

[3]Taken from the Mill-Max website: www.mill-max.com

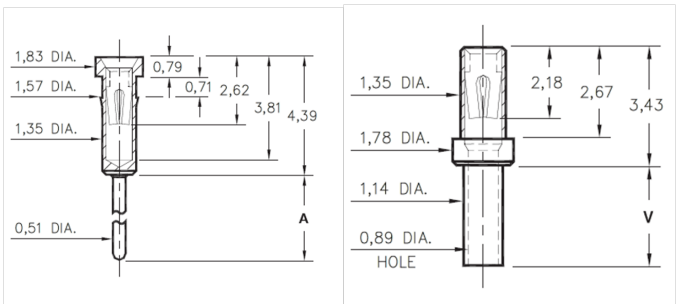

(a) (b)

Figure 6.10: All dimensions are in mm. a) 0133 Press fit pin receptacle, dimension A = 9.7 mm. b) 0672 Pin receptacle, dimension V = 3.71 mm.

been pushed into place. Though they can still be removed with a small amount of force should they require replacement. The base of the receptacle then fits inside the rear plate with the long male tail extending down a 1.14 mm diameter hole. This fits the 0672 female receptacle which is crimped to the Kapton coated wire. Figures 6.11(a)-(f) show SolidWorks drawings of the top plate, rear plate and top and bottom clamps.

The top plate is clamped to the rear plate by four screws, which pass through holes in the corners of the two plates. To prevent virtual leaks the top plate has raised slotted spacers on either side, shown in Fig. 6.11(b). These hold the top plate the correct distance from the rear plate and help prevent virtual leaks. The plates are attached to two clamps fitted to the top and bottom, these are shown in Fig. 6.11(a)-(f). These are screwed to the two PEEK plates, these clamps slot onto the chip rail and have threaded holes for the four alignment screws. Figure 6.8 shows the chip bracket assembly.

At the bottom of this assembly there are two additional holes in the clamp. These are to allow two atomic ovens to be mounted on the chip bracket. These can be used for loading surface electrode traps. These ovens need to remain in the same position relative the the trap and so are clamped to the chip bracket so they can move with the chip bracket. This can now be fitted to the chip rail.

6.5.2 Chip rail

The chip rail is shown in Fig. 6.12, this is machined from a single piece of aluminium. It is designed so that the chip bracket closely fits between four rails, there are also screws so that atomic ovens can be attached as well as plates required to hold the four adjustment screws.

The design was to use groove grabbers at the back of the spherical octagon to mount the chip assembly. However upon delivery it was discovered that these mounting grooves had been removed by Kimball. This meant that the chip assembly had to be mounted from the front. This required a modification to the design, with two mounting plates being designed and fabricated to allow the chip rail to be mounted from the front. Figures 6.13(a) and 6.13(b) show the two plates.

These connect to groove grabbers that clamp onto the front ring in the spherical octagon, slots in the plate match threaded holes machined into the chip rail. Once the plates have been aligned, screws clamp them into position. These plates now support the chip assembly.

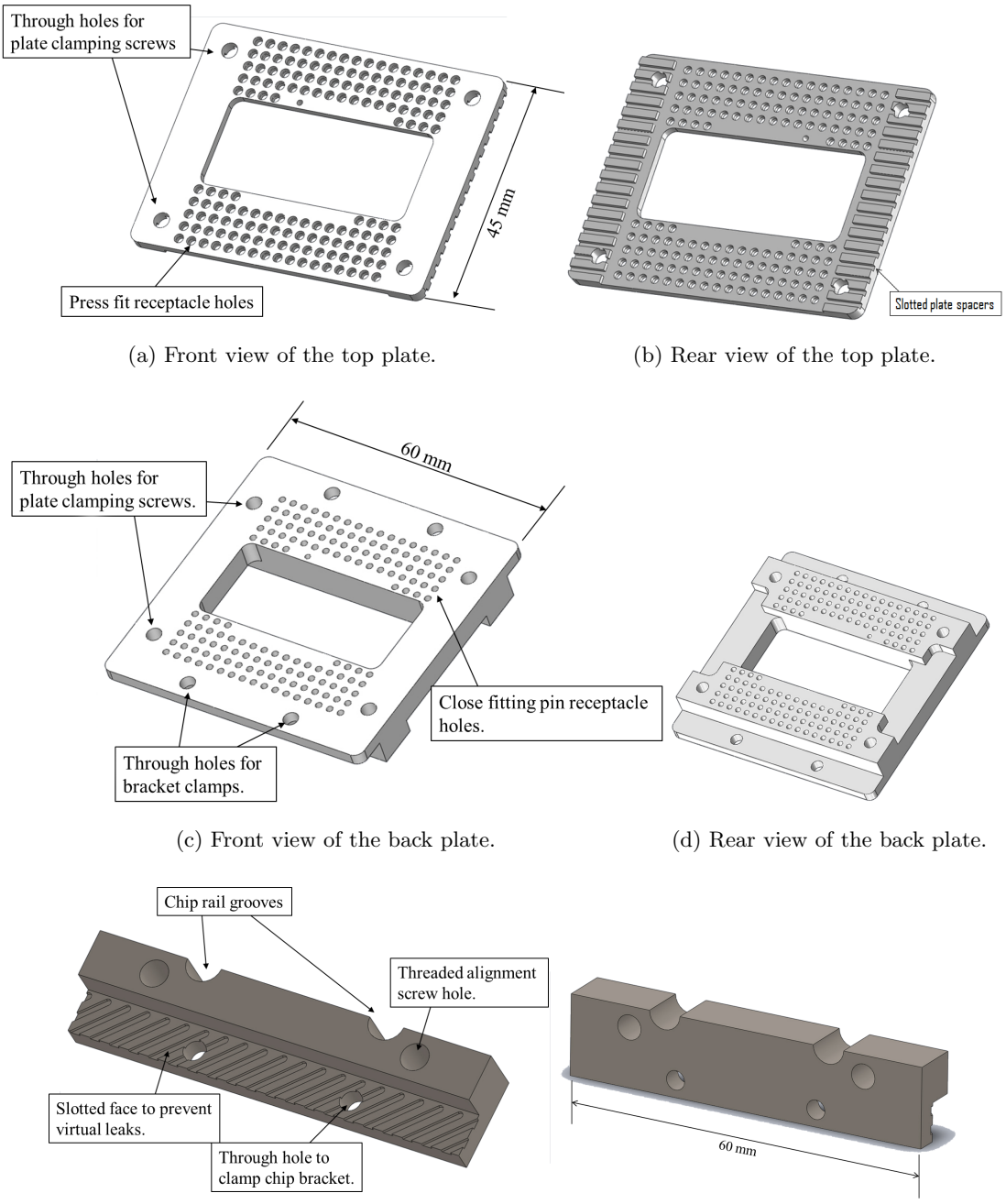

(a) Front view of the top plate.

(b) Rear view of the top plate.

(c) Front view of the back plate.

(d) Rear view of the back plate.

(e) Front view of the chip bracket clamp.

(f) Rear view of the chip bracket clamp.

Figure 6.11: Chip bracket clamps, they screw to the PEEK plates and slot into the chip rail.

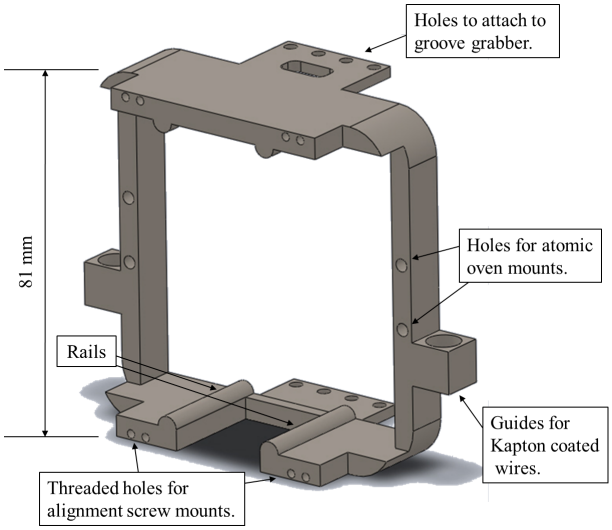

Figure 6.12: Drawing of the chip rail. It was machined from a single piece of aluminium.

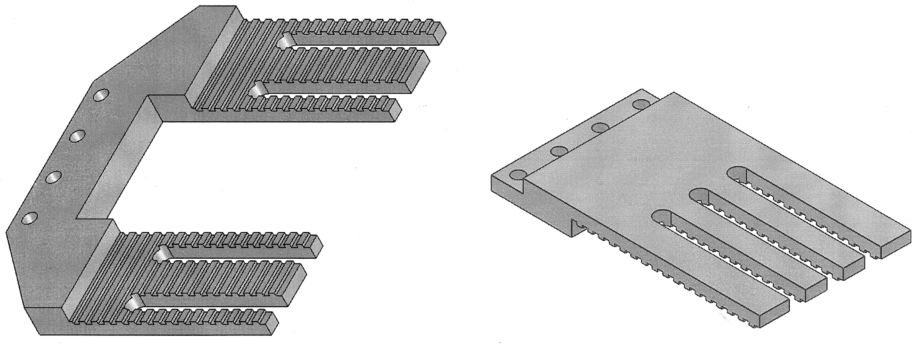

(a) (b)

Figure 6.13: a) Bottom mounting plate two grooves either side slot onto screws in the chip rail, the central groove is to provide space for the atomic ovens. b) Top mounting plate, this slot onto three screws screwed into the top of the chip rail.

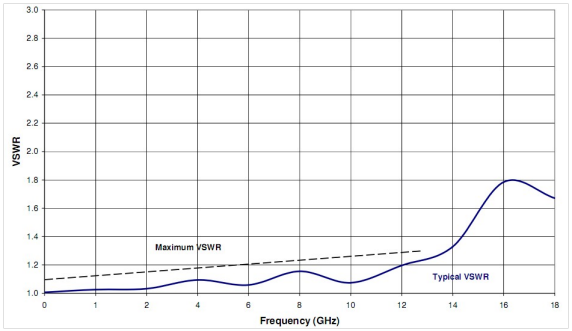

Figure 6.14: VSWR for Vacom UHV SMA feedthroughs.

6.6 Microwave feedthroughs

Another requirement for the new system was for microwave feedthroughs. These are for potential experiments with microwave sources either on chip or near the trapping region. The requirement for the feedthroughs is to have minimum loss at our microwave transmission frequency of 12.6 GHz and to be UHV compatible. A Vacom coaxial feedthrough, part no. CF16-SMA50-SH-DE-CE-INC, was chosen for the transmission properties. The transmission is shown in Fig. 6.14. This shows that the ratio of reflected power to transmitted power at the feedthrough has a voltage standing wave ratio (VSWR) ≈ 1.3 at 12.6 GHz. VSWR is a measure of the ratio between the amplitude at the antinode and the amplitude at the node of a standing wave. The standing wave is generated by interference between the incoming wave and a reflected wave, from a none perfectly impedance matched junction. In the ideal case with two perfectly impedance match transmission lines the VSWR = 1.

The feedthroughs are mounted on $1\frac{1}{3}$" CF flanges, and accept standard SMA connections. Two feedthroughs are required, this is so microwave power can be transmitted into the system onto our trap then transmitted back out of the vacuum system where it can be properly terminated. Since the vacuum system uses $2\frac{3}{4}$" CF flanges a reducing cross piece was added, (KJL, part number: C-0275-133).

6.6.1 Microwave vacuum coaxial transmission line

To deliver the microwaves from the feedthrough to the ion trap vacuum compatible microwave coaxial cable needed to be found. Typical vacuum coax uses Kapton as an insulator but suffers from large attenuation at high frequencies, to the point of being useless at 12.6 GHz. Due to the limited amount of vacuum compatible materials very few cables are compatible to be used in a UHV environment. However PTFE is often used as the die-

Physical properties	Material	Diameter (mm)
Inner conductor	Silver plated copper clad steel	0.51
Dielectric	PTFE	1.68
Outer conductor	Silver plated copper	2.20
Min. inside bend radius (mm)		7.63
Outer conductor integrity temp (°C)		200
Operating temp (°C)		-55 to 200

Table 6.1: The physical properties of the microwave coaxial cable.

Electrical characteristics	
Capacitance (pFm^{-1})	95.1
Impedance (Ω)	50
Corona extinction voltage (VRMS@60Hz)	1500
Voltage withstanding (VRMS@60Hz)	5000
Moding frequency (GHz)	61

Table 6.2: The electrical properties of the microwave coaxial cable.

lectric in microwave transmission lines and is compatible up to 10^{-12} Torr. RG-405 high frequency coaxial cable was found to be suitable for our application. The cable has a 0.51 mm diameter silver plated copper clad steel conducting core, 1.68 mm PTFE dielectric and a 2.20 mm diameter silver plated copper sheild. This forms a stiff cable that when bent will retain its shape. This is useful as for microwave transmission as any corners need to have the largest radius of curvature to avoid unwanted reflections. The cable specifications are given in Tables 6.1, 6.2, 6.3.

Using vacuum compatible SMA connectors, (KJL, part number: FTASMA), the coax cable can be screwed onto the SMA feedthroughs and chip launch connectors (launch connectors attach an SMA connector to a planar waveguide, eg microstrip on PCB). The cable will pass from the SMA feedthroughs through the custom elbow entering the vacuum camber from the rear. When not in use they will grounded and left out of the way inside the system.

Attenuation and average power @ 20 °C and sea level		
Frequency (GHz)	Attenuation (dB/100m)	Power (Watts CW)
0.5	45.0	232.0
1.0	64.0	162.4
5.0	151.0	69.8
10.0	222.0	47.9
20.0	329.0	32.6

Table 6.3: The attenuation properties of the microwave coaxial cable.

6.7 100 pin feedthrough

To provide electrical connection to the 100 pins on the chip carrier a 100 pin feedthrough was needed. This was designed to match that used on the existing system. This consists of two sub D type 50 pin connectors mounted on a 6" CF flange, shown in Fig. 6.15.

Figure 6.15: Top view of the 100 pin feed through with the two sub D type 50 pin connectors.

Connection between the feedthrough and the chip carrier is made by 100 Kapton coated wires. Kapton is a good electrical insulator and vacuum compatible for UHV. These wires are mounted in two PEEK blocks that plug into the sub D type connectors. The other end is loose. These are then stripped of the Kapton and a 0672 pin receptacle is crimped onto the wire.

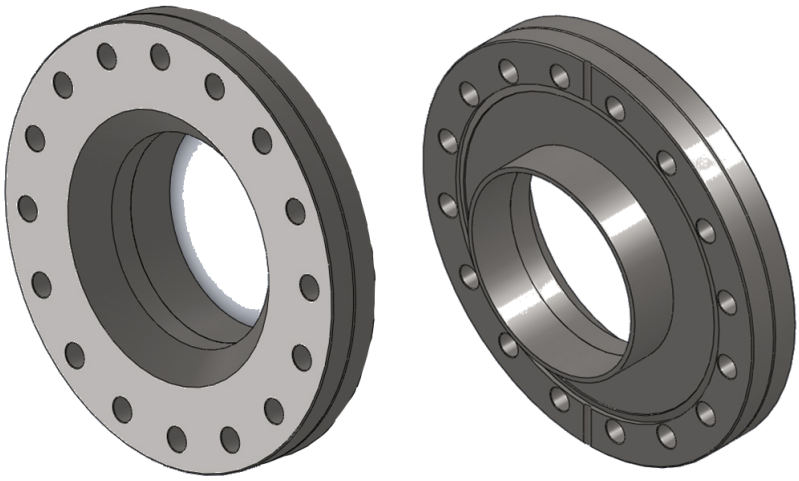

(a) (b)

Figure 6.16: Custom recessed imaging window.

6.8 Custom window and anti reflection coatings

To be able to image a trapped ion down to the diffraction limit, the distance between the imaging objective lens and the ion has to be precisely aligned. To allow the imaging system to get close to the trapping region requires a customised imaging window. This needs to mount onto the 6" CF flange on the spherical octagon and recess back into the chamber. A similar design was used for the first vacuum system but it was discovered that due to the small size and the design it is very difficult to prevent reflections back into the vacuum system and into the imaging optics. Ultimately this was solved on the first system by carefully positioned black card to absorb the stray light.

To prevent the same problem the design was modified to include a tapered lip. A 73.5 mm diameter tub is recessed by 17.5 mm into the chamber. Lasers passing from behind the chamber for through traps would clip the tub side wall before exiting the system. To stop this from happening a 45° tapered lip is machined away from the flange. This allows the beam to exit uninhibited. Figures 6.16 and 6.17 show the window design.

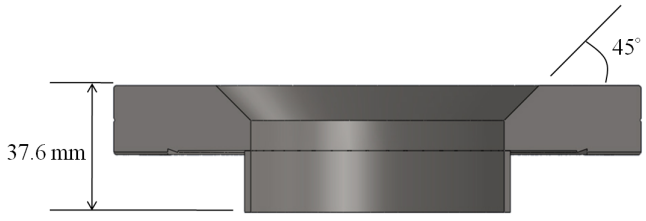

Figure 6.17: Cut side view of the recessed imaging window, this shows the tapered lip allowing for lasers to leave the vacuum system.

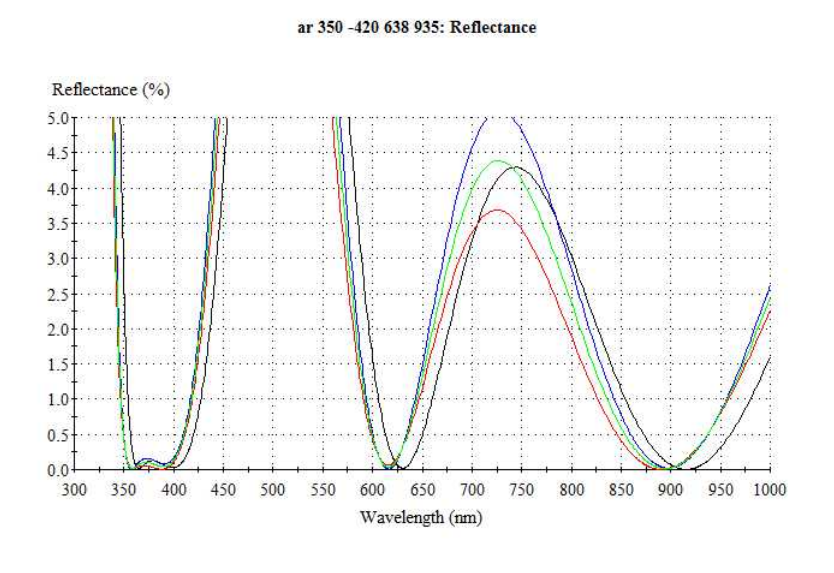

Figure 6.18: Theoretical reflectance curves for the $2\frac{3}{4}$" window coating, green is mean polarization, blue is s polarization and red is p polarization.

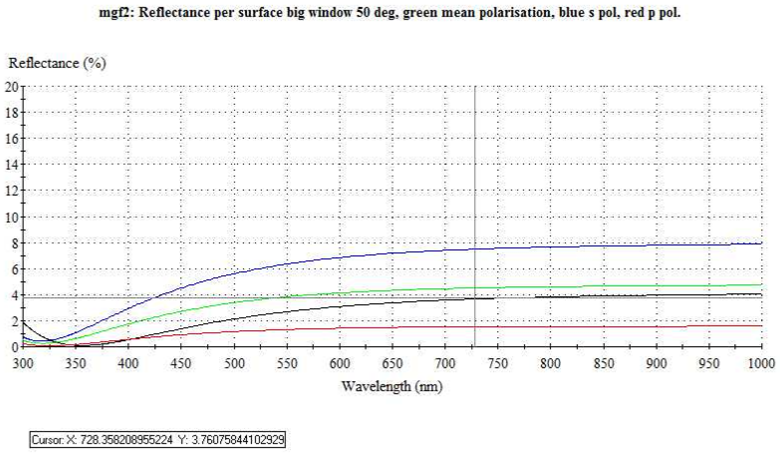

Figure 6.19: Theoretical reflectance curves for the imaging window coating. Green is mean polarization, blue is s polarization, red is p polarization and black is at an AOI = 0°.

The windows were anti reflection coated to reduce reflections from lasers both entering and exiting the system. The $2\frac{3}{4}$" windows were coated for all the laser wavelengths and for a zero angle of incidence (AOI) and an AOI of 20°. The theoretical reflectivity curves for this coating is given in Fig. 6.18. The re-entrant imaging window was coated for 0° and 40° at 369 nm but not the other wavelengths. This is because additional coatings would degrade the 369 nm transmission performance and a bandpass filter in front of the camera removes all non 369 nm light, therefore making coating for the other wavelengths unnecessary. The theoretical reflectance for this coating is given in Fig. 6.19.

6.9 Full system

The full vacuum system is shown in figures 6.20 and 6.21 which shows a SolidWorks drawing of all the vacuum system components. These include a titanium sublimation pump, ion pump and ion gauge. The specification of these parts is explained in the following sub sections.

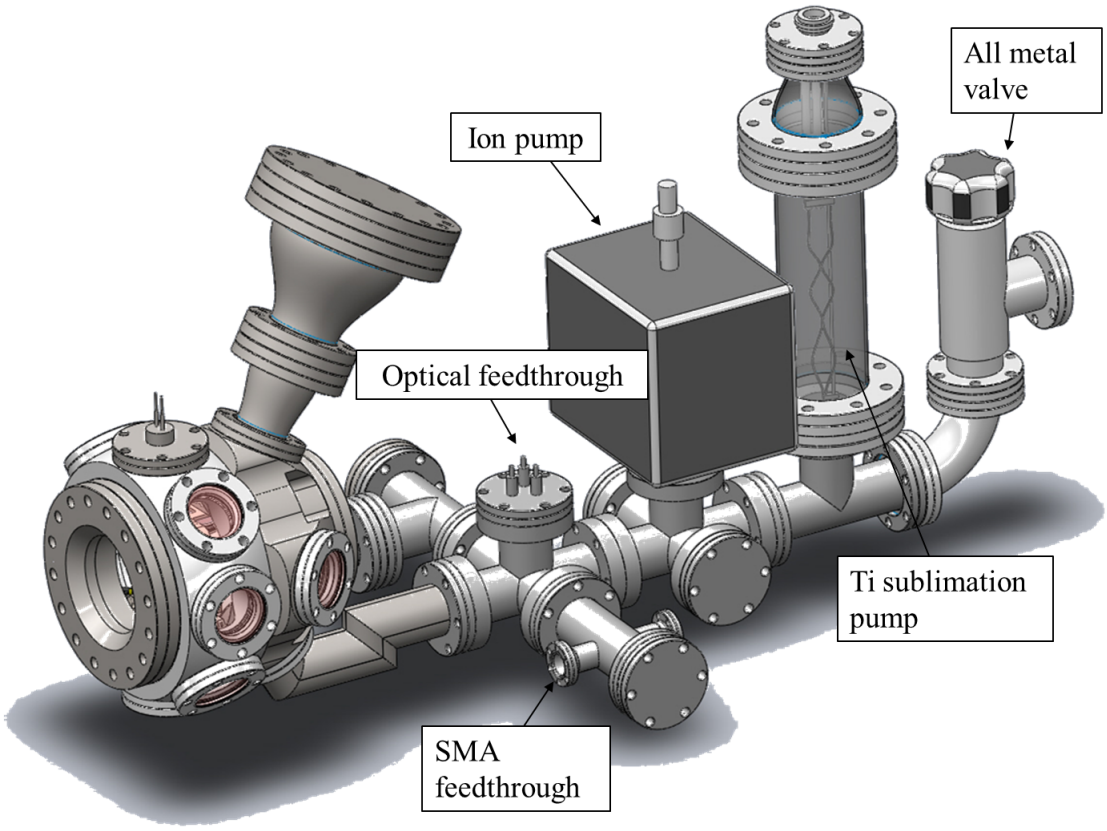

Figure 6.20: SolidWorks drawing of the whole vacuum system assembly.

The drawing shows two optical feedthroughs, each with three fibre couplers. For the initial build of the system these have been left out and replaced with blank flanges. This is because currently without any specific designs of experiments involving fibre optics close to the trap the specifications of the feedthroughs is not known. The blank flanges can easily be replace in the future with fibre feedthroughs when such an experiment requires them. Alternatively they might prove useful for unforseen attachments.

6.9.1 Ion pump

To pump down and maintain the vacuum pressure a Varian Starcell 20 liter per second ion pump, (part number: 9191145), is used. This is connected to the system via a $2\frac{3}{4}$" CF

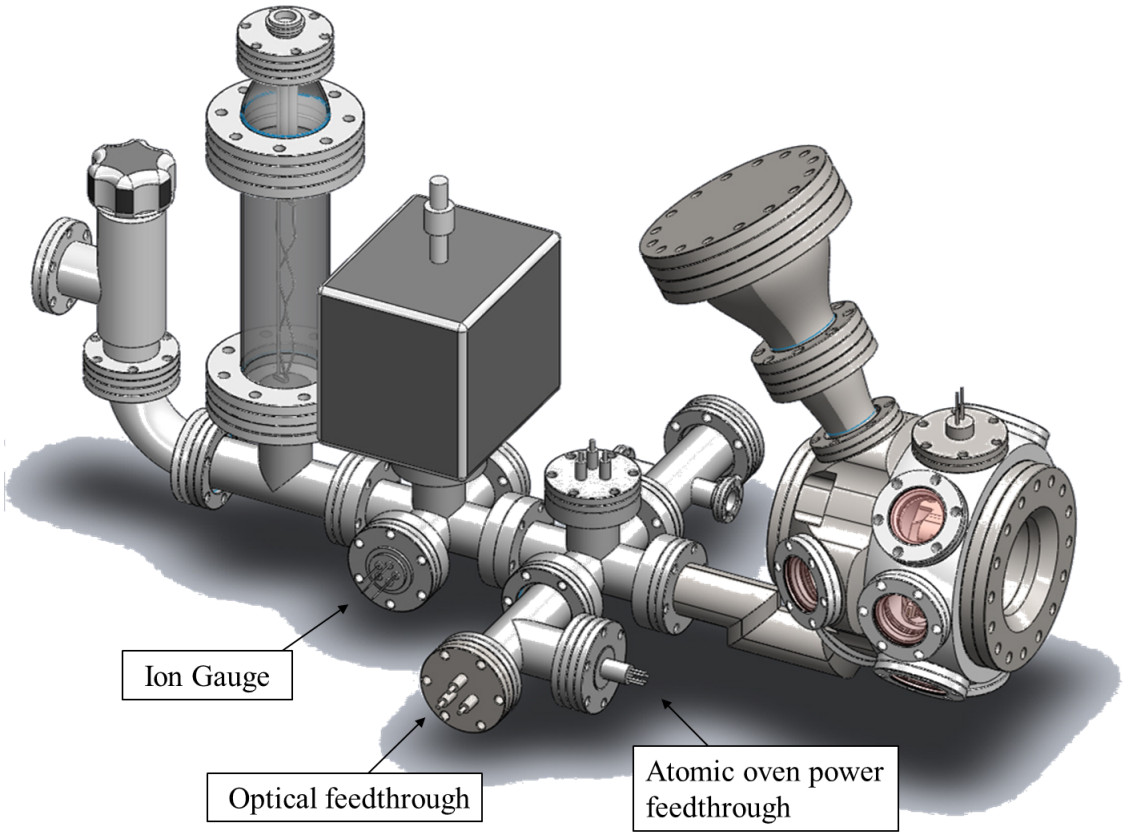

Figure 6.21: SolidWorks drawing of the whole vacuum system assembly.

flange. The ion pump works by ionising and trapping the residual gas in penning cells in the vacuum system and using a large electric field, on the order of kV, accelerates the ions into a chemically active solid. This then traps the ions removing them from the vacuum. The ion pump is controlled by a Varian Dual controller, (part number: 9297012M002).

6.9.2 Ion Gauge

To measure the pressure of the vacuum system a Varian UHV-24p Bayard-Alpert ion gauge is used. This uses a filament to continuously produce electrons that can ionise the surrounding gas, the ions are then attracted to the collector. The current on the collector is a function of gas pressure. The ion gauge controller, a Varian XGS-600 gauge controller, measures the collector current and is calibrated to give the corresponding vacuum pressure.

The ion gauge and controller have a operating pressure range of 5×10^{-12} to 1×10^{-3} Torr.

6.9.3 Titanium sublimation pump

Once the vacuum system has been baked the system pressure is $\approx 10^{-10}$ Torr, to reach the desired 10^{-12} Torr a Varian titanium sublimation pump, (part number: 9160050), deposits a layer of titanium on the vacuum system walls. The titanium reacts with any free atoms[4], sticking them to the wall.

To deposit the titanium a large current is passed through Ti filaments heating them. This is repeated several times, first the pressure raises then will slowly fall again, falling below its initial value. This is done until a pressure of 10^{-12} Torr is achieved.

6.9.4 Chip carrier temperature measurement

To achieve large peak rf voltage on microfabricated ion traps it may be required to apply several watts of power. This power will be dissipated in the form of heat from the trap electrodes. Due to there small size this can lead to quite significant localised heating of the chip and chip carrier. A temperature dependance between the anomalous heating rate and chip temperature has been observed, but only between room temperature and 6 K, [86]. Typically traps are quoted to be at room temperature but are likely to be significantly hotter due to power dissipation. To measure this heating, to both provide information on power dissipation and safe trap operation but also investigate a potential ion heating rate relationship to electrode temperature, a thermocouple was placed inside the vacuum system. The thermocouple used is a J type from RS Components, (part number 621-2142). This comes with a PTFE insulator, despite PTFE being UHV compatible it had been coloured and was stripped for fear of outgassing. The wires were then insulated using ceramic fish beads. The thermocouple was fixed inside a female pin receptacle using ceramic paste. This was then connected via crimped pin receptacles to two Kapton coated copper wires attached to the 100 pin feedthrough. The pin receptacle can then be plugged into a free pin in the chip carrier. Due to intermetal contacts between the thermocouple, pin receptacles and the copper wires, the potential difference measured across the thermocouple junction would be altered. This required the thermocouple to be calibrated against another thermometer. Three temperatures were measured against a mercury thermometer, assumed to be accurate, the results from these measurements is shown in Fig. 6.22, along with a fitted straight line. This shows that the thermocouple mounted in the pin receptacle and attached to the multimeter via the pin receptacles and coppers wires measures temperature linearly and within errors of the mercury thermometer.

[4]This does not work for noble gases.

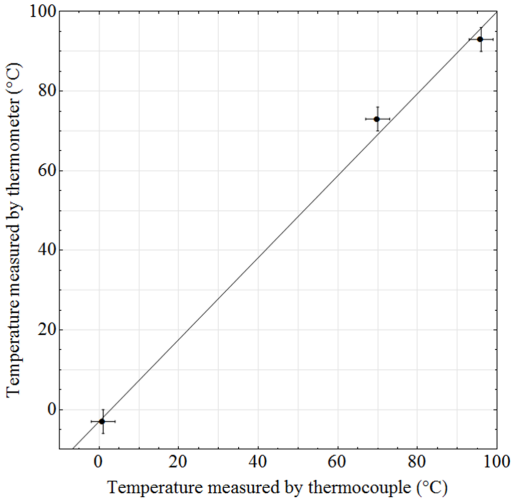

Figure 6.22: Thermocouple measured temperature against mercury filled thermometer measured temperature.

The second measurement of the thermocouple was to calibrate the temperature drop across the chip carrier, to measure this a test carrier was assembled. This consisted of a loop of copper wire and a thermocouple glued, using epoxy, to where the chip will sit, shown in the insert of Fig. 6.23. Passing current through the loop will heat the chip carrier similarly to a chip, a second thermocouple was glued in the center of the copper wire loop and was used to measure the temperature at the chip. The chip carrier was then plugged into the chip bracket, with the vacuum thermocouple being plugged into a free chip carrier pin. Heat will be conducted away from the chip carrier through the chip bracket and connecting wires. The copper wires will act as a heat sink removing heat quickly from the chip carrier. The measurement was taken by passing a set current through the wire and leaving for thirty minutes to allow the chip bracket to thermally equilibrate. The temperature of both thermocouples was then recorded. Measurements were taken for room temperature and two different currents, Fig. 6.23 shows a graph of the vacuum system thermocouple temperature against the chip thermocouple temperature.

Assuming a linear relationship and fitting a line to the data we can determine that the chip temperature as a function of chip carrier thermocouple temperature is given by

$$T_{Chip} = \frac{T_{tc} - 12.95}{0.43} \tag{6.1}$$

where T_{Chip} is the temperature at the chip and T_{tc} is the temperature measured by the thermocouple. This should now allow a measurement of the chip temperature when operating the trap.

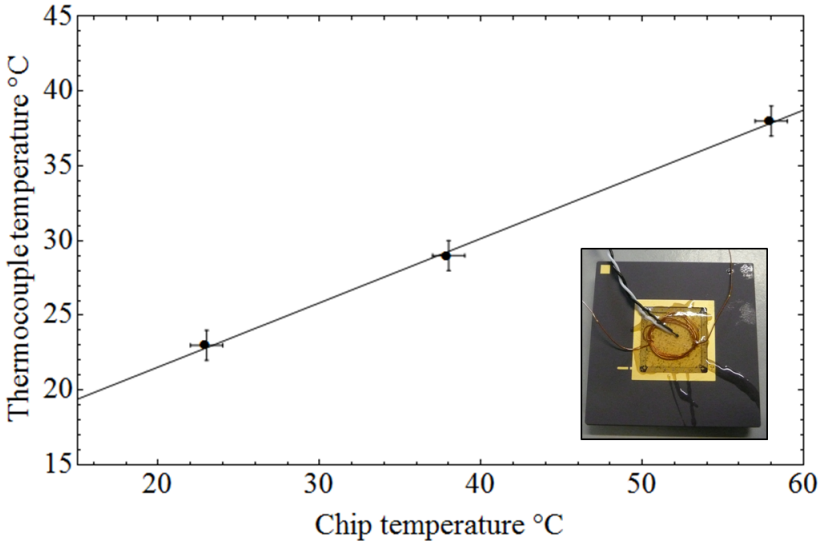

Figure 6.23: Graph of chip temperature against measured chip carrier temperature. Insert is a photo of the chip carrier with the copper coil and thermocouple attached

6.9.5 Full parts list

6.10 Atomic oven testing

In the vacuum system there are four atomic ovens, two ovens for surface loaded traps and two for backside loaded traps. The ovens are either filled with natural ytterbium or ytterbium isotope enriched for 171. In the existing vacuum system it has been noticed that there is no difference in isotope selectivity between using either the natural ytterbium ovens or the enriched ovens. To ensure the isotope enrichment and to calibrate the oven output with current several measurements of isotope partial pressure were taken. The first measurement was to measure the relative isotope abundances of the two sources. The measurement was taken using a residual gas analyzer (RGA), (Extorr, part number: XT200M). An atomic oven was placed facing the RGA, the system was pumped to $\approx 10^{-6}$ Torr. Passing current through the oven causes ohmic heating until ytterbium begins to evaporate from the oven towards the RGA, it is then possible to measure the partial pressures of the different Yb isotopes. An initial calibration measurement was taken to measure the accuracy of the RGA, Fig. 6.24 shows a graph of isotope partial pressures with time.

After 3 minutes the oven is sufficiently hot to start out gassing Yb. By measuring the area under the curves it is possible to calculate the relative percentages of Yb isotopes, Tab. 6.4 shows the measured percentage next to the literature value.

This shows that the RGA has an accuracy of $\geq 96\%$. The measurement was then

Kurt J. Lesker		
Description	Part number	Quantity
Custom re-entrant window	XTEMP	1
Custom nipple	XTEMP	1
$2\frac{3}{4}$" CF UV fused silica viewport	VPZL-275Q	8
$4\frac{1}{2}$" CF UV fused silica viewport	VPZL-450Q	1
6"-$3\frac{3}{8}$" CF conical reducer	CRN600X337	1
$3\frac{3}{8}$"- $2\frac{3}{4}$" CF conical reducer	CRN337X275	1
$4\frac{1}{2}$"- $2\frac{3}{4}$" CF conical reducer	CRN450X275	1
Zero length reducer $4\frac{1}{2}$"- $2\frac{3}{4}$" CF	RF450X275	1
5-way cross	C5-0275	2
T-piece	T-0275	3
Full nipple $2\frac{3}{4}$" CF	FN-0275	1
Full nipple $4\frac{1}{2}$" CF	FN-0450	1
90° elbow	L-0275	1
All metal valve	VZCR40R	1
Blank flange	F0275X000N	5
6" CF 2x50 pin D-type electrical feedthrough	IFDGG501056AX	1
6-pin electrical feedthrough 2kV, 10A/pin	EFT0265063	1
RF feedthrough	EFT0523093	1
4-way reducing cross	C-0275-133	1
Varian		
TSP filament cartridge	V9160050	1
Plus 20 starcell ion pump	V9191145	1
Bakeable cables	V9290705	1
Ion gauge B/A	V9715014	1
XGS-600 ion gauge controller	VL91103010100	1
Bakeable cables	VL64403010	1
Dual ion pump controller (negative)	V9297012M002	1
Kimball Physics		
Spherical octagon	MCF600-SphOct-F2C8	1
Weldable cluster	MCF450-WldClstr-E1A4	1
Groove grabbers	MCF600-GrvGrb-C01	2
Vacom		
SMA vacuum feedthrough	CF16-SMA50-SH-DE-CE-INC	2
Mill-Max		
Male pin receptacle	0133-0-15-15-30-27-04-0	500
Female pin receptacle	0672-4-15-15-30-27-10-0	500

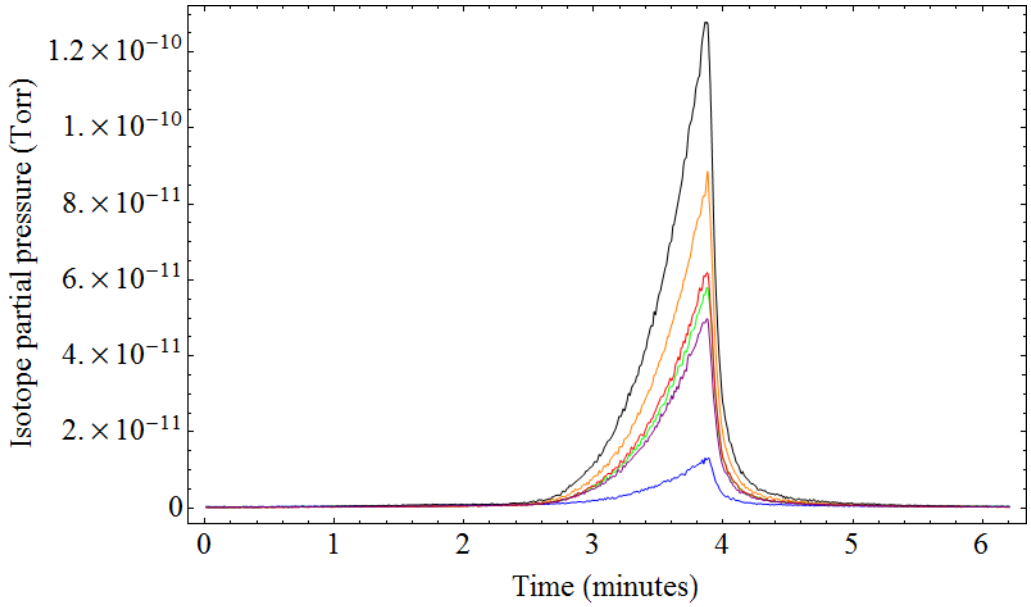

Figure 6.24: Graph of Yb isotope partial pressures for the natural Yb source. Blue = 170, green = 171, orange = 172, red = 173, black = 174 and purple = 176.

Isotope	**Measured isotope abundance %**	**Literature isotope abundance %**
170	3.3	3.04
171	14.5	14.28
172	22.2	21.83
173	15.5	16.13
174	32.1	31.83
176	12.4	12.76

Table 6.4: Measured Yb isotope abundances against literature values [1].

repeated with an oven filled with the isotope enriched source, the graph if shown in Fig. 6.25. Table 6.5 gives the isotope abundances, from this we can see that the ytterbium is indeed 85.6 % enriched for the 171 isotope however below the specified enrichment of 90.69 %.

Before the ovens could be placed in the oven it was important to test each oven and measure the partial pressure of ytterbium over time with different currents. This is to find the current at which the oven will begin to emit ytterbium. Due to each oven being slightly different, having a different resistance at the spot weld the current needed to be applying to each oven varies. Several runs of each oven were taken to find the minimum current that the oven would "switch on". Each run was taken over a ten minute period

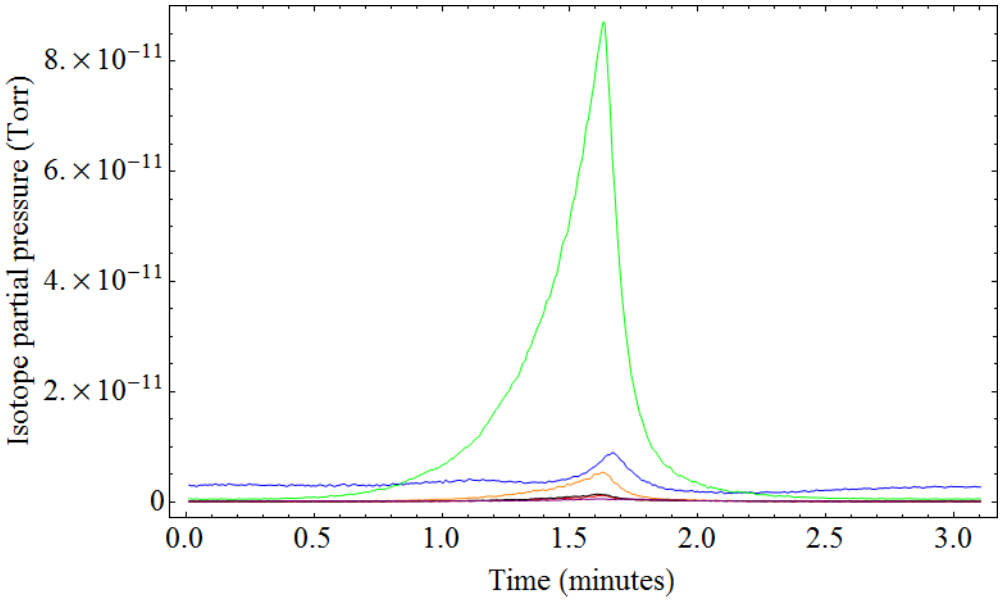

Figure 6.25: Graph of Yb isotope partial pressures for the enriched source. Blue = 170, green = 171, orange = 172, red = 173, black = 174 and purple = 176.

Isotope	**Measured isotope abundance %**
170	5.8
171	85.6
172	5.3
173	1.2
174	1.4
176	0.6

Table 6.5: Measured isotope abundance of the ^{171}Yb isotope enriched source.

and measured the partial pressures for all the isotopes. The test time was so long as it can be seen from Fig. 6.24 which was taken with a current of 10 amps that the time taken to reach the minimum temperature is still $\approx$ 2 minutes. Figures 6.30, 6.31, 6.32 and 6.33 in Sec. 6.12 at the end of the chapter show partial pressure curves for the natural oven 1, natural oven 2, enriched oven 1 and enriched oven 2.

The four atomic ovens were attached to a 6 pin power feedthrough. Figure 6.26 shows the six pin configuration and the oven connections. Pins 2 and 4, labeled N/A, are not attached to anything but a wire does extend from the feedthrough to the hemisphere. These wires are placed to the side and just behind the chip rail, with a barrel connector attached to the end. For the first microtrap these have been connected to magnetic coils

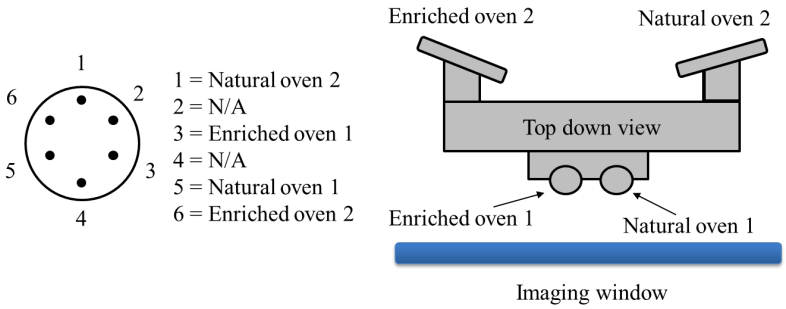

Figure 6.26: Oven power feedthrough pin configuration, and a top down view of the chip rail and the mounting of the atomic ovens.

mounted on the chip carrier itself, discussed in Chap. 8, Sec. 8.9.

Figure 6.26 also shows how the atomic ovens are mounted on the chip rail. This shows a top down drawing of the chip rail, with enriched oven 1 and natural oven 1 serving as the front loading ovens with enriched and natural ovens 2 for rear loading.

6.11 Cleaning, pre bake, assembly and bake

To reach 10^{-12} Torr it is extremely important that all the vacuum parts are clean, any residual grease or dirt will limit the achievable pressure. To make sure all of the parts of system are clean a careful cleaning procedure is undertaken. First the large metal parts are submerged in an ultrasonic bath of acetone and cleaned for a minimum of 15 minutes. After this they are sprayed in methanol to remove any residue left by the acetone. Now they are wrapped in aluminum foil, ensuring that the shining side faces the part. Then all the parts are subjected to a pre bake. They are placed in an oven at 200 °C for a week. This builds a layer of oxide on the surface of the stainless steel parts and has been shown to reduce outgassing [87]. At the end of the week the metal has a yellowy tint.

The pre baked parts are now again washed in an ultrasonic bath of acetone followed by being rinsed in methanol. They are now ready to be assembled. The windows need to be treated differently to the rest of the vacuum components. Due to the custom anti reflection and the glass seal, acetone and methanol will damage the window additionally the ultrasonic bath can not be used for the same reason. To clean these parts they are soaked in propanol for 15 minutes to dissolve any dirt, they are then removed and rinsed with clean propanol and left to dry.

When coming to assemble the chip bracket it was found that due to a purchasing error the female pin receptacles, part number beginning 0672-4, had been incorrectly

purchased. This meant that the received receptacles were 0672-1..., this means that the length available to be crimped onto the Kapton coated wires was only 1.3 mm, instead of the intended 3.7 mm. This meant that the crimp between the wire and receptacle was very weak, adding to problem the Kapton coated copper wires are very stiff and hard to position. The combination of these two problems meant that the chip bracket needed to be assembled with the female receptacles already inserted, the wires were then inserted into the receptacle and crimped. If the receptacle broke then the wire and receptacle could be removed and a new receptacle inserted. This made the assembly of the chip bracket considerably harder than anticipated. This could have been avoided by using the correct receptacles but more crucially braided copper wire instead of solid wire. This is significantly more flexible and will deform easily allowing a very strong crimp to be made. Dispute these advantages braided wire is silver plated and has a much larger surface area. Due to the large number of wires used this could leading to increased outgassing and difficulty in reaching 10^{-12} Torr. For this reason the more solid wire was used.

When the first microtrap was mount and placed into the vacuum system it was noticed that due to the way in which the trap had been mounted on the chip carrier, using a 5 mm stainless steel spacer, the ovens no longer had line of sight of the trap region. This means that the direction of motion of any Yb atoms in the trap region would be randomly distributed, with only a small percentage resonant with the perpendicular ionisation laser, tuned to be resonant with Yb atoms with no motion along the laser's wave vector. To avoid this, a spacer was fabricated to be positioned between the oven mount and the chip bracket. The spacer is a 4.5 mm deep stainless steel block with two 3.2 mm diameter holes to allow the fixing screws through. This now positions the ovens so they have line of sight access to the trap region.

6.11.1 Electrical testing

Once the vacuum system was assembly electrical testing and measurement of all the pin receptacles and ovens was undertaken. This was to ensure all the receptacles were connected to the 100 pin feedthrough. Figure 6.27 shows which pin receptacle matches which feedthrough pin.

The resistance between the feedthrough and pin receptacle was measured and recorded, Fig. 6.28 shows the resistance value between the pin and the feedthrough for each connection. Capacitance measurements between adjacent pins was also taken, the capacitance ranged from 12-14 pF. This can be used for diagnostics when operating the system under

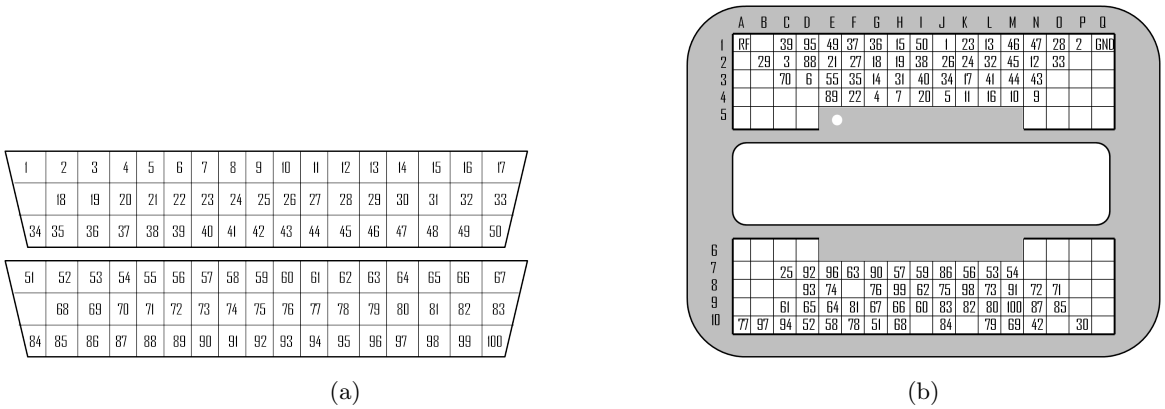

(a) (b)

Figure 6.27: a) 100 pin feedthrough pin numbering. b) Chip bracket pin arrangement, with each pin receptacle labeled to the appropriate feedthrough pin.

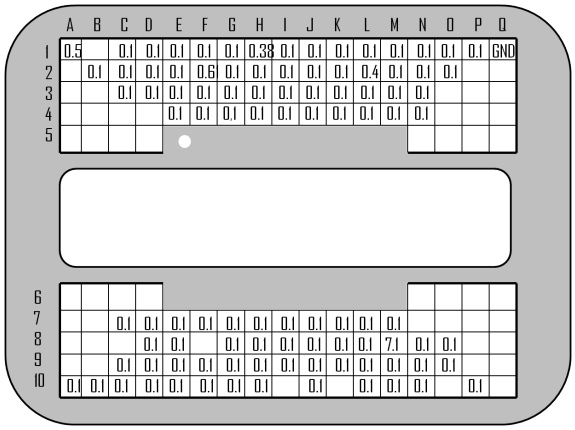

Figure 6.28: Resistance values measured between the pin receptacle and the 100 pin feedthrough. All values are in Ohms.

vacuum. Should the capacitance of one pin suddenly change this is a good indication that it has potentially become disconnected. The capacitance of the rf feedthrough was measured to be 4.7 ± 0.5 pF with respect to feedthrough ground pin which is connected to the vacuum chamber.

Figure 6.29 shows photographs of the fully assembled vacuum system, with photos taken through the imaging and laser access windows. These show the chip carrier, thermocouple and atomic ovens.

6.12 Oven test results

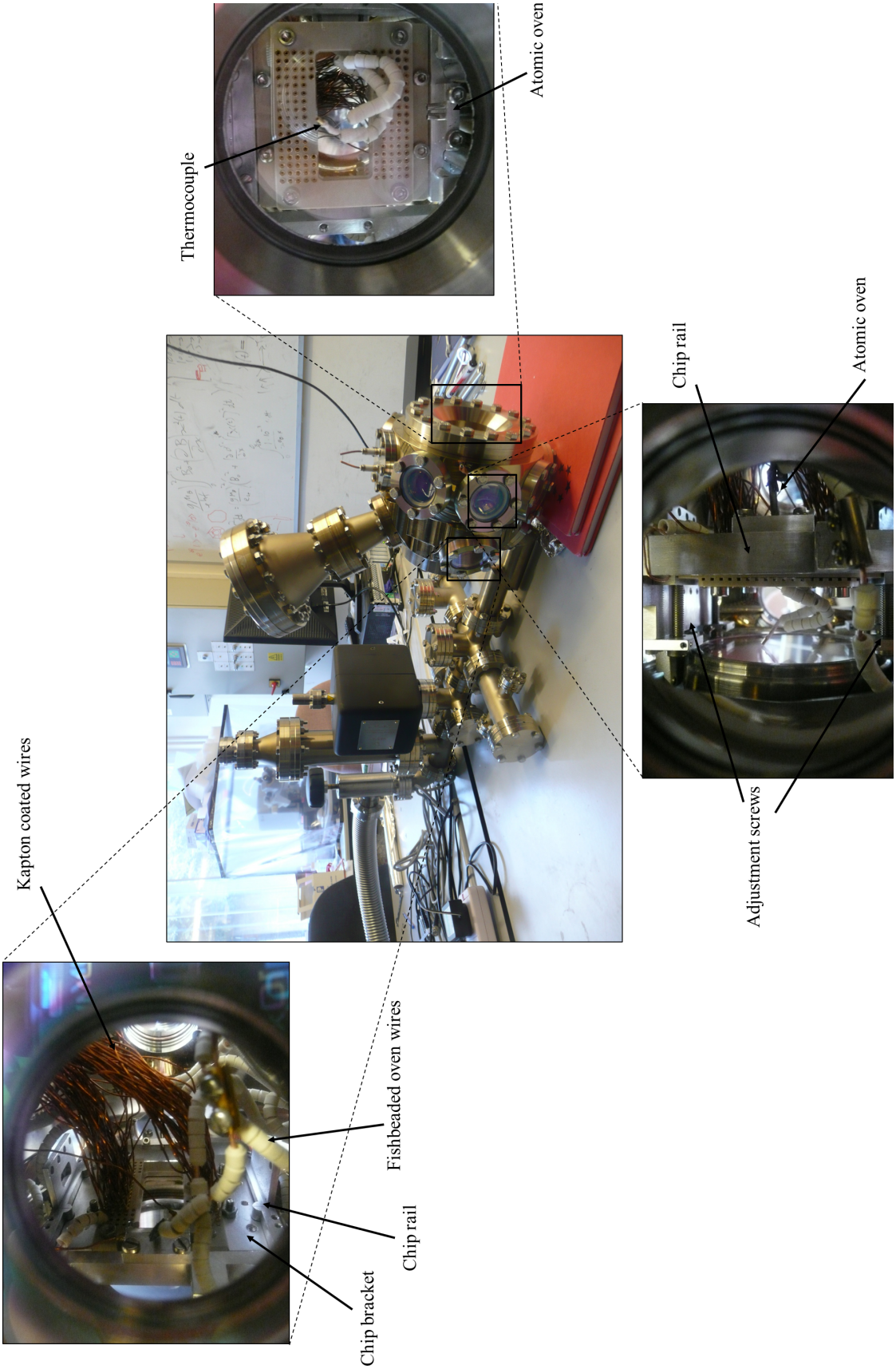

Figure 6.29: The assembled vacuum system.

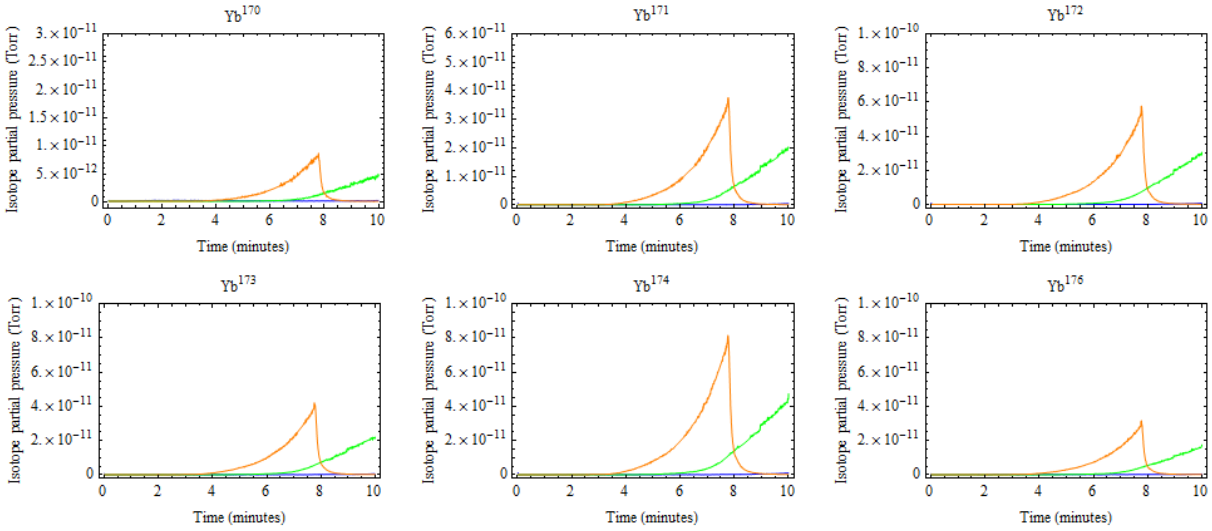

Figure 6.30: Graph of isotope partial pressures for the natural Yb oven 1: blue = 8 A, green = 8.5 A, orange = 9 A.

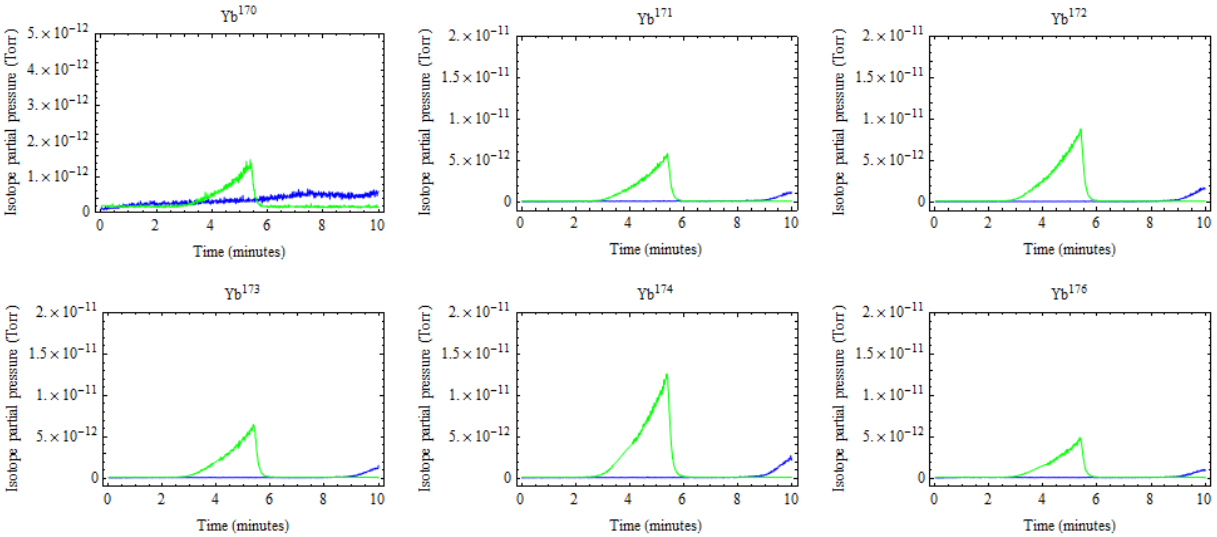

Figure 6.31: Graph of isotope partial pressures for the natural Yb oven 2: blue = 6.5 A, green = 7.5 A.

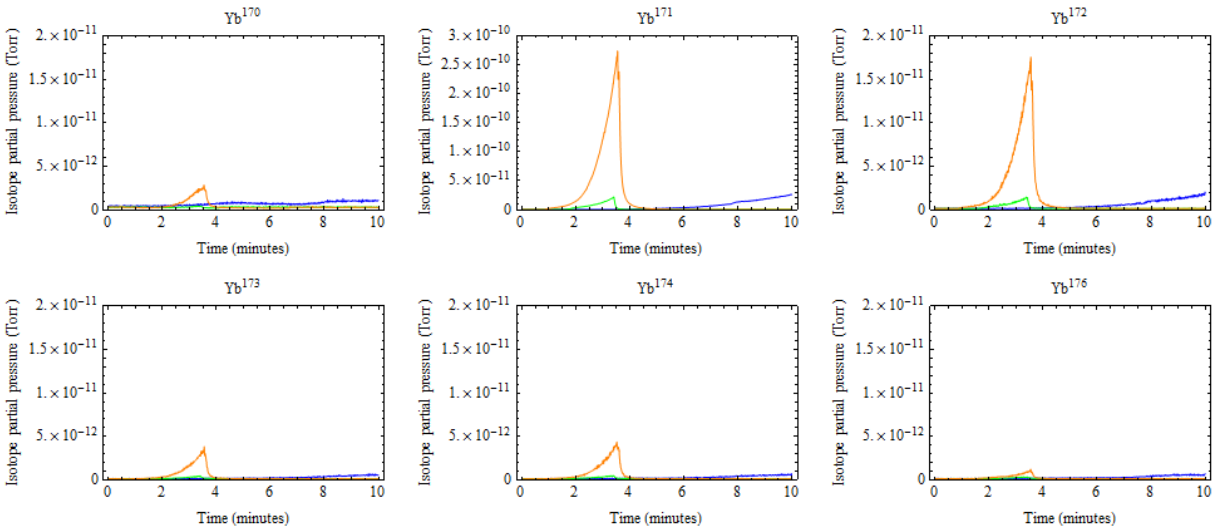

Figure 6.32: Graph of isotope partial pressures for the enriched ^{171}Yb oven 1: blue = 7 A, green = 8 A, orange = 9 A.

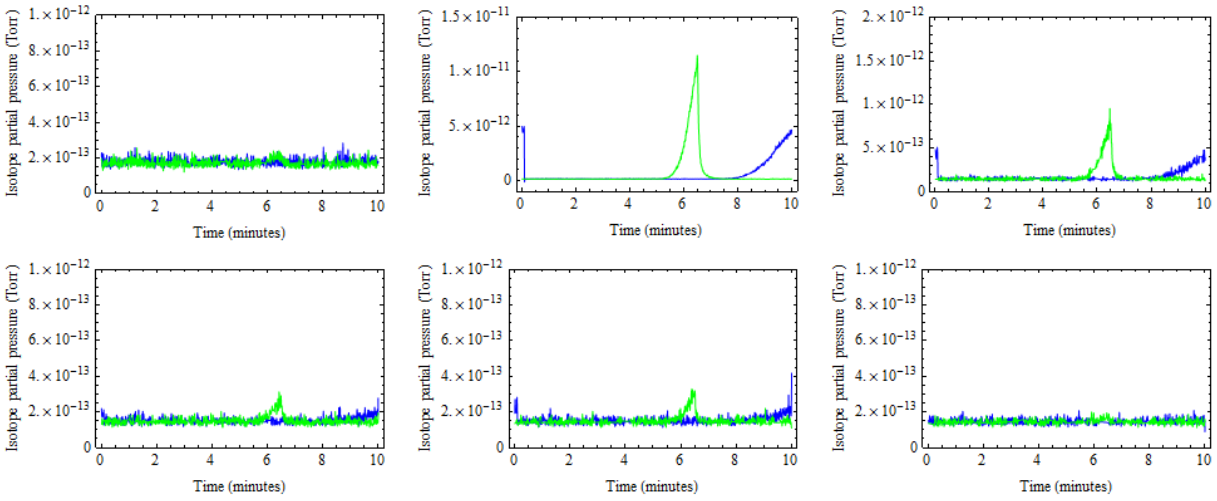

Figure 6.33: Graph of isotope partial pressures for the enriched ^{171}Yb oven 2: blue = 6 A, green = 6.5 A.

Chapter 7

Microfabrication

HA HA, not to scale.

- Phil Ken Sebben - Harvey Birdman, Attorney at Law

7.1 Introduction

Microfabrication is the process of building structures on the micrometer scale. This is a well developed field of research and industry that has yielded great technological advances. This field has been driven by the electronics industry utilizing semiconductor materials to make ever smaller electronic components. Instead of traditional machining techniques where tools physically remove and shape the object being fabricated the material is grown and using chemical and plasma etching technologies the device is fabricated. This has seen such success for several reasons: first is the ability to make smaller and smaller devices with the latest electronic components on the nanometer scale, where individual atoms begin to play a role in the devices performance. Another significant advantage over traditional fabrication is that of massive parallelism. Each process step is performed universally leading to very little increase in over head between creating 1 transistor or 10,000,000 transistors.

For these reasons microfabrication has great appeal to researchers working to scale ion trap arrays. With the requirement for hundreds and eventually thousands of electrodes to control hundreds of trapped ions the task of machining and manually assembling such a large trap is a daunting prospect. If a set of standard electrodes could be generated then it is imaginable that extremely large arrays could be designed and fabricated using techniques already with a long and successful history. Before this though, several challenges still need to be overcome before microfabricated ion traps can become a successful technology.

Firstly a Paul ion trap uses large radio frequency electric fields to trap an ion. To successfully trap and store an ion for periods long enough to perform experiments the energy the ion requires to escape needs to be much greater than that of room temperature atoms, ≈ 0.025 eV [88]. This usually requires rf voltages on the order of several hundred volts to be applied via a helical resonator. With conventional ion traps, where electrodes are constructed out of low resistance metals and separated with thick insulators this is not a problem and it is common to apply many hundreds of volts. This is much more difficult in microfabricated structures were the electrodes are made from either semiconductors or thin metallic layers. This results in resistances and capacitances much greater than that of conventional ion traps and results in increased heat dissipation in the chip, limiting the voltage that can be applied. Additionally with insulating layers only micrometers thick the electrical breakdown of rf electrodes has been observed as low as 11 V [34].

MEMS fabrication is largely a 2-dimensional process with complicated structures in 3-dimensions requiring a greater number of processes, materials and fabrication masks. With each step having a less than 100 % yield, scalable multilayer ion traps quickly become challenging. Alternatively surface electrode geometries can often be fabricated more easily [89]. Yet exposed dielectric materials between electrodes can lead to uncontrolled electrical charging of these surfaces and has the potential to render such simple designs unfeasible for large scale ion trap arrays.

None of these problems though are fundamental in nature and so the challenge of fabricating and scaling ion trap arrays is purely a technical one. I will first introduce the common materials then fabrication processes that are standard in microfabrication facilities. This will give a rough toolbox as to what is available when designing an ion trap. I will then discuss the process design and fabrication of surface electrode ion traps in Chap. 8.

7.2 Fabrication materials

Microfabrication is based around semiconductors, with the most common being silicon. This is because all modern electronics rely on the electrical properties of semiconductors and the ability to dope these materials. We typically require that the resistance is as small as possible. However even heavily doped semiconductors have resistivities many orders of magnitude greater than that of metals. Unfortunately a well developed mature technology for MEMS fabrication using metals does not exist. This problem can be alleviated though by deposition of metal films on top of semiconductor structures. Even a thin layer of gold,

0.5 μm, can offer orders of magnitude less resistance than a 50 μm thick silicon wire.

When designing a microfabricated ion trap, one of the first considerations is the materials to be used. Primary semiconductors are silicon and gallium arsenide but there are many other materials available. Next is choosing the dopant and concentration which will give the semiconductors final resistivity. Then there are the insulators, their dielectric strength and loss tangents which affect the final rf voltage that can be applied. Finally an understanding of the processes available for each material and what etches are available. In Tab. 7.1 I give an overview of both silicon and gallium arsenide and the associated insulators as well as their electrical properties, dopants and common etches.

7.3 Processes

The success and ease with which a trap design can be fabricated is dependant on the processes available and the amount of development each process step requires. For obvious reasons steps that are standardised and well characterised are desirable and should be used whenever possible. This helps to reduce both the development time and cost. Below I describe some of the ubiquitous fabrication processes used in MEMS.

7.3.1 Photolithography

Photolithography is fundamental to all MEMS processes. A photosensitive chemical called photoresist is applied to the substrate. This is reactive to UV light and after it is exposed will form a protective mask. This protects areas of the wafer whilst exposing others for etching or deposition steps.

The wafer is coated with a layer of photoresist usually several microns thick, to achieve an even coating it is deposited then spun until the required thickness is reached. It is then baked to dry it. Once dry the resist is patterned using a fabrication mask of the design and a UV light source. Several different wavelengths can be used, with shorter wavelengths improving resolution due to a reduction in diffraction. Typically wavelengths are from a filtered mercury lamp, either the “g-line” at 436 nm or the “i-line” at 365 nm. Though deep UV lasers can also be used, with a krypton fluoride laser producing light at 248 nm or an argon flouride laser at 193 nm, beyond this it is possible to use x-rays in the LIGA process, capable of producing very high aspect ratio structures.

Once the photoresist has been exposed it is developed. Development is a chemical process where the developer reacts with the resist and depending on the polarity of the resist, either positive or negative, the developer will remove either exposed areas in the

Material	Dopant	Intrinsic resistivity (Ωm)	Degenerate resistivity (Ωm)	Dielectric constant	Loss tangent	Refractive index (@ 10 MHz)	Deposition process	Isotropic etches	Anisotropic etches
Silicon (Si)	Arsenic (N)	3.2×10^5	0.1	11.9	0.001	3.42	LPCVD (polysilicon)	HF/Nitric/ Acetic acid (HNA)	DRIE
	Boron (P)		0.1			MBE (single crystal)			
	Phosphorus (N)		0.1						
Silicon dioxide (SiO_2)	-	10^{16} - 10^{18}	-	3.9	0.001	1.46	Thermal oxidising of Si.	HF	Plasma etch
	-		-			LPCVD			
Silicon nitride (Si_3N_4)	-	10^{16}	-	7.5	0.0005 - 0.0009	2.05	LPCVD	Phosphoric acis	Plasma etch
Gallium Arsenide (GaAs)	Silicon	10^8	0.03	13.1	0.0004	3.3	LPCVD	Phosphoric acid	Plasma etch
	Germanium	-							
Aluminium Gallium Arsenide (AlGaAs)	-	10^8	0.03	13.1	0.0004	3.3	LPCVD	Phosphoric acid	Plasma etch

Table 7.1: Table of some of the common MEMS materials, including their physical and electrical properties, as well as etchant and etch processes. Semiconductor electric properties were taken from references [2, 3], the processes were taken from references [4, 3].

case of negative resist or remove the un exposed areas is the case of a positive resist. This leaves a patterned protective layer on the wafer ready for further processing.

7.4 Deposition

Deposition is a fundamental process in microfabrication, allowing thin films of materials to be deposited onto wafers and combined with etching processes allows complicated structures to be built from the bottom up. There are several primary method of deposition and their use will depend on the materials and application they are intended for.

7.4.1 Chemical vapour deposition (CVD)

In CVD the wafers are placed inside a reactor, gases are passed over the wafers and a chemical reaction between the wafer and the gases results in a thin layer being deposited onto the wafer surface. A typical CVD reaction is show below, this is the reaction to deposit polysilicon.

$$SiH_4 \rightarrow Si + 2H_2 \tag{7.1}$$

Silane (SiH_4) is pumped into the CVD chamber with the wafers at a temperature of $\approx$ 650°C. The silane reacts on the wafer surface depositing a layer of polysilicon, at a rate of $\approx$ 15 nm per minute.

There are many varieties of CVD but the most common forms are low pressure CVD (LPCVD) and plasma enhanced CVD (PECVD). LPCVD improves the quality of the deposited material, reducing the number of defects. However it requires higher temperatures and has a relatively slow deposition rate. Alternatively PECVD uses a plasma to enhance the reaction rate and reduces the temperature required.

7.4.2 Electroplating

Electroplating is a method of depositing layers of metals onto conducting surfaces. The wafer is placed in an electrolyte solution, with the areas to be coated electrically connected to a power supply. The other end of the power supply is connected to a counter electrode, typically made from platinum. Passing a current through the electrolyte solution causes the metal to be deposited on the conducting surfaces. This can be used to deposit very thick metal layers, >100 μm, but does require electrical connection to all the areas were deposition is desired.

An extension of electroplate is electroforming. In electroforming a mold, known as a mandrel, is placed in the electrolyte solution. By passing a current through the solution and depositing the metal onto the mandrel it is possible to form complicated geometries directly. However this does require a conducting mold to be fabricated.

7.4.3 Epitaxy

Epitaxial growth is that of growing a continuous crystal structure on top of an already ordered single crystal wafer. The process itself is very similar to CVD, the wafers sit inside a vacuum chamber while reactive chemicals are introduced. Though instead of the whole chamber being heated only the wafers are, with typical temperatures being at least 50% of the deposited materials melting point. It has the benefit over typical CVD in that it has very large deposition rates allowing thick films to be deposited.

7.4.4 Oxidisation

Oxidation is simply allowing the surface of the material to be oxidised in an oxygen rich enviroment. This can be used to grow layers of oxide up to several microns thick, however it is a self limiting process with the oxidisation rate exponentially dropping with increasing oxide thickness.

Wafers are placed inside a furnace at a temperature of $\approx 1000°C$, oxygen is then fed into the furnace and reacts with the wafer surface. This process is typically used to grow silicon dioxide layers on silicon substrates as SiO_2 provides extremely good electrical insulation and very selective etches.

7.4.5 Evaporation

The wafers are placed inside a vacuum chamber opposite a source material. The source is then heated, evaporating it. The source is either heated by resistive heating or e-beam evaporation. In resistive heating a large current heats the source, where e-beam evaporates the material by directing a beam of electrons into the source causing local heating and evaporation.

Evaporative deposition covers everything opposite the source and as a result there is a lot of waste. This makes the deposition of thick layers of rare metals such as gold and platinum very expensive and typically is not used for layer thicknesses greater than 500 nm.

7.4.6 Sputtering

Sputtering is similar to evaporating, the wafer is placed opposite a source material then a low pressure gas in the chamber is ionised with an rf field. The ions then accelerate towards the source material causing atoms to breakaway and condense on the substrate. This though happens at a much lower temperature than evaporation.

Unlike evaporation which displays very directional coverage, sputtering will cover most surfaces, even surfaces not in line of sight of the source. This could prove problematic as there is the potential for trap electrodes to be shorted to ground by the accidental coating of insulator surfaces.

7.5 Etches

7.5.1 Wet etches

Typical wet etches are isotropic, meaning they dissolve the substrate equally in all directions. A wafer coated with a patterned photoresist will be placed in a solution containing a reactive chemical, eg SiO_2 placed in an HF bath, this will then dissolve the material. By controlling the temperature of the etchant, it is possibly to control the speed at which the material is etched. Being isotropic there will also be lateral etching beneath the photoresist. This will typically have a circular cross section with the top etched horizontally as far as the depth of the etch. An isotropic etch profile is given in Fig. 7.1

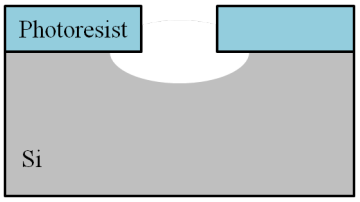

Figure 7.1: An isotropic etch profile. It can be seen that the substrate has been etched as far laterally as deep.

7.5.2 Anisotropic wet etches

Some wet etches also display anisotropic etch rates. This occurs when etching a single crystal wafer, different crystal planes will have varying etch rates. This is most commonly seen in single crystal silicon, where the $\langle 111 \rangle$ crystal plane etches more slowly than the $\langle 100 \rangle$ plane. A selectivity between planes of up to 400 is achievable with potassium

hydroxide (KOH) solution. An anisotropic etch profile for a KOH etch of silicon is shown in Fig. 7.2.

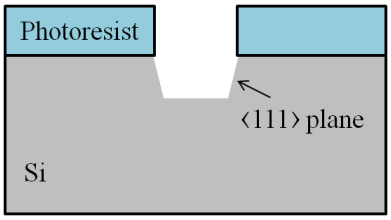

Figure 7.2: An anisotropic etch profile. It can be seen that there etch profile has straight angles walls corresponding to slower etching in the ⟨111⟩ plane.

7.5.3 Reactive ion etch (RIE)

An alternative to using wet chemical solutions is to use dry etching techniques. In a RIE process the wafers are placed in a vacuum chamber and several gases introduced. Using an rf source this gas is ionised and accelerates towards the substrate surface. At the substrate the ions hit the surface reacting with the material and forming a gas. Additionally to the chemical process the ions have sufficient energy to physically kick out atoms from the substrate, in a similar process to sputtering. This is predominantly an anisotropic etch, but the chemical aspect to the etch is isotropic, so the etch profile can still have rounded sidewalls.

An extension to RIE is deep RIE (DRIE), using DRIE it is possible to etch very deep trenches with nearly vertical sidewalls. This etch is performed by alternating between two different gases. The first gas forms a protective polymer on the surface of the substrate. Next the RIE gas is introduced and performs the etch, the highly anisotropic ion bombardment removes the protective layer from the bottom of the trench and allows the reactive part of the etch to take place. However the polymer attached to the side walls is unaffected and prevents any further chemical etching laterally. These steps are repeated allowing vertical trenches hundreds of microns deep to be etched with an aspect ratio of up to 50:1.

7.6 Electrical properties and RF loss in microfabricated ion traps

This section follows closely work presented in the following books: [90, 91, 92]. When designing and building microfabricated ion traps it is important to have an understanding

of the rf loss and the loss mechanisms that will ultimately lead to the ion trap working or failing. The following subsections will discuss the main source of loss and how to potentially minimise there impact.

7.6.1 Contact resistance

When depositing a metal onto a semiconductor it is not enough to assume that the resistance of the contact is the same as between two metal boundaries. There are two forms of contact that can arise, firstly the ohmic contact. This acts like a normal metal-metal connection, or it can form a rectifying contact. In a rectifying contact an electrostatic barrier forms between the metal and semiconductor, a result of there being a very thin gap between the two. This barrier, known as the Schottky barrier, is dependant on the work function of the metal and the electron affinity of the semiconductor [2]. This property is highly undesirable in microfabricated ion traps as we want a free flow of electrons between the deposited metal and the conducting semiconductor beneath. This is achieved if the metal and semiconductor layers are brought into physical contact, however practically there will always be a thin layer, 1-2 nm, separating them. Alternatively by heavily doping the semiconductor, with densities of $\geq 10^{19}$ cm^{-3} then the barrier between the metal layer and the semiconductor is sufficiently low as to allow the electrons to readily tunnel between the two [93].

7.6.2 Complex conductivity, loss tangent and power factor

When applying oscillating fields to certain dielectrics or lossy conductors, a proportion of the power will be lost due to heating of the material. This process is a result of dielectric hysteresis which can cause large in-phase ac currents to build up inside the material and dissipate energy. This means for oscillating electric fields the conductivity of the material will change. In these cases the permittivity of the material becomes complex and Maxwell's Ampere equation

$$\nabla \times \mathbf{H} = \mathbf{J} + \frac{\partial \mathbf{D}}{\partial t} = \sigma \mathbf{E} + j\omega\varepsilon\mathbf{E}$$

becomes [90]

$$\nabla \times \mathbf{H} = \sigma \mathbf{E} + j\omega(\varepsilon' - j\varepsilon'')\mathbf{E}. \tag{7.2}$$

Where $\mathbf{H}$ is magnetic field strength, $\mathbf{J}$ is current density, $\mathbf{D}$ is electric displacement, $\mathbf{E}$ is the electric field, σ is the conductivity, j is the square root of negative 1, ω is angular frequency and ε is the permittivity. The permittivity can be split into its real and

imaginary components, $\varepsilon = \varepsilon' - j\varepsilon''$, where ε' is the real lossless part of ε and ε'' is the imaginary lossy part of ε, rearranging Equ. 7.2 we get

$$\nabla \times \mathbf{H} = (\sigma' + j\omega\varepsilon')\mathbf{E} = J_{total}\mathbf{E} \tag{7.3}$$

where $\sigma' = \sigma + \omega\varepsilon''$ is the equivalent conductance. It can be seen from Equ. 7.3 that the equivalent conductance is frequency dependant. At $\omega/2\pi = 0$ Hz, then $\sigma' = \sigma$, but at large frequencies the $\omega\varepsilon''$ term can become significant. The frequency at which the complex conductivity begins to play a significant role is dependant on the average time, τ, between collisions of the free electrons and the positive ions in the lattice [91]. For most metals τ is on the order of $\tau \approx 10^{-14}$ s, meaning it begins to become relevant when frequencies reach the infra red. The mean free time of semiconductors depends on the carrier type and doping; for degenerate arsenic doped silicon, where the dominant charge carriers are electrons, the mean free time is $\tau \approx 4 \times 10^{-10}$ s, meaning the complex conductivity begins to be important for frequencies $\omega/2\pi > 1$ GHz. At MHz rf drive frequencies the conductivity will approximate the dc value and can be neglected, however with the latest generation of ion traps beginning to work towards implementing microwave sources on chip, discussed further in Chap. 10, then the complex conductivity will begin to become significant, with a ytterbium ground state hyperfine splitting of 12.6 GHz, well above the 1 GHz set by the silicon mean free time.

From Equ. 7.3 it is useful to define two quantities, the loss tangent and the power factor, these relate to the loss of power due to dielectric hysteresis, when dielectrics are subjected to oscillating electric fields. The loss tangent is given by [90]

$$\tan\delta = \frac{\sigma'}{\omega\varepsilon'} \tag{7.4}$$

and the power factor is the cosine of the angle θ where $\theta = 90° - \delta$. Which for small angles can be approximated as

$$PowerFactor = \cos\theta \approx \tan\delta = \frac{\sigma'}{\omega\varepsilon'}. \tag{7.5}$$

We can calculate the power dissipated per unit volume by multiplying the current density $\mathbf{J}$, where $\mathbf{J} = \sigma'\mathbf{E}$, by the electric field $\mathbf{E}$, giving [90]

$$P_v = \sigma' E^2. \tag{7.6}$$

Using equations 7.4, 7.5 and 7.6 it is possible to estimate the power lost due to dielectric hysteresis in the trap.

Alternatively it is possible to view the loss tangent as an equivalent series resistance (ESR) in a lumped element circuit. This is important as the impedance of the load circuit on the resonator can dramatically reduce the Q, and the ability to apply large rf voltages. The ESR can be understood by looking at Fig. 7.3, this shows a ideal capacitor connected to a signal generator. The insulating material between the two capacitor plates has an associated loss tangent, and results in an equivalent series resistance (R_{ESR}). The value

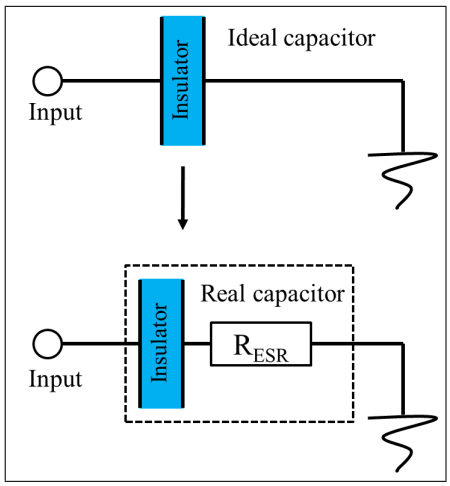

Figure 7.3: Top shows a capacitor connected to a signal generator, bottom shows the same circuit but with an additional resistance as a result of the loss tangent of the dielectric in the capacitor.

of R_{ESR} is given by

$$\tan\delta = \frac{R_{ESR}}{|X_c|} \tag{7.7}$$

Where X_c is the reactance of the capacitor and given by $X_c = \frac{-1}{\omega C}$, where ω is the rf drive angular frequency and C is the capacitance.

However just looking at the loss tangent of the insulating materials would not give a full understanding of the rf loss in MEMS structures, for this it is necessary to look at the full circuit including the resonator. The coupling of the resonator to the chip results in a frequency dependance of the power loss which can significantly change between 10 - 100 MHz. To understand the loss through a microfabricated structure and its coupling to helical resonator simulations were performed of the structures describing in the following chapter, the details of these simulations are given in Chap. 8, Sec. 8.6.

Chapter 8

Microfabricated ion traps

The difficulty lies not so much in developing new ideas as in escaping from old ones.
- John Maynard Keynes

8.1 Introduction

Ion traps offer one of the most promising systems for the construction of a quantum computer. A basic set of criteria was set out by D. DiVincenzo [94] in order to quantify the suitability of a system for quantum information processing (QIP). Experiments in ions traps have managed to demonstrate most of these criteria, such as long coherence times [95], state initialisation and detection [10, 11, 12], a set of universal quantum gates [16, 17, 18, 15, 23, 22, 24, 19] and a scalable architecture to store a large number of qubits [28, 30, 34, 37, 89, 36]. Due to the success of QIP experiments in ion traps there has been a great deal of progress towards building scalable microfabricated ion trap arrays [75]. This chapter will discuss my work towards the design and construction of our first microfabricated ion trap arrays.

There are many obstacles to building a scalable ion trap array architecture and there are several requirements any array must meet. Firstly its construction needs to take account of the fact that for a large ion trap array it is desirable to store and manipulate thousands or more ions. These ions will also need to be moved or shuttled between different regions of the ion trap in order to perform gate operations. This will require junctions in the linear array, where the ion can be shuttled along multiple different paths necessitating many more electrodes to trap and control all the ions. This also requires the ability to transport ions through the array adiabatically to preserve the qubit state, inhomogeneities in rf potential can heat the ion during shuttling and so smooth potentials throughout the

array is desirable.

Ion shuttling through junctions was first demonstrated by W. Hensigner *et al.* [28] and near adiabatic junction operations were performed by R. Blakestad *et al.* [30]. Both these ion trap geometries were symmetric ion traps, where the electrodes surround the ion, and fabricated from laser machined alumina. The alumina substrates were gold plated and manually assembled. These designs required micrometer precision in electrode fabrication and alignment. This is possible for a single junction, proof of principle ion traps, but would be prohibitively difficult for multi-junction arrays.

For this reason, using microfabrication technologies began to be employed to construct ion trap arrays. This allows the whole array to be fabricated in parallel and removes the need for manual alignment. This has been demonstrated for both surface and symmetric trap arrays. D. Stick *et al.* [34] used alternating layers of gallium arsenide (GaAs) and aluminium gallium arsenide (AlGaAs) to form parallel cantilevers, creating a two level ion trap geometry, with this, successful trapping of Cadmium ions was demonstrated [34]. However the fabrication for multi level ion traps is complex even for simple designs and so J. Chiaverini *et al.* [35] proposed a surface electrode geometry ion trap. This significantly reduces fabrication complexity and allows complex geometries to be fabricated relatively easily.

Initial traps were fabricated by depositing gold onto a quartz substrate [89], but significant advances in fabrication have allowed buried conductors and large arrays to be constructed [75]. J. Amini *et al.* [36] have constructed and demonstrated ion trapping and junction shuttling within a 150 zone, 6 junction surface ion trap array. However there still remain issues with anomalous heating from the electrode surfaces and stray electrical charges from exposed dielectrics [36]. The work undertaken in this chapter focuses on fabricating an ion trap array with totally shielded dielectrics to remove any stray charges from the line of sight of the ion. Parallel to my work and subsequently to it similar work was undertaken, with a good review of different fabrications given by M. Hughes *et al.* [75].

Here I will present the design and fabrication of several microfabricated surface electrode ion trap geometries. These geometries were designed to include junction shuttling capabilities as well as 2D ion trap arrays.

8.2 Fabrication design

The fabrication process for the trap structures was designed to include the least number of process steps, with each step remaining as standardised as possible. By reducing the number of process steps this helps reduce the amount of development time required to optimise the fabrication process. Silicon-on-insulator (SOI) wafers provide a layered structure that offers the ability to manufacture ion traps easily and with hidden dielectrics. SOI wafers consist of a thick handle layer, typically several hundreds of micrometers thick, a layer of buried silicon dioxide with a typical thickness of $\leq$10 μm and a top device layer of silicon several tens of micrometers thick. By etching trenches into the top device layer electrodes can be segmented. This leaves exposed SiO_2 at the bottom of each trench, an etch of the SiO_2 removes this oxide layer and being isotropic in nature will undercut beneath the electrodes. This exposes the conductive handle layer and removes all exposed dielectrics from line of sight of the ion. These wafers are used largely in the microelectronics industry to improve device performance and are available from a number of distributors.

There are several ways of manufacturing SOI wafers. The simplest method is by implanting oxygen at a desired depth and followed by a high temperature anneal [96], the annealing causes the oxygen to react with the silicon and to form a silicon dioxide layer in the wafer. This results in a buried SiO_2 layer beneath the top layer of silicon. Alternatively the surface of a wafer is thermally oxidised and followed by hydrogen implantation. The hydrogen is implanted below the oxide layer at a depth equal to the thickness of the device layer. The oxide layer is then bonded to a second wafer and the first wafer is broken along the hydrogen layer. This leaves a thin device layer of silicon on top of a buried oxide layer. The wafer is then chemically mechanically polished to smooth out any imperfections along the cut. This process is known as smart cut [97] and it is the process used in the production of our wafers. When buying the wafers it is possible to specify the device layer thickness, oxide thickness and handle thickness, as well as the dopant and dopant level of the silicon. The device layer was specified to have a thickness of 30 μm, and to be degenerately n-doped with arsenic. To increase breakdown voltage and reduce capacitance the buried silicon dioxide layer has a thickness of 10 μm, the maximum available. The handle layer has a thickness of 600 μm and the same doping as the device layer, resulting in a silicon resistivity of 0.001-0.005 Ωcm. Ten 6" SOI wafers were bought from Ultrasil Corporation for £1976.

The fabrication process to build the traps is to first evaporate an adhesion layer of chromium onto the silicon, this is then followed by evaporating a layer of gold up to

a thickness of 500 nm. After patterning with photoresist the gold and chrome layers are etched using first potassium iodine then cerric ammonium nitrate to expose the silicon device layer. These etches are isotropic and so some etching of the gold is expected beneath the photoresist. Next a DRIE etches the silicon device layer, exposing the buried silicon dioxide layer. A buffered hydrofluoric (HF) acid etch of the silicon dioxide isotropically removes the exposed silicon dioxide at the bottom of the trenches and undercuts beneath the electrodes. Finally the photoresist is removed and the chips are diced and wire bonded onto ceramic chip carriers. This fabrication process is shown in Fig. 8.1.

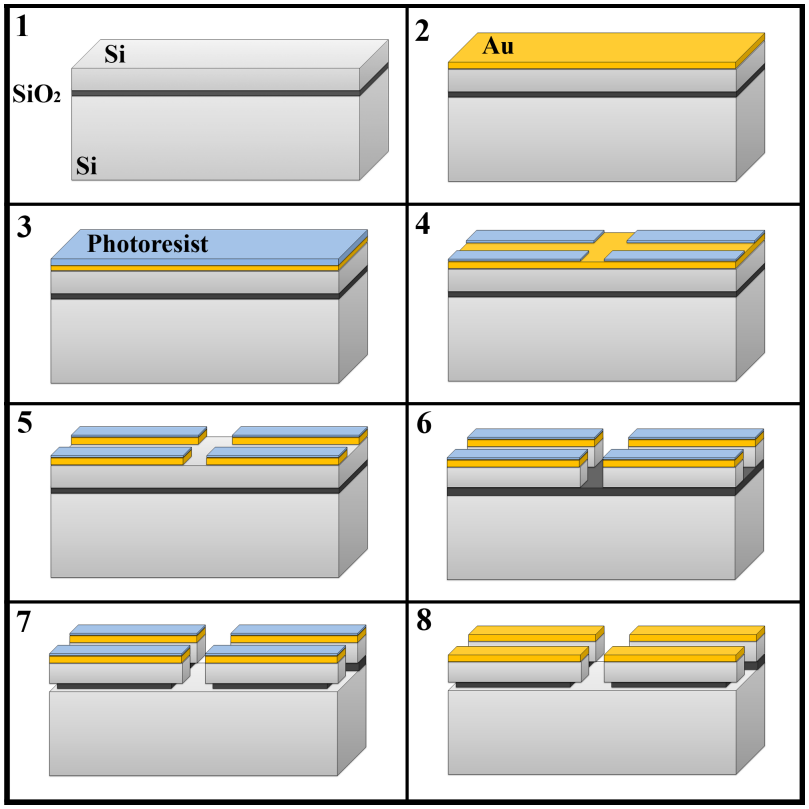

Figure 8.1: 1) Silicon-on-insulator wafer. 2) A 40 nm layer of chrome is evaporated onto the surface followed by 500 nm of gold. 3) Photoresist is spin coated on top of the gold. 4) The photoresist is exposed and developed with the trap geometry. 5) The gold and chrome are etched, exposing the silicon layer. 6) The silicon is deep reactive ion etched, exposing the buried oxide layer. 7) The silicon dioxide is isotropically etched with HF. 8) The photoresist is removed using acetone.

This fabrication will use the layered structure of the SOI wafer to simply fabricate a surface electrode structure where all the dielectrics are shielded from the ion. Additionally the fabrication steps are all standard clean room processes, reducing the time required for process development. During the development and fabrication of our traps J. Britton *et*

al. [37] demonstrated ion trapping in traps fabricated using similar fabrication methods.

8.3 Trap design and simulation

The design process of the ion trap was divided into three parts: junction design, interaction regions and storage areas. Optimization of all the control features and rf geometry in these regions is crucial if a high level of ion position manipulation is to be achieved. In an attempt to minimize ion heating, the rf nil height was chosen to be greater than 70 μm. The ion height, trap depth and secular frequency all scale with the rf rail width and separation [39, 47, 98], by adjusting these parameters it is possible to engineer the rf nil height, trap depth and ion secular frequencies.

To ensure efficient laser cooling it is also important to consider the principal axes of the trap [43]. The motion of the ion can be described as a three-dimensional uncoupled oscillator. The laser wave vector $\vec{k}_{laser}$ must have a component along each principal axis if the ion is to be efficiently cooled, as described in Chap. 2. Due to the symmetry of a 5 rail surface trap one principal axis lies perpendicular to the surface. Optical constraints require the laser to be parallel to the trap surface and so cooling of this axis would not be possible. A rotation of the two radial axes is possible by breaking the symmetry of the rf rails. For the linear sections in our trap the electrode configuration can be seen in Fig. 8.2.

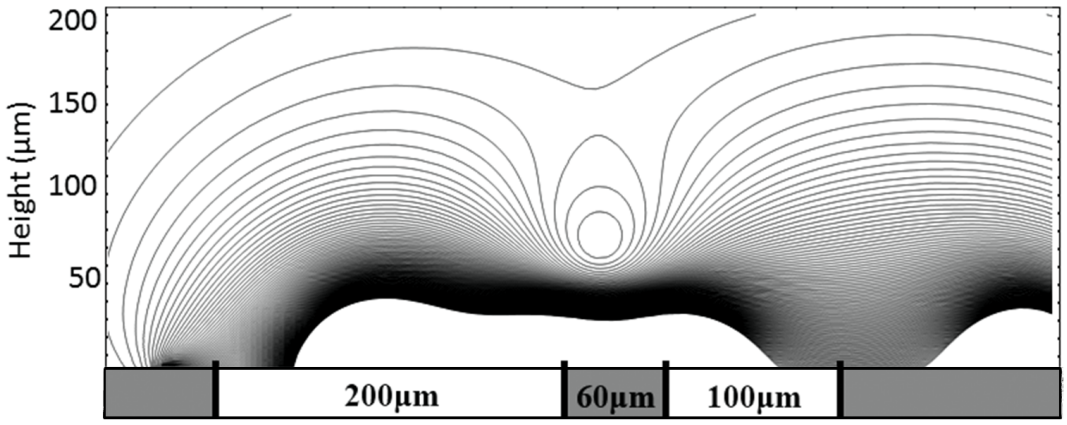

Figure 8.2: A cross section view of the linear rf structure. Asymmetric rf electrodes (white) provide a rotated rf nil approximately 75 μm above the trap surface. The static control electrodes (grey) can be considered to extend to infinity.

This structure yields an ion height of ≈ 75 μm. For an rf drive frequency of $\Omega/2\pi =$ 45 MHz, peak rf voltage of 280 V and an atomic mass of $^{171}Yb^{+}$ the trap depth is 0.19 eV and axial secular frequencies are $\omega_{x'}/2\pi \approx 3.4$ MHz and $\omega_{y'}/2\pi \approx 3.5$ MHz, where x'

and y' are the rotated principal axis of motion. This corresponds to a stability parameter of q = 0.72.

The trap can be considered to have four main regions as shown in Fig. 8.3: top linear section which is marked by a *red* box, bottom linear section *green*, right linear section *orange* and the junction *purple*. The top and bottom linear sections are designed for ion combination and separation required to perform quantum gate operations, whilst the right linear section is for ion storage.

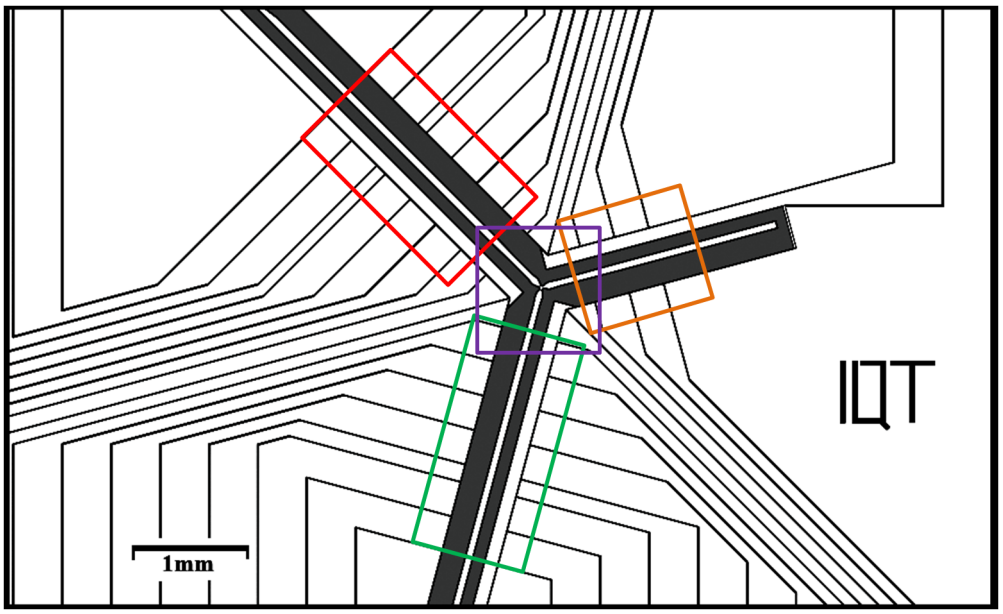

Figure 8.3: A view of the whole trap with the static control electrodes in white and the rf electrode shaded in black. The top and bottom interaction regions are surrounded by a red and green box respectively and the junction and the right storage areas are surrounded by purple and orange boxes respectively.

Adiabatic shuttling through the trap array is a key requirement in any scalable ion trap design [48]. To implement successful adiabatic shuttling protocols in a microfabricated ion trap, it is important to allow a smooth shuttling path through the trap junction. To aid adiabatic shuttling it is important to reduce the ponderomotive potential barriers that are intrinsic to intersections. As well as minimising this barrier there will also be a change in radial secular frequency, this is detrimental to adiabatic shuttling [48] and therefore an rf geometry which reduces both the potential barrier and variation of the radial secular frequencies is beneficial. Additionally, in surface geometries ion displacement in both radial dimensions can increase the complexity of shuttling procedures. Ion displacement in both radial axes for the modified rf geometry and the radial secular frequency changes and potential barrier suppression are shown in figures 8.4(a), 8.4(b), 8.5(a) and 8.5(b)

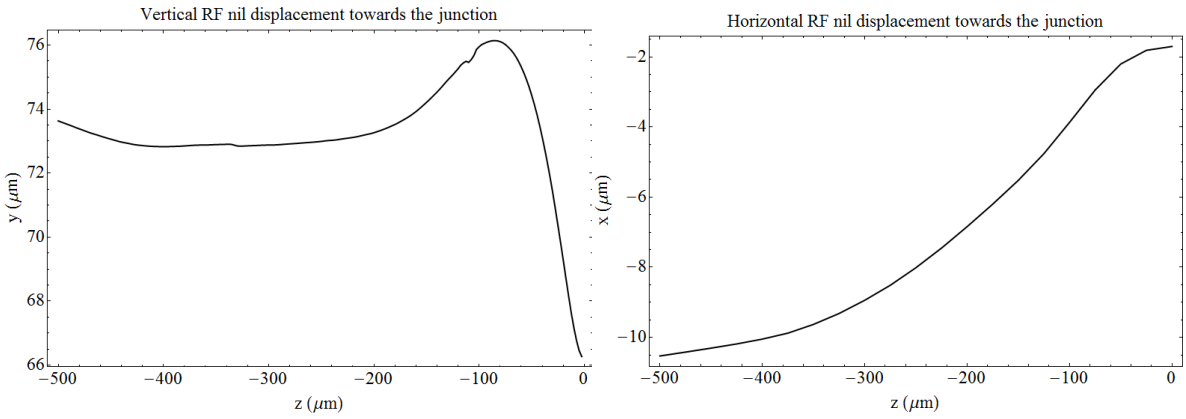

(a) (b)

Figure 8.4: a) The vertical displacement towards the junction, b) The horizontal displacement parallel to the trap surface, where $x = 0$ μm corresponds to the mid point between to two rf electrodes.

respectively. Figure 8.4(a) shows kinks in the rf nil position at z = -320 μm and z = -110 μm, these kinks are due to numerical noise in our simulation and do not reflect any real feature. From these figures it is clear that the modified rf electrode geometry both reduces the secular frequency changes and ponderomotive potential barrier height.

To reduce the rf barrier of our trap comprehensive simulations using the bemsolver [52] and the root compiler were performed. The simulations of the trap geometry not only use the top of the electrodes but also include trenches, side walls and trench bottom. Initially simulations were performed using the gapless plane approximation [47] but when a more complete model, accurately reflecting the geometry of the fabricated trap, was simulated it was found to alter the rf barrier suppression by up to a factor of two. Because of this discrepancy the final geometry was optimised using a realistic ion trap model including electrode gaps. The initial rf geometry and modified geometry can be seen in Fig. 8.6. Figure 8.6(a) and shows the standard rf geometry of a Y junction, where 8.6(b) is the final modified geometry.

The final electrode shape was reached by first simulating the standard geometry, then by making modifications to the rf electrode shape and simulating the new geometry the new barrier height could be found. This could then be used to iteratively modifying the junction geometry until a satisfactory suppression was found. Using this method a barrier suppression of ≈ 6 was found. This is not an optimised geometry and a numerical optimisation algorithm would be better suited. This has been demonstrated by J. M. Amini *et al.* [36], where a barrier suppression of 200 was found for a surface Y junction.

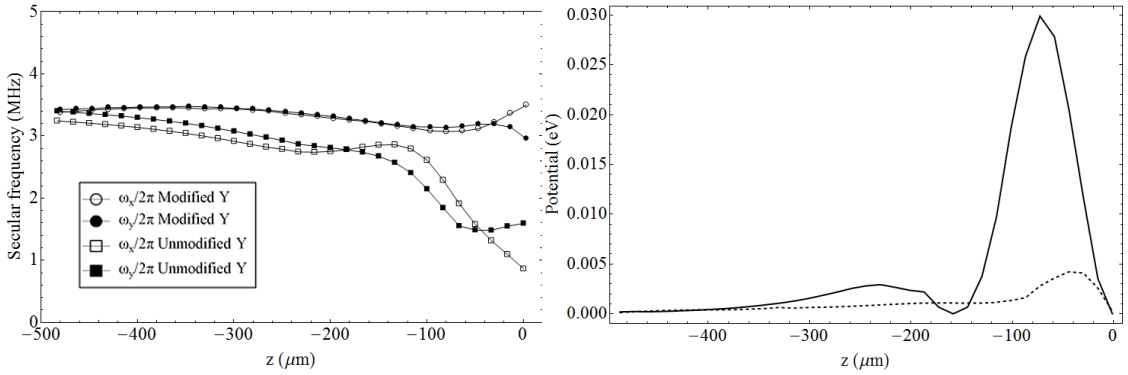

(a) (b)

Figure 8.5: a) The secular frequency variation along the rf nil and the potential barrier for both the unoptimised rf geometry and the modified geometry. b) A comparison of the initial rf barrier (solid) and the suppressed barrier (dashed), the nil potential corresponds to an rf drive frequency of $\Omega/2\pi = 45$ MHz and a peak rf voltage of 280 V.

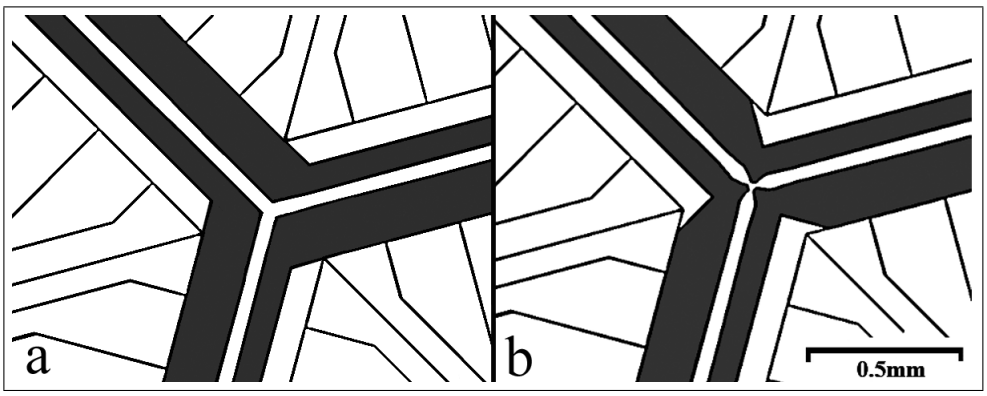

Figure 8.6: a) Before rf electrode shape was modified. b) After rf electrode was modified.

This however uses the gapless plane approximation which I found results in unfeasibly large errors on the ponderomotive potential at junctions. Extending their optimisation methods to a more complete model that reflects closely the fabricated geometry should provide improved barrier suppressions. Ultimately the rf barrier is dependant on small alterations of the rf geometry, often these alterations are smaller than the fabrication tolerance and so final junction rf barrier height is highly dependant of the fabrication of the actual trap, the surface quality of the electrodes as well as the electrode geometry tolerance. This may mean that for successful adiabatic shuttling in microfabricated arrays an initial calibration of the junction topology is required and used to optimise shuttling algorithms.

Figure 8.7 shows a 3D contour plot at the finalised junction. The closed contours show

that the ion is confined radially and they show how the nil position shifts as the ion moves towards to junction.

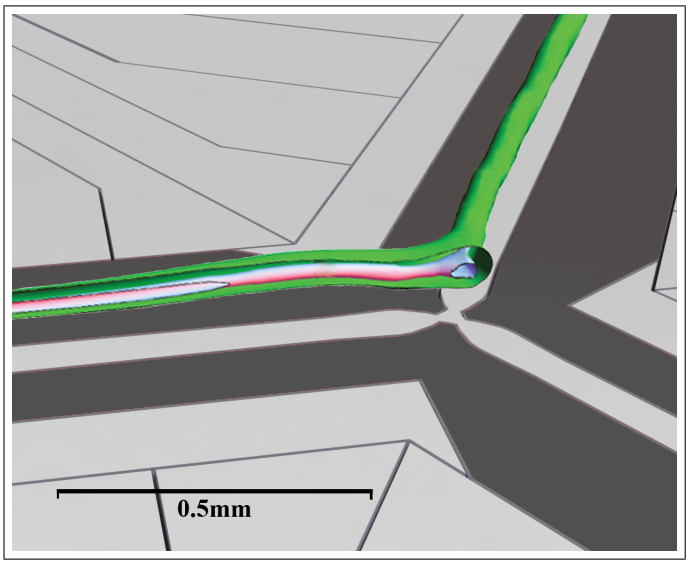

Figure 8.7: Isosurfaces of the ponderomotive pseudopotential through the junction. The green surface corresponds to ≈ 0.1 eV and the white surface corresponds to ≈ 0.04 eV

8.4 2D lattice trap

As well as ion trap arrays designed for shuttling and the transport of ions for scalable QIP it is possible to use multidimensional arrays of ions to perform quantum simulations [99]. In these systems an array of trapped ions is used to simulate a quantum system which we cannot directly control and measure. There have been several proposals of systems where trapped ions can be used to simulate the behavior of a more complicated system, [100, 101, 102, 103, 104], with several experiments demonstrating the implementation in linear ion traps [105, 106], however to extend these basic simulations it is necessary to move from 1D ion chains to 2D ion arrays. The first steps towards implementation have been shown by R. J. Clark *et al.* [107], here both atomic ions and micro particles were trapped in 2D ion trap arrays consisting of an rf metal mesh suspended above a grounded plane electrode.

Fabricating a suitable electrode structure to generate a 2-dimensional lattice potential results in several technical challenges. The 2D periodicy in the lattice structure must provide suitable trap depth to trap thermal ions but also keep ion secular frequencies low. A 2D lattice pseudopotential is easily generated by placing many ring and fork traps close to each other and extending the top electrode far away [107]. Here a perforated

metal sheet was used above a metal plane separated by glass spacers. This ring and fork construction whilst successful in trapping ions proves difficult to scale to many ions while keep decoherence times long. A solution to this would be to reduce the electrode geometry and bring the ions closer together, allowing for greater ion-ion interaction strengths.

Simulations demonstrating optimization of micro surface electrode structures where the local ion position and potential are arbitrarily optimized has been shown [108]. This though results in isolated electrode islands, these isolated islands can prove difficult to fabricate as electrical contact needs to be made via buried conducting layers. This has been shown successfully [36] but involves a significant increase in fabrication complexity and overhead. Unfortunately without these isolated islands it is challenging to generate a scalable two dimensional array. However the SOI fabrication allows a multilevel ion trap structure to be built. Using the top device layer as the rf electrode and etching islands that expose the conductive handle layer produces isolated grounded islands. Above each island will be a rf nil capable of trapping an ion. A hexagonal lattice design, with each ion having six nearest neighbors is shown in Fig. 8.8. The ion lattice region is surrounded by a border of rf and micromotion compensation electrodes which extend from the edge of the rf electrode to the the trap edge.

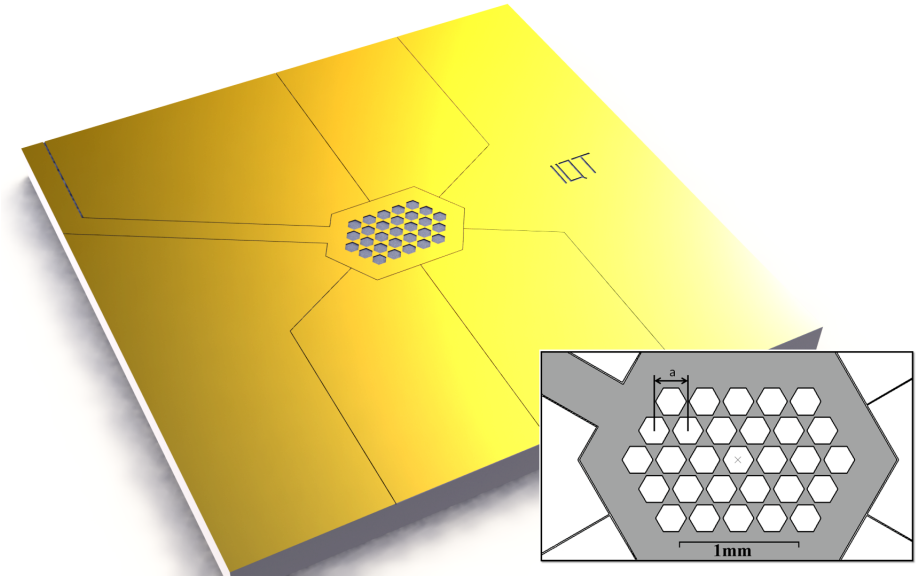

Figure 8.8: SolidWorks drawing of the hexagon lattice trap design, the inset shows the trapping region the ions trap above the center of each hexagon, the width of a hexagon is a = 260 μm.

BEM simulations of the trap show that the ion is trapped 120 μm above the trap surface and for an rf drive frequency of $\Omega/2\pi$ = 45 MHz and rf peak voltage of 500 V it

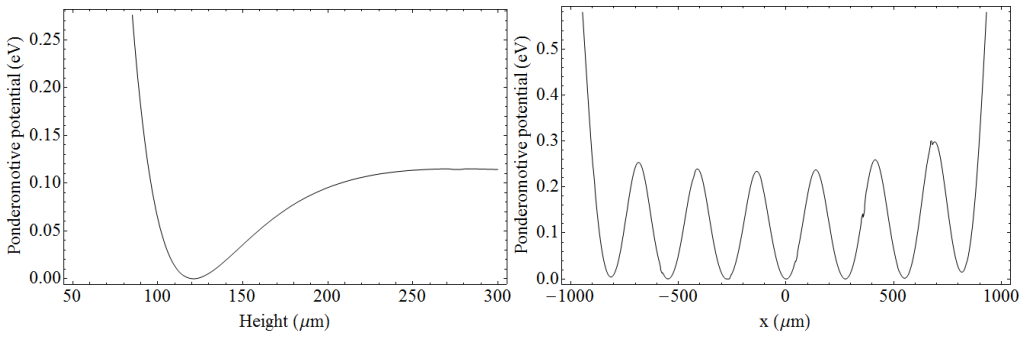

(a) (b)

Figure 8.9: a) The ponderomotive potential from the surface of lattice trap, with the potential minimum at 120 μm above the surface and a trap depth of 0.11 eV. b) Ponderomotive potential along the central line of traps.

has a trap depth of ≈ 0.11 eV and radial secular frequencies of $\omega_{radial}/2\pi \approx 7.5$ MHz, with a q stability parameter of q = 0.48. The ponderomotive potential from the trap surface is shown in Fig. 8.9(a).

8.5 Electrical characteristics

To apply large rf voltages to the trap electrodes a helical resonator is inductively coupled to the trap electrodes, with an equivalent circuit shown in Fig. 8.10. The voltage applied is determined by the Q factor of the resonator which is dependent on the capacitance and resistance of the trap and experiment, as discussed in Chap. 3.5. Where R_t and C_t are the equivalent resistance and capacitance as shown in Fig. 8.10(b). To ensure that ytterbium ions can be trapped, sufficient rf voltages needs to be applied. Making an estimate of the trap resistances and capacitances should ensure that the trap is operable.

There are two dominant sources of capacitance in the trap, the first is from the surrounding control static electrodes, C_1, and the second is the capacitance between the rf electrode and the handle layer C_2, as shown in Fig. 8.11. To calculate the total trap capacitance these surfaces can be modelled as a parallel plate capacitor, $C = k\varepsilon_0 A/d$, where A is plate area, d is plate separation and k is the relative permittivity of the dielectric between the plates. For C_1, A is the side wall surface area in the trenches that lays parallel to the static electrodes, d is the trench width of 5 μm and k = 1. For C_2, A is the surface area of the electrode base, d is the SiO_2 thickness of 10 μm and k = 3.9. Using this model the predicted capacitance for the y junction trap is $C_Y \approx 15$ pF, and for the hexagon trap the capacitance is $C_{HEX} \approx 19$ pF .

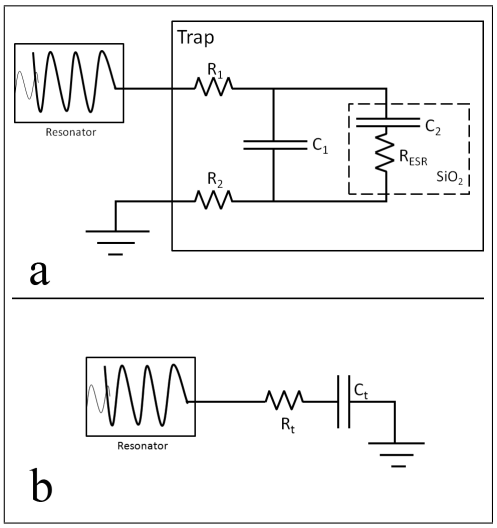

Figure 8.10: a) Circuit diagram of the ion trap. R_1 = rf electrode resistance, R_2 = static electrode resistance, C_1 = capacitance between rf electrode and vacuum separated static electrodes, C_2 = capacitance between the rf electrode and the handle layer, R_{ESR} = equivalent series resistance of the silicon dioxide. b) Equivalent circuit diagram in terms of the total resistance R_t and the total capacitance C_t.

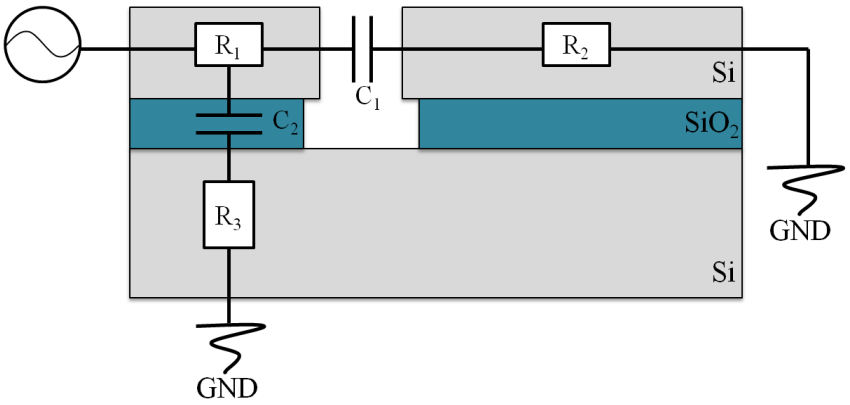

Figure 8.11: Diagram showing where the dominant sources of resistance and capacitance arise in the trap structure.

The resistances R_1, R_2 and R_3 are a combination of the deposited gold surface layer, the higher resistance silicon device layer and the silicon handle layer. The resistivity of evaporated gold is very dependant on the fabrication process but by making an estimate of the gold and silicon resistivities an estimation of the trap resistance can be found. The predicted resistance of the rf electrode is on the order of $R_Y \approx$ 10-15 Ω for the Y junction and $R_{HEX} \approx$ 5-10 Ω for the hexagon trap.

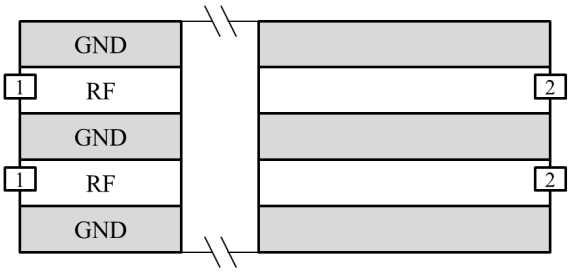

Figure 8.12: Top view of the Sonnet simulation model, the rf electrodes are 200 μm wide separated by a 190 μm static electrode with two 195 μm static electrodes either side of the rf electrodes. The electrodes are separated by a 5 μm gap. The edges of the static electrodes are automatically connected to ground.

8.6 EM simulations of RF loss in SOI structures

The following work (Sec. 8.6) was primarily undertaken by a visiting postdoctoral fellow Dr Luke Simkins and I contributed with some discussions. This demonstrates how the loss in the ion trap is coupled to the behaviour of the combined chip and resonator circuit. His work focuses on traps fabricated in a similar manner to the ones discussed in this chapter but in more general terms.

Two types of simulation were used, firstly an electromagnetic (EM) simulation of a microfabricated device. This can be used to model the materials and precise geometry of the trap, and can tell us how the trap will perform when altering material resistivity and drive frequency. Then using this information a discrete component simulation of the resonator with ion trap load was performed.

The EM simulation was performed using Sonnet lite[1], a free version of the Sonnet electromagnetic simulation software. Using a CAD style interface a 5 wire surface electrode trap structure, consisting of a metal top layer, a 10 μm silicon dioxide layer and finally a 600 μm silicon handle layer at the bottom, was simulated. The 30 μm device layer directly below the top gold layer was not included since the lite version limits the number of layers that can be used. The model has symmetric 200 μm wide rf electrodes separated by a 190 μm static electrode and with two 195 μm static electrodes either side of the rf rails. The electrodes are separated by 5 μm gaps, with the edges of the electrodes all connected with ground. The model geometry is shown in Fig. 8.12. RF power is applied to port 1, shown in Fig. 8.12, and exits via port 2, Sonnet calculates the attenuation between these two ports.

Sonnet will output a complex impedance that corresponds to the trap structure given

[1]Can be downloaded free from: www.sonnetsoftware.com

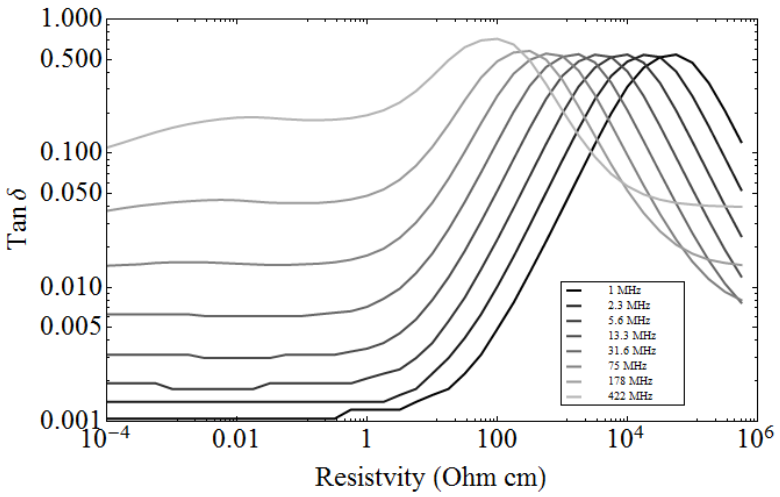

Figure 8.13: The loss tangent of the model chip, as substrate resistivity increases so does the loss, until very large resistivities where we see that it begins to drop. We also see that the loss increases with an increase in drive frequency.

by $Z_{trap} = ESR + iX$, where ESR is the equivalent series resistance through the substrate at a given frequency and X is the reactance. In Chap. 7 loss tangent was defined as $\tan\delta = \frac{ESR}{|X_c|}$, by defining the loss tangent to be across the whole substrate we can take the real part of Z_{trap} which is the ESR and the imaginary part of Z_{trap} which is equal to X_c and find the loss tangent of our SOI trap structure.

Figure 8.13 shows the loss tangent through the substrate as a function of the silicon resistivity and frequency. We can see that the loss increases with increasing resistivity up to $\approx$ 10 kΩcm, after this it begins to reduce. We can also see that the loss increases with an increase in frequency, suggesting that it is beneficial to operate traps with low drive frequencies.

If we assume the reactance from Z_{trap} is dominated by the capacitance it is now possible to calculate the capacitance for the trap, figures 8.14(a) and 8.14(b) show how the ESR and capacitance vary with a change in substrate resistivity and frequency. These figures all show a clear switch in behaviour between low and moderate resistivity substrates and high resistivity substrates. This can be explained because as the resistance of the silicon increases the impedance will increase, however when the resistivity becomes sufficiently high the silicon will act as an insulator. This reduces trap capacitance as now there is a much greater separation between the rf and ground. However this switch from conductor to insulator is not instantaneous and hence we see a slow change of behaviour of the loss tangent between $\rho = 100$ - 10^4 Ωcm (dependant on frequency), during which the $\tan\delta$ will peak, then as the capacitance begins to reduced the total rf loss through the substrate

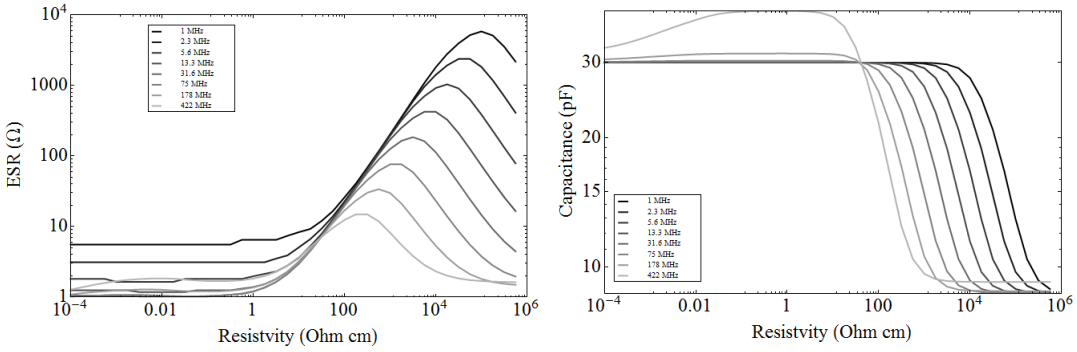

(a) (b)

Figure 8.14: a) The ESR of the trap with changing substrate resistivity and frequency. b) The change in capacitance with changing substrate resistivity and frequency.

will also decrease.

This suggests that either very low resistivity or very high resistivity should be used, but the worst case being somewhere in between. This means that either highly doped, low resistivity substrates, like degenerately doped silicon or insulating substrates like quartz should be used. The worst substrates to use would be those with moderate resistivity like undoped or lightly doped silicon.

Finally it is possible to calculate the power dissipated by the circuit. Dissipated power will cause heating and potential damage to the trap, ideally we want to maximise peak rf voltage whilst dissipating the minimum of power. Figure 8.15(a) shows the power required to apply $V_{rms} = 280$ V to the chip, again this worsens with increasing resistivity and frequency, for frequencies $\Omega/2\pi < 25$ MHz and resistivity $\rho < 0.1$ Ωcm this is less than 1 W of dissipation. However this increases to 3 W for $\Omega/2\pi \approx 50$ MHz. Again highlighting the benefit of operating at lower drive frequencies. If we now set the power dissipation to 1 W we can plot the peak voltage that can be applied, this is shown in Fig. 8.15(b).

8.6.1 Discrete component model

Using Spice a discrete component model of the trap whilst attached to the resonator could be simulated. This allows us to vary the chips resistance and capacitance to see the interplay between the chip and resonator. Figure 8.16a shows the circuit diagram for a resonator connected to a load, with the load corresponding the circuit in Fig. 8.16(b).

It is possible to obtain values for R, L, R_g, C_g and C_{sub} from Sonnet. Setting the substrate resistance, $R_{sub-g} = \infty$ and the electrode length to 2 cm then we can obtain the capacitance from the rf electrodes to surrounding electrodes which gives us $C_g = 8.8$

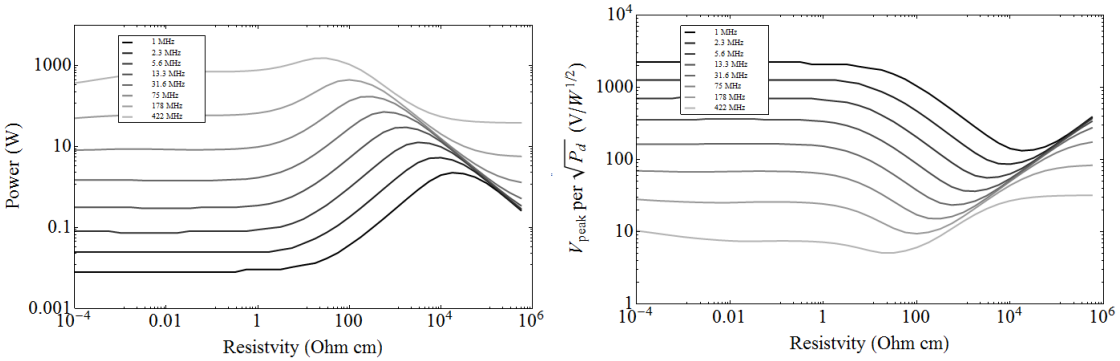

(a) (b)

Figure 8.15: a) The power dissipation of the trap with changing substrate resistivity and frequency. b) The peak rf voltage with a set power dissipation of 1 W with changing substrate resistance and frequency.

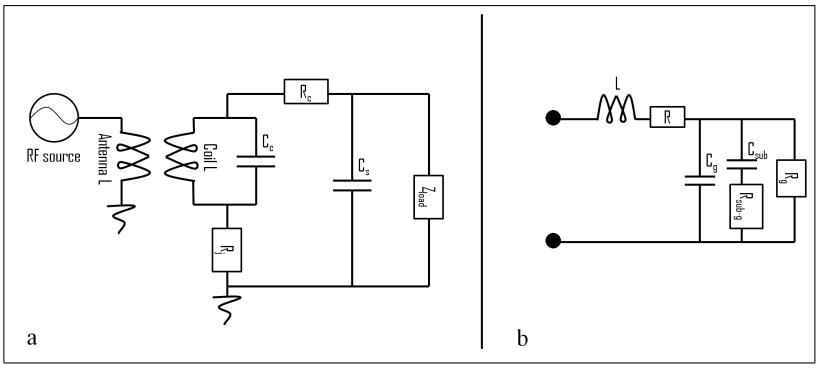

Figure 8.16: a) Circuit diagram for a resonator with attached load. The resistances and capacitances correspond to: R_c is the resistance of the resonator coil, C_c is the self capacitance of the coil, R_j is the resistance of the soldier joint connecting the coil to the grounded shield, C_s is the capacitance of the shield and Z_{load} is the impedance of the trap. b) Circuit diagram show a detailed breakdown of the load Z_{load}, L is the trap inductance, R in the trap resistance, C_g is the capacitance of the rf electrode to neighboring ground electrodes, C_{sub} is the capacitance from the electrode through the substrate, R_{sub-g} is the substrate resistivity and R_g is the resistivity from the rf electrode to ground.

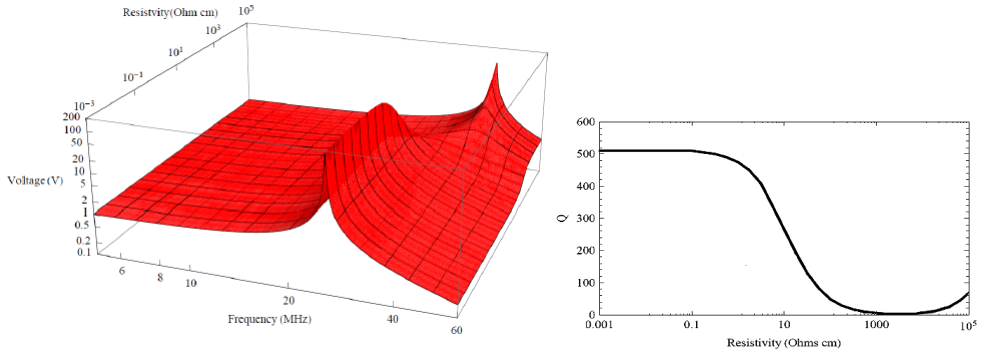

(a) (b)

Figure 8.17: a) The resonator response with changing substrate resistivity. b) Change in resonator Q with substrate resistivity.

pF. For $R_{sub-g} = 0$ we get the capacitance equal to the sum of C_g and C_{sub}, giving a $C_{sub} = 21.2$ pF. Sonnet will output an N-line model of the device giving values for an equivalent transmission line. From this and the values for C_g and C_{sub} we can find $R = 2.44\Omega$, $L = 5$ nH and $R_g = 10$ MΩ. This now allows us to varying R_{sub-g} the substrate resistance and see the interplay between the load and resonator. Figure 8.17(a) shows the voltage output from the resonator with a changing substrate resistivity, this shows two possible resonant frequencies, this is because of the two different capacitances, as the substrate moves from a conductor to an insulator the capacitance between the gold layer through the substrate to ground decreases. This transition is not instantaneous and in the region between conductor and insulator the resonator Q significantly drops, only beginning to recover at much higher resistivities. This is show in Fig. 8.17(b), the resonator Q starts high, then as resistivity is increased will fall until there is effectively no resonance, only beginning to recover at $\rho \approx 10^5$ Ωcm.

8.7 Fabrication mask

A fabrication photolithography mask needed to be drawn for the trap structures as well as the electrical testing pads. This was drawn using TurboCAD, with the trap structures taken directly from the simulation models. To increase the probability of successfully fabricating the traps, traps with both 5 μm and 7 μm electrode gaps were drawn. These were then repeated to fill the central region of the mask with a total of 32 5 μm gap traps and 32 7 μm gap traps. This leaves space for another 48 traps around the edge of the wafer. 12 of these spaces was used for the electrical testing structures, 24 for traps consisting of just the linear section from the Y junction and 12 hexagon lattice traps. The

finished mask can been seen in Fig. 8.18.

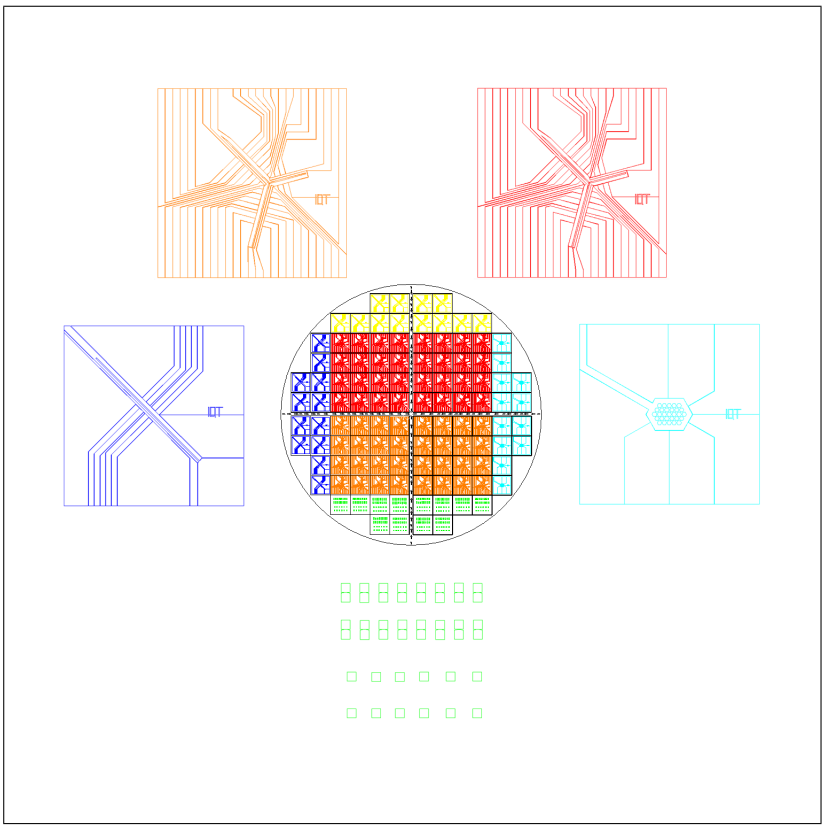

Figure 8.18: The full mask is shown in the center with the individual trap drawings surrounding it.

8.8 Trap fabrication

Most of the clean room work was carried out by Hwanjit Rattanasonti, a PhD student of the University of Southampton. Each step in the fabrication needed to be tested and optimised before a final trap could be fabricated.

8.8.1 Evaporation

The first steps of fabrication are evaporately depositing a thin adhesion layer of chromium followed by a layer of gold. This was deposited using an e-beam evaporator, depositing 40 nm of chromium followed by $\approx$ 500 nm of gold. This is then followed by depositing a layer of photoresist, AZ 9260, and exposing for 10 seconds. After development this patterns the electrode geometry onto the wafer and protects the electrodes from first the wet etches of both gold and chrome and then the DRIE used to segment the device layer into electrodes.

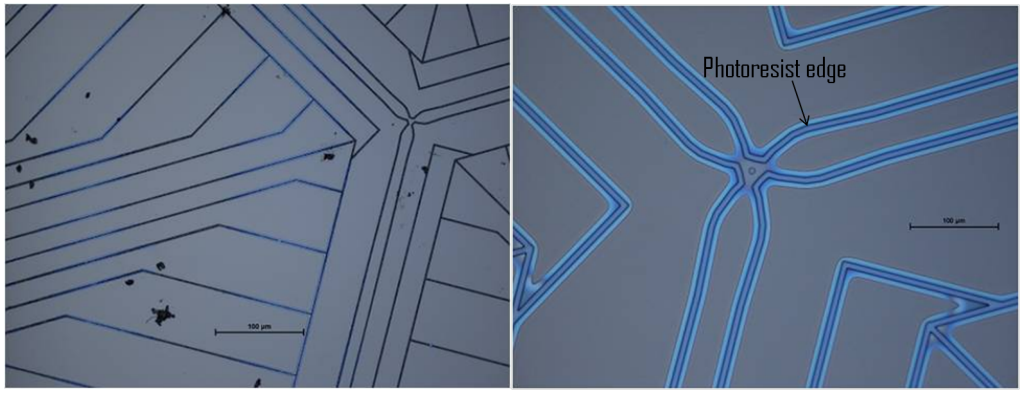

(a) (b)

Figure 8.19: a) An under etched trap the black lines correspond to partially etched gold and the blue is exposed chrome. b) A sample with over etched gold, the etching has removed gold from beneath the protective photoresist.

8.8.2 Metal etch

The gold etch was performed using potassium iodide and the chrome etch used ceric ammonium, these have an etch rate of 1 μm per minute.

Figures 8.19 shows optical microscope images of the first attempts at the gold and chrome etches. These show the initial steps of characterizing the gold etch, Fig. 8.19(a) shows trap features with an incomplete etch. Dark black lines correspond to partially etched gold trenches, whilst blue is exposed chrome. Figure 8.19(b) shows the result of over etching of the gold, because potassium iodide etches gold isotropically this results in an undercut beneath the photoresist. Additionally because the mask has several ion trap geometries non uniform etch rates also presented a problem. At trenches with widths of 5-7 μm the etch rate of the gold is fast however for the 2D ion trap lattice and rf testing structures there are large areas of gold that need to be etched. Potassium iodide in these areas becomes saturated and the etch rate decreases, this results in different etch times between the Y trap structures and the 2D lattices and rf test samples. Figure 8.20 shows a 2D ion trap lattice after a Au etch, the gold has only been partially removed from the hexagons.

By adjusting the recipe it was possible to minimise the undercut from the gold etch. Figure 8.21 shows the Y junction and 2D ion trap after this optimisation. However because of the same saturation effect the static electrodes did not fully etch close to the edge of the chip because they are close to large areas of exposed gold. This leaves the electrodes connected around the edge of the trap. To prevent this the etch time was increased as a

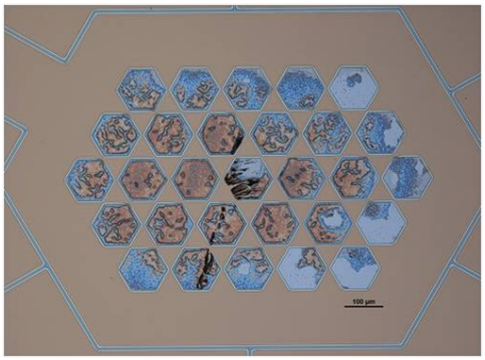

Figure 8.20: The gold has only been partially etched from the hexagons due to saturation of the etchant in these areas.

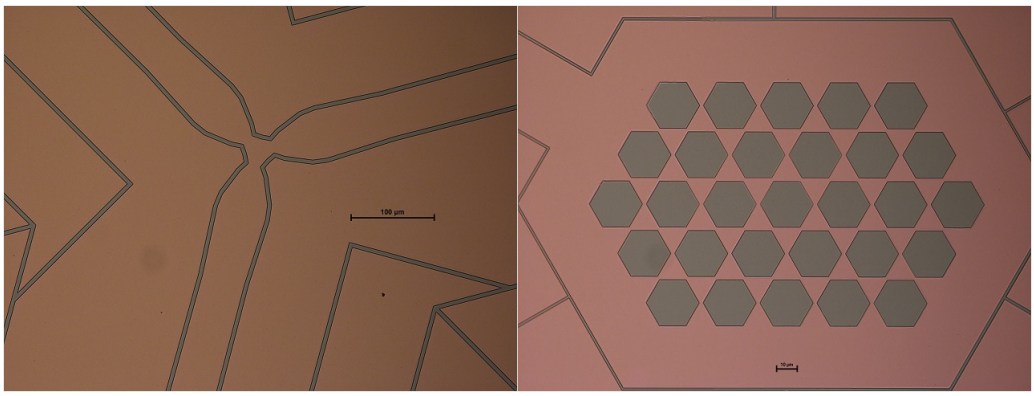

(a) (b)

Figure 8.21: a) The Y junction after the optimised Au and Cr etches. b) The 2D ion trap lattice after the optimised Au and Cr etches.

comprimise between over etching the electrode features and ensuring the gold was fully etches at the edge. Figure 8.22 shows this problem.

8.8.3 DRIE

After the metal etches a deep reactive ion etch segments the device layer into the individual electrodes. Initial etches on dummy wafers resulted in thin strands of the silicon being left at the bottom of the trench, known as grassing. To solve this problem the platten power of the DRIE was increase, this is a bias between the chamber walls and the sample holder. This bias is used to accelerate the ions towards the sample, by increasing this power it increases the number of ions that reach the bottom of the trench. This increases the directionality and speed of the etch, however it will also etch the photoresist faster. Figure 8.23 shows a grassy etch and an optimised trench. The deposited Au and the isotropic metal etch can be seen.

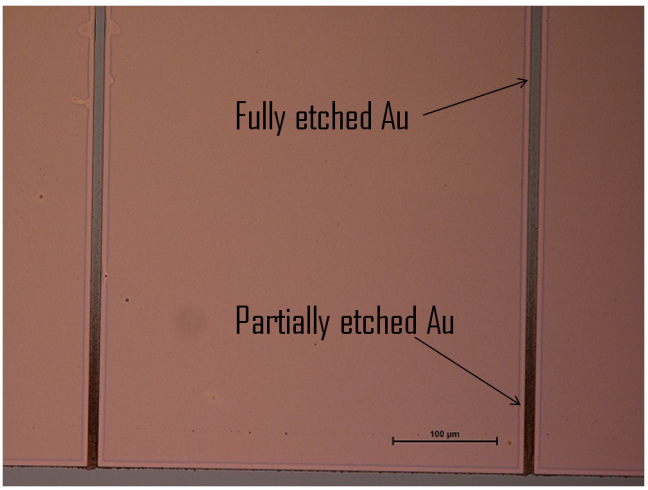

Figure 8.22: The gold has only been partially etched close to the edge of the trap because of the etchant becoming more saturated at large exposed areas of Au.

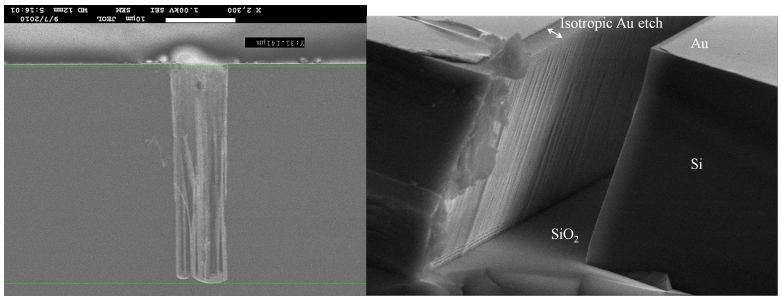

(a) (b)

Figure 8.23: a) An example of the initial DRIE, resulting in a an uneven bottom with thin pillars. b) An optimised DRIE.

8.8.4 Buffered hydrofluoric acid etch (BHF)

To expose the grounded handle layer and to hide any dielectrics a buffered HF etch is used to etch the silicon dioxide. This is an isotropic etch and etches beneath the silicon device layer. The SOI wafers have a 10 μm thick layer of SiO_2 and requires a long etch time. This isotropic BHF etch can is shown in Fig. 8.24. This etch was 100 min and shows how only 5-6 μm of the SiO_2 layer was removed. To expose the handle layer it requires an etch time of 150 minutes.

However after a 150 minute BHF etch the Au developed a pitted structure. Small holes form in the deposited gold layer, as shown in Fig. 8.25, the small black dots correspond to pits in the gold.

To reduce this effect the BHF was reduced into short etches. The chips were placed in the BHF for 10 minutes, after which they were removed and rinsed with deionised water.

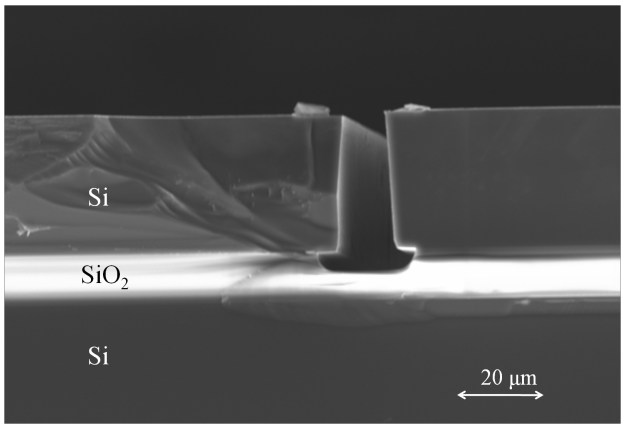

Figure 8.24: A 100 minute buffered HF etch has isotropically removed the silicon dioxide and etched ≈ 6 μm both laterally and down.

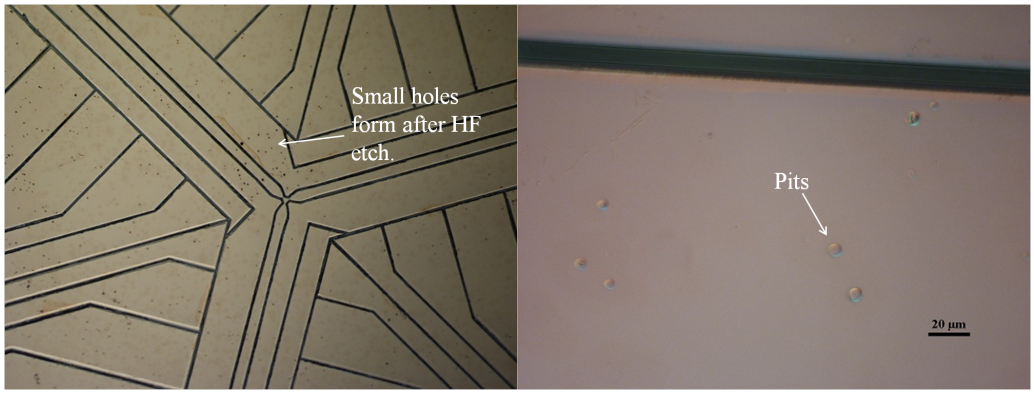

(a) (b)

Figure 8.25: a) A 150 minute buffered HF etch leaves the gold layer with small pits in the surface. b) High magnification view of an Au pit.

They were then placed back into the BHF. This processes was repeated until they have been etched for a total time of 120 minutes. Figure 8.26 shows the gold after the optimized BHF etch, this shows no sign of bubbles or damage to the gold. However this problem was still seen on some traps.

An SEM image after the BHF shows the sever undercut of the SiO_2, this forms a v shape and is most likely caused by the repeated short etches to the SiO_2, as shown in Fig. 8.27.

This is very beneficial for the electric breakdown of the devices as will be explained in Chap. 9, however this deep undercut is problematic for traps with narrow electrodes. This undercut can be so sever that it results in the full removal of all the buried oxide under narrow electrodes. Without this supportive oxide layer the electrode is left free hanging and will bend upwards, this stiction problem is shown in Fig. 8.28.

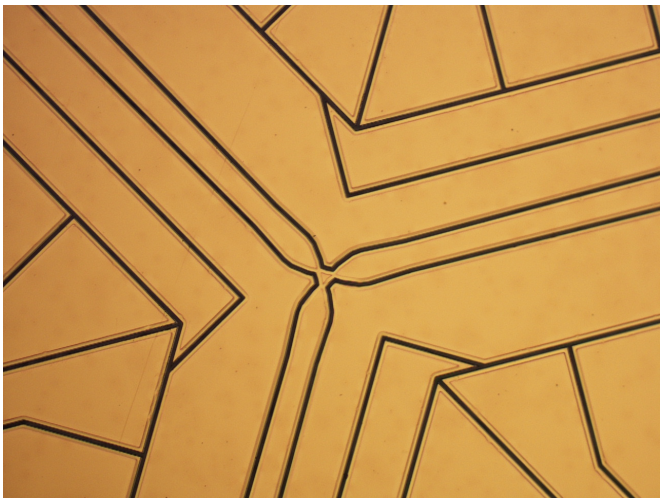

Figure 8.26: The trap after the optimized BHF etch, this shows no sign of bubbles.

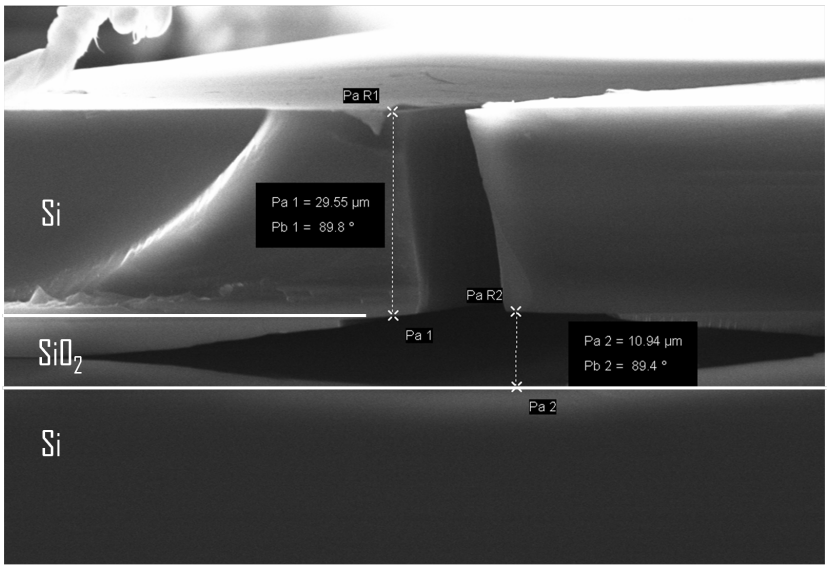

Figure 8.27: An SEM image of the SiO_2 undercut left after the optimised BHF etch.

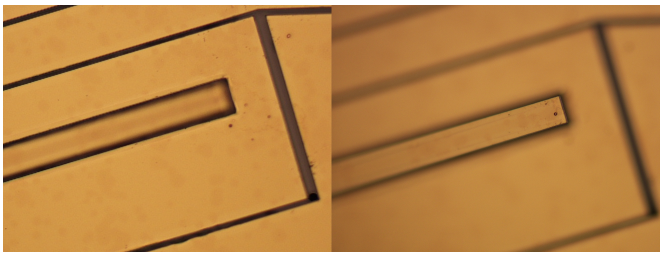

Figure 8.28: An example of stiction, the SiO_2 has been fully etched from beneath the central electrode resulting in it to bend upwards, as shown by the two different focuses for the electrode and trap surface.

Despite these problems it was possible to fabricate a small number of traps of each design, however the yield was low. SEM images of a finished hexagon lattice trap are

shown in Fig. 8.29. There is damage to one of the surrounding static electrodes, which can be seen in the left image. This is were the top layer of silicon has broken away from the buried silicon dioxide layer.

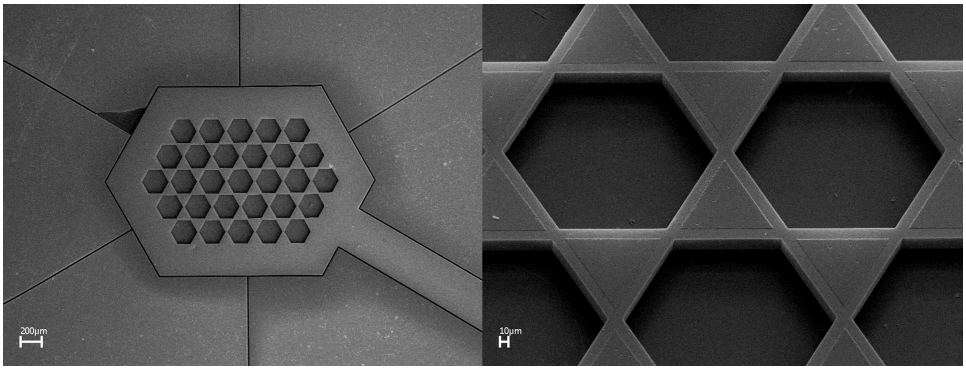

Figure 8.29: Two SEM images of a finished hexagon lattice. There is slight damage to one of the surrounding static electrodes which can be seen in the left image.

8.8.5 Addition processes and further work

The process just described was successful in producing a small number of traps that could be used for trapping and electrical testing. However the majority suffered from damaged gold or stiction because of the long BHF step. Electrical contact of the handle layer to the chip carrier is achieved by using a UHV compatible conductive glue. It was found that this bond would make electrical contact but with a large contact resistance, on the order of several kΩ. A possible reason for this is a native oxide layer developing on the exposed silicon during the time between fabrication and mounting. This large resistance would prevent high Q coupling of the resonator to the chip and in the case of the hexagon lattice traps potentially expose the ions to large areas of dielectric. A solution to both Au damage during the HF etch and the development of native oxide is to leave the metalization until after the HF etch. This was used by Britton *et al.* [37] in the fabrication of their traps. Alternatively a second evaporation stage can be used in the case of our traps. After the BHF of the SiO_2 the chips are then coated with another 50 nm of Cr and 500 nm of Au. This coats the areas of exposed handle layer, covers damaged Au and protects against native oxide build up. The back side is also coated to ensure good electrical contact with the UHV conductive glue. Figure 8.30 shows a hexagon trap mounted on a CPGA chip carrier, this chip has had a second evaporation of Cr and Au, coating the front and back of the chip. It is glued onto a stainless steel block to raise the chip surface above magnetic coils glued to the chip carrier, this ensures clear laser access across the chip surface. The

insert shows a microscope image of this trap after the second Cr and Au deposition. A hexagon on the bottom right has not been etched, this is because the initial gold layer was not fully removed in the initial wet etch stage. This defect however will not interfere with the operation of the other trap sites.

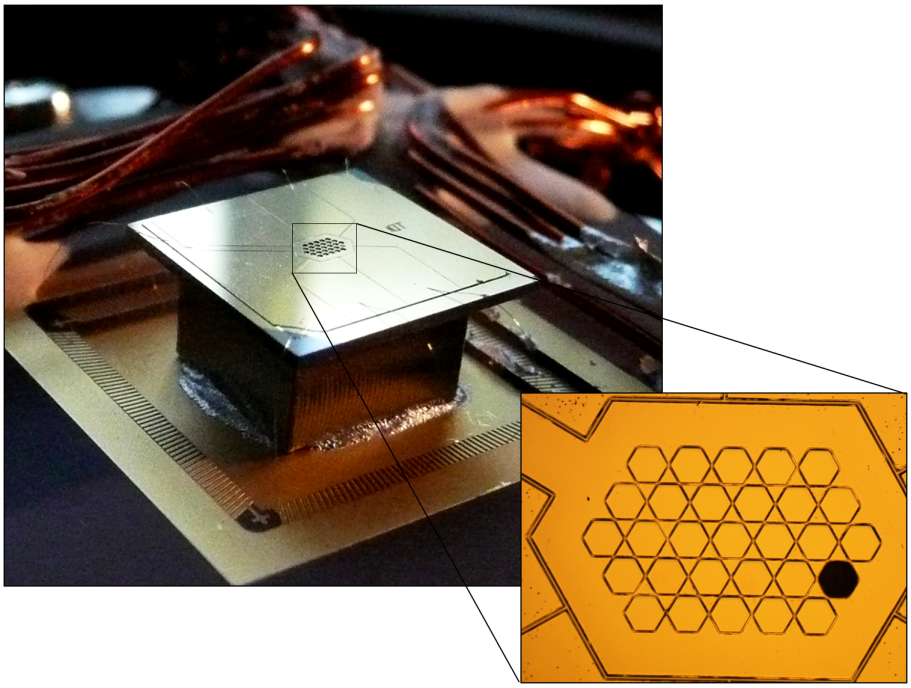

Figure 8.30: Photo of the hexagon trap mounted on a CPGA chip carrier. The chip is mounted on a stainless steel block to raise it above current carrying wires and ensure optical access. Also shown is a microscope image of the trap region, a defect in fabrication resulted in a hexagon in the bottom right not being etched, this should not impact trapping in the rest of the trap.

To prevent stiction of narrow electrodes the BHF etch has been abandoned and instead a combination of dry and wet etches is being developed. First 5 μm will be etched using a RIE, then etching the remaining 5 μm with a BHF solution. This should reduce the HF etch time so that it will not damage the Au and will reduce the lateral undercut that releases narrow electrodes.

8.9 Experiments in the 2D hexagon lattice trap

The 2D hexagon lattice trap was mounted and placed in vacuum in order to perform several experiments. Firstly to demonstrate trapping in a microfabricated ion trap array and to measure the ion heating rate. Additionally it should be possible to perform individual ion addressing in frequency space in two dimensions. Johanning *et al.* [109] demonstrate

individual addressing and coupling of the ions spin and motional states for ^{172}Yb in a linear string of ions in a magnetic field gradient. By producing a magnetic field across the ion string each ion will experience a unique Zeeman shift, allowing individual ion addressing in frequency space. This magnetic field also results in a state dependant force and allows coupling between the ion's spin and its motional state. This scheme lifts the degeneracy of the Zeeman-manifold so that the need for focusing optics becomes redundant; all the ions can be irradiated with only the resonant Zeeman splittings being addressed.

Individual ion addressing in 2D lattice traps is necessary to the implementation of quantum simulations, but due to the trap topology and ion location, optical addressing of individual ions is inherently problematic. By producing a magnetic field gradient across the trap such that the gradient in the y axis is much greater than the gradient along the x axis, $\partial B_y \gg \partial B_x$, then this should result in a unique Zeeman shift for each ion across the 2D ion trap array. This now allows individual ion addressing and state manipulation across a 2D ion trap lattice. To implement this on our hexagon trap two magnetic coils were glued to the CPGA chip carrier using ceramic paste, the assembly is shown in Fig. 8.31. The coils are made from Kapton coated copper wire, with the top coil containing 10 turns and to provide the strong magnetic field gradient ∂B_y, labeled strong coil. A perpendicular coil consisting of 5 turns provides the weaker x axis gradient ∂B_x and is labeled weak coil. These are connected to a power feedthrough on the vacuum system and are capable of carrying up to 10 amps.

A simulation of the magnetic field was performed using CPO. Four current carrying wires approximate the current loop, a contour plot of the magnetic field generated by the two loops is shown in Fig. 8.32.

The frequency difference between adjacent $^{172}Yb^{+}$ ion positions is given by [109]

$$\Delta f = \frac{g_j \mu_B \delta z \partial B}{h}. \tag{8.1}$$

Where g_j is the Landé g-factor and δz is the ion-ion separation. From this we can calculate that the frequency separation at adjacent ions along the weak axis for a weak coil current of 5A is $\delta f = 55$ kHz, approximately half that used by Johanning *et al.* This is limited by the maximum achievable strong magnetic field gradient. Figure 8.33(b) shows the magnetic field along three parallel ion trap lines, positioned at y = -260, 0, 260 μm, shown in Fig. 8.33(a). This corresponds to a strong coil current of 10 amps, the maximum current that can be supplied without risk of damage. It can be seen that the magnetic fields begin to overlap which would result in either ions seeing the same magnetic field or with only very small δf's. This however can be significantly improved if pulsed currents are used, this

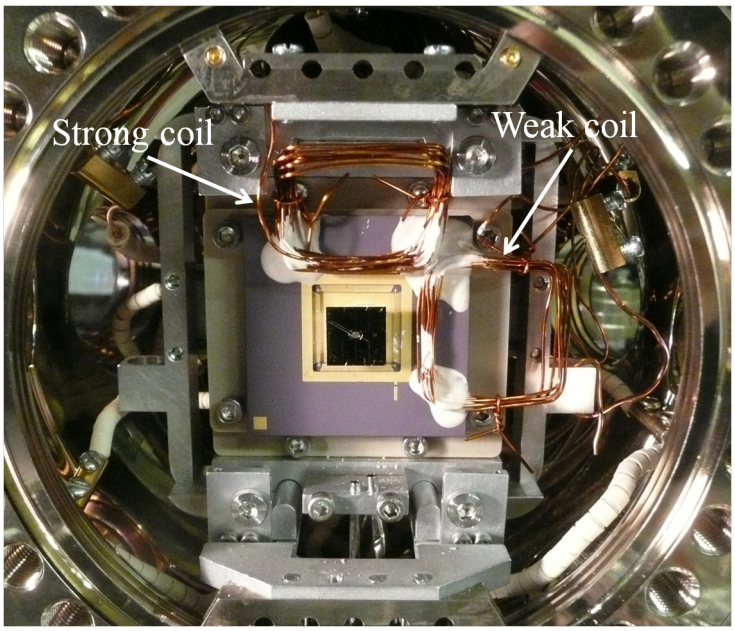

Figure 8.31: Photo of the hexagon trap mounted on a CPGA chip carrier inside the vacuum system. The two magnetic field coils can be seen glued to the CPGA chip carrier, they are labeled strong coil and weak coil.

would allow brief but very large currents to be applied without the risk of damage.

Despite the limited magnetic field achievable this setup should be sufficient to lift the degeneracy of a 5 trap area, allowing individual addressing of all 5 ions with minimal unwanted excitations of neighboring ions. However to effectively couple the ions spin and motional states significantly larger magnetic field gradients will be required [110].

8.10 Y junction electrical characteristics

Once the traps had been fabricated it is necessary to characterise the chip's electrical properties; rf capacitance and rf electrode resistance. To measure this a Y junction was mounted onto a CPGA chip carrier. All the static voltage electrodes were wire bonded to the surrounding bond pads and all the bond pads connected together. There is a gold surround outside of the chip carrier bond pads and the rf electrode was wire bonded to this surround. The handle layer of the chip was glued to the gold base of the chip carrier using the conductive glue, this will result in a large contact resistance between the handle layer and chip carrier as discussed earlier, however we are only concerned with capacitance so a large resistance does not matter. Using a capacitometer the capacitance between the rf Y electrode and rf ground (surrounding static electrodes and handle layer) was measured to be 14 $\pm$ 1 pF. This is consistent with the predicted capacitance of 15 pF discussed in

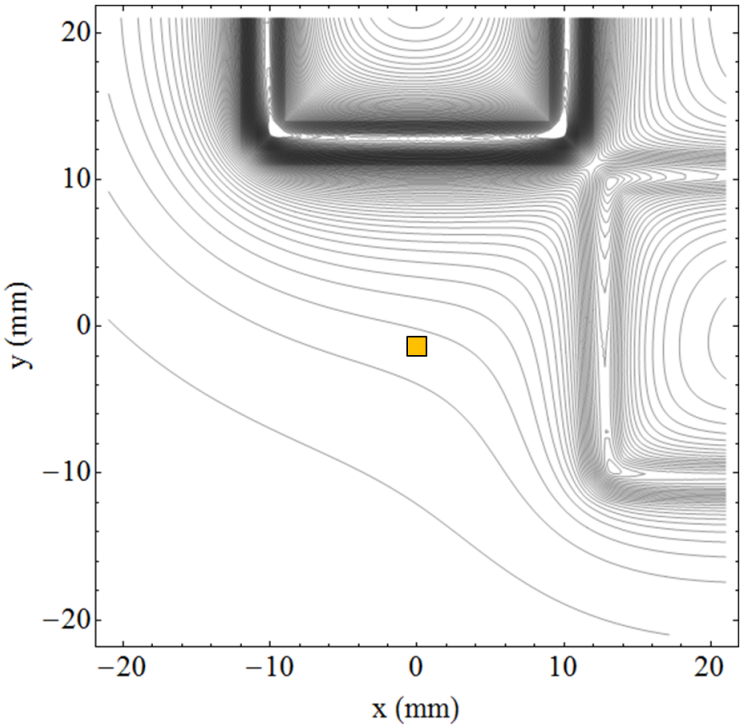

Figure 8.32: A contour plot of the magnetic field lines from the two coils, the trap is marked by an orange square in the center. The strong coil has a current of 10 amps while the weak coil has a current of 5 amps, the contours are spaced by 0.2 mT.

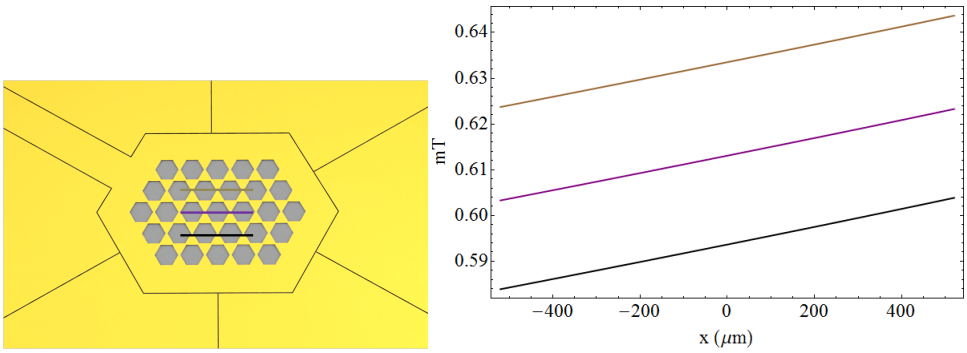

(a) (b)

Figure 8.33: a) Solidworks drawing of the hexagon trap, the three lines correspond to the lines plotted in Fig. 8.33b. b)The magnetic field along horizontal ion trap lines at y = -260 μm (black), y = 0 μm (purple), and y = 260 μm (brown).

Sec. 8.5.

Next the resistance of the rf electrode was measured at different points along the geometry. The Y electrode is split at the bottom linear section to allow electrical connection to the central static electrode. This results in two different path lengths for the rf electrode and therefor the resistance was measured between the wire bond at point A in Fig. 8.34, and both ends of the bottom linear section labeled B and C. The resistance from point A→B was measured to be $R_{AB} = 10 \pm 1\ \Omega$, the resistance from points A→C was measured to be $R_{AC} = 15 \pm 1\ \Omega$, again consistent with the predicted resistance from Sec. 8.5.

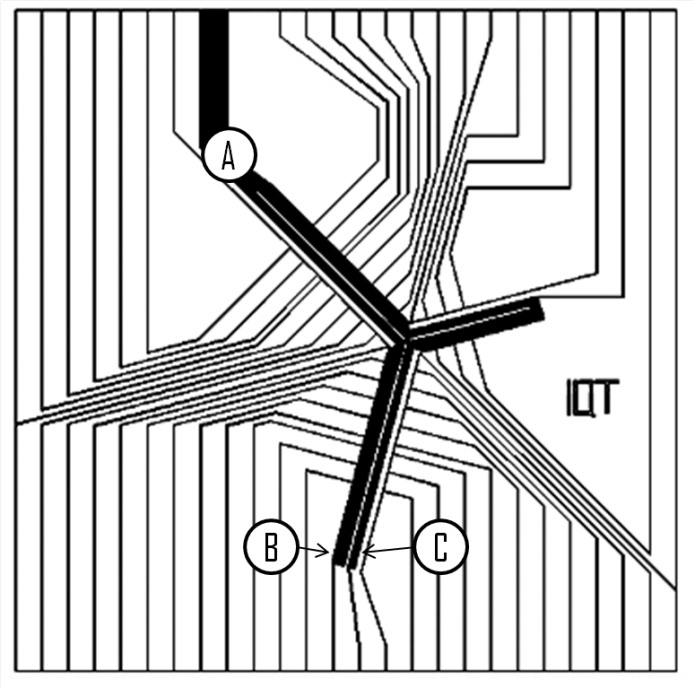

Figure 8.34: The points between which the resistance was measured between.

There will be a phase difference between the two arms of the Y junction as a result of the differing path lengths and different impedances. First by looking at the difference in path length the phase difference is simply given by:

$$\phi_{path} = 360\frac{\Delta d}{\lambda} \tag{8.2}$$

Where Δd is the additional electrode path length of ≈ 4 mm and λ is the rf wavelength, which for $\Omega/2\pi = 45$ MHz is ≈ 6.7 m. This yields a path length phase difference of $\phi_{path} \approx 0.22°$.

An additional phase different will result from the differing path impedances. Assuming that the electrodes inductance in negligible then the phase difference between points A

to B and A to C can be calculated using the standard equation for the phase angle of an impedance:

$$\phi_{impedance} = \arctan\left(\frac{X}{R}\right) \tag{8.3}$$

Where X is the reactance of the electrode capacitance, given by X = $\frac{-1}{\Omega C}$ and R is the electrode resistance. Assuming that the total electrode capacitance is divided between the two paths as $C_{AB} \approx \frac{1}{3}C_{total}$ and $C_{AC} \approx \frac{2}{3}C_{total}$ and that the electrodes can be modeled as discrete components the phase difference as a result of impedance in the lower trapping region is $\phi_{impedance} = 1.5°$. This gives a total rf phase difference between there two electrodes in the bottom linear section of $\phi_{total} \approx 1.7°$.

In Ref. [111] the effect of a phase difference between trap electrodes on the minimum ion temperature has been discussed. They show that the micromotion resultant from a phase difference of 1° increases the minimum ion temperature from mK to the order of 1 K. Furthering the problem it is impossible to compensate for this micromotion in the standard way of applying static voltages to neighboring electrodes. This demonstrates that in building ion trap junctions considerable care must be taken to ensure similar path lengths and electrode impedances. The phase difference from the different rf electrodes renders this geometry unfeasible for successful adiabatic shuttling operations. In future fabrications buried wires will allow electrical contact to be made without breaking the rf electrode and should eliminate this problem. Subsequently to writing this section I found a similar derivation by J. Britton in Ref. [112] which reaches a similar conclusion.

A simple solution would be to wire bonding between points B and C, the resistance of the bond joint and wire would be negligible and so provide equal paths for rf. However now there is the potential for phase mismatch at the junction, the center of the junction consists of three rf electrodes, two share equal path length but the third opposite electrode has traveled significantly longer. Performing similar phase calculations for path length and impendence the phase mismatch between the electrodes would be of the order $\phi_{junc} \approx 0.35°$.

What this shows is that for junctions made from high impedance materials such as thin metals or semiconductors, the phase shift between rf electrodes has the potential to seriously inhibit performance. This may require significant changes away from current design, where rf electrodes snake around the trap array and resulting in inevitable phase mismatch.

Phase shifts resultant from the electrodes impedance could be reduced by using thick gold electrodes, with Au electrodes of several micrometers commonly used in neutral atom

chips [113]. Additionally reducing capacitance by using insulating substrates, both reduces phase shift but also aids resonator coupling.

8.11 Cantilevered gold electrode trap

A silicon on insulator design, whilst successful in removing the problem of exposed dielectrics also suffers from several limitations. Electrical connections can only be made on the surface, making isolated island control electrodes impossible. By positioning control electrodes directly beneath the ion, between the rf rails, reduces the voltage required to perform fast combination and separation operations [114] but also reduces the number electrodes required. For large scale ion trap arrays conducting paths on the surface would quickly run out of space, as can been seen from Fig. 8.34 where we are already reaching the limit to the number of electrodes that can be fit onto a chip. For these reasons an alternative fabrication was designed along side the SOI Y trap. The aim of this design was to use the same rf geometry but use central control electrodes, as well as ensuring all dielectrics remain shielded from the ion.

This process is significantly more involved than the SOI traps since it is required to both shield dielectrics from the ion and provide buried wires for static electrodes. To fabricate the trap but also shield the ion for any insulators a cantilevered gold electrode structure was devised. Using several layers of electroforming, electrodes that cantilever over each other can be constructed. This process of layering photoresist and performing electroforming has been demonstrate to build complex 3D objects from nickel successfully [115]. The fabrication guide can be seen in Fig. 8.35, this shows how by layering photoresist cantilevered gold electrodes can be built.

First a quartz wafer is patterned with photoresist, then using a DRIE trenches are etched for buried wires. An adhesion layer of chromium and a gold seed layer are evaporated on to the substrate. The photoresist is removed and the gold in the trenches is electroplated, filling the trench depth with Au. The wafer is then planerised using a chemical mechanical polish (CMP). Next a plasma enhanced chemical vapor deposition (PECVP) deposits a silicon dioxide layer, 0.5-1 μm thick on top of the quartz wafer. A layer of photoresist is then deposited and patterned exposing the SiO_2 in areas where connecting through holes are to be etched. To avoid lateral etching of the silicon dioxide a DRIE can be used to expose the buried gold. Once the SiO_2 etch has been performed the through holes are filled by another electroplating step, bringing the gold up to the level of the SiO_2. Next a photoresist mold is formed for the first level of the rf cantilevers. After the first

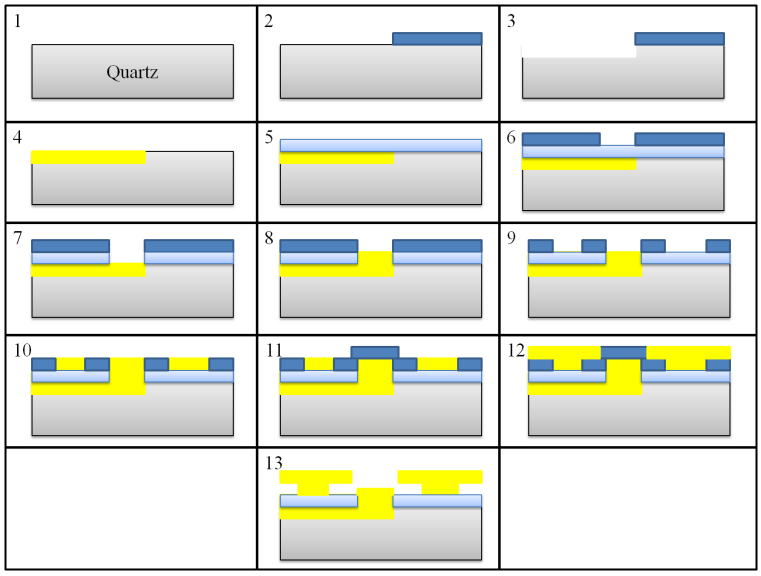

Figure 8.35: Process guide for the cantilevered Au trap. 1) Quartz wafer. 2) Photoresist is deposited and developed. 3) A DRIE etches trenches into the quartz wafer. 4) A Cr adhesion layer and Au seed layer are evaporated onto the wafer, this is followed by Au electroplating, filling the trench to the level of the quartz wafer. 5) A CMP planerises the wafer surface followed by a PECVD which deposits a layer of SiO_2. 6) A layer of photoresist is deposited, exposed and developed. 7) A DRIE removes the exposed SiO_2. 8) Au electroplating fills the through hole. 9) The photoresist is stripped and another layer is deposited and exposed. 10-12) Au is electroplated using the photoresist as a mold, this is repeated to build the full trap. 13) The photoresist is removed leaving the cantilevered Au electrodes.

level of gold has been electroplated another layer of photoresist is deposited, patterned and electroplated. This process is repeated to construct a cantilevered Au structure.

8.11.1 Progress

Initial progress on this fabrication has taken place, with all clean room work being performed by David Brown, a PhD student at the California Institute of Technology. First measurements of electrical breakdown across quartz needed to taken. This is to ensure that a final trap will be capable of having large rf voltages applied without breakdown between electrodes. The results of these electrical tests are discussed in Chap. 9. The first fabrication mask has been draw and is shown in Fig. 8.36, the buried Au tracks are shown in blue with the rf electrode outlined in black, this is not included on the actual mask but is included to shown the relative position of the buried wires. The buried wires narrow as

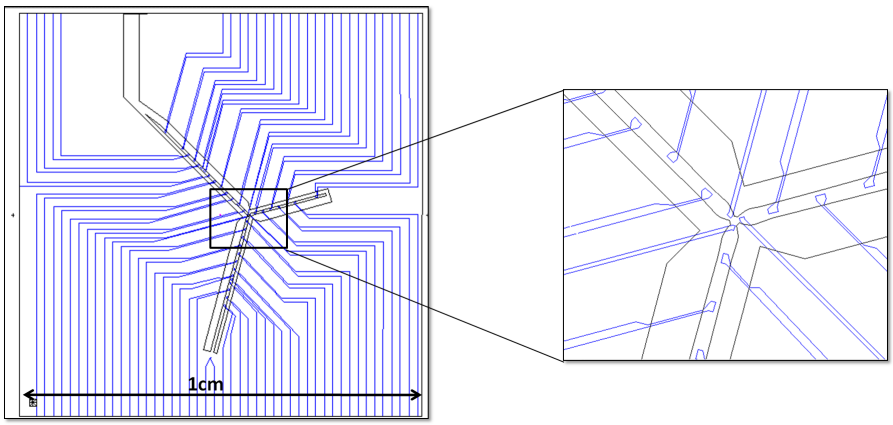

Figure 8.36: Mask for the buried wires, blue lines outline the buried Au tracks, the black line shows where the rf electrode will be placed but is not drawn on the actual mask. Insert shows a close up of the junction region.

they pass beneath the rf electrode. This is to reduce potential capacitance between these wires and the rf electrode.

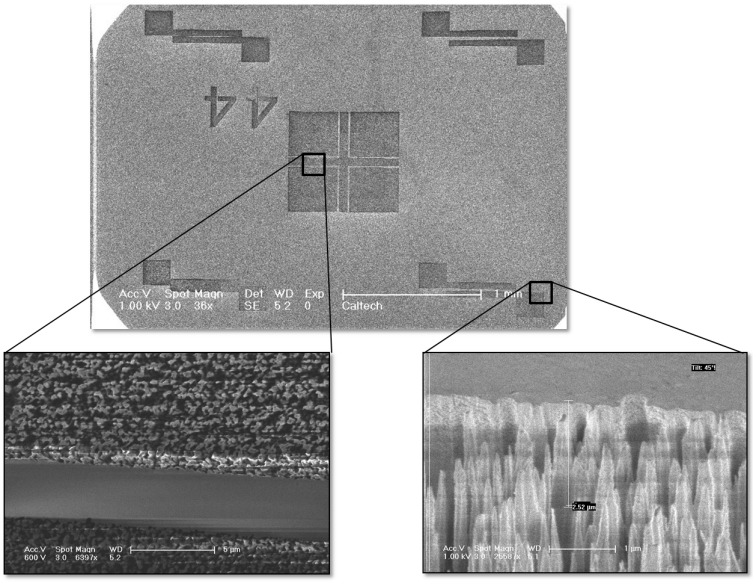

Figure 8.37: Three SEM images of a test DRIE run. This is to optimise the etch process for the quartz wafer. The two close ups show similar grassing problems that was found with the SOI fabrication.

Work has also been carried out to optimise the DRIE used to etch the buried Au trenches in the quartz wafer. Figure 8.37 shows three SEM images of a DRIE performed on a quartz substrate. This shows a similar grassing problem that was observed in the SOI fabrication.

Chapter 9

Electrical breakdown measurements

1.21 JIGAWATTS!

- Emmett Brown - Back to the Future

9.1 Introduction

Significant progress has been made in building microelectromechanical system (MEMS) devices whose operation relies on the application of electrostatic fields. With the increasing popularity of such devices the inevitable reduction of size and requirement for greater performance has led to the application of increasingly large electric field gradients. Most commonly, such devices operate within a dielectric gas, where electrical breakdown is governed by Paschen's law [116]. This has been the focus of detailed research [117, 118, 119, 120, 121], resulting in an underlying understanding of the physical process for breakdown between electrodes separated by several micrometers in gas.

However within high vacuum the mean free path of electrons and molecules is much greater than the electrode separation and Paschen's law can no longer be used to explain the breakdown process. Instead electrical breakdown in high vacuum occurs along the surface of the insulator, often referred to as surface flashover. This is of interest for several applications, such as MEMS nanoelectrospray thruster arrays for spacecraft [122, 123, 124, 125, 126], spacecraft solar arrays [127, 128, 129] and more recently within MEMS ion trap arrays [75].

There are several reasons why accurately predicting the flashover voltage for micrometer separations is beneficial in the design of ion trap arrays. Exposed dielectric gaps

between electrodes are susceptible to collecting stray charges and with no direct path to ground these charges result in a slowly varying static field, impeding the performance of the trap. Bringing the electrodes close minimises exposed areas, or the use of shielded dielectrics can totally eliminate any stray charges from the line of sight of the ion [130]. However these methods result in high voltage electrodes separated by only several micrometers from ground. To ensure sufficient trap depth whilst keeping the electric field gradient low, the ion-electrode distances are kept small, on the order of 30-80 μm. Such small ion-electrode separations leave the ion susceptible to heating from the electrode surface and limiting the usefulness for quantum information processing [131]. Increasing the peak rf voltage would allow geometries with greater ion-electrode separation whilst maintaining sufficient trap depth and ion control. To this end we perform measurements of rf and static surface flashover for electrodes fabricated in a manner similar to ion trap arrays, with electrode gaps ranging from 3-20 μm. This was necessary as to date, there is only a limited amount of data for flashover across micrometer spaced electrodes [122, 123], insufficient to accurately predict the flashover voltage.

9.2 Background and theory

The process through which flashover occurs is split into three distinct stages [132], shown schematically in Fig. 9.1. The first stage, which lasts for a few nanoseconds, involves electrons being emitted from the triple point at which the conductor, dielectric and vacuum meet. Microscopic defects at this interface amplify the electric field and allow electrons to tunnel from the cathode into the vacuum through field emission. The electrons are emitted from the triple point with an energy, A_0, on the order of 1 eV [133] and are accelerated by the electric field towards the anode, with some electrons hitting the insulator surface. Through secondary emission these collisions release more electrons into the electrode gap, which in turn are accelerated and strike the surface and release further electrons. These initial electron collisions leave the surface with a slight positive charge and so attract more electrons to the surface increasing the positive surface charge density. As the positive surface charge increases, the distance traveled by the electrons before impact reduces, only allowing the electron to be accelerated to increasingly lower energies. As a result the number of secondary electrons released on impact reduces until equilibrium is reached, at which point, on average an electron impact with the surface will only release one electron. This electron impact energy is denoted by A_1 and is on the order of a few tens of eV [134]. This process is known as secondary electron emission avalanche (SEEA) and is

characterised by a fast current growth between the electrodes over several nanoseconds to a value on the order of 10-100 mA [133].

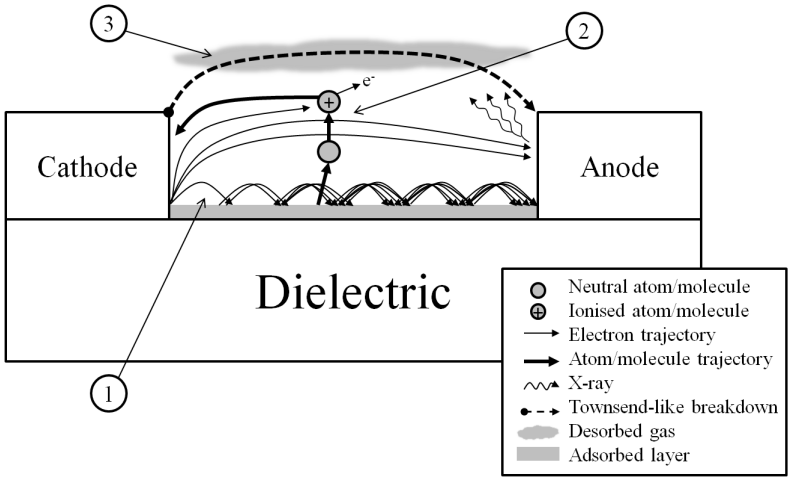

Figure 9.1: Diagram of the development of the three stages leading to surface flashover. 1) Secondary electron emission avalanche across the dielectric surface. 2) Gas desorption leading to charge collection at the cathode and amplifying the electric field near the triple point. 3) Townsend-like electric discharge through a desorbed gas layer above the dielectric surface.

The second stage is a relatively slow (few hundred nanoseconds) current amplification. Neutral and ionised atoms and molecules are desorbed from the surface by electron impact desorption. These particles are released from the surface with a velocity, v_0, of several thousand metres per second and will either escape into the vacuum or, if not already charged, are ionised by passing electrons. Electrons emitted above the SEEA layer are shielded from the positive surface charge and can be accelerated sufficiently to ionise neutral atoms and molecules. Once ionised these particles will then accelerate towards the cathode were a layer of positive charge collects. This amplifies the electric field at the triple point and increases electron emission. This positive feedback amplifies the current between the electrodes to approximately an ampere [133]. At this point sufficient gas desorption has taken place that the local pressure in the electrode gap allows the final stage of flashover to occur, a Townsend-like breakdown through the desorbed gas layer [133].

A. Pillai and R. Hackam derived an equation for the flashover voltage and it is given by [134]

$$V_b = \left[\frac{dM_{cr}A_1v_0e}{2\epsilon_0\gamma v_e \tan\theta}\right]^{\frac{1}{2}} \tag{9.1}$$

where d is the electrode separation, M_{cr} is the number of desorbed molecules per m^2 at

the point of flashover, A_1 is the electron impact energy, v_0 is the molecule velocity, e is the electron charge, ϵ_0 is the permittivity of free space, γ is the desorption efficiency, v_e is the electron velocity given by $v_e = 5.94 \times 10^5 \sqrt{A_1}$ ms^{-1} [134] and θ is the electron emission angle in degrees.

The emission angle is the angle that electrons are emitted from the triple point once SEEA is at equilibrium. This is a result of the parallel and perpendicular electric fields and is given by $\tan\theta = E_\perp / E_\parallel$. $E_\perp$ is a function of the parallel electric field and given by [134],

$$E_\parallel = E_\perp \left[\frac{1}{2} \left(\frac{A_1}{A_0} - 1 \right) \right]^{\frac{1}{2}} \tag{9.2}$$

hence the emission angle can be written as a function of electron energies,

$$\tan\theta = \frac{E_\perp}{E_\parallel} = \left[\frac{2A_0}{(A_1 - A_0)} \right]^{\frac{1}{2}}. \tag{9.3}$$

The angle θ is now given by A_0 which is generally assumed to be ≈ 1 eV [133, 135] and A_1 which will vary depending on the dielectric used. For quartz A_1 has been measured to be 30 eV [136], yielding a emission angle of $\theta = 14.7°$.

We can qualitatively estimate the velocity of a neutral particle by estimating both the mass and the energy with which it was released. By performing emission spectroscopy during surface flashover the dominant gas species have been observed to be hydrogen and carbon [137]. The energy with which these atoms are released will follow a distribution but they will have a typical energy on the order of an electron volt [138]. This puts the range of atom velocities from several to tens of thousands of metres per second, this is consistent when comparing to velocities found in literature which are in the range of $1.5 - 8 \times 10^3$ ms^{-1} [133, 135, 136].

M_{cr} is the number of desorbed molecules per m^2 at the point of Townsend breakdown through the desorbed gas layer. This can be thought of as the minimum density of molecules required to allow a Townsend breakdown to occur. This is calculated by finding the product between the gas density, N_d, and the electrode separation [136],

$$M_{cr} = N_d d \tag{9.4}$$

where

$$N_d = \frac{2E_\parallel^2 \gamma \epsilon_0 v_e \tan\theta}{e v_0 A_1}.$$

From this A. Pillai and R. Hackam found that the amount of gas desorbed was in the range of $1.4 - 3.5 \times 10^{22}$ molecules m^{-2} [136], consistent with earlier work and suggesting a local pressure between the electrodes of 50-100 Torr [139]. However later work by A.

Neuber *et al.* predicted the current behavior over the second and third stages of flashover and allowed a measurement of gas desorbed during this time [133]. They found, for their experiment, the number of molecules desorbed was 8.6×10^{19} molecules m^{-2} with a local pressure of ≈ 1 Torr, significantly lower than previously reported [133].

Despite this large disparity there is some agreement on the desorption efficiency, with A. Avdienko and M. Malev [139] and A. Neuber *et al.* [133] reporting a $\gamma \approx 100$ with A. Pillai and R. Hackam using a desorption efficiency on the order of $\gamma = 10$ [136]. However here their also remains a large margin of error, with R. Anderson and J. Brainard presenting a desorption efficiency as low as 0.03 [135]. As a result the predicted flashover voltage can range over several orders of magnitude depending on which values of M_{cr}, γ and v_0 are chosen.

It is likely that both the amount of gas required for flashover and the efficiency with which atoms and molecules are ejected is highly dependant on experimental conditions, such as: sample history, cleanliness and electrode geometry. As a result, "correct" values for these constants with regards to the individual experiment are unlikely to be found in literature and must be measured for the experiment taking place. Within our experiment it is not possible to measure any of these properties directly and so it is more useful to redefine these parameters as a single constant, defined as

$$\varphi = \frac{v_0 M_{cr} A_1}{\gamma v_e \tan\theta},$$

Equ.9.1 is now given by,

$$V_b = \left[\frac{\varphi de}{2\epsilon_0}\right]^{\frac{1}{2}}. \tag{9.5}$$

By comparing Equ. 9.5 to experimental results we can find a value of φ. Whilst this does not inform us of the individual value of M_{cr}, γ, v_0 or A_1 (when unknown) it can be used to compare measurements between dc and rf and between different fabrication processes and materials.

To examine this further we performed measurement of surface flashover across gaps of between 3 and 15 μm on both a polished quartz substrate and on a silicon on insulator trap where the electrode is separated from a ground plate by a layer of silicon dioxide. This was performed for both static and oscillating bipolar waveforms. It is expected that the voltage at which flashover initiates for both static and rf voltages will be the same since the electrodes are both small compared to the rf wavelength and the oscillation period is long compared to the prebreakdown time delay, $\tau \approx 1$ ns [135], this is the time for feedback mechanisms to enhance the electric field between the electrodes and for sufficient gas

desorption to take place to allow flashover. Despite this however, unexpectedly low flashover voltages at radio frequencies have been observed [34]. Here two cantilevers separated by 4 μm of aluminium gallium arsenide (AlGaAs) maintained a static hold-off voltage of up to 70 V without flashover occurring, however flashover at a peak voltage of 11 V was observed when applying an rf voltage at 14.75 MHz [34]. This is inconsistent with the current understanding of flashover and potentially limiting for ion trap development.

9.2.1 Ion trapping considerations

There are three stages to surface flashover, first an initiation stage which is followed by a development stage and a final stage, consisting of discharge through gas desorbed from the insulators surface. The initiation of flashover develops from the triple point where the conductor, insulator and vacuum meet. Electron emission processes at this point provide the initial stage of flashover. There are several processes through which this initial electron emission can take place, but it is generally field emission. Though for ion trapping the use of UV and in some cases VUV laser beams provides a source of electrons from the photoelectric effect. For photoemission to occur a photon must have enough energy to overcome the electrons work function such that $\frac{hc}{\lambda} > e\Phi$, where h is planks constant, c is the speed of light, λ is the wavelength of light, e is the electron charge and Φ is the materials work function. However the workfunction is reduced in the case of an electric field, with the effective work function now being given by [140]

$$\Phi_{eff} = \Phi - \sqrt{\frac{e^3 E}{4\pi\epsilon_0}}, \tag{9.6}$$

where E is the electric field. For example, the workfunction of silicon is $\approx$ 4.05 eV corresponding to a wavelength of $\approx$ 300 nm, however when an electric field is applied across the sample the work function will decrease and allow photons of lower energy to free electrons from the surface of the material, Fig. 9.2 shows how the effective work function varies with applied electric field, and the corresponding photon wavelength.

This maybe an important consideration when operating ion traps, especially in the early stages of optical alignment. At this point it is common to irradiate the trap surface with high intensity laser beams. These may prove a good source of electron emission which will lead to flashover between trap electrodes.

It is also important to note that while the typical electric field in an ion trap is on the order of 40 MVm^{-1}, for 10 μm separation at 200 V, that electric field at the triple point will be significantly enhanced from microscopic protrusions and positive charge collection.

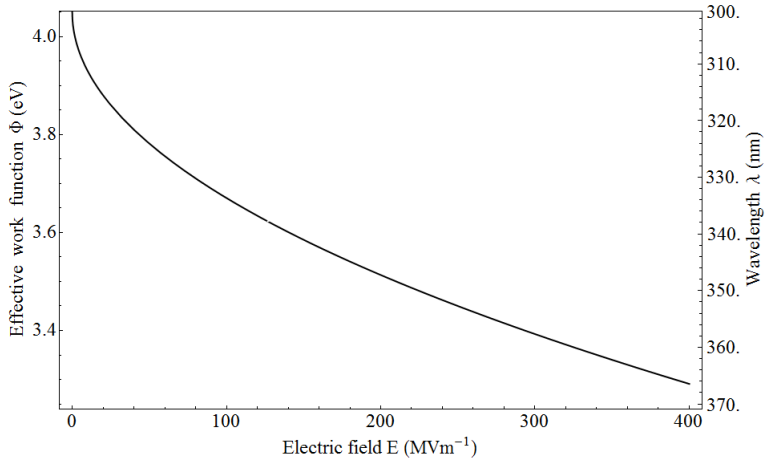

Figure 9.2: The effective work function as a function of electric field, also showing the corresponding wavelengths required for photon emission.

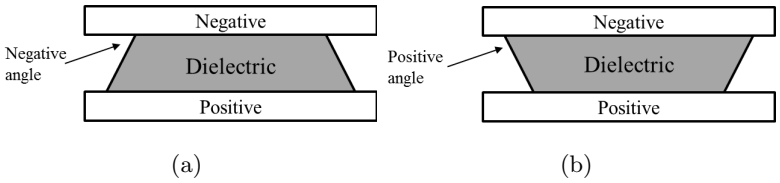

Figure 9.3: a) Negatively angled insulator. b) Positively angled insulator.

9.2.2 Effects of geometry

As discussed the point at which breakdown begins is the triple point where the vacuum, dielectric and conductor meet. This can be made worse by the physical geometry of the intersection. Small defects close to this point have the effect of greatly increasing the electric field at the intersection, ultimately reducing the voltage that can be applied to the electrode [141]. By ensuring smooth transitions between the conductor and insulator the breakdown voltage can be increased. This should not be too challenging using MEMS, where selective wet etches leave smooth rounded edges.

Additionally the breakdown electric field can be increased by modifying the angle where the insulator and conductor meet. Introducing an angle of 45° will result in higher flashover voltages, with positive angles slightly better than negatively angled walls. The insulator angles are shown in Fig. 9.3. It is also shown that the worst performing geometries are when these angles are slightly negative [141].

This maybe problematic in isotropic MEMS etches of insulators. The isotropic etch profile inherently leave a chamfered insulator wall, corresponding approximately to a negative angle at both conductors, shown in Fig. 9.4. If this angle is small it could result in

a reduced flashover threshold. This will need to be considered when optimising fabrication processes to ensure the resulting angle between conductor and insulator does not result in a small angle. This angle may also be used to our advantage; if the angle at the triple point can be fabricated to be close to 45° this will result in an increase in the voltage that can be applied.

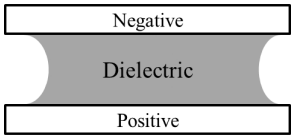

Figure 9.4: Showing the isotropic etch profile, which could potentially lead to the worst geometry for surface flashover.

9.3 Experiment setup

9.3.1 Chip fabrication

The flashover voltage was measured for both static and oscillating electric fields across test structures fabricated similarly to a typical MEMS ion trap geometry. This was divided into two batches, the first consisted of gold electrodes on a quartz wafer, the electrode geometry was that of two parallel tracks with bond pads at opposite ends. The separation between the two electrodes was varied between 3 and 15 μm. Figure 9.5 shows a photograph of a mounted quartz chip on a ceramic chip carrier, the inset shows a drawing of the electrode configuration. The second batch were silicon islands etched from a SOI wafer, these were square electrodes supported on 10 μm of buried SiO_2. The geometry of these samples is shown in Fig. 9.6.

The Au-quartz test structures were fabricated by e-beam evaporation, depositing a 40 nm chrome seed layer and a 200 nm gold layer onto a quartz substrate, photoresist was deposited onto the wafer and then patterned using standard photolithography. The gold and chrome were then etched and the photoresist stripped. The samples were then coated in a protective layer of photoresist before being shipped. To remove the photoresist the chips were placed in acetone and using an ultrasonic bath they were cleaned for 15 minutes. After the chips were removed from the acetone they were rinsed with methanol and left to dry. Inspection of the samples under a scanning electron microscope (SEM) after cleaning showed no signs of residual photoresist. The test samples were then glued onto a ceramic chip carrier using superglue and wire bonded with 30 μm diameter Au wire. The chip

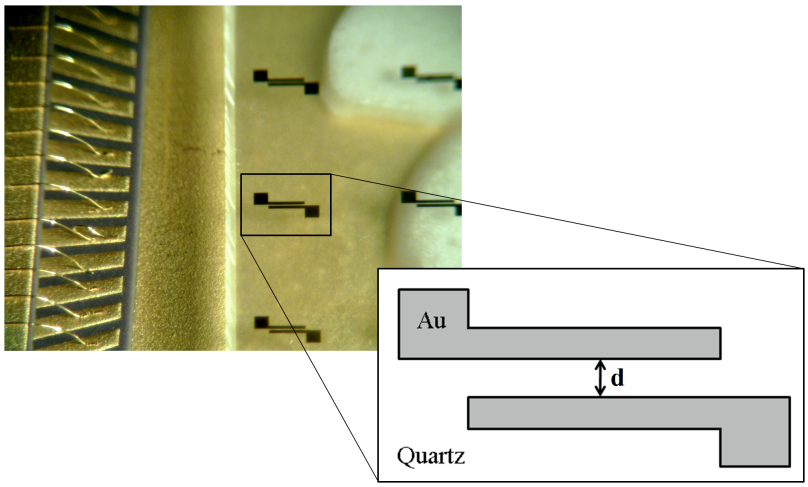

Figure 9.5: Au electrodes on a quartz substrate. The electrodes were fabricated with a separation, d, ranging from 3-15 μm, in 2 μm steps.

sample was then connected to a high power vacuum feedthrough and placed inside a glass belljar. The system was pumped using a turbo-molecular pump to a pressure ranging between $1 - 8 \times 10^{-6}$ Torr.

The SOI test structures were fabricated in parallel to the ion traps described in Chap. 8, Fig. 9.6 shows some SOI test structures mounted to a ceramic chip carrier with conductive glue.

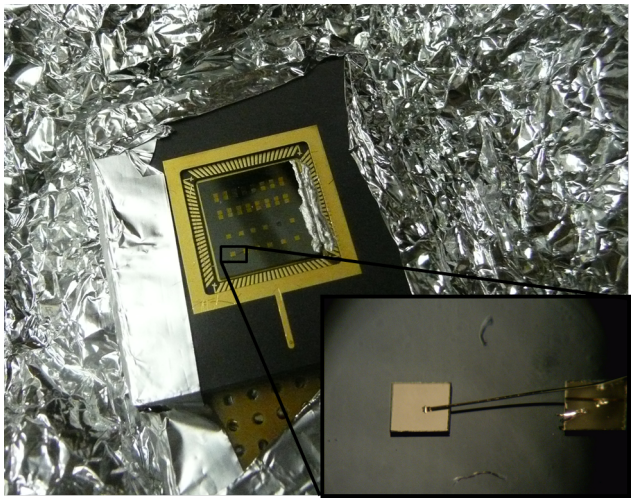

Figure 9.6: An SOI sample mounted with conductive Ag glue onto a chip carrier, inset shows a wirebonded silicon island, the surrounding black is the grounded silicon handle layer.

9.3.2 Electrical setup

To apply large rf voltages an rf amplifier was connected via a 2 μH inductor. This formed a resonant LCR circuit, allowing impedance matching between the amplifier and sample, maximising the applied voltage and reducing unwanted reflections. The experiment setup is shown in Fig. 9.7 with the circuit diagram is shown in Fig. 9.8.

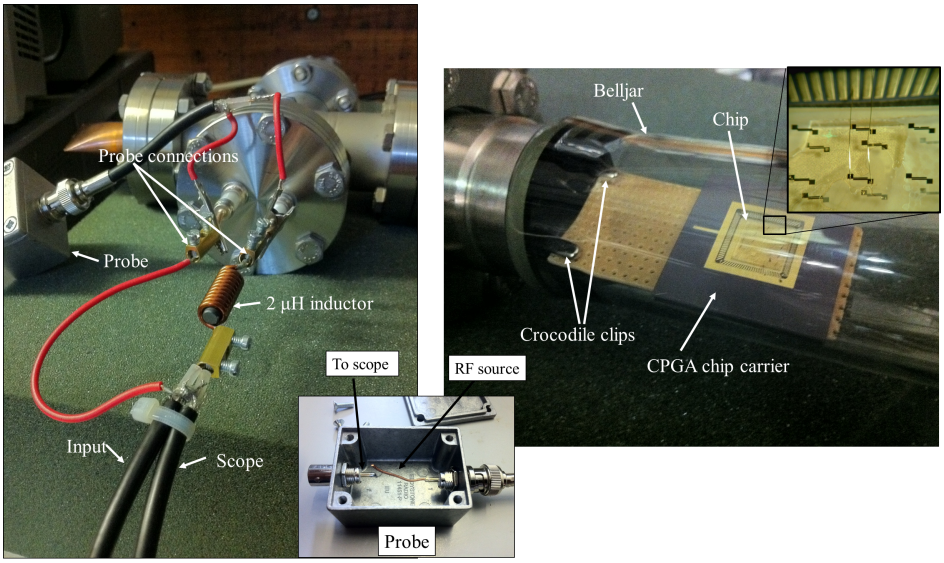

Figure 9.7: Circuit diagram for rf testing. An rf source is connected to a 30 W amplifier, this passes through a bidirectional coupler which protects the amplifier from reflected power. It is then connected to an inductor attached to the vacuum system. A capacitive probe protects the oscilloscope, allowing a small percentage of the applied voltage ($V' - V_2$) to be measured.

Figure 9.8 shows how the different capacitances of the test circuit are distributed. A capacitive probe is in series with an oscilloscope (LeCroy WaveJet 324A), while both the rf feedthrough and sample are in parallel. The voltage drop from V_1 to V_2 is the same across the probe and oscilloscope, rf feedthrough and sample, only the power will be divided depending on the individual impedances. The impedance from C_{probe} results in a voltage drop from V_1 to V'. The oscilloscope then measures the voltage drop from V' to V_2. The high impedance probe protects the oscilloscope and allows high voltage to be applied across the sample.

To calibrate the probe a signal at the circuits resonant frequency was sent to the probe with the output from the probe being displayed on an oscilloscope. Additionally the output from the signal generator was sent directly to the oscilloscope, comparing the voltage output from the signal generator and that measured after the probe allowed

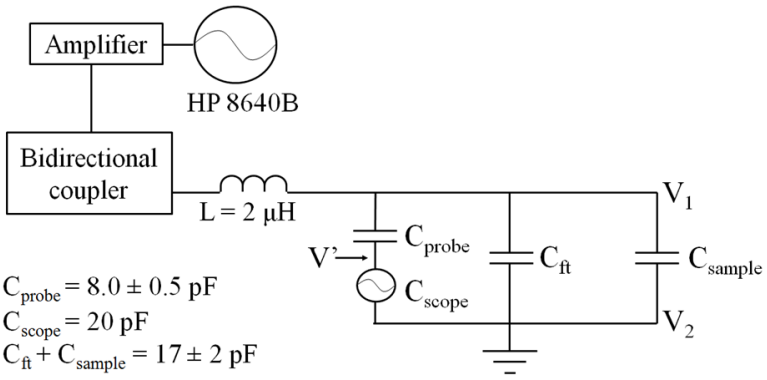

Figure 9.8: Circuit diagram for rf testing. An rf source is connected to a 30 W amplifier, this passes through a bidirectional coupler which protects the amplifier from reflected power. It is then connected to an inductor attached to the vacuum system. A capacitive probe protects the oscilloscope, allowing a small percentage of the applied voltage ($V' - V_2$) to be measured.

the percentage of the signal measured to be calculated. This was repeated after every flashover measurement as slight changes in frequency result in the percentage measured to also slightly vary, with the percentage measured being 0.070 ± 0.005 % of the input voltage.

The circuits resonant frequency was found by connecting an oscilloscope in parallel to the input of the LCR circuit. The frequency of the signal generator (HP 8640B) was scanned until the circuits resonant frequency was found, at which point the voltage measured by the oscilloscope peaks. The value of the resonance frequency of the circuit obeys,

$$f_0 = \frac{1}{2\pi\sqrt{LC}} \tag{9.7}$$

where L is the circuit inductance and C is the circuit capacitance. The dominant inductance is the 2 μH inductor attached outside the vacuum system with the capacitance being a combination of the probe, sample, feedthrough, oscilloscope and a short length of BNC cable connecting the probe to the feedthrough. The capacitance of the feedthrough, chip carrier and sample was 17 ± 2 pF, as measured with a capacitometer. The capacitance of the probe was measured to be 8.0 ± 0.5 pF and the oscilloscope has a capacitance of 20 pF. With additional capacitance from the BNC cable, which is specified to have a capacitance of 100 pFm^{-1}, adding 3.5 ± 0.5 pF to the circuit. Using these values for the inductance and capacitances of our experiment, Equ. 9.7 results in a resonant frequency of 22 MHz. When measured, the resonant frequency was found to be 22.0 ± 0.5 MHz, showing good agreement between prediction and measurement.

For static voltage flashover measurements a high voltage power supply capable of supplying up to 5 kV was connected to the feedthrough. The supply had a built in voltage divider outputting a voltage ranging from 0-10 V, with 1 V corresponding to 500 V across the sample. The voltage divider output was then measured using a voltmeter, the voltmeter was calibrated and had a measurement error of ± 10 mV, corresponding to an error on the flashover voltage of ± 5 V.

Flashover was recorded for the rf voltage upon viewing a discharge between the two electrodes, whilst static flashover was measured by observing the output voltage, upon flashover the voltage droops to zero due to the breakdown forming a short circuit to ground. No high temporal resolution was used to monitor the point at which flashover occurred, this resulted in an error for an individual measurement of no more than ± 7%. The distribution of flashover voltages was significantly larger than the individual error on a measurement, implying microscopic defects and variations in fabrication were the dominant sources of error.

9.4 Results

9.4.1 Au-quartz samples

The flashover process showed significant visual differences between static and rf flashover. Figure 9.9 shows two samples before and after flashover has occurred. Figure 9.9(a) shows a 7 μm test sample before flashover, Fig. 9.9(c) shows the same sample after rf flashover. Flashover occurred between the full length of the electrodes, with the gold at the closest edge being eroded until the distance between the electrodes is sufficiently far that flashover can no longer be sustained. This differs from static flashover which occurred at the sharp edges of the electrodes, where electric charge collects. Without a current limiting resistor, upon breakdown a large current will flow and results in large portions of the electrodes and even bond wire being destroyed. A static sample is shown before and after flashover in Fig. 9.9(b) and (d).

The observed difference between the damage caused by rf flashover opposed to static flashover suggests that there is no charge collection at the sharp edges and that flashover happens uniformly along the closest edge. Also as a result of the changing polarity, plasma dissipation appears to limit the current flow between the electrodes and reduced the damaged sustained to the gold electrodes.

The peak rf flashover voltage can be seen in Fig. 9.10, individual flashover voltage

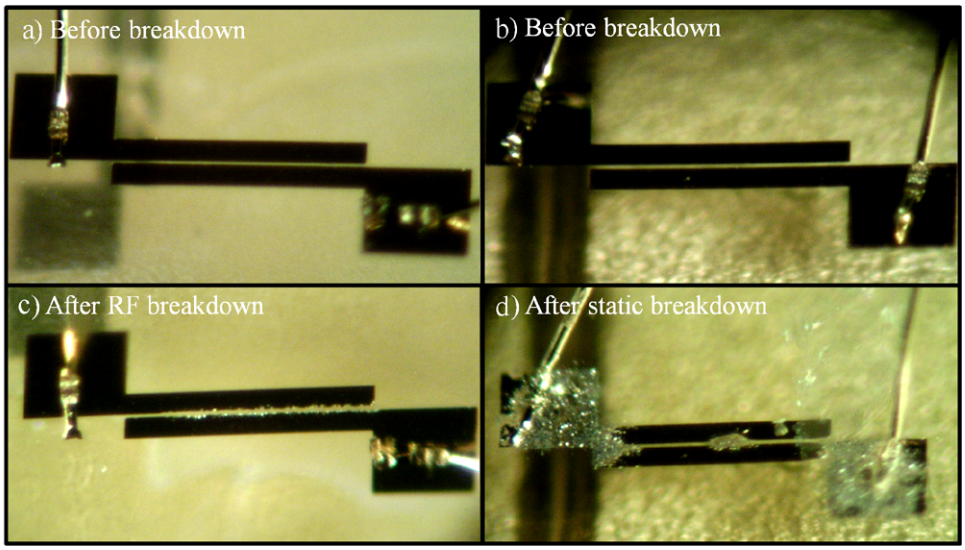

Figure 9.9: a) Au on quartz test sample, a 7 μm gap before electric flashover. b) Au on quartz test sample, an 11 μm gap before electric flashover. c) The 7 μm test sample after rf flashover. d) The 11 μm test sample after static voltage flashover.

measurements are shown as empty circles. The mean flashover voltages are shown as solid circles, the error bar corresponds to the standard error. Measurements were taken across a range of 3 - 11 μm, it was found for separations of greater than 11 μm it was not possible to apply sufficient voltage for flashover to occur in our setup.

Static flashover voltages are shown in Fig. 9.11, with the individual voltage measurements shown as empty squares. The mean flashover voltage is shown as solid squares. Static flashover measurements were performed across a range of 5 - 15 μm.

Equation 9.5 was solved for the rf and static data using a weighted least squares algorithm to find the value of φ^2. The value of φ for rf flashover was found to be $\varphi_{rf} = 4.62 \pm 0.10 \times 10^{18}$ molecules eV m and $\varphi_{dc} = 4.88 \pm 0.19 \times 10^{18}$ molecules eV m for static flashover. Equation 9.5 is plotted for φ_{rf} and φ_{dc} in figures 9.10 and 9.11. The values of φ_{rf} and φ_{dc} show very good agreement with a percentage difference of just over 5%, within measurement errors and demonstrating that there is no significant difference in flashover voltage between peak rf voltage and static voltage.

Figure 9.12 shows the flashover voltage for both the rf and static measurements, with the mean rf voltages shown as solid circles and mean static flashover shown as empty squares. Equation 9.5 was also plotted for φ_{rf} and φ_{dc}, plotted as a solid line and a dashed line respectively.

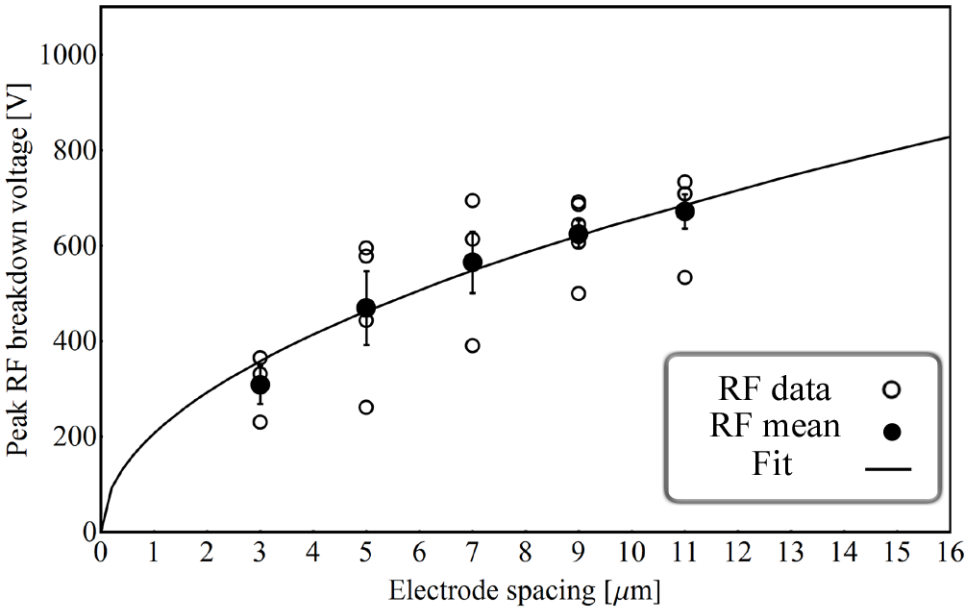

Figure 9.10: RF flashover voltage as a function of electrode separation. Individual flashover measurements are shown as empty circles, the mean flashover voltage is shown as a solid circle. Equation 9.5 is plotted for a $\varphi_{rf} = 4.62 \pm 0.10 \times 10^{18}$ molecules eV m, shown as a solid line.

9.4.2 SOI samples

The electrical tests on the SOI samples were carried out slightly differently because of the different geometry of the chips. The chip geometry is an isolated silicon island on silicon dioxide on a silicon handle layer. Breakdown occurs between the silicon island and the grounded silicon handle layer. This required the chips to be mounted differently, ensuring the handle layer was grounded. The chip was glued to the chip carrier using UHV compatible conductive glue, (LewVac, part number: A-H21D). This is a two part epoxy and specified for wire bonding and UHV applications. Once the chip was glued to the chip carrier, the glue provided electrical contact between the grounded chip carrier and the handle layer. The island was then wirebonded to the rf chip carrier bond pads.

To apply rf power to the chip test sample a helical resonator was coupled to the device. This was used instead of the inductor because the resonant circuit Q using the inductor limited the peak rf voltage to $\approx$ 450 V, not sufficient for breakdown to occur. The resonator allowed coupling between the amplifier and the chip with $\approx$ 90 % of the power being delivered to the chip at a resonant frequency of 28 $\pm$ 0.5 MHz and a Q = 210 $\pm$ 15. The breakdown was measured for four samples and the peak breakdown voltages are given in Tab. 9.1.

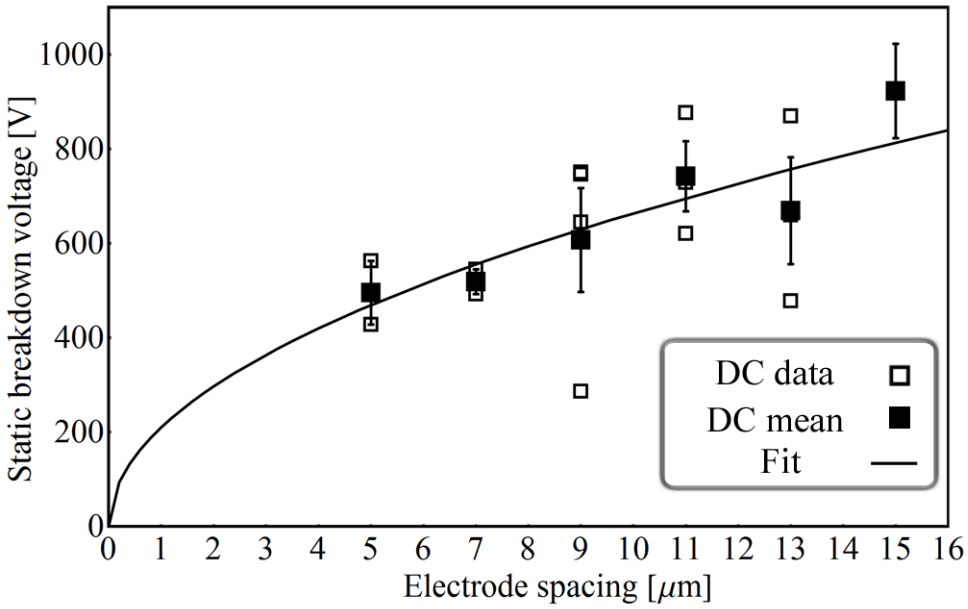

Figure 9.11: DC flashover voltage as a function of electrode separation. Individual flashover measurements are shown as empty squares, the mean flashover voltage is shown as a solid square. Equation 9.5 is plotted for a $\varphi_{dc} = 4.88 \pm 0.19 \times 10^{18}$ molecules eV m, shown as a solid line.

This shows that the breakdown voltage of the samples are very repeatable, showing little spread, with the average rf breakdown voltage of 1061 ± 5 V.

Static voltage was applied in the same manner as the gold on quartz samples, the static breakdown voltages are given in Tab. 9.2. The mean breakdown voltage is 1298 ± 32 V, Fig. 9.13 shows the same sample after static breakdown has occurred. After breakdown it was usual that the sample would now be electrically connected to ground, meaning that for an ion trap electrical breakdown is likely to leave the trap inoperable.

Slight damage can be see round the top right corner of the island and the wirebond, however it does not display the same level of damage as the gold tracks. This is likely

Breakdown voltage (V)	Error (± V)
1060	10
1074	10
1060	10
1050	10

Table 9.1: RF surface flashover between silicon island and grounded silicon handle.

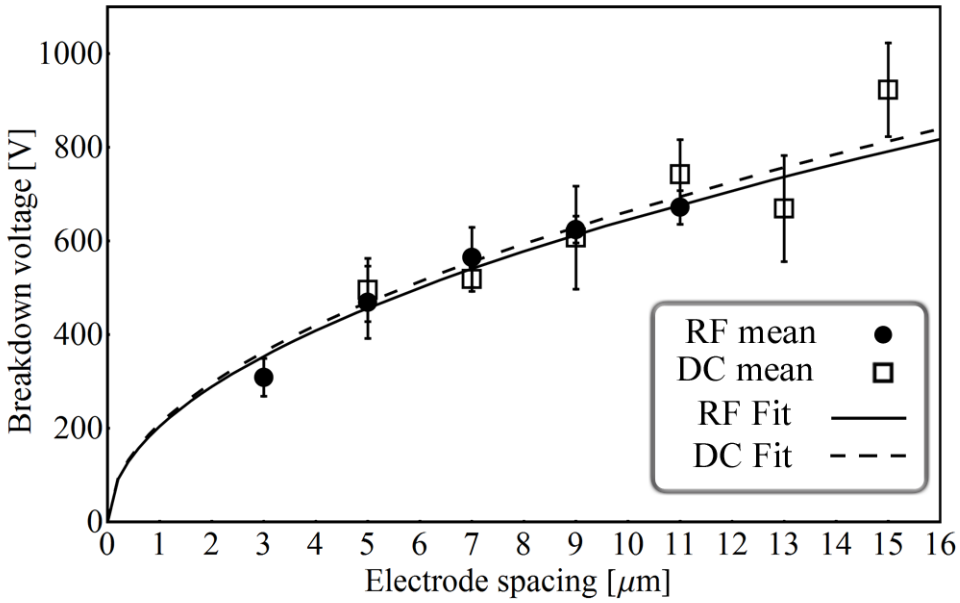

Figure 9.12: RF and static flashover electric field measures. The rf mean flashover voltages are shown as circles with the mean static flashover voltage shown as empty squares. Equation 9.5 is plotted for both the rf and static fits, the rf fit is shown as a dotted line and the static fit is shown as a dashed line.

a result of the much larger silicon electrodes. These electrodes will happily pass several amps without causing extensive damage.

Unlike the Au on quartz samples there is a difference in break down voltage between static and periodic with rf voltages breaking down $\approx$ 20 % lower than for static voltages, though still sufficiently high for ion trap applications. The mechanism for this reduction is not know, but could be a result of substrate heating. To achieve sufficient voltage to observe breakdown, approximately 30 W of power was required to drive the resonator. This power would be predominantly dissipated across the chip, resulting in significant heating. This localised heating will not be sufficient for thermionic electron emission, which for silicon and gold is $\approx$ 1500 °C, however it is reasonable to assume heating of several hundred degrees. This will cause outgassing of the material and result in higher pressures close the substrate surface. It is through this gas that breakdown could occur.

If we compare the average breakdown voltage of the SOI samples to the gold tracks, which have a breakdown voltage of $\approx$ 750 V for a 10 μm gap, then we see that there is a large difference. This may be explained by looking at the etch profile of the insulating silicon dioxide. In Chap. 8, Fig. 8.27 we can see that the SiO_2 has been etched in a sharp v shape. This greatly increases the path length between the electrode and ground.

Breakdown voltage (V)	Error (± V)
1295	5
1294	5
1353	5
1150	5
1331	5
1365	5

Table 9.2: Static surface flashover between silicon island and grounded silicon handle.

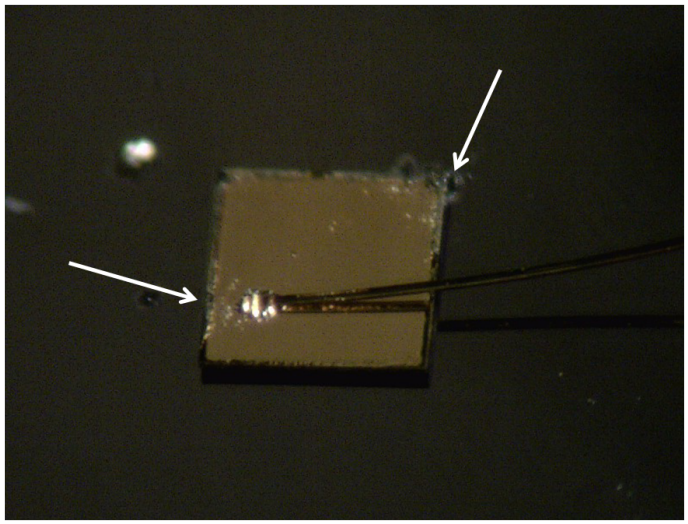

Figure 9.13: A wirebonded silicon island after breakdown, slight damage to the gold around the top right corner and wirebond can be seen, but it does not show the same damage as the gold tracks.

The observed increase in breakdown voltage is consistent with an increase in breakdown voltage with inclined walls as discussed in Sec. 9.2.2.

Despite close agreement between our mean flashover data and theory there is a large spread from the mean, the large standard deviations are likely a result of microscopic defects and variations in fabrication. Examining the samples under an SEM shows irregularities in some of the electrodes, such as that shown in Fig. 9.14.

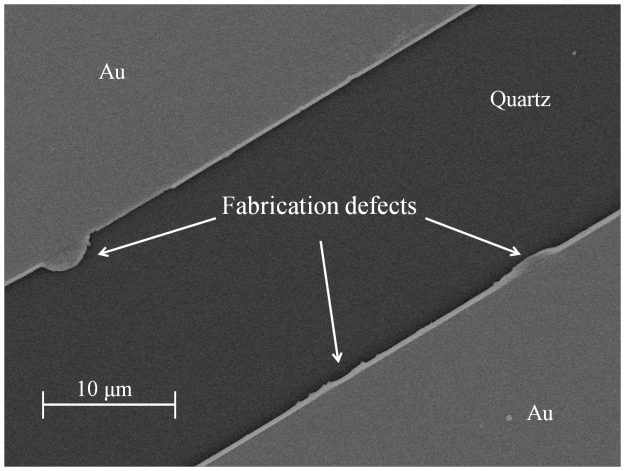

Figure 9.14: SEM image of Au-Quartz sample showing defects along the edges of the Au electrodes.

These defects will often lead to initial small sparks between electrodes as irregular edges and protrusions are a source for an amplified electric field. These sparks were treated as conditioning of the electrodes and the flashover voltage only measured when a discharge the full length of the electrodes was seen. However they may contribute to an increase in the flashover standard deviation.

9.5 Conclusion

In this work the surface flashover across micrometer scale gaps has been investigated. Here we have performed measurements of gaps ranging between 3 and 15 μm for both static and oscillation bipolar voltages and on bulk quartz and SOI trap like structures. The results from these measurements show that surface flashover between micrometer separated electrodes is still governed by SEEA and Equ. 9.1 and that there is no significant difference between the flashover voltage for static or peak rf voltages for Au on quartz and a slight increase in static flashover over rf for SOI traps, likely a result of high heat dissipation.

However we observed a large spread in our data for the Au on quartz samples. This is most likely the result of fabrication defects like those shown in Fig. 9.14. Ensuring smooth

edges along electrodes and at the triple point will reduce points of field amplification which enhance electron emission. This can be achieved either from fabrication processes during construction or post fabrication, such as annealing [142]. Annealing has been used by J. Labaziewicz *et al.* [142] in the fabrication of surface traps to produce smooth electrode edges in order to reduce electron field emission. This will improve the electric field gradients that can be applied to these traps and maybe an option when designing high voltage MEMS devices for operation within vacuum.

Examining literature we find that similar measurements were performed by J. Mueller *et al.* [123] on a layer of PECVD oxide at separations of 5, 10 and 20 μm and up to 600 μm. These results show an increase in flashover voltage when compared to our Au-quartz measurements. However the improvement seen between our measurements and Mueller's deposited oxide may be a result of sample preparation. The samples in Ref. [123] were cleaned using acetone and an ultrasonic bath, they were then rinsed in isopropanol and finally they were cleaned with an oxygen plasma etch. This will remove any remaining organic molecules and therefore reduce the density of molecules on the dielectric surface. This will reduce the value of γ in their experiment and increase φ, improving flashover voltage.

The results presented in Ref. [123] suggest further cleaning processes prior to placement in vacuum can result in significant improvements to the flashover voltage. Ideally in vacuum cleaning would not only remove molecules from the dielectric surface but also avoid recontamination. Glow discharge has been shown to reduce the desorption efficiency of molecules from the surfaces of metals by several orders of magnitude [143], and will remain low for significant amounts of time whilst in vacuum (10^{-6} Torr), such reductions would have a significant impact of the flashover voltages achieved. In vacuum cleaning has recently been reported and has been shown to significantly reduce ion anomalous heating [144]. This would have a twofold improvement for future ion trap arrays, both in reducing anomalous heating and allowing greater electrode voltages and ion-electrode separations

We have shown that within microfabricated electrode geometries the surface flashover is still governed by SEEA and that there is no significant difference between rf and static flashover. This could be advantageous in both increasing the trap depth and allowing geometries with an increased ion-electrode separation to be designed.

Chapter 10

Microwaves and magnetic field gradients on chip

It is nice to know that the computer understands the problem. But I would like to understand it too.

- Eugene Wigner

10.1 Introduction

In order to reduce the technical challenges faced by optically driven qubit transitions, proposals and proof of principle experiments have shown coupling of the internal and motional degrees of freedom using either near field microwave radiation [21, 145] or plane-wave microwave radiation in a magnetic field gradient [110, 109, 146]. They show that all operations that require coupling between the internal and motional states of the ion can be performed directly from microwave sources. Incorporating magnetic field gradients and microwave sources onto microfabricated ion trap arrays would significantly reduce the laser requirements for quantum information processing. The only lasers required would be those for Doppler cooling and photoionisation. Additionally with the application of static magnetic field gradients this would allow addressing of individual ions in frequency space instead of position, further relaxing the requirements. By choosing a large magnetic field gradient this removes any requirement for focusing as frequency splittings between adjacent ions reduce resonant excitations of neighboring ions.

Here I present the design of a microfabricated surface electrode ion trap that incorporates both magnetic field gradients and a microwave source.

10.2 Driving qubit transitions in $^{171}Yb^{+}$

Whilst there are many advantages to using microwave sources to perform arbitrary gate operations, there are several atomic constraints that must first be overcome. The qubit of interest is the 12.642 GHz hyperfine splitting of the $^2S_{1/2}$ $^{171}Yb^{+}$ ground state, defining $^2S_{1/2}|F=0,m_F=0\rangle$ as the $|\downarrow\rangle$ state and $^2S_{1/2}|F=1,m_F=0\rangle$ as the $|\uparrow\rangle$ state, where F is the total angular momentum. Cirac and Zoller [147] showed that any quantum gate can be performed on a trapped ion with an arbitrary qubit rotation and coupling of the spin and motional states, hence to use microwaves to perform a quantum gate they must be able to perform both a qubit rotation and couple the internal and motional states of the ion.

The interaction between the trapped ion and light can be described by an interaction Hamiltonian in the Lamb-Dicke regime [148]. The Hamiltonian described by D. Leibfried *et al.* in Ref. [148] contains three resonances, the first resonance, with no detuning is called the carrier resonance. This is when the light, either a microwave source tuned to the hyperfine splitting or a pair of Raman beams detuned with exactly the hyperfine separation, drives the electron between the $|\downarrow\rangle$ and $|\uparrow\rangle$ states, but with no change in the motional state of the ion. This happens at the Rabi frequency and the electron will oscillate between the two hyperfine states with a frequency proportional to the intensity. Alternatively when the radiation is detuned such that the Raman beams or microwaves have a frequency that is the hyperfine splitting minus the ion secular frequency this will drive the *red* side band. This will transfer the electron between the $|\downarrow\rangle$ and $|\uparrow\rangle$ states but because the light is slightly detuned the additional energy required to perform the transition is taken from the motion of the ion, coupling the internal state of the ion to its motion. Alternatively it is possible to tune so that the incident light has a frequency of the carrier plus the ion secular frequency, the *blue* sideband. In this case the ion will be taken from state $|\downarrow\rangle$ to $|\uparrow\rangle$ but will gain one unit of motional energy. These three different interactions are given in Tab. 10.1, where Ω_0 is the Rabi frequency, η is the Lame-Dicke parameter, n is the motional state of the ion, ω_i is the ions secular frequency and $\omega = 12.6$ GHz.

To quantify how well the incident radiation couples to the transition we need to calculate both the Rabi frequency and the Lamb-Dicke parameter for microwaves. To calculate the Rabi frequency we need to look at the Hamiltonian of a trapped ion. The Hamiltonian is given by [149, 150]

$$H_0 = \frac{\hbar\omega_0}{2}\hat{\sigma_z} + \hbar\omega_1\hat{a}^\dagger\hat{a} \tag{10.1}$$

Resonance	Transition	Detuning	Coupling
Carrier	$\|\downarrow, n\rangle \leftrightarrow \|\uparrow, n\rangle$	$\delta\omega = 0$	Ω_0
Red sideband	$\|\downarrow, n\rangle \leftrightarrow \|\uparrow, n-1\rangle$	$\delta\omega = -\omega_i$	$\Omega_0\sqrt{n}\eta$
Blue sideband	$\|\downarrow, n\rangle \leftrightarrow \|\uparrow, n+1\rangle$	$\delta\omega = +\omega_i$	$\Omega_0\sqrt{n+1}\eta$

Table 10.1: Three resonances of the interaction Hamiltonian, between the ions state and the incident radiation, where Ω_0 is the Rabi frequency, η is the Lame-Dicke parameter, n is the motional state of the ion, ω_i is the ions secular frequency and $\omega = 12.6$ GHz.

where $\hat{a}^\dagger$ and $\hat{a}$ are the creation and annihilation operators respectively, $\hat{\sigma_z}$ is the z-Pauli spin matrix; $\hat{\sigma_z} = \begin{pmatrix} 1 & 0 \\ 0 & -1 \end{pmatrix}$, $\hbar\omega_0$ is the splitting between the two qubit states and ω_z is the ion secular frequency along the z-axis. If we applied an electromagnetic field to our ion this will perturb its Hamiltonian so it is now given by $H \rightarrow H_0 + H'$ where H' is

$$H' = \mu_b \vec{B} \tag{10.2}$$

where μ_b is the magnetic dipole moment of the transition and $\vec{B}$ is the applied magnetic field of the microwave and given by

$$\vec{B} = B_x \cos(\vec{k}.\vec{r} - \omega t + \phi) \tag{10.3}$$

where B_x is the microwave magnitude, $\vec{k}$ is the wavevector and $\vec{r}$ is the propagation direction. Re-expressing in terms of exponentials and substituting into Equ. 10.2 the Hamiltonian is now given by

$$H' = \frac{\hbar\Omega_0}{2}(\sigma_+ e^{i(\vec{k}\vec{r}-\omega t+\phi)} + \sigma_- e^{-i(\vec{k}\vec{r}-\omega t+\phi)}) \tag{10.4}$$

where $\Omega_0 = \frac{-\mu_b B_x}{2\hbar}$ is the Rabi frequency. The effective magnetic moment for the $^{171}Yb^+$ ground state is equal to the Bohr magneton; $\mu_b = \mu_B$. In practice the Rabi flopping will actually occur at the generalized Rabi frequency which is given by $\Omega' = \sqrt{\Omega_0^2 + \delta^2}$ [151], where δ is the microwave detuning from resonance. Using a microwave source exactly resonant with the hyperfine splitting, $\delta = 0$, and with an intensity at the ion of 100 Wm^{-2} will give a Rabi frequency of $\Omega_0 \approx 40$ kHz.

The coupling strength is given in terms of the Rabi frequency, Ω_0, and the Lamb-Dicke parameter (LDP) η. The LDP is given by $\eta = kz_0$, where $z_0 = \sqrt{\frac{\hbar}{2m\omega_z}}$ and z_0 is the spread of the ion's wavepacket in the ground state, k is the wavevector, m is the ion mass and ω_z is the ion secular frequency. For tunings that couple the ions spin to the motional

state; transitions from $|\downarrow, n\rangle$ to $|\uparrow, n \pm 1\rangle$, are easily obtainable for optical transitions where $\eta \approx 0.2$[1], however for microwave transitions the Lamb-Dicke parameter becomes negligible[2] and hence the coupling between the ions spin state and motional state vanishes.

This would suggest that it is virtually impossible to efficiently use only microwaves for quantum information processing, compounded by the fact that due to their long wavelength it would not be possible to singularly address the ions, it seems that only optical transitions are available. However because of the technical challanges of using optical transitions, there have been several proposals and proof of principle experiments to couple the internal and external states directly with either microwaves or magnetic fields, these include placing the ions in a magnetic field gradient [110, 109, 146], shuttling over static magnetic fields [152] and using oscillating magnetic fields [21, 145]. In the following I will discuss these proposals.

10.2.1 Static magnetic field gradients

As shown above, using long wavelength radiation to drive the qubit state does not couple the ion to its motion, due to a vanishingly small LDP. However Mintert and Wunderlich [110] showed that in the presence of a large magnetic field gradient, the Lamb-Dicke parameter is replaced by an effective Lamb-Dicke parameter (eLDP) and now allows coupling between the ion's spin and motion. As well as coupling the internal state to motion it also allows individual ion addressing since the ions, now in a static magnetic gradient, each experience a unique Zeeman shift.

The ytterbium qubit is the ground state $m_F = 0$, first order magnetic insensitive hyperfine states. This is beneficial because, being insensitive to magnetic fields, this decouples the qubit state from background magnetic field fluctuations. These fluctuations have the potential to introduce changes in the Zeeman splittings and result in decoherence. However the Mintert and Wunderlich proposal is reliant on using the $m_F \pm 1$ hyperfine states. In a magnetic field gradient this lifts the ion's energy splittings degeneracy and allows individual addressing in frequency space. However it does leave the ions susceptible to background magnetic field noise.

The energy levels of the hyperfine levels for an atom with total angular momentum of

[1] For $^{171}Yb^{+}$, with a secular frequency of $\omega/2\pi = 1$ MHz and counter propagating Raman beams with a wavelength of $\lambda = 369$ nm.

[2] The LDP of an incident microwave at 12.6 GHz is $\eta = 1.4 \times 10^{-6}$.

J = 1/2 is given by the Breit-Rabi equation [146]

$$E = \frac{E_{HFS}}{2(2I+1)} - g_I \mu_N B m_F \pm \frac{E_{HFS}}{2}\sqrt{1 + \frac{4m_F\chi}{2I+1} + \chi^2} \tag{10.5}$$

where

$$\chi \equiv \frac{(g_J + g_I \frac{m_e}{m_p})\mu_B B}{E_{HFS}}, \tag{10.6}$$

and E_{HFS} is the energy splitting between the F = 0 and F = 1 states in zero magnetic field, I is the nuclear spin, m_F is the total angular momentum projected along the quantization axis, B is the magnetic field, g_J is the electronic g-factor, g_I is the nuclear g-factor, m_e is the electron mass, m_p is the proton mass, μ_B is the Bohr magneton and μ_N is the nuclear magneton.

Figure 10.1(a) shows the energy levels for the ground state of $^{171}Yb^+$ as a function of the scaled magnetic field χ, Fig. 10.1(b) shows the allowed transitions for weak magnetic field and strong magnetic field, where π polarisation is when the microwave electric field vector is parallel to the magnetic field. π transitions follow the selection rules $\Delta m_F = \pm 1$ and $\Delta F = 0, \pm 1$ and σ transitions follow the selection rules $\Delta m_F = 0$ and $\Delta F = \pm 1$ in a weak magnetic field. In a strong magnetic field, $\chi \geq 1$, the allowed transitions for σ polarized light are $\Delta m_s = 0$ and $\Delta m_I = 0$, there are no allowed transitions. For π polarized light the transitions following the selection rules $\Delta m_S = \pm 1$ and $\Delta m_I = 0$ [146].

A result of the ion being placed in a position dependant Zeeman shift is that it will experience a force that is dependant on the internal state of the ion [146]. When the ion is excited to the $|\uparrow\rangle$ state there will be an additional force on the ion and shifting its equilibrium position from that of when in the $|\downarrow\rangle$ state. Mintert and Wunderlich [110] showed that this state dependant force on the ion results in an effective LDP. The eLDP is given by [146]

$$\eta'_{nj} e^{i\phi_j} \equiv \eta_n S_{nj} + i\epsilon_{nj}. \tag{10.7}$$

Since the standard LDP is $\eta_n \approx 0$ for microwave sources we can approximate the eLDP as $\eta'_{nj} \approx \epsilon_{nj}$ [146], where ϵ_{nj} is given by

$$\epsilon_{nj} = S_{nj} \frac{\Delta z_n \partial_z \omega_{01}^{(j)}}{\omega_z}, \tag{10.8}$$

where Δz_n is the extension of the ions ground state, $\omega_{01}^{(j)}$ is the ion transition frequency with j = 1...N for each individual ion in a chain and ω_z is the axial ion secular frequency. Because the transition frequency, $\omega_{01}^{(j)}$, of the ion is dependant on the position in the magnetic field gradient, the strength of the coupling between the ions internal state and

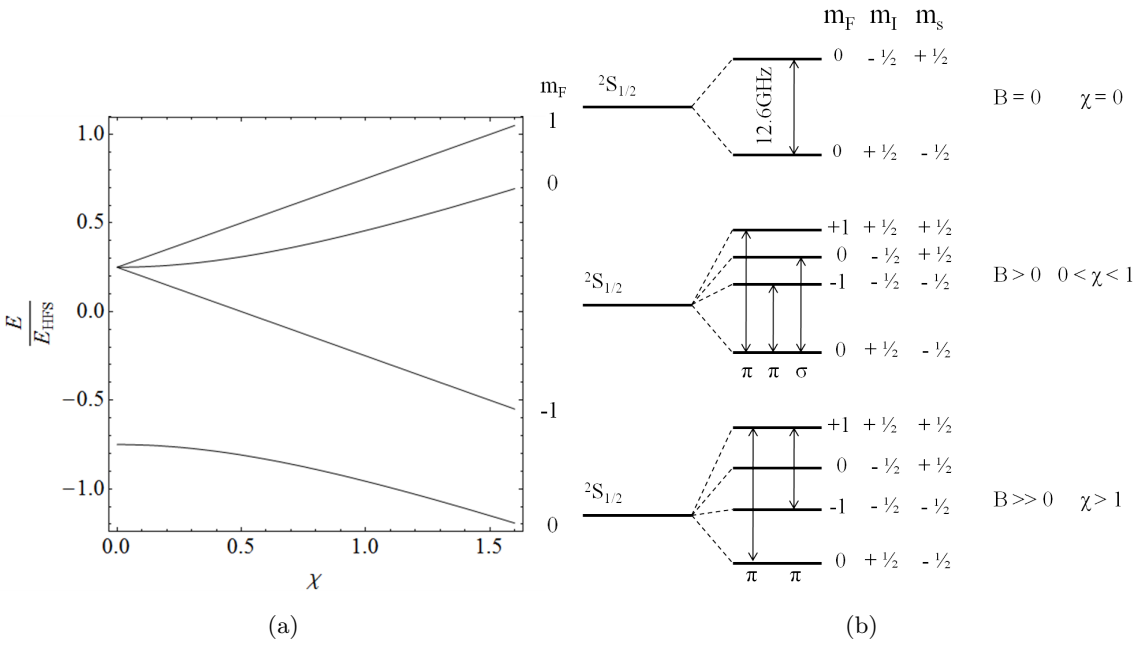

Figure 10.1: a) A Breit-Rabi plot of the energy levels of $^{171}Yb^{+}$ with the scaled magnetic field χ. b) The energy levels and allowed transitions for $^{171}Yb^{+}$ in a weak and strong magnetic field.

the motion state will depend on the ratio between the frequency variation and the axial secular frequency, ω_z, with S_{jn} giving a measure of how much ion j interacts with the chain motional mode n.

Experimentally individual ion addressing and coupling of the spin to motion has been demonstrated [109, 40], however these experiments only manage small magnetic field gradients, $\partial B_z < 1$ Tm^{-1}, significantly lower than those outlined in the proposal, $\partial B_z \geq 10$ Tm^{-1}. To achieve sufficient frequency separation and spin-motion coupling at least an order of magnitude greater magnetic field gradients will be required.

10.2.2 Transport gates and oscillating magnetic fields

In 2007 D. Leibfried *et al.* [152] outlined a method to simplify the optical requirements for implementing QIP. Here instead of single qubit rotations and two-qubit gates being performed on ions stationary in the lab reference frame and using precisely timed pulsed lasers, the ions are shuttled through cw lasers across the trap array. It was shown that all operations could be performed in this manner but the requirements for precise pulse timing and beam stability of the lasers is relaxed, however it does require adiabatic shuttling procedures. As an extension they also introduced the idea of transporting ions across a

magnetic field gradient wash board. Parallel current carrying wires or permanent magnets laying perpendicular to the shuttling direct would then induce the qubit rotations and gate operations.

Extending this idea C. Ospelkaus *et al.* [21] proposed that quantum logic gates can be performed by oscillating magnetic fields. Here they present an interaction Hamiltonian between an oscillating magnetic field and a string of ions. They discuss two gate operations, the $\sigma_z\sigma_z$ and $\sigma_\varphi\sigma_\varphi$ gates, which correspond to a geometric phase gate [16] and Mølmer-Sørensen gate [153] respectively. A $\sigma_z\sigma_z$ geometric phase gate can be implemented by using oscillating currents at rf frequencies, but can only be implemented on states that are first order sensitive to magnetic fields [21]. However it should be possible to rotate from the insensitive qubit state manifold to perform the gate then rotate back, limiting the time the qubit is susceptible to magnetic field fluctuations [21]. Generating currents oscillating at these frequencies on chip does not pose any significant challenge, as it is already a requirement for generating the ponderomotive pseudopotential, however the $\sigma_\varphi\sigma_\varphi$ Mølmer-Sørensen gate operates directly at the hyperfine splitting of the ion, which for $^{171}Yb^+$ is 12.6 GHz. This requires microwave engineering of the chip structure to permit sufficient microwave power to propagate beneath the ion. By positioning the ion close to the electrodes the ion will experience large magnetic field gradients from the microwave source, and allows coupling of the hyperfine states to the ions motion. This had been experimentally demonstrates recently by C. Ospelkaus *et al.* [145], where they demonstrate Rabi flopping, side band cooling and two qubit entangling using near field microwaves, though with fidelities far lower than that required for scalable QIP.

10.2.3 Overview

Both proposals offer unique methods for coupling the internal qubit state of the ion to its motion, without the use of lasers. This is advantageous as large scale architectures puts very strict requirements on any optical setup which would be hugely reduced by using microwave sources. However both proposals require significant engineering if they are to be successfully implemented. In the following I will present my work towards implementing both magnetic fields and microwaves onto a MEMS ion trap chip.

10.3 Ion trap design

The ion trap design was initially based on that of the first generation of SOI traps described in Chap. 8. The linear geometry of these traps have rf electrode widths of 100 μm and 200

μm and with a central static width of 60 μm. By modifying the existing geometry both magnetic fields and microwave source can be incorporated into standard linear surface trap designs. This allows individual addressing to be incorporated on existing surface trap technologies with a minimal increase in fabrication steps.

To provide a microwave source close to the ion the central static electrode can double as a microwave waveguide. There are several common forms of waveguides used in microwave monolithic integrated circuits (MMIC) and printed circuit board (PCB) technologies, but the most suited of these is the coplanar waveguide (CPW). In a CPW configuration all the electrodes lay on a single plane, removing any requirement for buried conducting layers that would increase the complexity of any fabrication process.

A CPW design requires three individual electrode strips, the central conductor slot and two parallel ground planes, which in the ideal case extend to infinity. This geometry can easily fit between the two rf trap electrodes, with the rf electrodes serving as microwave ground. To ensure that the CPW does not reflect the incoming microwave it is important to ensure that it has a characteristic impedance that matches the source, which is 50 Ω. The characteristic impedance of a CPW is dependant on the geometry of the transmission line and is discussed in Sec. 10.5. For the trap design it requires a rf-rf electrode separation of 54.5 μm with a central electrode of width 14.5 μm, with gaps between the rf electrode and central electrode of 20 μm. The geometry for the ion trap is show in Fig. 10.2, along with the static and ponderomotive potential Fig. 10.2(a).

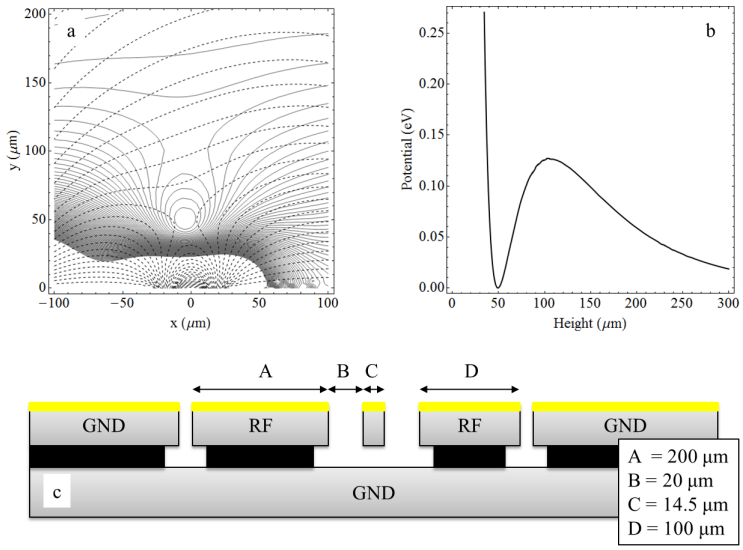

Figure 10.2: a) Contour plot of the static and ponderomotive ion trap potentials. b) The ponderomotive potential along the y-axis, showing the trap depth is ≈ 0.13 eV. c) Drawing of the ion trap electrode configuration including the CPW.

In this new geometry when trapping $^{171}Yb^{+}$ with an rf drive frequency of $\Omega/2\pi =$ 45 MHz, rf peak voltage of $V_{RF} = 140$ V the trap depth is ≈ 0.13 eV with ion secular frequencies in the x' and y' principal axes of $\omega_{x'}/2\pi \approx \omega_{y'}/2\pi \approx 3.7$ MHz and stability parameter of q = 0.8. The static electric field and ponderomotive potential can be seen in Fig. 10.2(a).

For confinement along the z-axis, six static voltage control electrodes have been included, providing end cap potentials as well as micromotion compensation. These electrodes also serve a secondary purpose in that they provide the magnetic field gradient. Each electrode is split down the center by a 5 μm trench. This trench allows a current to flow around the end of the electrode in a current loop. By applying an offset current to each electrode a magnetic field is generated. The precise B-field from these electrodes is discussed in Sec. 10.4.

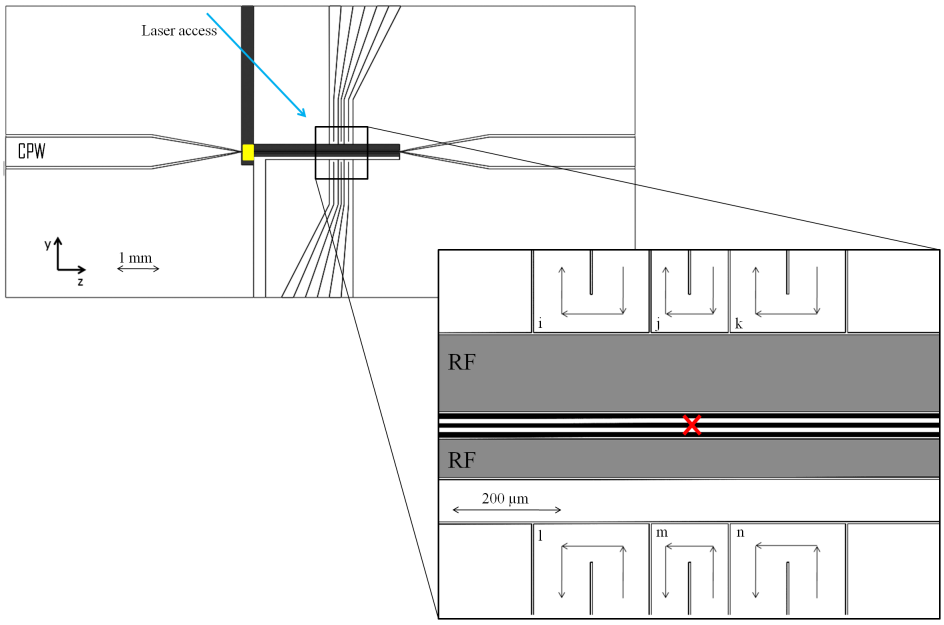

Figure 10.3: The full trap geometry. RF electrodes are shown in gray, the CPW extends from the right and left edges of the chip and narrows to fit between the rf electrodes. The insert shows a black line between the two rf electrodes corresponding to the CPW, arrows on each of the six static electrodes show the current loops used to generate the magnetic field gradient.

The trap geometry is shown in Fig.10.3, the coplanar waveguide extends from the left edge and narrows to fit between the rf electrodes. Connection is made via a launch connector, this accepts a standard SMA connector and clamps onto the edge of the chip. Electrical connection is made by applying pressure between the central SMA pin and the CPW central slot. To allow impedance matched termination of the microwaves and avoid

reflections, the coplanar waveguide connects with a second launch connector after the trap, on the right of the chip, and allows the microwaves to be terminated outside of the vacuum system.

Electrical connections to the trap electrodes are made by wirebonding bond pads on the upper and lower chip edge to a ceramic chip carrier. The bond pads fan out in opposite directions to allow diagonal laser access to the trapping region. An additional wirebond bridge over the CPW connects the two rf electrodes, and is marked in yellow in Fig.10.3. The inset shows the trapping region with the ion position marked by a red cross, the CPW is shown as a black line between the rf electrodes, and current loops are marked by three arrows.

10.4 Magnetic field gradient

Individual addressing of ions in a linear chain and the coupling of the ions motional and spin states using microwave radiation has been shown by M. Johanning *et al.* [109]. Here $^{172}Yb^{+}$ ions were used and the first order Zeeman splittings addressed with rf radiation in a magnetic field gradient of $\partial_z B = 0.51(2)$ Tm^{-1}. Separately individual addressing and Rabi flopping of ions has been shown by S. Wang *et al.* [40] in a microfabricated ion trap with electrode geometry to provide the magnetic field gradient, here they demonstrated a cross talk between ions of 2.2 ± 1.0 % with gradients of $\partial_z B = 0.23$ Tm^{-1}.

To calculate the magnetic field gradient desired to separate the ion qubit resonance frequencies we must ensure that there is no overlap with motional sidebands. For N ions this can be estimated using [110]

$$\partial_z B \geq \frac{\hbar}{2\mu_B} \sqrt[3]{\frac{4\pi\varepsilon_0 m}{e^2}} \omega_z^{\frac{5}{3}} (4.7N^{0.56} + 0.5N^{1.56}) \tag{10.9}$$

where ε_0 is the permittivity of free space, m is ion mass and ω_z is the highest vibrational frequency. Figure 10.4 shows how with increasing ion frequency a greater magnetic field gradient is required, this is shown for N = 5 (solid), 10 (dot-dash) and 20 ions (dots).

For 5 ions with a secular frequency of $\omega_z/2\pi = 100$ kHz this requires a magnetic field gradient of $\partial_z B = 4.98$ Tm^{-1}, this increases to $\partial_z B = 231.15$ Tm^{-1} for $\omega_z/2\pi = 1$ MHz.

To produce a magnetic field gradient along the ion chain the ion traps control electrodes have been split down the center. This allows a current to flow in a loop around each electrode, and it is this current loop that produces a magnetic field. The current in each electrode is biased on top of the static voltage so that it does not disrupt the operation of the ion trap. Inhomogeneous field gradients resulting in uneven Zeeman splittings

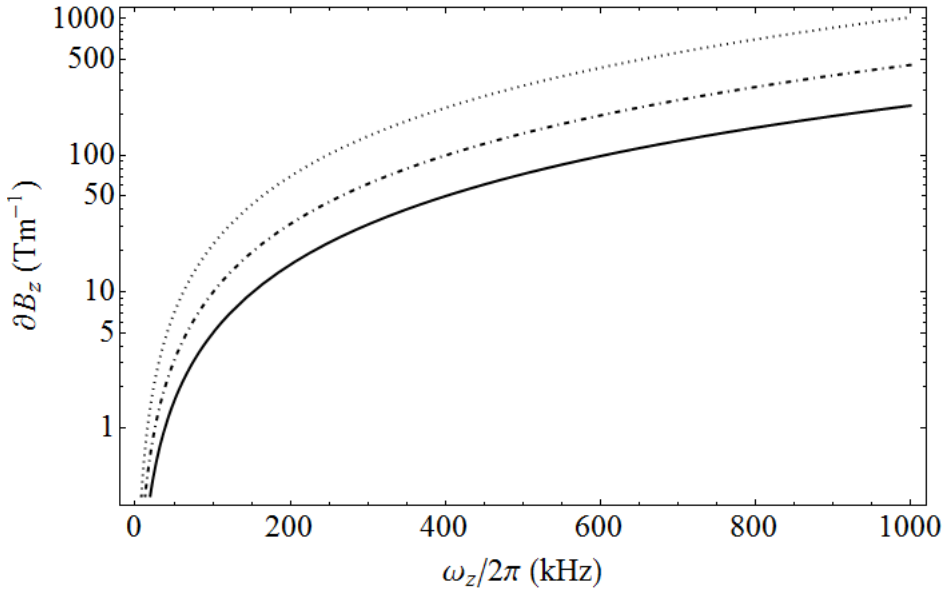

Figure 10.4: The magnetic field gradient required to separate ions in different strings lengths of N = 5 (solid), N = 10 (dot-dash) and N = 20 (dots) as the ion secular frequency increases.

have been observed and is thought to be caused by asymmetric currents paths along a single current carrying electrode [40]. The increased degrees of freedom from six electrodes allows the magnetic field gradient to be tweaked and allow magnetic field gradient inhomogeneities along the ion chain to be reduced.

10.4.1 CPO simulation

Using CPO, simulations of the magnetic field B and the magnetic field gradient ∂B_z were found. CPO uses the Biot-Savart law to calculate the magnetic field from a conducting wire and assumes there are no materials with a high permeability close by.

The current was simulated as eighteen current lines, shown in Fig. 10.3, with each electrode modeled as three current carrying lines, with the arrow direction corresponding to the direction of positive current flowing. To generate the magnetic field gradient along the z-axis, opposite pairs of electrodes share similar currents. For example if electrodes i and l in Fig. 10.3 carry + 1 amps, electrodes j and m carry 0 amps and electrodes k and n carry - 1 amps then the magnetic field gradient at the ion is $\partial_z B = 0.8$ Tm^{-1}. The limiting factor on the magnitude of the magnetic field gradient is set by the ohmic heating of the trap electrodes. To get an estimate of the current that can be applied, the thermal properties of the chip need to be modeled.

10.4.2 Thermal properties

The heat transfer of thermal energy through a medium, as a result of a negative temperature gradient, is described by Fourier's law, given by $\mathbf{q} = -k\vec{\nabla}T$. The heat flux $\mathbf{q}$ is equal to the thermal conductivity, k, multiplied by the negative temperature gradient $-\nabla T$. As a crude model of our system we can view the heat transfer as a 1-D model. Treating Fouriers's law 1-dimensionally, the heat transfer is now expressed as $q_x = -k\frac{dT}{dx}$. Applying this equation to a homogenous material the rate of flow between the two end points can be found using

$$\frac{\Delta Q}{\Delta t} = -kA\frac{\Delta T}{\Delta x}, \tag{10.10}$$

where $\Delta Q/\Delta t$ is the heat transfer per unit time (in W), A is the cross sectional area, ΔT is the temperature difference and Δx is the distance between the two ends. The heat dissipation from the electrode can be seen schematically in Fig. 10.5. The majority of the current will flow through the gold surface layer, by assuming the only heat source is the gold wire heat transfer through the SOI wafer can be modelled using Equ. 10.10. The power dissipated by the wire can be found using $P = I^2R$, where I is current and R is the wire resistance, now equating with Equ. 10.10 we get

$$P = \frac{kA\Delta T}{x}. \tag{10.11}$$

Applying 2 amps to the gold tracks, which have an estimated resistance of $\approx 0.2\ \Omega$, it is realistic that 1 W of power will need to be dissipated. Assuming that the chip bracket is capable of dissipating power much faster than power dissipated by the wire an estimation of the temperature difference with power can be found.

The heat transfer can be divided into three distinct stages, first the silicon device layer, then the silicon dioxide layer and finally the silicon handle layer, as shown in Fig. 10.5. If we take a time $t \to \infty$ then we can say that each section must be conducting 1 W. Working backwards from the back side of the wafer the temperature difference between the rear side, T_4, of the chip and the silicon-silicon dioxide interface, T_3, can be found using Equ. 10.11. For a surface area $A = 2.2 \times 10^{-6}$ m^2, $k = 120$ and $x = 600$ μm the temperature difference is $\Delta T_{Handle} = 2.2$ K. Repeating this process for the SiO_2 layer, $T_3 \to T_2$, with $k = 1$ and thickness $x = 10$ μm yielding a $\Delta T_{SiO_2} = 4.5$ K. Finally repeating the procedure between the silicon dioxide layer and the wire, $T_2 \to T_1$, where $x = 30$ μm and $k = 120$, $\Delta T_{Device} = 0.11$ K. This gives for 1 W of dissipation a total temperature change between the wire and the rear wafer side of $\Delta T_{Total} = 6.9$ K.

This model ignores radiative heat loss and lateral conduction through the wafer. It also

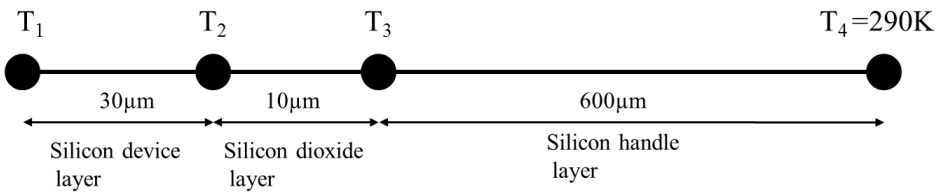

Figure 10.5: 1D thermal schematic of the silicon wafer, T_1 corresponds to the wire temperature and T_4 is thermally connected to a heat sink.

makes the assumption that the chip bracket, which is attached to the vacuum system, can remove power faster than that dissipated by the wire. This assumption becomes less valid as higher currents are applied. Figure 10.6 shows how the temperature change increases as more current is applied to the wire. In reality it is likely that a much larger thermal increase than predicted will result when applying larger currents. However magnetic field gradients as low as 0.27 Tm^{-1} have been successfully used to individually address ions [109], comparable gradients can be achieved with currents as low as 0.33 amperes, requiring only ≈ 0.03 W of power dissipation. To achieve frequency separation between 5 ions, with secular frequency $\omega_z/2\pi = 100$ kHz, as discussed earlier requires a magnetic field gradient of $\partial B_z = 4.98$ Tm^{-1}, which would correspond to a current of 4 amps and an increase in chip temperature of $\Delta T \approx 50$ K.

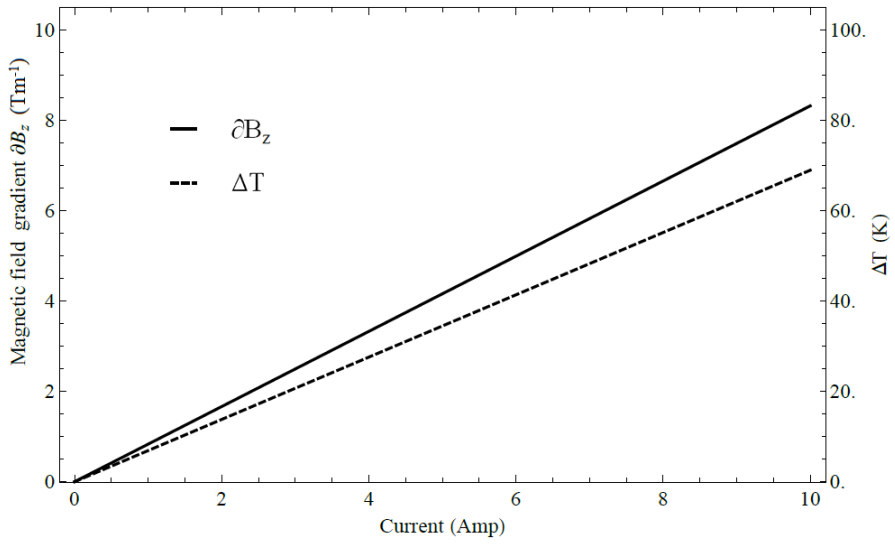

Figure 10.6: The solid line shows the magnetic field gradient at the ion with the current in the wires. The dashed line shows the calculated temperature change in the wires with current.

The temperature increase of the electrodes is not significant compared to the tempera-

tures required to destroy the chip. However a relationship between trap temperature and the ions heating rate has been observed [154] so excessive trap heating needs to be avoided, it was also observed in Chap. 9 that an increase in substrate temperature is likely to lead to a reduction of breakdown voltage of the electrodes. This design is also self limiting as ultimately ohmic heating will limit the current that can be applied. Incorporating a cryogenic design would allow electrodes to be fabricated from superconducting materials, allowing significantly larger currents and magnetic field gradients to be generated.

10.5 Coplanar waveguide

For PCB and MMIC technologies various planar transmission lines have been developed. The most suitable topology for our ion trap is the coplanar waveguide, shown in Fig. 10.7. A coplanar waveguide consists of a three parallel strips mounted on top of a dielectric, the central strip is connected to the microwave source with the two parallel strips grounded. The microwaves propagate between the central slot and the ground planes, through both the dielectric and air gap. Impedance matching can be achieved by adjusting the slot width w and gap width g, but is also a function of metal thickness t, dielectric thickness h and the dielectric constant ε_r.

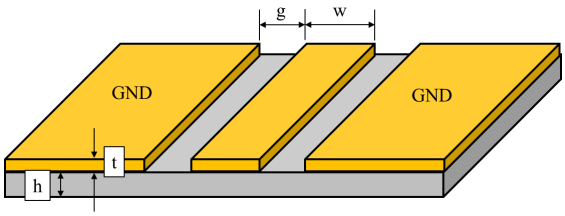

Figure 10.7: Coplanar waveguide, the central track carries the microwaves with two parallel ground planes.

To ensure that the microwave can be efficiently delivered to the ion first the CPW geometry was simulated then analytical solutions for magnetic fields above the CPW surface were solved, this allowed the Rabi frequencies as a function of microwave power to be calculated.

10.5.1 Characteristic Impedance

To ensure propogation of the microwaves the CPW geometry needs to have a characteristic impedance of 50 Ω, matching the source. Using TX-Line transmission line calculator[3] the

[3]Available free from AWR, http://web.awrcorp.com/Usa/Products/Optional-Products/TX-Line/

characteristic impedance of various forms of waveguide can be calculated. The impedance is a function of the track width w, gap width g, metal thickness t, dielectric thickness h and dielectric constant ε_r, where silicon is viewed as a lossy dielectric. Because of the severe SiO_2 undercut observed during fabrication it is expected that all the silicon dioxide will be removed from beneath the conductor. So the CPW was simulated as a CPW ground, where there is a ground plane beneath the dielectric, with an air gap of 10 μm. Using TX-Line the CPW geometry for the trap could be simulated giving a geometry of central conductor width w = 14.5 μm, gap width g = 20 μm, dielectric (air) thickness h = 10 μm and conductor thickness t = 40 μm. The conductor thickness is a combination of the 10 μm gold thick layer and 30 μm silicon device layer, we can do this because the resistivity of doped silicon has been measured up to THz and shown to be only slightly modified at $\approx$ 12 GHz [155].

10.5.2 Analytical results

To calculate the microwave intensity at the ion, analytical expressions for the **B** field components from a CPW were evaluated, these equations as well as equations for the **E** fields can be found in App. E. Calculations of the **H** and **E** fields within the CPW show the propagation of the fields through the dielectric and the vacuum above the surface. As shown previously the Rabi frequency is given by $\Omega_0 = \frac{-\mu_b B_x}{2\hbar}$, it is possible to analytically calculate the B_x field from the trap CPW and therefore derive the power required to drive Rabi oscillations.

From the equations in App. E the **B** field is given as a function of the CPW voltage, to convert this to a power we can examine the circuit diagram for the entire system, as shown in Fig. 10.8. Using $P = \frac{V^2}{R}$ where V is the voltage and R = 50 Ω is the resistance we can convert the waveguide voltage to a power. Figure 10.9 shows the ion Rabi frequency as a function of the power applied to the CPW.

In reality the impedance matching will not be perfect causing microwave reflections and additional attenuation from vacuum feedthroughs and coaxial cable means that the applied microwave power will need to be increased.

10.6 Fabrication design

To fabricate the trap several considerations needed to be made: ensure all dielectrics are hidden from the ion, low electrode resistance to allow large currents to be applied and compatible with CPW designs. For simplicity the fabrication is based on the approach

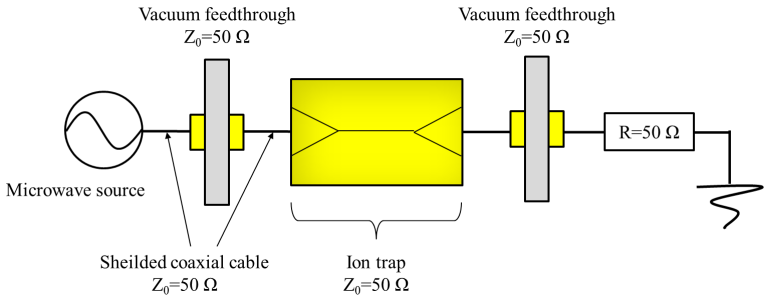

Figure 10.8: Schematic of the microwave circuit, with all components impedance matched at 50Ω, the resistor before ground acts as an impedance matched load. This set up acts as an infinite transmission line with a total resistance of 50Ω.

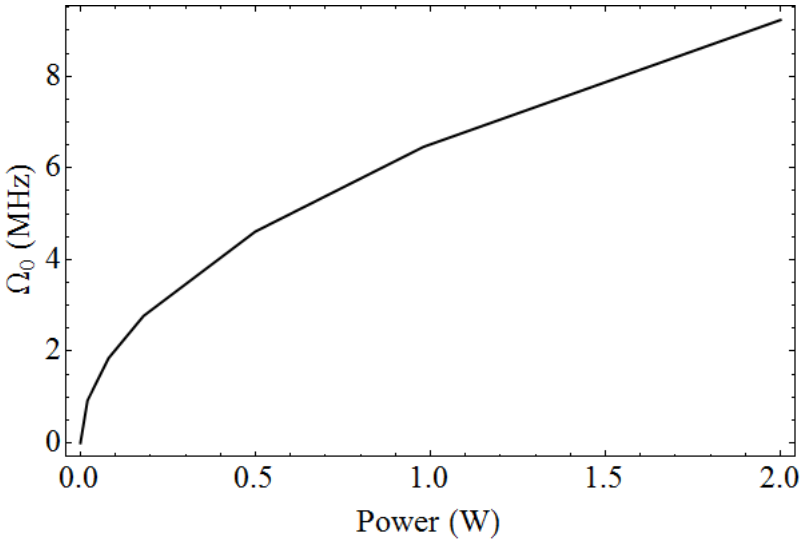

Figure 10.9: Graph showing the Rabi frequency, Ω_0, against the applied CPW power.

described in Chap. 8, where the ion trap structure is etched from a silicon on insulator wafer, however modified to produce a thick gold layer.

Figure 10.10 shows the fabrication guide, to begin with the SOI wafer has a chrome adhesion layer and thin Au seed layer evaporated onto the surface. Photoresist is then spun onto the substrate and pattered, leaving resist covering all the areas that correspond to trenches. The wafer is then electroplated, using the photoresist as a mold, to build up an Au thickness of 10 μm. The photoresist is then stripped and the gold seed layer and chrome are etched from the trench sites. A deep reactive ion etch etches the exposed silicon, cutting trenches between the electrodes and exposing the buried silicon dioxide. An HF etch will then remove the exposed SiO_2 and undercut beneath the electrodes, leaving the central CPW electrode free hanging, but supported at either end. The wafer is then coated with another Cr adhesion layer and gold layer, to cover any areas of exposed

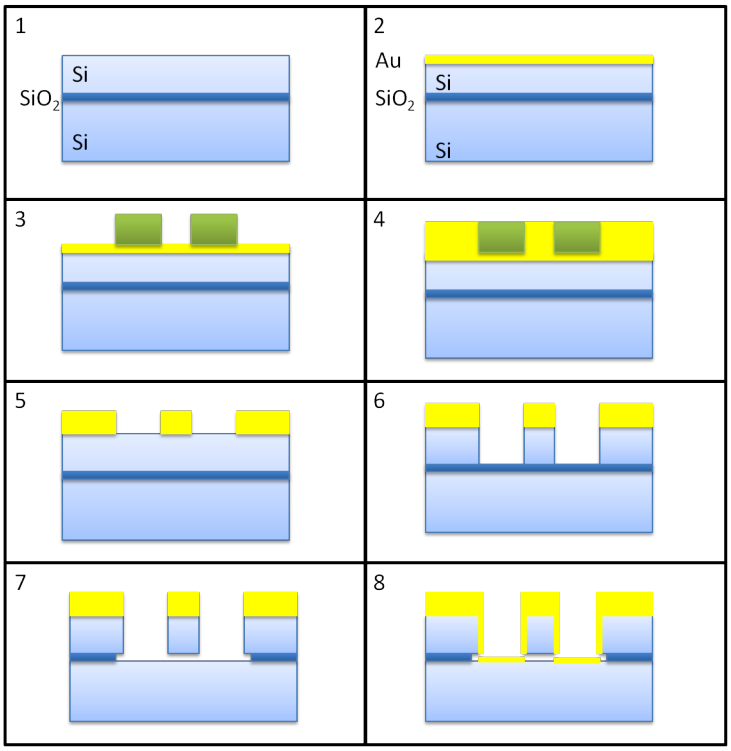

Figure 10.10: 1 SOI wafer, with 30 μm device layer, 10 μm oxide layer and 600 μm handle layer. 2 Evaporate adhesion layer of chrome followed by a Au seed layer. 3 Photoresist is deposited and pattered with the trap geometry, leaving resist covering the trenches. 4 Au electroplated to 10 μm thickness. 5 Photoresist is stripped and Au seed layer removed to expose Si. 6 A DRIE etches the device layer and exposes the buried oxide. 7 An HF etch removes the exposed SiO_2, undercutting beneath the electrodes. 8 Chrome and gold are evaporated over the trap to cover any exposed silicon.

silicon.

10.7 Conclusion

I have present work towards integrating both magnetic field gradients and microwave source onto a MEMS chip. This design would be suitable for implementing the Mintert & Wunderlich proposal [110] for coupling the spin state of the ion to its motion using microwaves. However it is not compatible with using the microwave near field to generate an oscillating magnetic field gradient [21] as this requires a zero B field at the ion. This is accomplished by Ospelkaus *et al.* [145] by using three parallel microwave sources. However this chip design should be capable of producing an order of magnitude greater magnetic field gradient than previously shown [109, 40], allowing reduced cross talk between ions and greater coupling between the internal and motion states of the ion.

Chapter 11

Conclusion

I can't be a legend yet. I'm not dead.

- Maynard James Keenan

In this thesis I have discussed the experimental setup for the successful trapping of Yb ions. This covers the design and fabrication of a macroscopic ion trap, the implementation of a laser locking scheme and the construction of a new ultra high vacuum system. This new system was designed to overcome the short comings of the existing design, which suffered from limited optical access and limits the ion trap designs that can be mounted and tested. Through the use of an adjustable mounting bracket this has opened up the ion trap experiments that are possible, offering the possibility for advanced on-chip features to be fabricated and tested.

Successful ytterbium trapping was demonstrated with the transition wavelengths measured to a greater accuracy than previously reported. Additionally an ion heating measurement showed a Yb ion heating rate consistent with traps of comparable size, alleviating concerns about ytterbium having an increased heating rate.

I presented the design and construction of several ion trap arrays, including a Y junction and 2-D ion trap lattice. The design of the Y junction is to aid the implementation of adiabatic shuttling protocols, a requirement if ions are to be shuttled through trap arrays. The 2-D ion trap lattice is a structure in which quantum simulations have been proposed. Quantum simulations have been reported in linear ion chains [105, 106], however it is necessary to extend these experiments into 2-dimensions if more detailed simulations are to be achieved. This is to my knowledge the first microfabricated 2-D ion trap lattice and should provide a key step towards multidimensional quantum simulations.

Electrical testing of microfabricated devices was performed and offers useful information into the electrical breakdown of microfabricated ion traps. These tests showed that

the electrical breakdown voltage for both rf and static voltages in our optimised fabrication is significantly above that currently using in microfabricated ion traps. This opens the door for improved surface ion trap designs and the reduction of anomalous heating. In order to achieve suitable trap depths in microfabricated surface ion traps, the ion is kept close to the electrode surface, with trap depth scaling as h^{-2} [98], where h is the ion-electrode distance. However anomalous heating, thought to result from surface patch potentials scales as h^{-4}, this can seriously inhibit the performance of ion traps with a small ion-electrode spacing and limits the quantum information processing that can be achieved. By demonstrating a fabrication design in which the electrical breakdown of electrodes occurs significantly above that currently used allows ion traps with greater ion-electrode separations to be fabricated therefore reducing anomalous heating.

Lastly a design for a microfabricated ion trap that is capable of producing a static magnetic field gradient with integrated microwave source is presented. This design is capable of generating an order of magnitude greater magnetic field gradient than previously reported [109, 40] meeting the requirements initially set by the Mintert & Wunderlich proposal [110]. This proposal is an important step towards scalable quantum computing, simplifying the requirements for entanglement of states by the use of microwaves and B-field gradients.

Bibliography

[1] J. K. Böhlke, J. R. de Laeter, P. De Bièvre, H. Hidaka, H. S. Peiser, K. J. R. Rosman, and P. D. P. Taylor. Isotopic compositions of the elements, 2001. *Institute for reference materials and measurements*, 2005. Cited on xvii, 114

[2] C. Hilsum. *Handbook on semiconductors*, volume 4. North-Holland, 1993. Cited on xvii, 126, 131

[3] Mohamed Gad el Hak, editor. *The MEMS handbook*, volume 2. CRC Press, 2005. Cited on xvii, 126

[4] Sami Franssila. *Introduction to microfabrication*, volume 1. Wiley, 2004. Cited on xvii, 126

[5] S. Kraft, A. Deninger, C. Truck, J. Fortagh, F. Lison, and C. Zimmermann. Rubidium spectroscopy at 778-780nm with a distributed feedback laser diode. *Laser physics letters*, 2(2):71–76, 2005. Cited on xxii, 66, 71, 72

[6] R. P. Feynman. Simulating physics with computers. *International journal of theoretical physics*, 21(6/7), 1982. Cited on 3

[7] D. Deutsch. Quantum theory, the Church-Turing principle and the universal quantum computer. *Proceedings of the Royal Society of London*, 400:97–117, 1985. Cited on 3

[8] P. W. Shor. Polynomial time algorithms for prime factorization and discrete logarithms on a quantum computer. *SIAM J. Comp.*, 26:1484 1509, 1997. Cited on 4

[9] D. Deutsch. A fast quantum mechanical algorithm for database search. *arXiv:quant-ph/9605043v3*, 1995. Cited on 4

[10] T. Schaetz, M. D. Barrett, D. Leibfried, J. Britton, J. Chiaverini, W. M. Itano, J. D. Jost, E. Knill, C. Langer, and D. J. Wineland. Enhanced quantum state detection

efficiency through quantum information processing. *Phys. Rev. Lett.*, 94:010501, 2005. Cited on 4, 27, 135

[11] M. Acton, K.-A. Brickman, P. C. Haljan, P. J. Lee, L. Deslauriers, and C. Monroe. Near perfect simultaneous measurement of a qubit register. *Quant. Inf. Comp*, 6(6):465–482, 2006. Cited on 4, 27, 135

[12] Chr. Wunderlich, T. Körber Th. Hannemann, H. Häffner, Ch. Roos, W. Hänsel, R. Blatt, and F. Schmidt-Kaler. Robust state preparation of a single trapped ion by adiabatic passage. *J. Mod. Opt.*, 54(11):1541–1549, 2007. Cited on 4, 27, 135

[13] A. H. Myerson, D. J. Szwer, S. C. Webster, D. T. C. Allcock, M. J. Curtis, G. Imreh, J. A. Sherman, D. N. Stacey, A. M. Steane, and D. M. Lucas. High-fidelity readout of trapped-ion qubits. *Phys. Rev. Lett.*, 100(20):200502, May 2008. Cited on 4, 27

[14] A. H. Burrell, D. J. Szwer, S. C. Webster, and D. M. Lucas. Scalable simultaneous multi-qubit readout with 99.99 single-shot fidelity. *Phys. Rev. A*, 81:040302, 2010. Cited on 4, 27

[15] C. A. Sackett, D. Kielpinski, B. E. King, C. Langer, V. Meyer, C. J. Myatt, M. Rowe, Q. A. Turchette, W. M. Itano, D. J. Wineland, and C. Monroe. Experimental entanglement of four particles. *Nature*, 404(256-259), 2000. Cited on 4, 27, 135

[16] D. Leibfried, B. DeMarco, V. Meyer, D. Lucas, M. Barrett, J. Britton, W. M. Itano, B. Jelenkovic, C. Langer, T. Rosenband, and D. J. Wineland. Experimental demonstaration of a robust, high-fidelity geometric two ion-qubit phase gate. *Nature*, 422(412-415), 2003. Cited on 4, 27, 135, 195

[17] Ferdinand Schmidt-Kaler, Hartmut Häffner, Mark Riebe, Stephan Gulde, Gavin P. T. Lancaster, Thomas Deuschle, Christoph Becher, Christian F. Roos, Jürgen Eschner, and Rainer Blatt. Realization of the Cirac-Zoller controlled-not quantum gate. *Nature*, 422(408-411), 2003. Cited on 4, 135

[18] J. Chiaverini, D. Leibfried, T. Schaetz, M. D. Barrett, R. B. Blakestad, J. Britton, W. M. Itano, J. D. Jost, E. Knill, C. Langer, R. Ozeri, and D. J. Wineland. Realisation of quantum error correction. *Nature*, 432(602-605), 2004. Cited on 4, 27, 135

[19] K.-A. Brickman, P. C. Haljan, P. J. Lee, M. Acton, L. Deslauriers, and C. Monroe.

Implementation of Grover's quantum search algorithm in a scalable system. *Phys. Rev. A*, 72:050306(R), 2005. Cited on 4, 135

[20] J. P. Home, M. J. McDonnell, D. M. Lucas, G. Imreh, B. C. Keitch, D. J. Szwer, N. R. Thomas, S. C. Webster, D. N. Stacey, and A. M. Steane. Deterministic entanglement and tomography of ion spin qubits. *New J. Phys.*, 8:188, 2006. Cited on 4

[21] C. Ospelkaus, C. E. Langer, A. H. Burrell, D. J. Szwer, S. C. Webster, D. M. Lucas, J. M. Amini, K. R. Brown, D. Leibfried, and D. J. Wineland. Trapped-ion quantum logic gates based on oscillating magnetic fields. *Phys. Rev. Lett.*, 101:090502, 2008. Cited on 4, 27, 189, 192, 195, 205

[22] T. Monz, K. Kim, W. Hänsel, M. Riebe, A. S. Villar, P. Schindler, M. Chwalla, M. Hennrich, and R. Blatt. Realization of the quantum Toffoli gate with trapped ions. *Phys. Rev. Lett.*, 102:040501, 2009. Cited on 4, 135

[23] Shannon X. Wang, Jaroslaw Labaziewicz, Yufei Ge, Ruth Shewmon, and Isaac L. Chuang. Demonstration of a quantum logic gate in a cryogenic surface-electrode ion trap. *Phys. Rev. A*, 81:062332, 2010. Cited on 4, 27, 135

[24] N. Timoney, V. Elman, S. Glaser, C. Weiss, M. Johanning, W. Neuhauser, and Chr. Wunderlich. Error-resistant single-qubit gates with trapped ions. *Phys. Rev. A*, 77:052334, 2008. Cited on 4, 135

[25] M. A. Rowe, A. Ben-Kish, B. DeMarco, D. Leibfried, V. Meyer, J. Beall, J. Britton, J. Hughes, W. M. Itano, B. Jelenkovic, C. Langer, T. Rosenband, and D. J. Wineland. Transport of quantum states and separation of ions in a dual rf ion trap. *Quant. Inf. Comp*, 2(4):257, 2002. Cited on 4

[26] R. Reichle, D. Leibfried, R.B. Blakestad, J. Britton, J.D. Jost, E. Knill, C. Langer, R. Ozeri, S. Seidelin, and D. J.Wineland. Transport dynamics of single ions in segmented microstructured paul trap arrays. *Fortschr. Phys.*, 54:666–685, 2006. Cited on 4

[27] Stephan Schulz, Ulrich Poschinger, Kilian Singer, and Ferdinand Schmidt-Kaler. Optimization of segmented linear paul traps and transport of stored particles. *Fortschr. Phys.*, 54:648–685, 2006. Cited on 4

[28] W. K. Hensinger, S. Olmschenk, D. Stick, D. Hucul, M. Yeo, M. Acton, L. Deslauriers, C. Monroe, and J. Rabchuk. T-junction ion trap array for two-dimensional ion shuttling, storage, and manipulation. *Appl. Phys. Lett.*, 88:034101, 2006. Cited on 4, 135, 136

[29] G. Huber, T. Deuschle, W. Schnitzler, R. Reichle, K. Singer, and F. Schmidt-Kaler. Transport of ions in a segmented linear paul trap in printed-circuit-board technology. *New J. Phys.*, 10(1):013004, 2008. Cited on 4

[30] R. B. Blakestad, C. Ospelkaus, A. P. VanDevender, J. M. Amini, J. Britton, D. Leibfried, and D. J. Wineland. High-fidelity transport of trapped-ion qubits through an x-junction trap array. *Phys. Rev. Lett.*, 102:153002, 2009. Cited on 4, 135, 136

[31] D. Hucul, M. Yeo, W.K. Hensinger, J. Rabchuk, S. Olmschenk, and C. Monroe. On the transport of atomic ions in linear and multidimensional ion trap arrays. *Quant. Inf. Comp*, 8(6-7):0501–0578, 2008. Cited on 4

[32] J. I. Cirac and P. Zoller. A scalable quantum computer with ions in an array of microtraps. *Nature*, 404:579–581, 2000. Cited on 4

[33] D. Kielpinski, C. Monroe, and D. J. Wineland. Architecture for a large-scale ion-trap quantum computer. *Nature*, 417:709–711, 2002. Cited on 4

[34] D. Stick, W. K. Hensinger, S. Olmschenk, M. J. Madsen, K. Schwab, and C. Monroe. Ion trap in a semiconductor chip. *Nature Phys.*, 2:36–39, 2006. Cited on 4, 124, 135, 136, 174

[35] J. Chiaverini, R. B. Blakestad, J. Britton, J. D. Jost, C. Langer, D. Leibfried, R. Ozeri, and D. J. Wineland. Surface-electrode archietchture for ion-trap quantum information pocessing. *Quant. Inf. Comp*, 5(6):419–439, 2006. Cited on 4, 136

[36] J. M. Amini, H. Uys, J. H. Wesenberg, S. Seidelin, J. Britton, J. J. Bollinger, D. Leibfried, C. Ospelkaus, A. P. VanDevender, and D. J. Wineland. Toward scalable ion traps for quantum information processing. *New J. Phys.*, 12:033031, 2010. Cited on 4, 135, 136, 141, 144

[37] J. Britton, D. Leibfried, J. Beall, R. B. Blakestad, J. J. Bollinger, J. Chiaverini, R. J. Epstein, J. D. Jost, D. Kielpinski, C. Langer, R. Ozeri, R. Reichle, S. Seidelin, N. Shiga, J. H. Wesenberg, and D. J. Wineland. A microfabricated surface-electrode ion trap in silicon. *arXiv:quant-ph/0605170*, 2006. Cited on 4, 135, 139, 158

[38] A. P. VanDevender, Y. Colombe, J. Amini, D. Leibfried, and D. J. Wineland. Efficient fiber optic detection of trapped ion fluorescence. *Phys. Rev. Lett.*, 105:023001, Jul 2010. Cited on 4

[39] C. E. Pearson, D. R. Leibrandt, W. S. Bakr, W. J. Mallard, K. R. Brown, and I. L. Chuang. Experimental investigation of planar ion traps. *Phys. Rev. A*, 73:032307, 2006. Cited on 4, 27, 139

[40] Shannon X. Wang, Jaroslaw Labaziewicz, Yufei Ge, Ruth Shewmon, and Isaac L. Chuang. Individual addressing of ions using magnetic field gradients in a surface-electrode ion trap. *Applied Physics Letters*, 94(9):094103, 2009. Cited on 4, 194, 198, 199, 205, 208

[41] H. G. Dehmelt. Radiofrequency spectroscopy of stored ions. Cited on 8, 9

[42] D. J. Wineland, C. Monroe, W. M. Itano, D. Leibfried, B. E. King, and D. M. Meekhof. Experimental issues in coherent quantum-state manipulation of trapped atomic ions. *J. Res. Natl. Inst. Stand. Technol.*, 103, 1998. Cited on 10, 12

[43] M. J. Madsen, W. K. Hensinger, D. Stick, J. A. Rabchuk, and C. Monroe. Planar ion trap geometry for microfabrication. *Appl. Phys. B*, 78(5):639–651, 2004. Cited on 10, 80, 139

[44] Wolfgang Paul. Electromagnetic traps for charged and neutral particles. *Rev. Mod. Phys.*, 62:531–540, Jul 1990. Cited on 10

[45] Brian E. King. *Quantum State Engineeriong and Information Processing with Trapped Ions*. PhD thesis, University of Colorado at Boulder, 1999. Cited on 12

[46] Steven M. Olmschenk. *Quantum Teleportation Between Distant Matter Qubits*. PhD thesis, University of Michigan, 2009. Cited on 12

[47] M. G. House. Analytic model for electrostatic fields in surface-electrode ion traps. *Phys. Rev. A*, 78:033402, Sep 2008. Cited on 13, 14, 139, 141

[48] D. Hucul, M. Yeo, S. Olmschenk, C. Monroe, W. K. Hensinger, and J. Rabchuk. On the transport of atomic ions in linear and multidimensional ion trap arrays. *Quantum Info. Comput.*, 8(6):501–578, July 2008. Cited on 13, 17, 18, 19, 140

[49] Bryan S. Morse. Lecture 11: Differential geometry. Lecture notes. Cited on 16

[50] Mary L. Boas. *Mathematical methods in the physical sciences.* Wiley, 3rd edition, 2006. Cited on 16

[51] John D. Jackson. *Classical Electrodynamics.* Wiley, 3rd edition, 1999. Cited on 17

[52] Kilian Singer, Ulrich Poschinger, Michael Murphy, Peter Ivanov, Frank Ziesel, Tommaso Calarco, and Ferdinand Schmidt-Kaler. *Colloquium* : Trapped ions as quantum bits: Essential numerical tools. *Rev. Mod. Phys.*, 82:2609–2632, Sep 2010. Cited on 20, 141

[53] M. R. Dietrich, A. Avril, R. Bowler, N. Kurz, J. S. Salacka, G. Shu, and B. B. Blinov. Barium ions for quantum computation. *arXiv:0905.2701*, 2009. Cited on 27

[54] D.J. Wineland, C. Monroe, W.M. Itano, B.E. King, D. Leibfried, D.M. Meekhof, C. Myatt, and C. Wood. Experimental primer on the trapped ion quantum computer. *Fortschr. Phys.*, 46(4-5):363–390, 1998. Cited on 27

[55] H.C. Nägerl, W. Bechter, J. Eschner, F. Schmidt-Kaler, and R. Blatt. Ion strings for quantum gates. *Appl. Phys. B*, 66:603–608, 1998. Cited on 27

[56] D. M. Lucas, C. J. S. Donald, J. P. Home, M. J. McDonnell, A. Ramos, D. N. Stacey, J.-P. Stacey, A. M. Steane, and S. C. Webster. Oxford ion-trap quantum computing project. *Phil. Trans. R. Soc. A*, 66:603–608, 1998. Cited on 27

[57] R. J. Hughes, D. F. V. James, J. J. Gomez, M. S. Gulley, M. H. Holzscheiter, P. G. Kwiat, S. K. Lamoreaux, C. G. Peterson, V. D. Sandberg, M. M. Schauer, C. M. Simmons, C. E. Thorburn, D. Tupa, P. Z. Wang, and A. G. White. The Los Alamos trapped ion quantum computer experiment. *Fortschr. Phys.*, 46:329–361, 1998. Cited on 27

[58] K. Koo, J. Sudbery, D. M. Segal, and R. C. Thompson. Doppler cooling of Ca^+ ions in a Penning trap. *Phys. Rev. A*, 69:043402, 2004. Cited on 27

[59] Stephan A. Schulz, Ulrich Poschinger, Frank Ziesel, and Ferdinand Schmidt-Kaler. Sideband cooling and coherent dynamics in a microchip multi-segmented ion trap. *New J. Phys.*, 73:045007, 2008. Cited on 27

[60] B. B. Blinov, L. Deslauriers, P. Lee, M. J. Madsen, R. Miller, and C. Monroe. Sympathetic cooling of trapped Cd^+ isotopes. *Phys. Rev. A*, 65:040304(R), 2002. Cited on 27

[61] M. D. Barrett, B. DeMarco, T. Schaetz, V. Meyer, D. Leibfried, J. Britton, J. Chiaverini, W. M. Itano, B. Jelenković, J. D. Jost, C. Langer, T. Rosenband, and D. J. Wineland. Sympathetic cooling of $^{9}Be^{+}$ and $^{24}Mg^{+}$ for quantum logic. *Phys. Rev. A*, 68:042302, 2003. Cited on 27

[62] V. Letchumanan, G. Wilpers, M. Brownnutt, P. Gill, and A. G. Sinclair. Zero-point cooling and heating-rate measurements of a single $^{88}Sr^{+}$ ion. *Phys. Rev. A*, 75:063425, 2007. Cited on 27

[63] D. Kielpinski, M. Cetina, J. A. Cox, and F. X. Kärtner. Laser cooling of trapped ytterbium ions with an ultraviolet diode laser. *Opt. Lett.*, 31(6):757, 2006. Cited on 27

[64] S. Olmschenk. *Quantum teleportation between distant matter qubits.* PhD thesis, University of Michigan, 2009. Cited on 27, 28

[65] Chr. Balzer, A. Braun, T. Hannemann, Chr. Paape, M. Ettler, W. Neuhauser, and Chr. Wunderlich. Electrodynamically trapped Yb^{+} ions for quantum information processing. *Phys. Rev. A*, 73:041407(R), 2006. Cited on 27

[66] A. S. Bell, P. Gill, H. A. Klein, A. P. Levick, Chr. Tamm, and D. Schnier. Laser cooling of trapped ytterbium ions using a four level optical-excitation scheme. *Phys. Rev. A*, 44(1):20–23, 1991. Cited on 27

[67] Peter Blythe. *Optical frequency measurement and ground state cooling of single trapped Yb^{+} ions.* PhD thesis, University of London, 2004. Cited on 28

[68] Kazumoto Hosaka, Stephen A. Webster, Peter J. Blythe, Adrian Stannard, David Beaton, Helen S. Margolis, Stephen N. Lea, and Patrick Gill. An optical frequency standard based on the electric octupole tansition in $^{171}Yb^{+}$. *IEEE Trans. Instr. Meas.*, 54(2):759–762, 2005. Cited on 28

[69] D. J. Wineland and Wayne M. Itano. Laser cooling of atoms. *Phys. Rev. A*, 20:1521–1540, Oct 1979. Cited on 29, 30

[70] J. Siverns, L. Simkins, S. Weidt, and W. Hensinger. On the application of radio frequency voltages to ion traps via helical resonators. *Applied Physics B: Lasers and Optics*, pages 1–14. 10.1007/s00340-011-4837-0. Cited on 34

[71] F. Diedrich, J. C. Bergquist, Wayne M. Itano, and D. J. Wineland. Laser cooling to the zero-point energy of motion. *Phys. Rev. Lett.*, 62(4):403–406, 1989. Cited on 38, 40

[72] J. H. Wesenberg, R. J. Epstein, D. Leibfried, R. B. Blakestad, J. Britton, J. P. Home, W. M. Itano, J. D. Jost, E. Knill, C. Langer, R. Ozeri, S. Seidelin, and D. J. Wineland. Fluorescence during doppler cooling of a single trapped atom. *Phys. Rev. A*, 76:053416, 2007. Cited on 38

[73] James J. McLoughlin, Altaf H. Nizamani, James D. Siverns, Robin C. Sterling, Marcus D. Hughes, Bjoern Lekitsch, Björn Stein, Seb Weidt, and Winfried K. Hensinger. Versatile ytterbium ion trap experiment for operation of scalable ion-trap chips with motional heating and transition-frequency measurements. *Phys. Rev. A*, 83:013406, Jan 2011. Cited on 39, 40, 41

[74] Q. A. Turchette, D. Kielpinski, B. E. King, D. Leibfried, D. M. Meekhof, C. J. Myatt, M. A. Rowe, C. A. Sackett, C. S. Wood, W. M. Itano, C. Monroe, and D. J. Wineland. Heating of trapped ions from the quantum ground state. *Phys. Rev. A*, 61:063418, 2000. Cited on 41, 42

[75] M. D. Hughes, B. Lekitsch, J. A. Broersma, and W. K. Hensinger. Microfabricated ion traps. *arXiv:1101.3207v1*, 2011. Cited on 42, 135, 136, 169

[76] A. S. Arnold, J. S. Wilson, and M. G. Boshier. A simple extended-cavity diode laser. *Review of Scientific Instruments*, 69(3):1236–1239, 1998. Cited on 43, 50

[77] Adrien Schoof, Jan Gruenert, Stephan Ritter, and Andreas Hemmerich. Reducing the linewidth of a diode laser below 30 Hz by stabilization to a reference cavity with finesse above 10^5. *Optics Letters*, 26:1562, 2001. Cited on 44

[78] W. Z. Zhao, J. E. Simsarian, L. A. Orozco, and G. D. Sprouse. A computer-baser digital feedback control of frequency drift of multiply lasers. *Rev. Sci. Instrum.*, 69(11):3737–3740, 1998. Cited on 44, 48, 49

[79] Wolfgang Demtröder. *Laser Spectroscopy basic concepts and instrumentation*. Springer, 3rd edition, 1981. Cited on 46, 47

[80] L. Ricci, M. Weidemuller, T. Esslinger, A. Hemmerich, C. Zimmermann, V. Vuletie, W. Konig, and T. W. Hansch. A compact grating-stabilized diode laser system for atomic physics. *Optics Communications*, 117, 1995. Cited on 50

[81] K. C. Harvey and C. J. Myatt. External-cavity diode laser using a grazing-incidence diffraction grating. *Optics Letters*, 16, 1991. Cited on 50, 51

[82] Eugene Hecht. *Optics*. Addison Wesley, 4th edition, 2002. Cited on 55

[83] Hamamatsu. *Si PIN photodiode S5971, S5972, S5973 series datasheet*, 2005. Cited on 62

[84] Ayan Banerjee and Vasant Natarajan. Saturated-absorption spectroscopy: eliminating crossover resonances by use of copropagating beams. *Opt. Lett.*, 28(20):1912–1914, Oct 2003. Cited on 65

[85] D. W. Allan. Time and frequency (time-domain) characterization, estimation, and prediction of precision clocks and oscillators. *IEEE Transactions on ultrasonics, ferroelectrics and frequency control*, 34(6):647–654, November 1987. Cited on 70

[86] Jaroslaw Labaziewicz, Yufei Ge, Paul Antohi, David Leibrandt, Kenneth R. Brown, and Isaac L. Chuang. Suppression of heating rates in cryogenic surface-electrode ion traps. *Phys. Rev. Lett.*, 100:013001, 2008. Cited on 110

[87] K. Odaka and S. Ueda. Dependance of outgassing rate on surface oxide layer thickness in type 304 stainless steel before and after surface oxidation in air. *Vacuum*, 47:689–692, 1996. Cited on 116

[88] D. Stick, W. K. Hensinger, S. Olmschenk, M. J. Madsen, K. Schwab, and C. Monroe. Ion trap in a semicondunctor chip. *Nature Physics*, 2005. Cited on 124

[89] S. Seidelin, J. Chiaverini, R. Reichle, J. J. Bollinger, D. Leibfried, J. Britton, J. H. Wesenberg, R. B. Blakestad, R. J. Epstein, D. B. Hume, W. M. Itano, J. D. Jost, C. Langer, R. Ozeri, N. Shiga, and D. J. Wineland. Microfabricated surface-electrode ion trap for scalable quantum information processing. *Phys. Rev. Lett.*, 96:253003, 2006. Cited on 124, 135, 136

[90] John D. Kraus and Daniel A. Fleisch. *Electromagnetics with applications*. Mc Graw-Hill, 5 edition, 1999. Cited on 130, 131, 132

[91] R. G. Chambers. *Electrons in metals and semiconductors*. Chapman and Hall, 1990. Cited on 130, 132

[92] J. D. Jackson. *Classical electrodynamics*. Wiley, 3 edition, 1999. Cited on 130

[93] B. Van Zeghbroeck. *Principles of semiconductor devices*. 2007. Cited on 131

[94] D. P. DiVincenzo. Quantum computation. *Science*, 269:255–261, 1995. Cited on 135

[95] J.J. Bollinger, D.J. Heizen, W.M. Itano, S.L. Gilbert, and D.J. Wineland. A 303-mhz frequency standard based on trapped Be+ ions. *Instrumentation and Measurement, IEEE Transactions on*, 40(2):126 – 128, apr 1991. Cited on 135

[96] Jingbao Liu, S. Sundar Kumar Iyer, Chenming Hu, Nathan W. Cheung, Ron Gronsky, Jing Min, and Paul Chu. Formation of buried oxide in silicon using separation by plasma implantation of oxygen. *Appl. Phys. Lett.*, 67(16):2361–2363, 1995. Cited on 137

[97] Michel Bruel, Bernard Aspar, and Andre-Jacques Auberton-Hervé. Smart-cut: A new silicon on insulator material technology based on hydrogen implantation and wafer bonding*[1]. *Japanese Journal of Applied Physics*, 36(Part 1, No. 3B):1636–1641, 1997. Cited on 137

[98] A. H. Nizamani and W. K. Hensinger. Optimum electrode configurations for fast ion serparation in microfabricated surface ion traps. *arXiv:1007.3542v1*, 2010. Cited on 139, 208

[99] Michael Johanning, Andrés F. Varón, and Christof Wunderlich. Quantum simulations with cold trapped ions. *J. Phys. B*, 42(15):154009, 2009. Cited on 143

[100] D. Porras and J. I. Cirac. Effective quantum spin systems with trapped ions. *Phys. Rev. Lett.*, 92:207901, May 2004. Cited on 143

[101] D. Porras and J. I. Cirac. Quantum manipulation of trapped ions in two dimensional coulomb crystals. *Phys. Rev. Lett.*, 96:250501, Jun 2006. Cited on 143

[102] X.-L. Deng, D. Porras, and J. I. Cirac. Effective spin quantum phases in systems of trapped ions. *Phys. Rev. A*, 72:063407, Dec 2005. Cited on 143

[103] D. Porras and J. I. Cirac. Bose-einstein condensation and strong-correlation behavior of phonons in ion traps. *Phys. Rev. Lett.*, 93:263602, Dec 2004. Cited on 143

[104] J. P. Barjaktarevic, G. J. Milburn, and Ross H. McKenzie. Fast simulation of a quantum phase transition in an ion-trap realizable unitary map. *Phys. Rev. A*, 71:012335, Jan 2005. Cited on 143

[105] A. Friedenauer, H. Schmitz, J. T. Glueckert, D. Porras, and T. Schaetz. Simulating a quantum magnet with trapped ions. *Nature Phys.*, 4:757–761, 2008. Cited on 143, 207

[106] K. Kim, M.-S. Chang, S. Korenblit, R. Islam, E. E. Edwards, J. K. Freericks, G.-D. Lin, L.-M. Duan, and C. Monroe. Quantum simulation of frustrated Ising spins with trapped ions. *Nature*, 465(590-593), 2010. Cited on 143, 207

[107] Robert J. Clark, Tongyan Lin, Kenneth R. Brown, and Isaac L. Chuang. A two-dimensional lattice ion trap for quantum simulation. *J. Appl. Phys.*, 105:013114, 2009. Cited on 143

[108] Roman Schmied, Janus H. Wesenberg, and Dietrich Leibfried. Optimal surface-electrode trap lattices for quantum simulation with trapped ions. *Phys. Rev. Lett.*, 102:233002, Jun 2009. Cited on 144

[109] M. Johanning, A. Braun, N. Timoney, V. Elman, W. Neuhauser, and Chr Wunderlich. Individual addressing of trapped ions and coupling of motional and spin states using rf radiation. *Phys. Rev. Lett.*, 102:073004, 2009. Cited on 159, 160, 189, 192, 194, 198, 201, 205, 208

[110] Florian Mintert and Christof Wunderlich. Ion-trap quantum logic using long-wavelength radiation. *Phys. Rev. Lett.*, 87:257904, Nov 2001. Cited on 161, 189, 192, 193, 198, 205, 208

[111] D. J. Berkeland, J. D. Miller, J. C. Bergquist, W. M. Itano, and D. J. Wineland. Minimization of ion micromotion in a paul trap. *Journal of Applied Physics*, 83(10):5025–5033, 1998. Cited on 164

[112] Joe Britton. *Microfabrication techniques for trapped ion quantum information processing.* PhD thesis, University of Colorado, 2008. Cited on 164

[113] S. Groth, P. Kruger, S. Wildermuth, R. Folman, T. Fernholz, J. Schmiedmayer, D. Mahalu, and I. Bar-Joseph. Atom chips: Fabrication and thermal properties. *Appl. Phys. Lett.*, 85(14):2980–2982, 2004. Cited on 165

[114] A. H. Nizamamni and W. K. Hensinger. Optimum electrode configurations for fast ion separation in microfabricated surface ion traps. *arXiv:1007.3542v1*, 2010. Cited on 165

[115] C. H. Cheng, S. C. Chen, and Z. S. Chen. Multilevel electroforming for the components of a microdroplet ejector by uv liga technology. *J. Micromech. Mircoeng.*, 15. Cited on 165

[116] Friedrich Paschen. Ueber die zum funkenübergang in luft, wasserstoff und kohlensäure bei verschiedenen drucken erforderliche potentialdifferenz. *Annalen der Physik*, 273(5):69–96, 1889. Cited on 169

[117] Takahito Ono, Dong Youn Sim, and Masayoshi Esashi. Micro-discharge and electric breakdown in a micro-gap. *J. Micromech. Microeng.*, 10:445–451, 2000. Cited on 169

[118] F. W. Strong, J. L. Skinner, and N. C. Tien. Electrical discharge across micrometer-scale gaps for planar MEMS structures in air at atmospheric pressure. *J. Micromech. Microeng.*, 18:075025, 2008. Cited on 169

[119] Ching-Heng Chen, J. A. Yen, and Pei-Jen Wang. Electrical breakdown phenomena for devices with micron separations. *J. Micromech. Microeng.*, 16:1366–1373, 2006. Cited on 169

[120] C.G. Wilson, Y.B. Gianchandani, and A.E. Wendt. High-voltage constraints for vacuum packaged microstructures. *Microelectromechanical Systems, Journal of*, 12(6):835 – 839, dec. 2003. Cited on 169

[121] P. Carazzetti, Ph. Renaud, and H. R. Shea. Experimental study of electrical breakdown in MEMS devices with micrometer scale gaps. *Proceedings of SPIE*, 6884, 2008. Cited on 169

[122] M. D. Paine, S. Gabriel, C. G. J. Schabmueller, and A. G. R. Evans. Realisation of very high voltage electrode-nozzle systems for MEMS. *Sensors and Actuators A: Physical*, 114(1):112 – 117, 2004. Cited on 169, 170

[123] J. Mueller, D. Pyle, I. Chakraborty, R. Ruiz, W. Tang, and R. Lawton. Feasibility study fo MEMS-based accelerator grid systems for micro-ion engines: electrical breakdown characteristics. *AIAA Journal of Propulsion and power U.S.A.*, 1999. Cited on 169, 170, 187

[124] R. Krpoun and H. R. Shea. Integrated out-of-plane nanoelectroscpray thruster arrays for spacecraft propulsion. *J. Micromech. Microeng.*, 19, 2009. Cited on 169

[125] R. Krpoun, M. Rdber, and H.R. Shea. Microfabrication and test of an integrated colloid thruster. In *Micro Electro Mechanical Systems, 2008. MEMS 2008. IEEE 21st International Conference on*, pages 964 –967, jan. 2008. Cited on 169

[126] B. Gassend, L.F. Velasquez-Garcia, A.I. Akinwande, and M. Martinez-Sanchez. A microfabricated planar electrospray array ionic liquid ion source with integrated extractor. *Microelectromechanical Systems, Journal of*, 18(3):679 –694, june 2009. Cited on 169

[127] J.-C. Mateo-Velez, V. Inguimbert, J.-F. Roussel, D. Sarrail, L. Levy, F. Boulay, E. Laffont, and D. Payan. Esds on solar cells-degradation, modeling, and importance of the test setup. *IEEE Transactions on Plasma Science*, 2008. Cited on 169

[128] J.-M. Siguier, V. Inguimbert, P. Sarrailh, D. Sarrail, G. Murat, J. Mateo-Velez, D. Payan, and N. Balcon. Parametric study of a physical flashover simulator. *Plasma Science, IEEE Transactions on*, 40(2):311 –320, feb. 2012. Cited on 169

[129] V. Inguimbert, D. Sarrail, J.-C. Mateo-Velez, R. Reulet, L. Levy, F. Boulay, and D. Payan. Electrostatic discharge and secondary arcing on solar array x2014;flashover effect on arc occurrence. *Plasma Science, IEEE Transactions on*, 36(5):2404 –2412, oct. 2008. Cited on 169

[130] J. Britton, D. Leibfried, J. A. Beall, R. B. Blakestad, J. H. Wesenberg, and D. J. Wineland. Scalable arrays of rf paul traps in degenerate Si. *App. Phys. Lett.*, 95(17):173102, 2009. Cited on 170

[131] Q. A. Turchette, Kielpinski, B. E. King, D. Leibfried, D. M. Meekhof, C. J. Myatt, M. A. Rowe, C. A. Sackett, C. S. Wood, W. M. Itano, C. Monroe, and D. J. Wineland. Heating of trapped ions from the quantum ground state. *Phys. Rev. A*, 61:063418, May 2000. Cited on 170

[132] H.C. Miller. Surface flashover of insulators. *Electrical Insulation, IEEE Transactions on*, 24(5):765 –786, oct 1989. Cited on 170

[133] A. Neuber, M. Butcher, L. L. Hatfield, and H. Krompholz. Electric current in dc surface flashover in vacuum. *Journal of Applied Physics*, 85(6):3084–3091, 1999. Cited on 170, 171, 172, 173

[134] A. Sivathanu Pillai and Reuben Hackam. Surface flashover of solid dielectric in vacuum. *Journal of Applied Physics*, 53(4):2983–2987, 1982. Cited on 170, 171, 172

[135] R. A. Anderson and J. P. Brainard. Mechanism of pulsed surface flashover involving electron-stimulated desorption. *Journal of Applied Physics*, 51(3):1414–1421, 1980. Cited on 172, 173

[136] A. Sivathanu Pillai and Reuben Hackam. Surface flashover of solid insulators in atmospheric air and in vacuum. *Journal of Applied Physics*, 58(1):146–153, 1985. Cited on 172, 173

[137] A. Neuber, M. Butcher, H. Krompholz, L.L. Hatfield, and M. Kristiansen. The role of outgassing in surface flashover under vacuum. In *Pulsed Power Conference, 1999. Digest of Technical Papers. 12th IEEE International*, volume 1, pages 441 –445 vol.1, 1999. Cited on 172

[138] J. H. Leck and B. P. Stimpson. Desorption from gas covered surfaces by electron impact: A review of the subject. *Journal of Vacuum Science and Technology*, 9(1):293 –300, jan 1972. Cited on 172

[139] AA Avdienko and MD Malev. Flashover in a vacuum. *Vacuum*, 27(12):643 – 651, 1977. Cited on 172, 173

[140] J. S. Blakemore. *Solid State Physics*. Cambridge university press, 2 edition, 1985. Cited on 174

[141] H.C. Miller. Surface flashover of insulators. *Electrical Insulation, IEEE Transactions on*, 24(5):765 –786, oct 1989. Cited on 175

[142] Jaroslaw Labaziewicz, Yufei Ge, Paul Antohi, David Leibrandt, Kenneth R. Brown, and Isaac L. Chuang. Suppression of heating rates in cryogenic surface-electrode ion traps. *Phys. Rev. Lett.*, 100:013001, Jan 2008. Cited on 187

[143] MQ Ding and EM Williams. Electron stimulated desorption of gases at technological surfaces of aluminium. *Vacuum*, 39(5):463 – 469, 1989. Cited on 187

[144] D. A. Hite, Y. Colombe, A. C. Wilson, K. R. Brown, U. Warring, R. Jördens, J. D. Jost, D. P. Pappas, D. Leibfriend, and D. J. Wineland. Reduction of anomalous heating in an in-situ-cleaned ion trap. *arXiv:1112.5419v1*, 2011. Cited on 187

[145] C. Ospelkaus, U. Warring, Y. Colombe, K. R. Brown, J. M. Amini, D. Leibfried, and D. J. Wineland. Microwave quantum logic gates for trapped ions. *arXiv:1104.3573v1*, 2011. Cited on 189, 192, 195, 205

[146] Ch. Wunderlich and Ch. Balzer. Quantum measurements and new concepts for experiments with trapped ions. *Advances in Atomic, Molecular, and Optical Physics*, 49:295–376, 2003. Cited on 189, 192, 193

[147] J. I. Cirac and P. Zoller. Quantum computations with cold trapped ions. *Phys. Rev. Lett.*, 74(20):4091–4094, 1995. Cited on 190

[148] D. Leibfried, R. Blatt, C. Monroe, and D. Wineland. Quantum dynamics of single trapped ions. *Rev. Mod. Phys.*, 75:281–324, Mar 2003. Cited on 190

[149] Patricia J. Lee. *Quantum Information Processing with Two Trapped Cadmium Ions*. PhD thesis, University of Michigan, 2006. Cited on 190

[150] Kathy-Ann Brickmann. *Implementation of Grover's quantum search algorithm with two trapped cadmium ions*. PhD thesis, University of Michigan, 2007. Cited on 190

[151] Harold J. Metcalf and Peter van der Straten. *Laser cooling and trapping*. Springer, 1999. Cited on 191

[152] D. Leibfried, E. Knill, C. Ospelkaus, and D. J. Wineland. Transport quantum logic gates for trapped ions. *Phys. Rev. A*, 76:032324, Sep 2007. Cited on 192, 194

[153] Klaus Mølmer and Anders Sørensen. Multiparticle entanglement of hot trapped ions. *Phys. Rev. Lett.*, 82:1835–1838, Mar 1999. Cited on 195

[154] Jaroslaw Labaziewicz, Yufei Ge, David R. Leibrandt, Shannon X. Wang, Ruth Shewmon, and Isaac L. Chuang. Temperature dependence of electric field noise above gold surfaces. *Phys. Rev. Lett.*, 101:180602, Oct 2008. Cited on 202

[155] Tae-In Jeon and D. Grischkowsky. Nature of conduction in doped silicon. *Phys. Rev. Lett.*, 78:1106–1109, Feb 1997. Cited on 203

Appendix A

Ion trap simulations with CPO-3D

To describe the process of simulating a trap structure I will demonstrate how to model a linear Paul trap with four rod electrodes. Once CPO-3D has been opened a demo file must be opened. By going to `File`→`Open for running and databuilding` this allows the user to open a demo file and amend the electrode structure as well as run simulations.

Once a demo file has been opened we now want to modify the electrodes. This is done by opening `Databuilder` from the top menu bar. The Databuilder has a list of options shown in Fig. A.1. These allow the user to modify the electrode geometry, assign electrode voltages, extract data and set up charged particles such as electrons and ions.

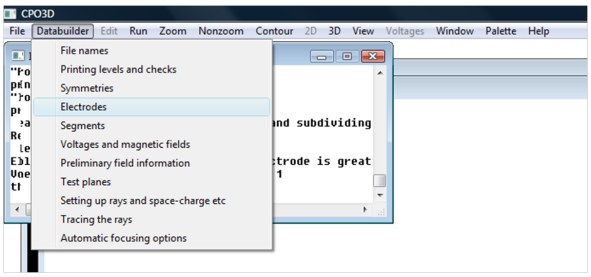

Figure A.1: The Databuilder drop down menu. Selecting `Electrodes` opens a dialog box in which electrodes can be added and manipulated.

Selecting `Electrodes` opens a dialog box as shown in Fig. A.2(a), first the existing electrodes are deleted and the cylindrical electrodes can be inputted. By selecting `Add` opens a list of possible electrodes already defined by CPO, shown in Fig. A.2(a).

Selecting `complete cylindrical surface` as shown in Fig. A.2b and selecting ok opens another dialog box shown in Fig. A.3.

In this box, it asks the user to enter the defining dimensions of the intended electrode, all units are in millimeters. For this example the rod electrodes have a radius of $r = 0.25$ mm and the first electrode is positioned to be parallel to the z axis with a length of 1 mm

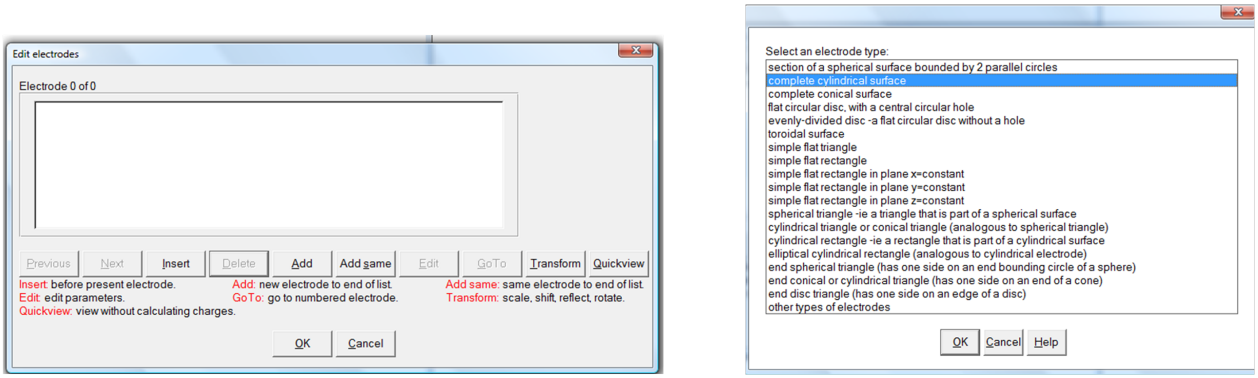

(a) Electrode navigation window.

(b) List of CPO preset electrode shapes.

Figure A.2: Electrode input dialog boxes.

and the center of the rod is at $x = 0.5$ mm and $y = 0.5$ mm, corresponding to the top right corner. Then the electrode has a voltage tag assigned, for this electrode a voltage tag of 1 is assigned. The voltage tag is used as an identifier, when running the simulation each tag is given a corresponding voltage. Then all the electrodes with the matching voltage tag have the appropriate voltage applied. For most simulations it is sufficient to only use two tags, one set to 1V for the static basis function and a second tag setting all other electrodes to 0V. Finally the number of segments that the electrode is to be divided up into is set. CPO generates all shapes from rectangles, with the most accurate results from square or nearly square rectangles. As this electrode is representing a cylinder, a sufficient number of segments round the axis is needed to ensure that it closely approximates a cylinder, if only 4 segments was chosen then it would have a square profile! For this the subdivisions around the axis was chosen to be 20 with the z-axis divided into 15 segments. This results in nearly square segments which can be seen in Fig. A.4(b) which is a view of the yz plane after all four rods have been input. The colour of the electrodes correspond to their voltage tag, red = voltage tag 1, green = voltage tag 2 etc. The colour key can be found in the `Palette` menu.

With the full trap geometry now uploaded, voltages to the electrodes need to be applied. By going to `Databuilder`→`Voltages and magnetic fields` opens a dialog box as shown in Fig. A.5

Here a voltage corresponding to the voltage tag can be assigned. The trap has rf potentials on the bottom right and top left electrodes, both with a voltage tag of 1. The other two electrodes have a voltage tag of 2 and remain at 0 volts. Now by selecting `Run`→`All 3 views` CPO evaluates the surface integrals of all the segments, displaying a progress bar, Fig. A.6

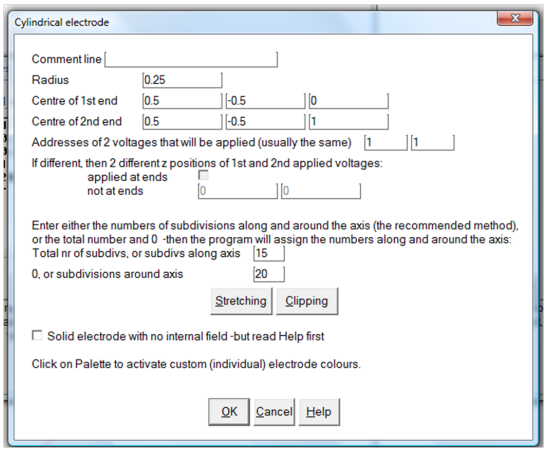

Figure A.3: Dialog box with several input boxes. The electrode geometry, voltage addresses and number of segments can all be entered.

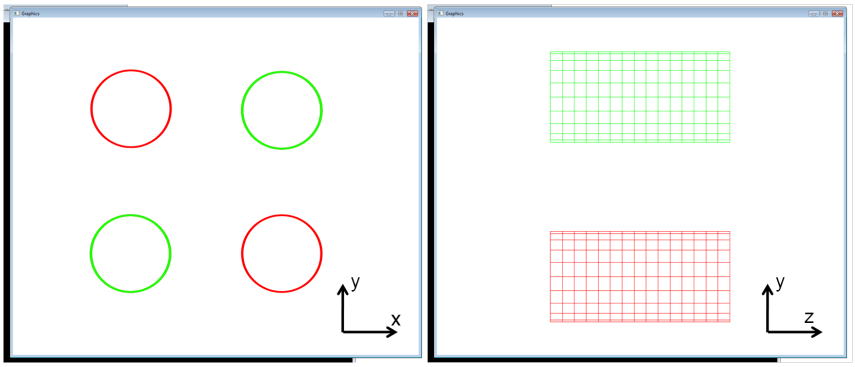

(a) (b)

Figure A.4: a) Front view of the four cylinder electrodes, red corresponds to rf, green is ground. b) Side view of two of the electrode cylinders.

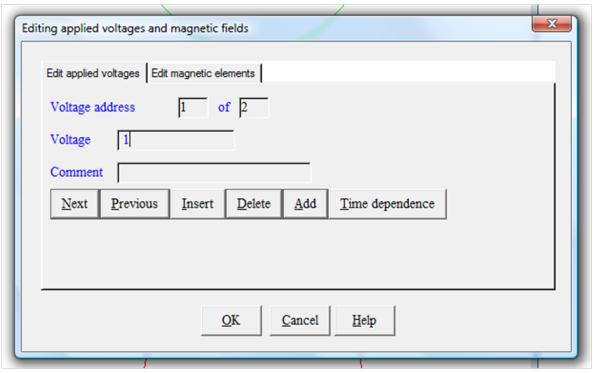

Figure A.5: Dialog box allows voltages to be assigned to the corresponding electrodes. To take the rf basis function 1 V is applied to the rf electrodes with all other electrodes at 0 V.

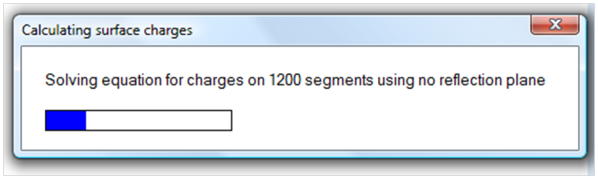

Figure A.6: Progress bar while CPO solves the equations over all the segments.

Once the simulation is complete it is possible to view colour, contour, vector or grid plots of the resulting potential or electric field. By selecting `Contour→Electric field→Contour` opens a dialog box in which contour parameters can be set. Increasing the number of contours to 50 and leaving the rest as default CPO will plot a contour plot as shown in Fig. A.7.

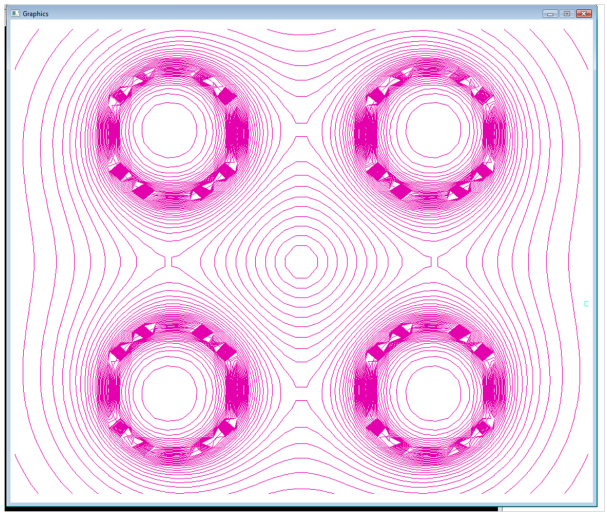

Figure A.7: Contourplot of the electric field contours.

Now to extract data from the trapping region we first need to open `Databuilder→Preliminary field information`. This allows data to be extracted from any arbitrary point in the simulation. The different data extract modes are `Along a line`, which takes a number of points n along any line defined by the user. `Along a circle`, takes n data points along a circular trajectory set by the user. `On a 2D grid`, this takes a 2D array of $i \times j$ data points in a plane through the simulation and finally `On a 3D grid` which takes a 3D array of $i \times j \times k$ data points. We wish to extract 3D data from the central trapping region, by setting the x, y, z start position, the number of data points i, j, k and the spacing between each data point we define the volume that CPO will extract data from.

Next the data type we wish to extract is chosen from `Electrostatic Potentials`, `Electrostatic Fields`, `Magnetic field` and `Magnetic vector potential`. We wish to extract the electrostatic potential and set the accuracy level to the maximum allowed

by CPO of 10^{-7} V.

Before we run the simulation the output data file name needs to be set. By going to `Databuilder→File names` and in the `Ray output data filename` box the output data filename can be set. Now the simulation is run again, this time the segments have already been solved so the potentials from the electrodes have already been calculated now these equations are solved at each node position of the 3D array and outputs a data file of x, y, z position followed by the value of the potential. The beginning of the data file contains a header and this must be removed before the data can be used in Mathematica.

Appendix B

Laser locking

B.1 Confocal cavity design drawings

Workshop design drawings for the 739/780 nm confocal cavity and mirror holder.

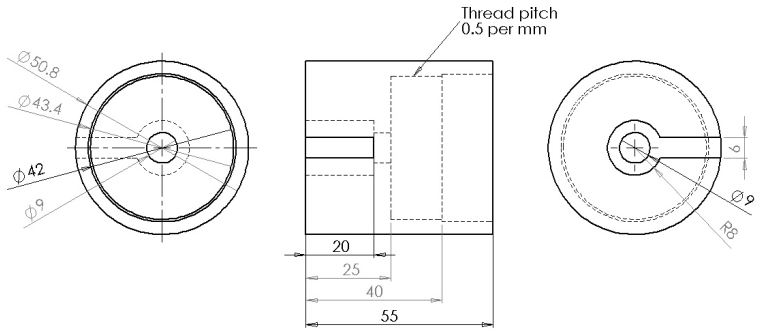

Figure B.1: The female section of the 739/780 nm cavity.

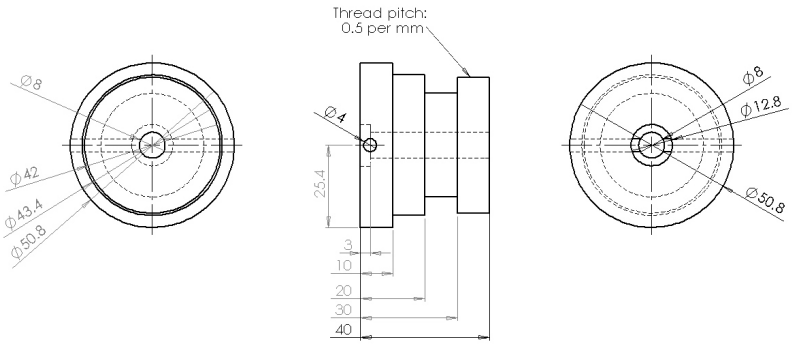

Figure B.2: The male section of the 739/780 nm cavity.

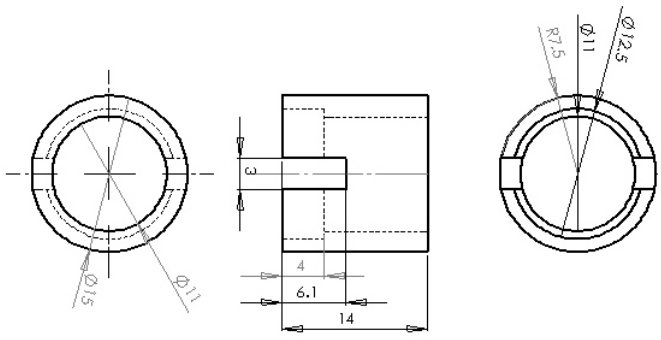

Figure B.3: The mirror holder, a mirror is glued into the holder which then screws onto a ring piezo.

Appendix C

Blade trap

C.1 Blade trap design drawings

Workshop design drawings for all the component parts of the blade ion trap.

Figure C.1: An isometic SolidWorks drawing of the PEEK base.

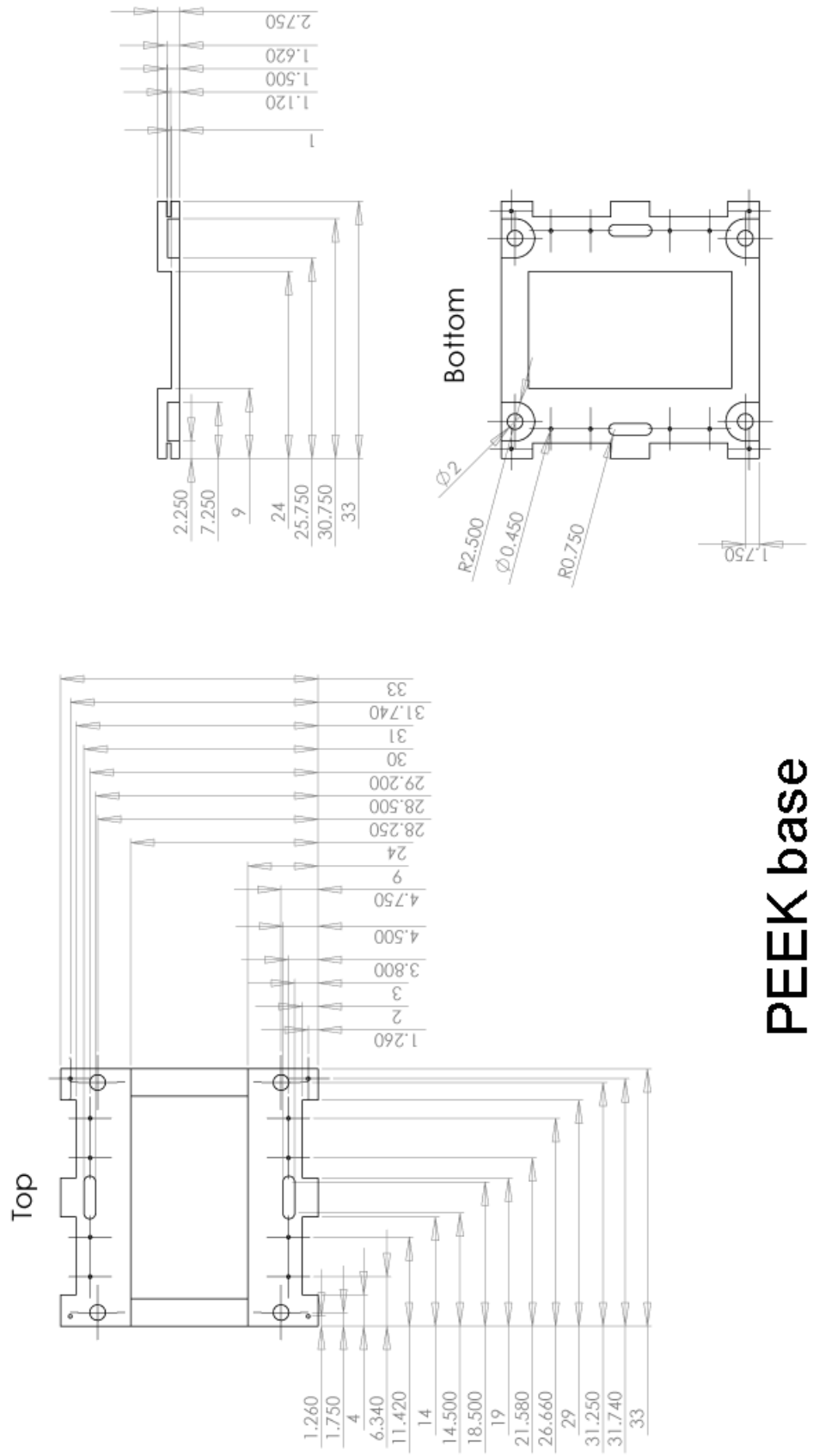

Figure C.2: A SolidWorks drawing of the PEEK base.

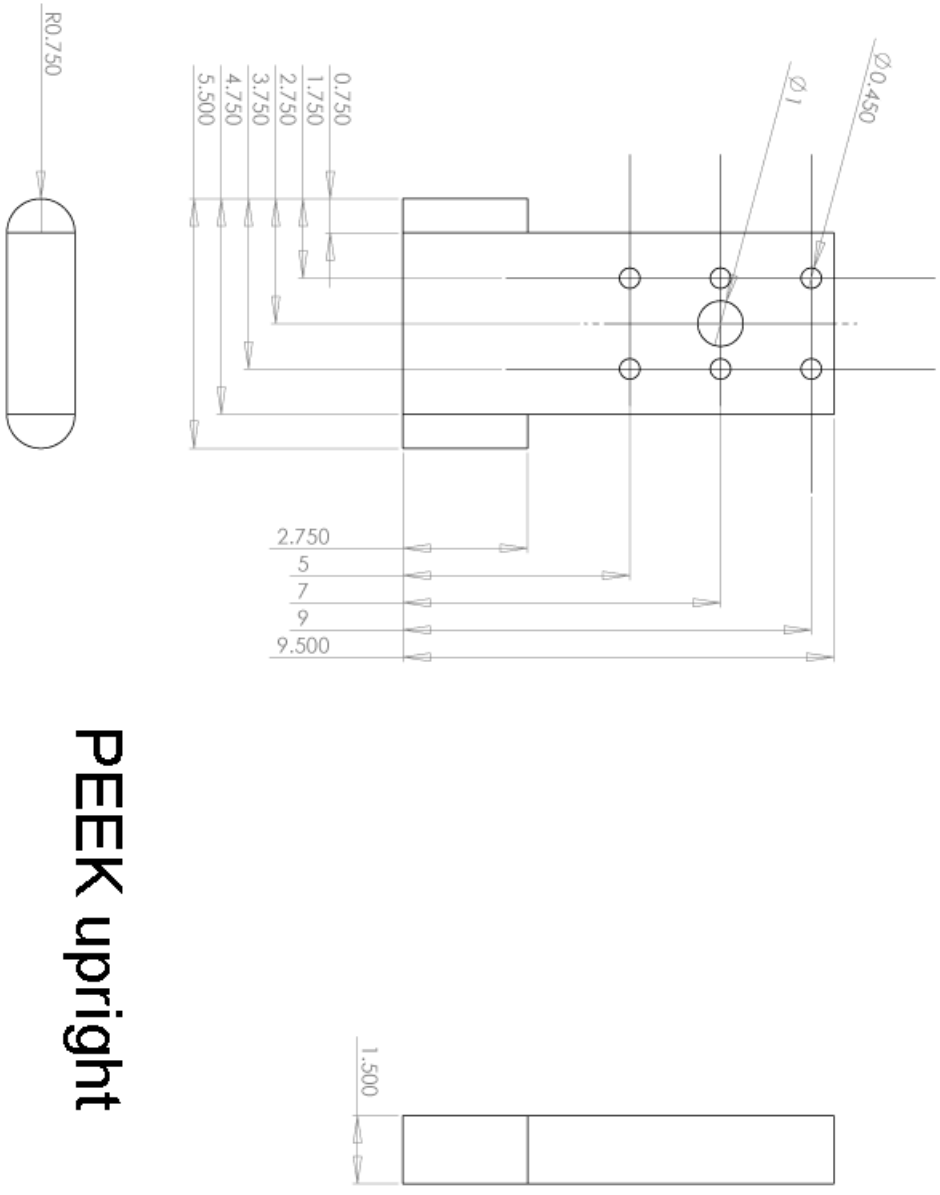

Figure C.3: A SolidWorks drawing of the PEEK upright.

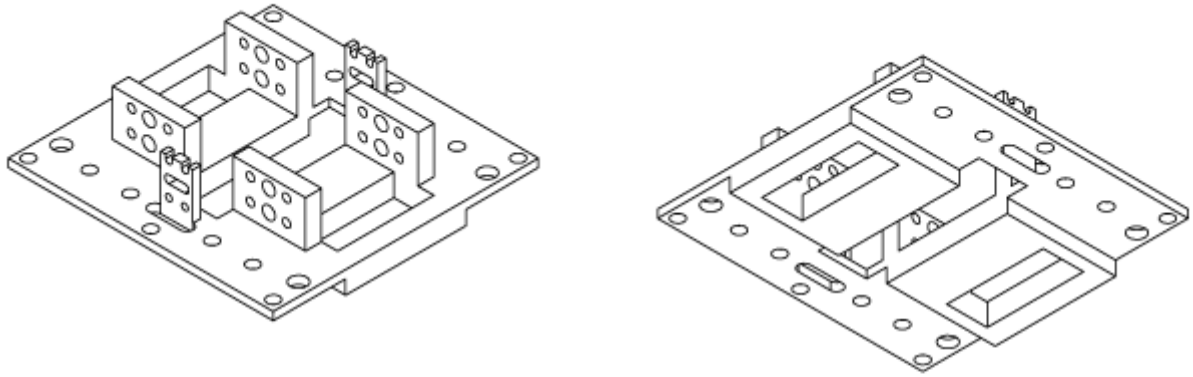

Figure C.4: An isometric SolidWorks drawing of the metal mount.

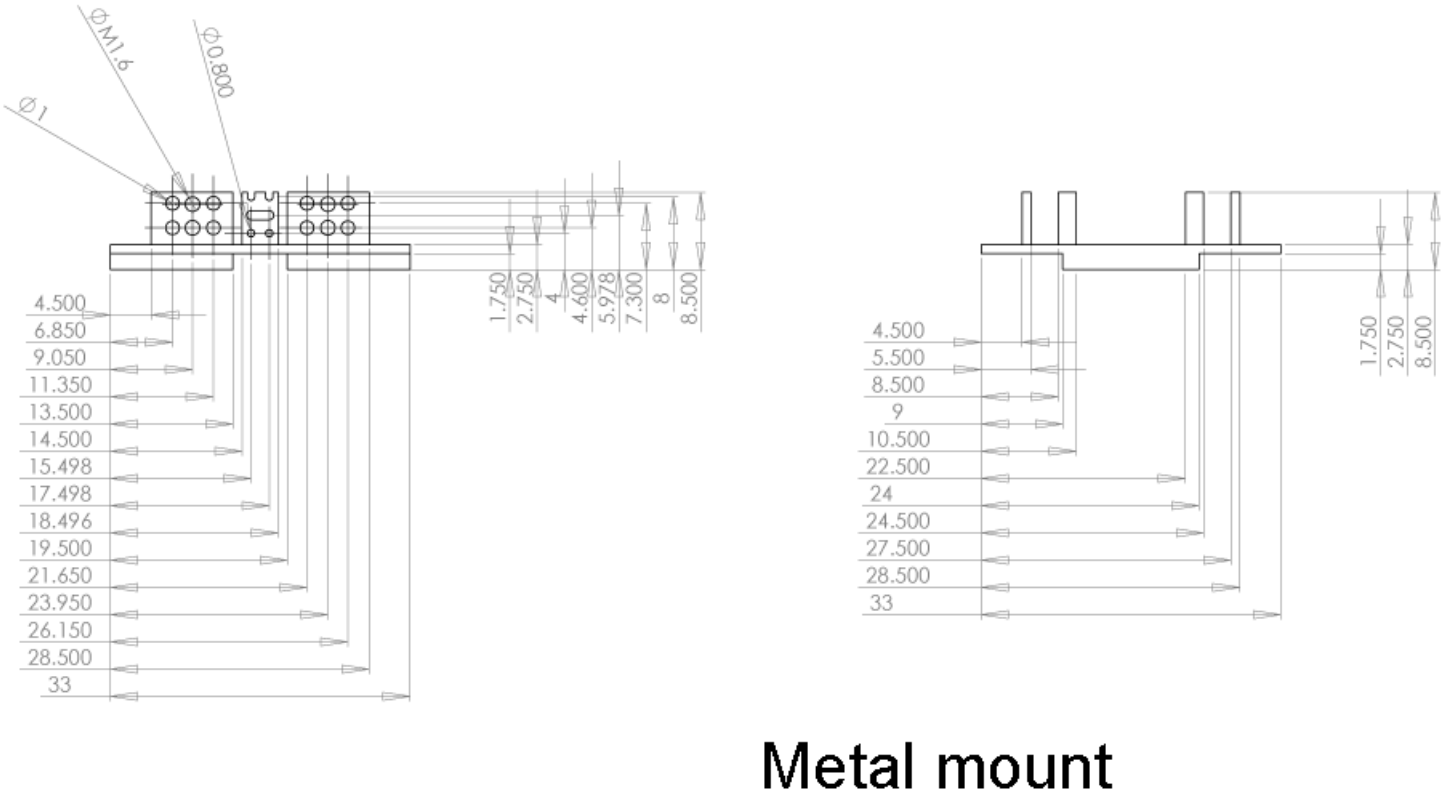

Figure C.5: A SolidWorks drawing of the side of the metal mount.

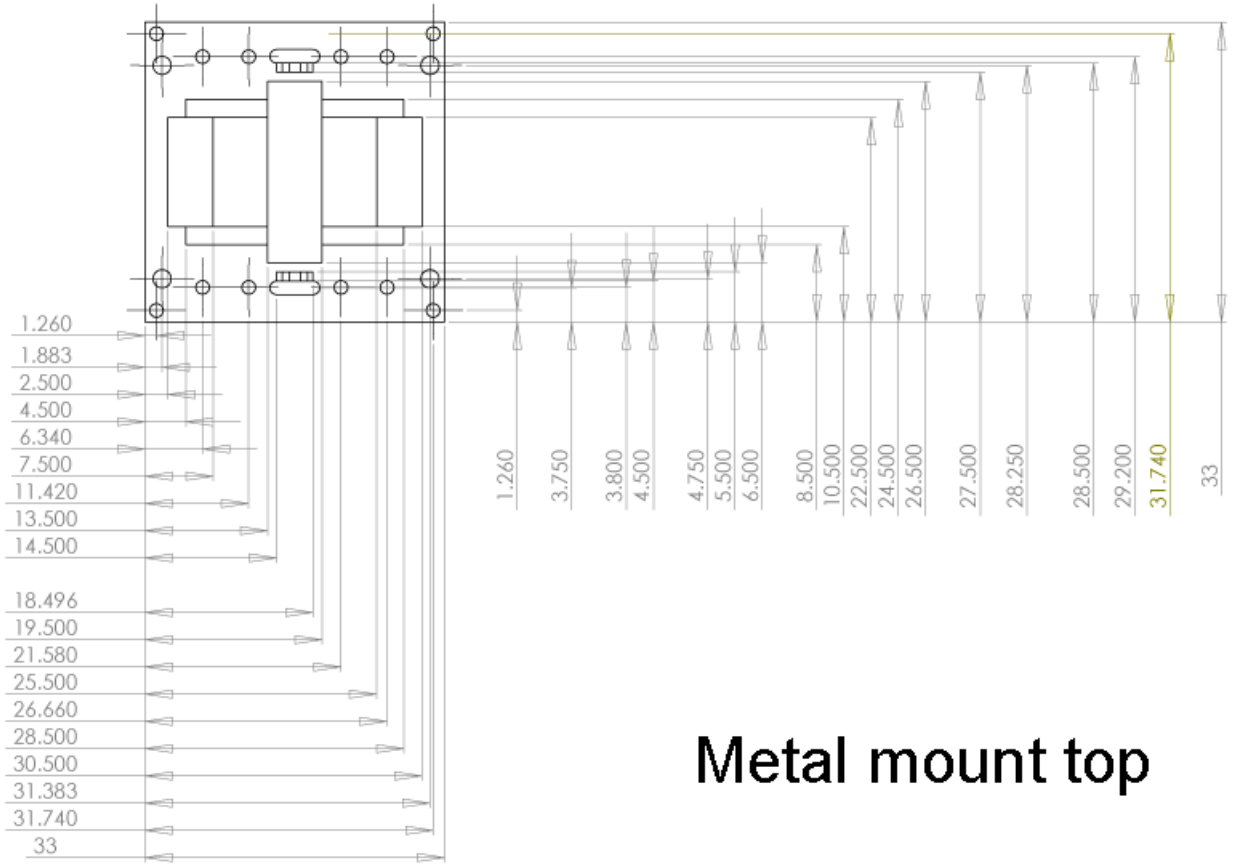

Figure C.6: A SolidWorks drawing of the top of the metal mount.

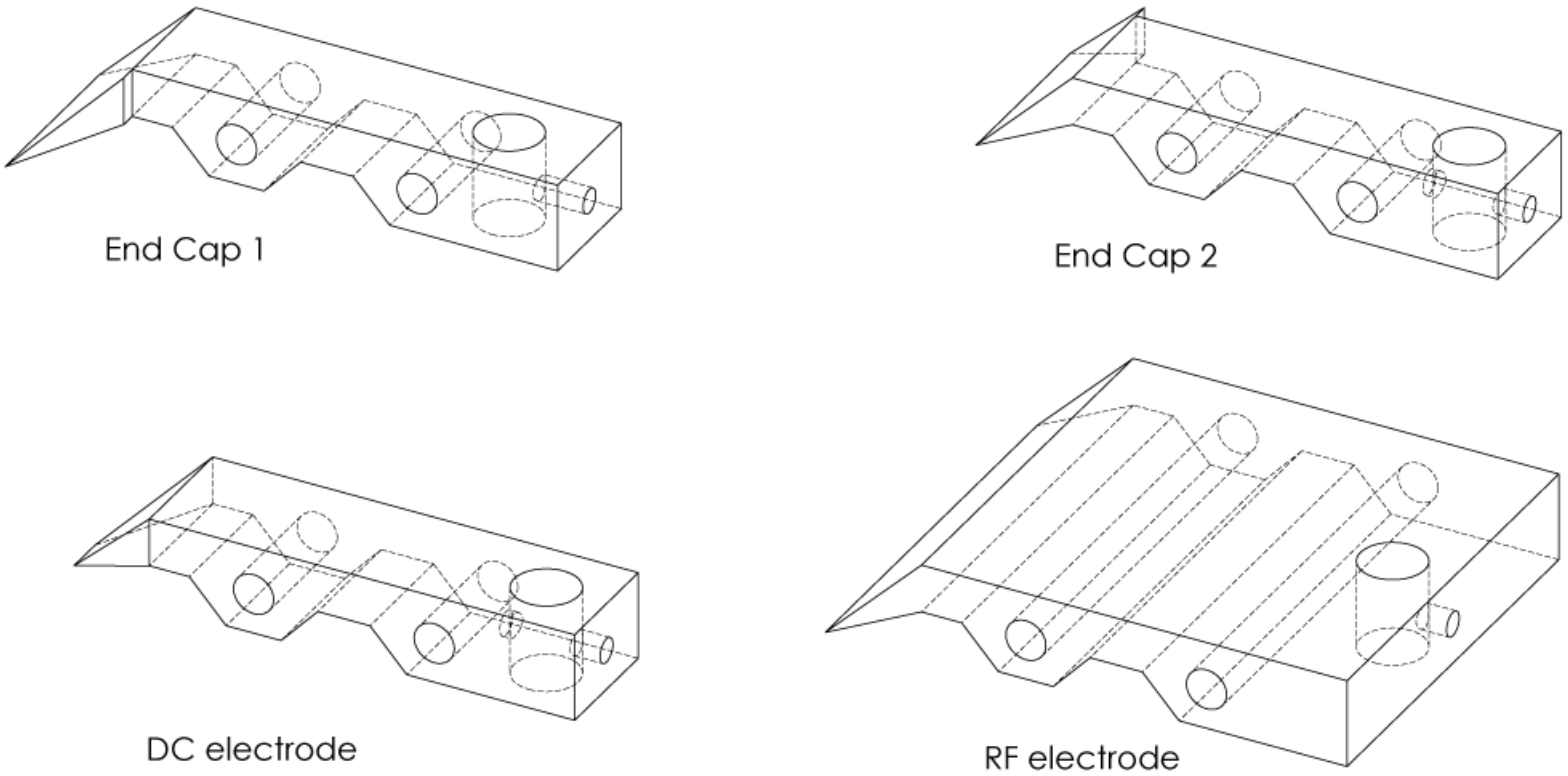

Figure C.7: Isometric SolidWorks drawings of the electrodes.

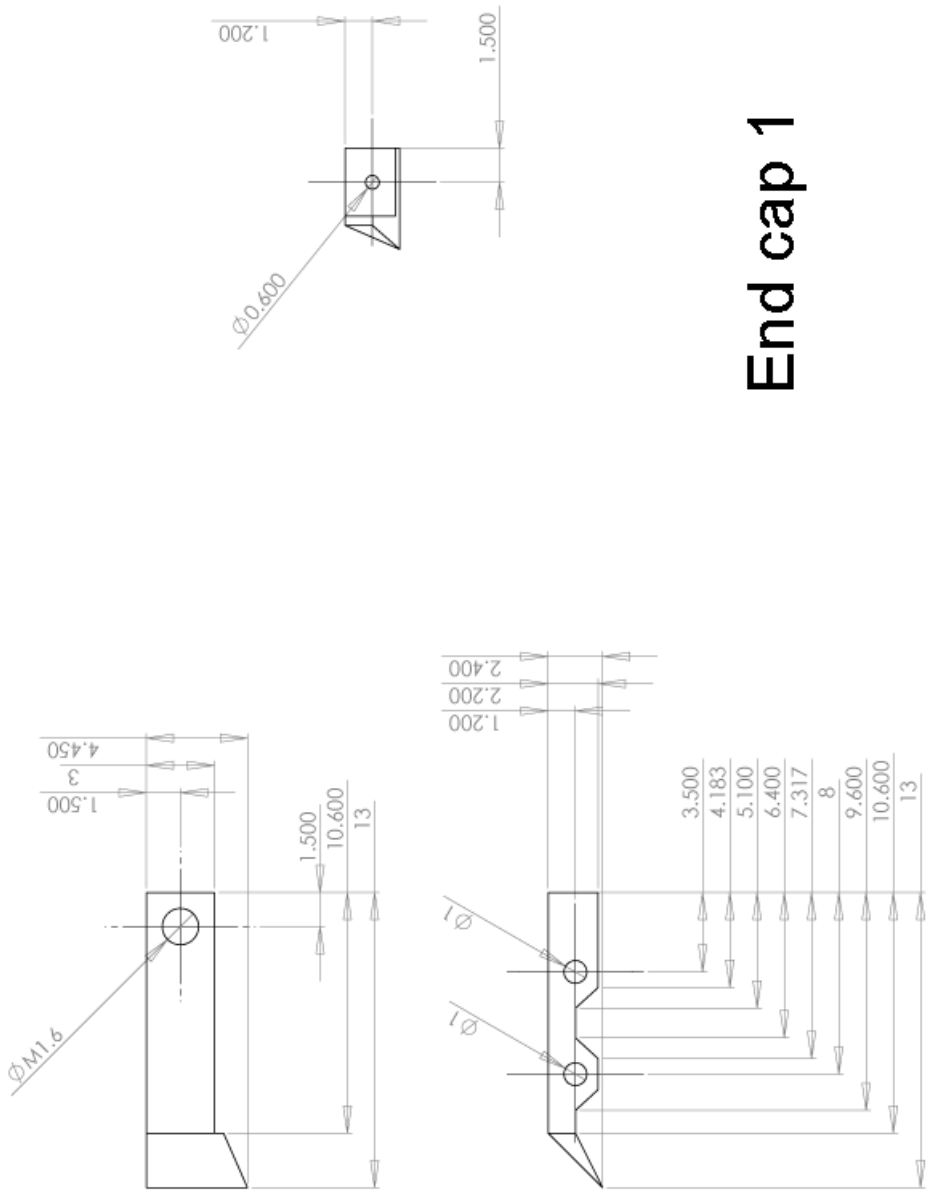

Figure C.8: A SolidWorks drawing of one of the end cap electrodes.

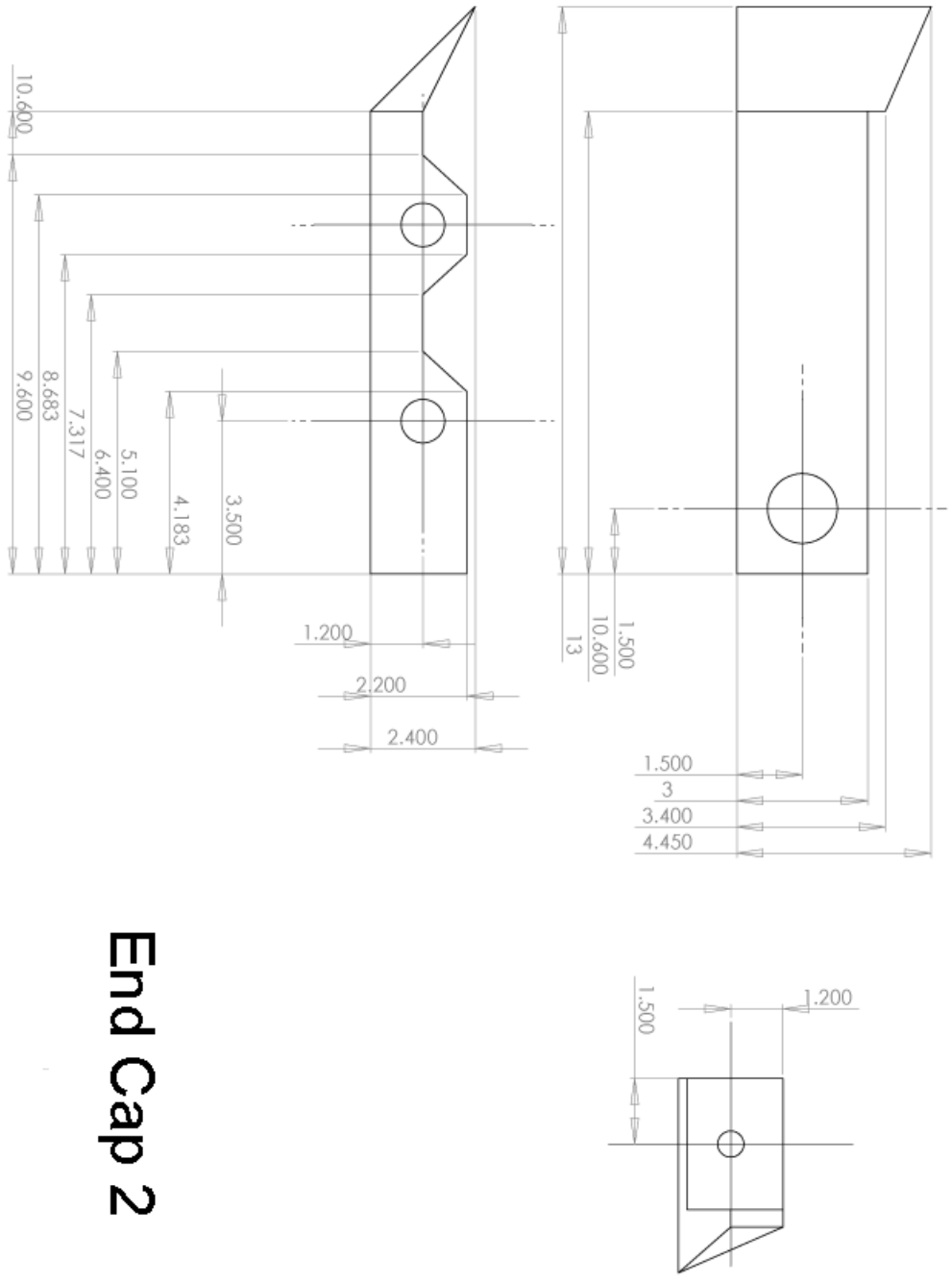

Figure C.9: A SolidWorks drawing of one of the end cap electrodes.

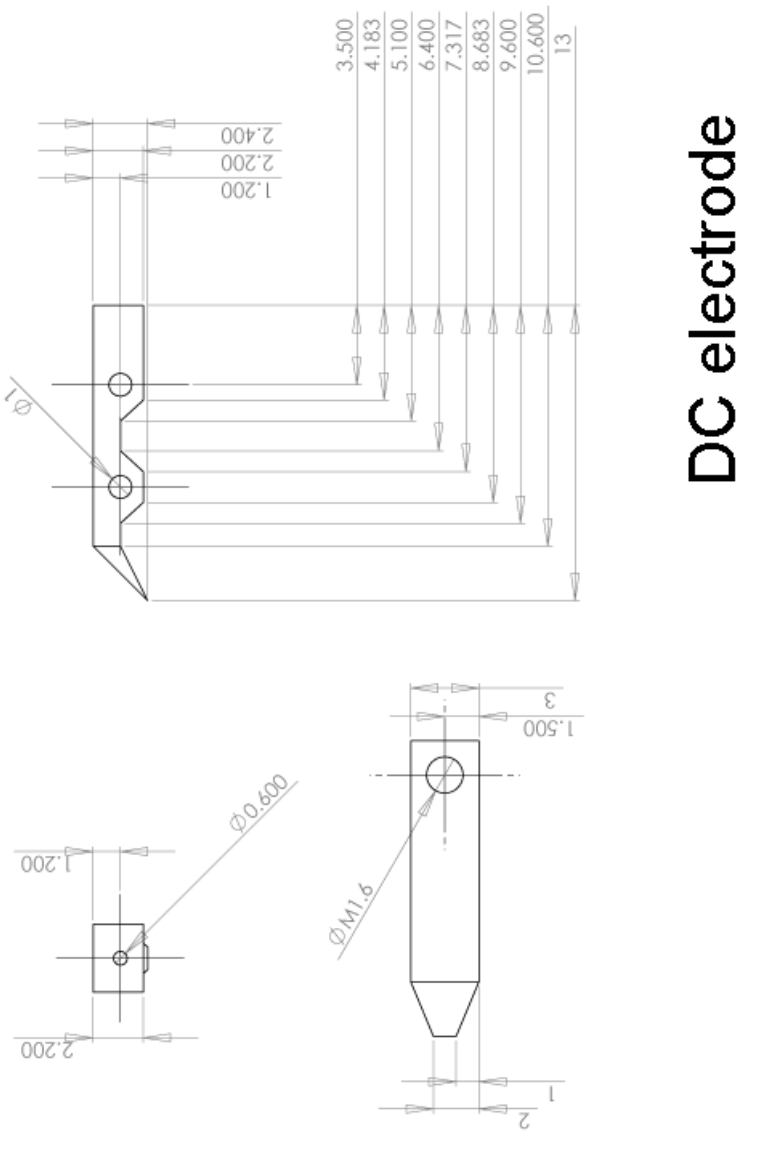

Figure C.10: A SolidWorks drawing of the central DC electrode.

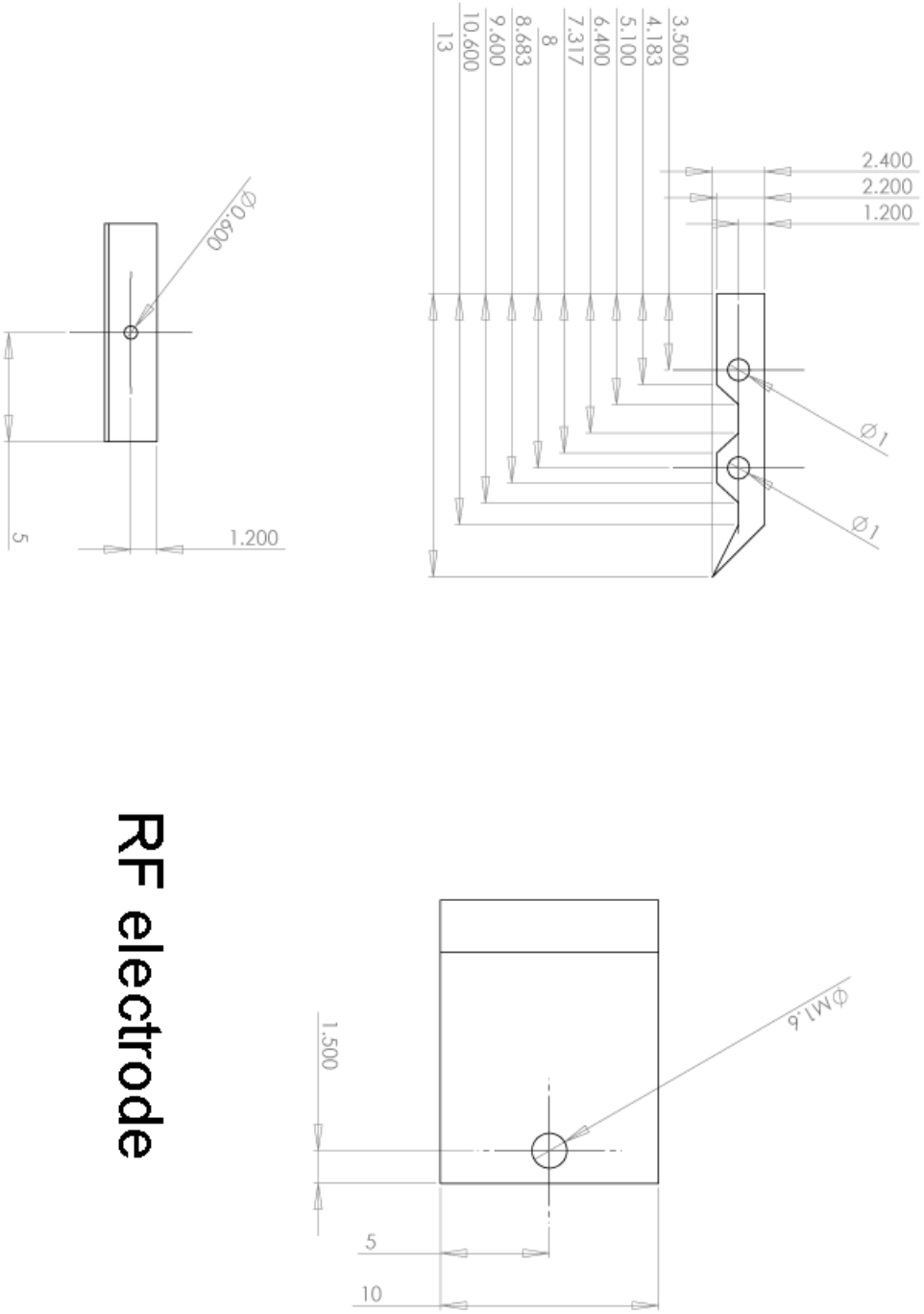

Figure C.11: A SolidWorks drawing of one the RF electrode.

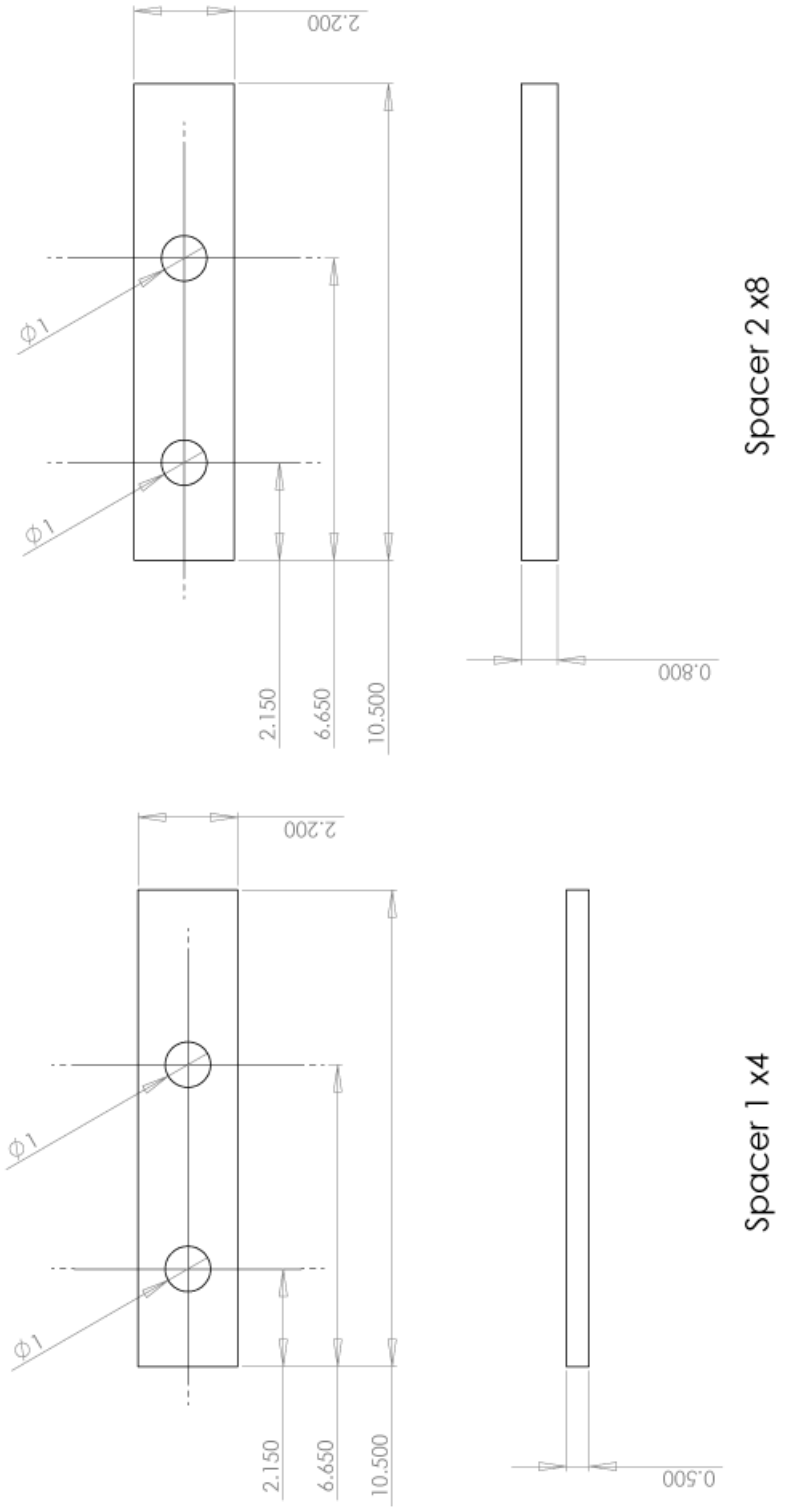

Figure C.12: A SolidWorks drawing of the spacers that separate the electrodes.

Appendix D

Vacuum system

D.1 Vacuum system design drawings

Workshop design drawings for all the custom vacuum components.

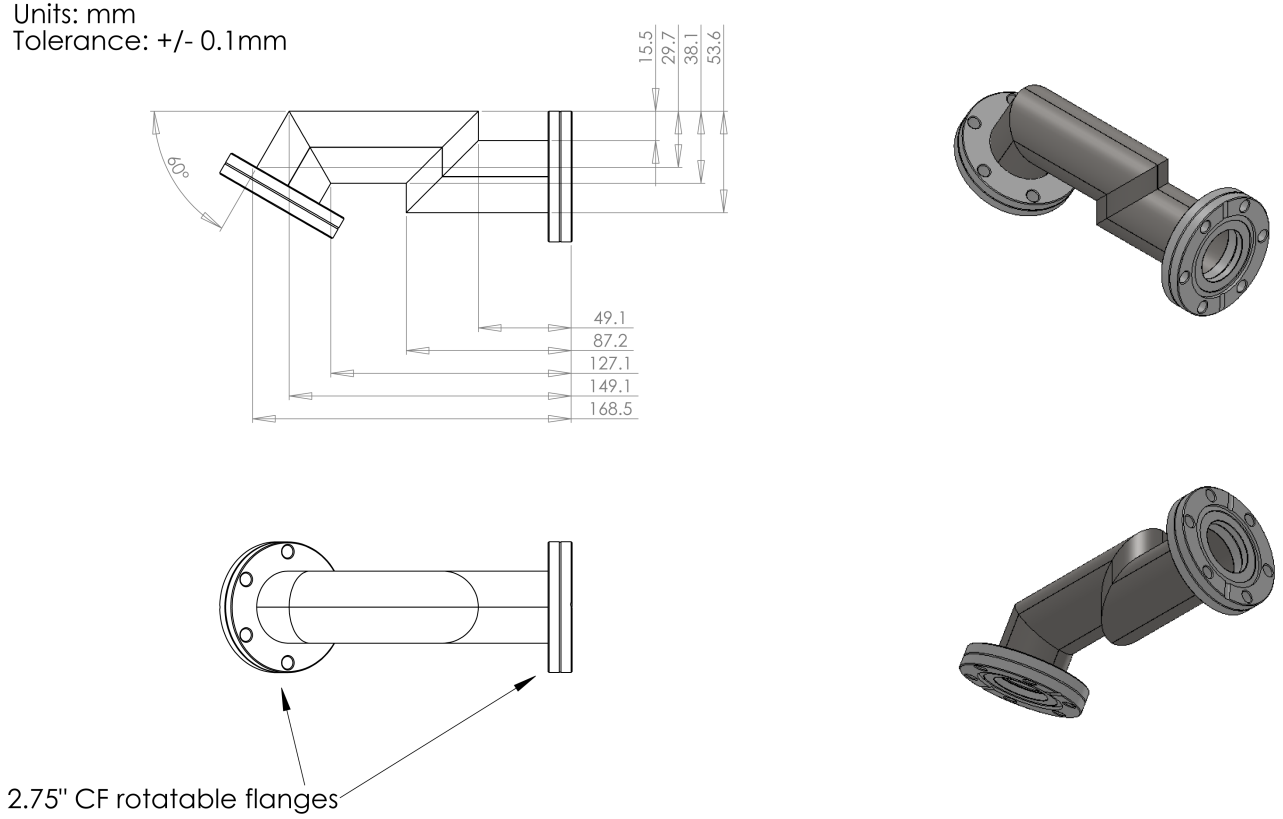

Figure D.1: A SolidWorks drawing of the custom elbow.

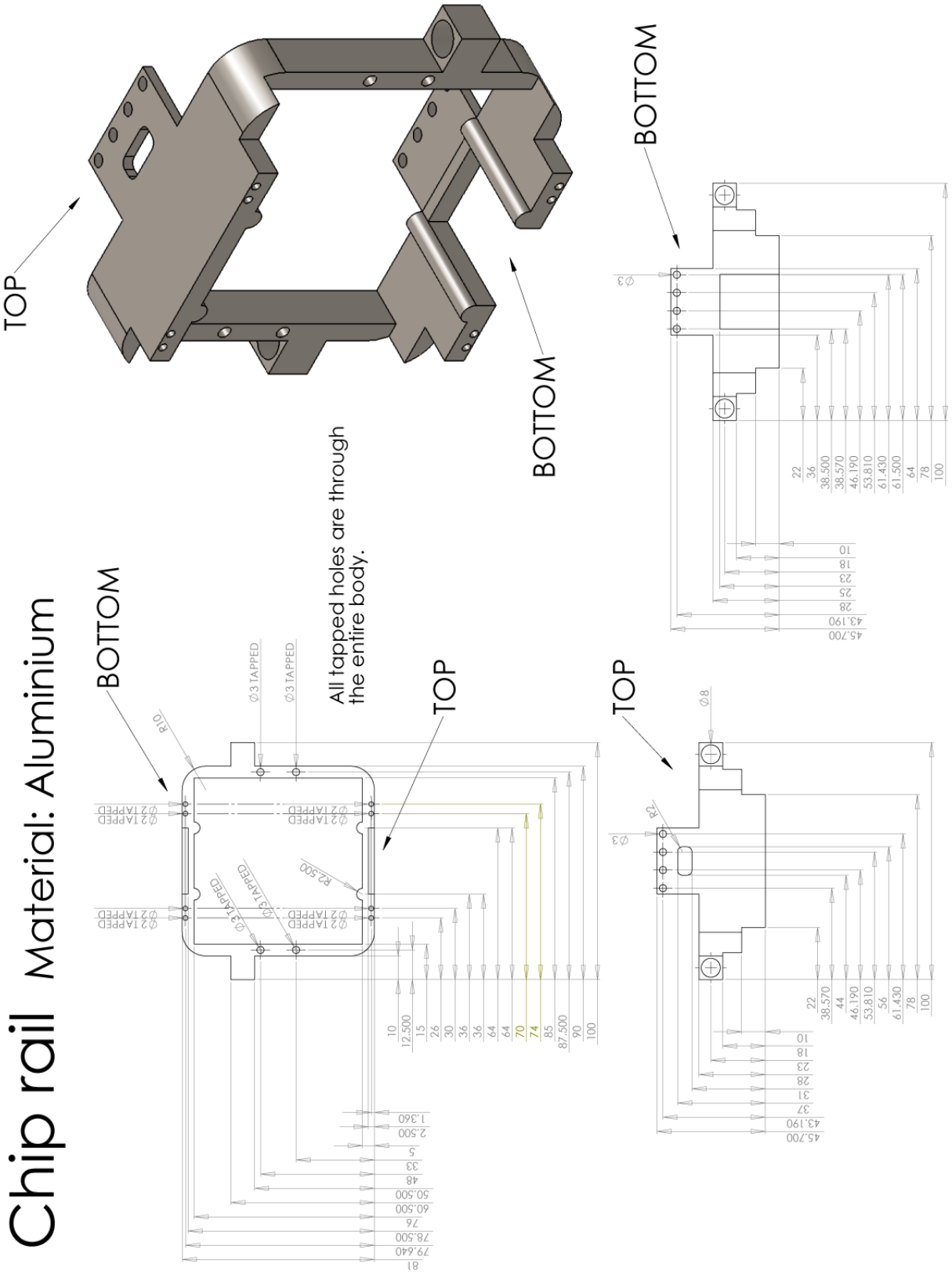

Figure D.2: A SolidWorks drawing of the chip rail.

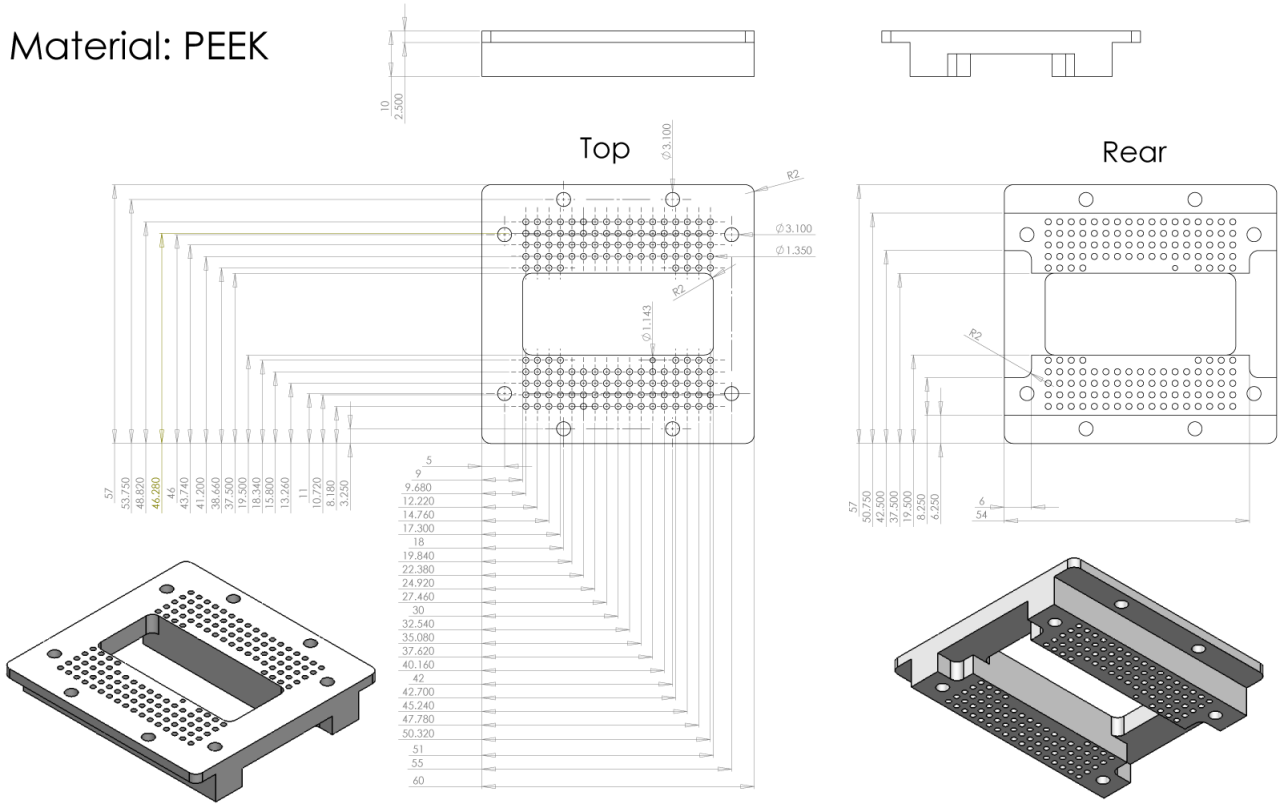

Figure D.3: A SolidWorks drawing of the middle PEEK plate.

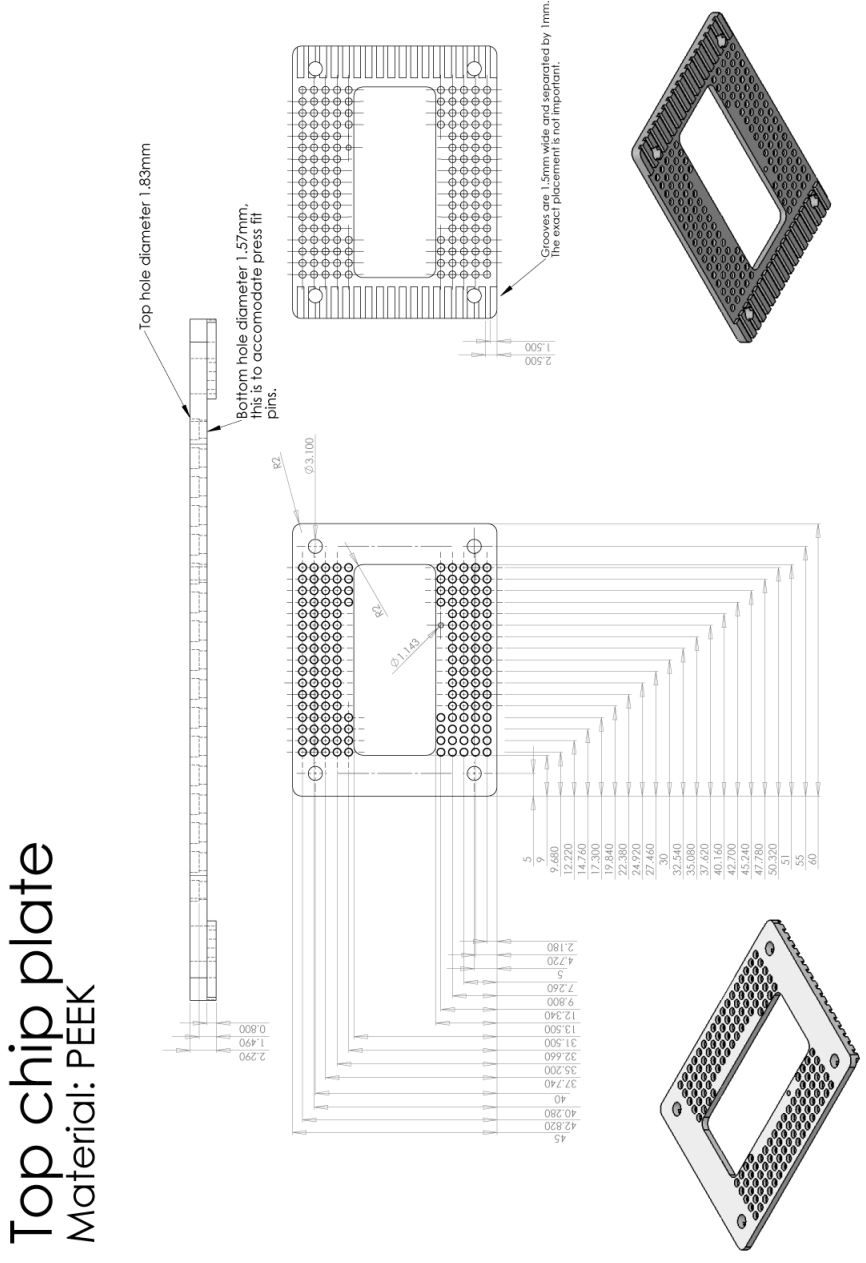

Figure D.4: A SolidWorks drawing of the top PEEK plate.

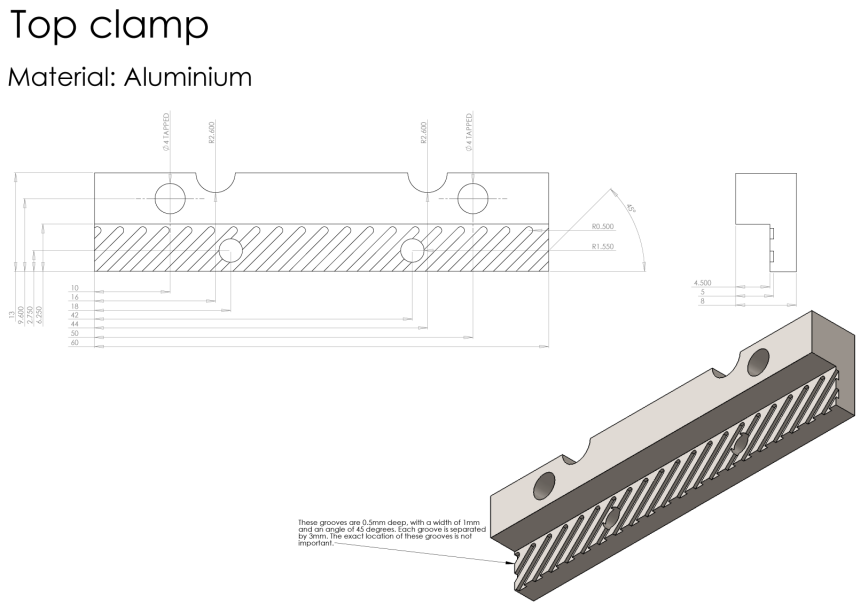

Figure D.5: A SolidWorks drawing of the top aluminium clamp.

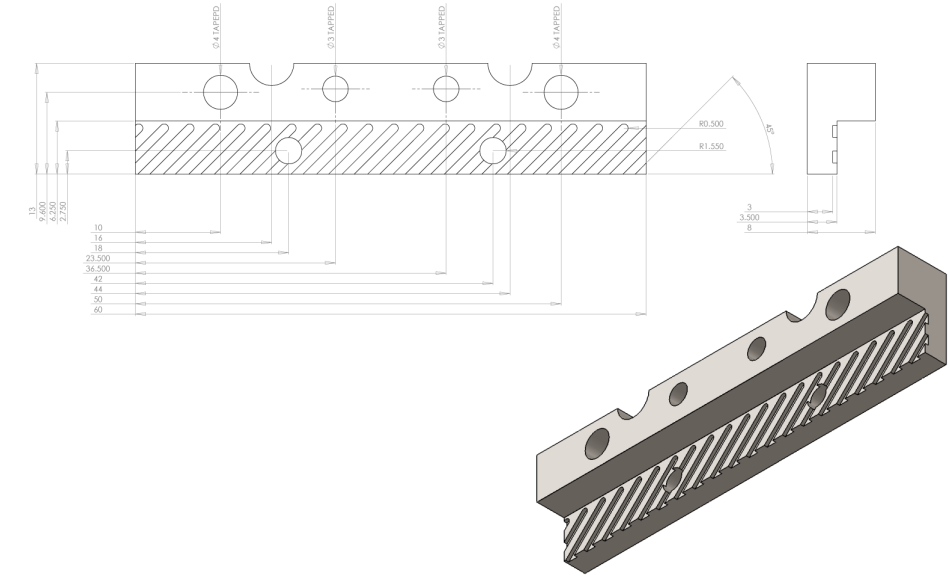

Figure D.6: A SolidWorks drawing of the bottom aluminium clamp.

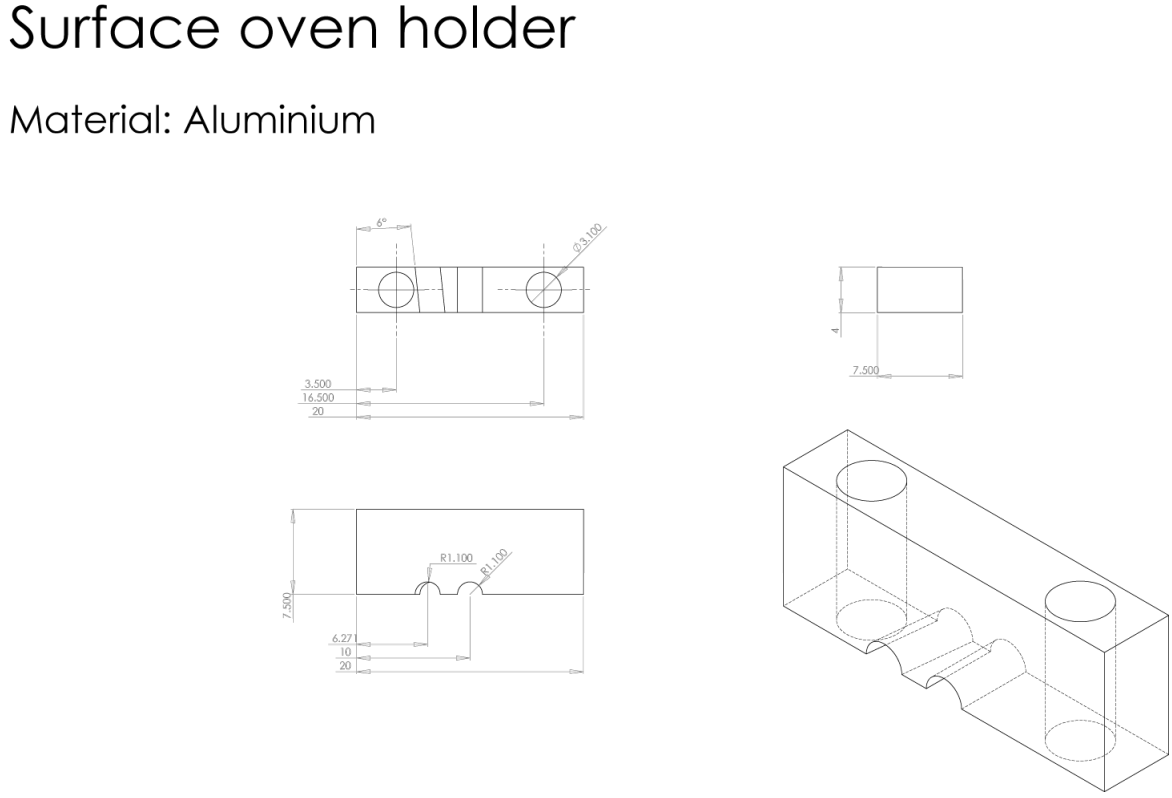

Figure D.7: A SolidWorks drawing of the surface ion trap oven holder.

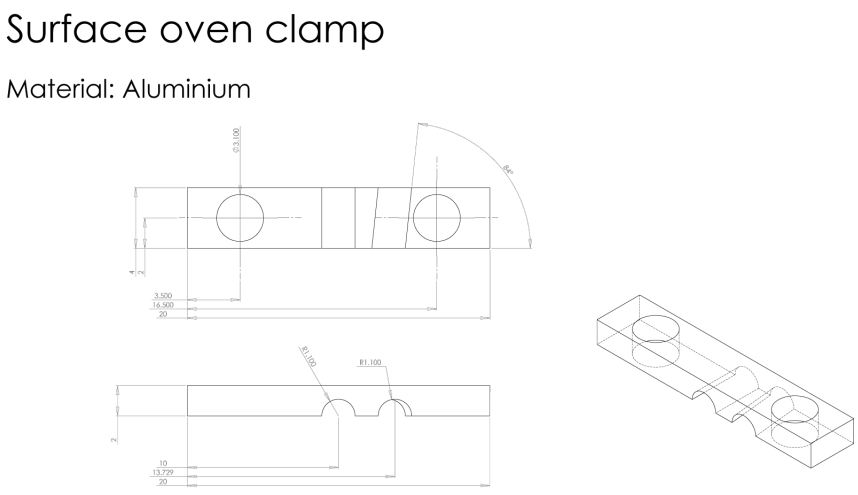

Figure D.8: A SolidWorks drawing of the surface ion trap oven holder clamp.

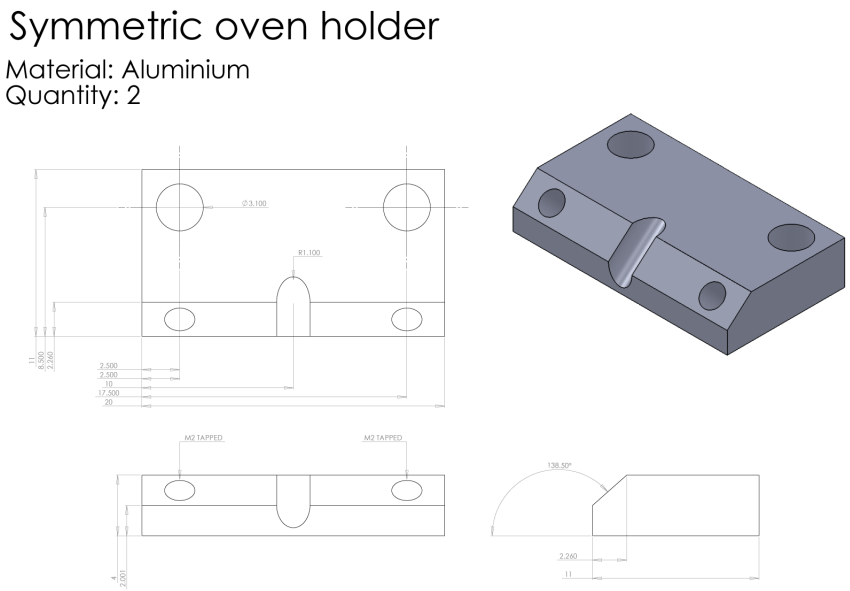

Figure D.9: A SolidWorks drawing of the symmetric ion trap oven holder.

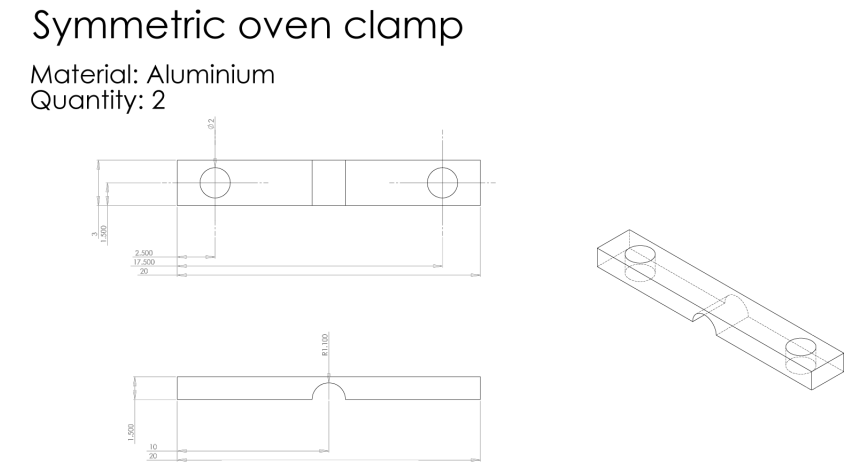

Figure D.10: A SolidWorks drawing of the symmetric ion trap oven holder clamp.

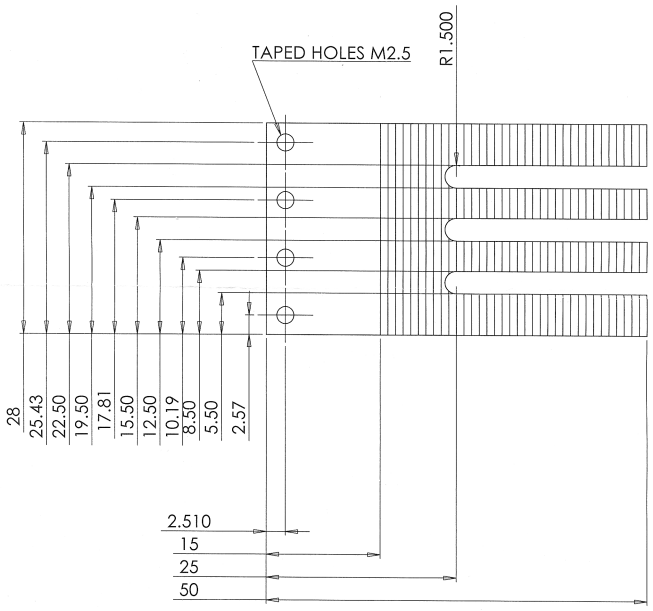

Figure D.11: A SolidWorks drawing of the top chip rail bracket.

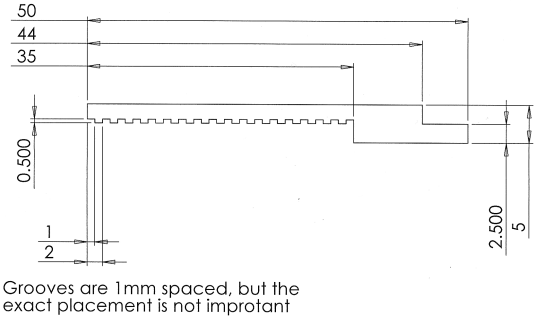

Figure D.12: A SolidWorks drawing of the top chip rail bracket.

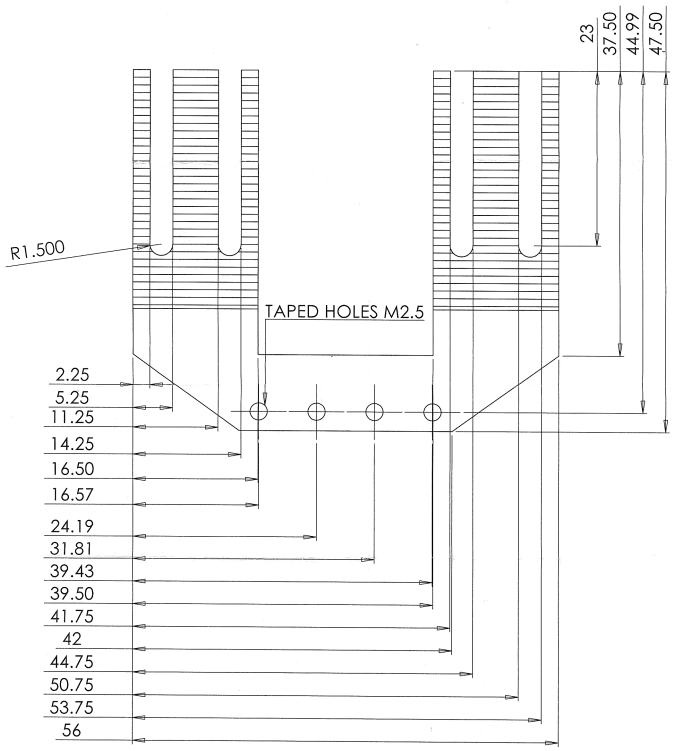

Figure D.13: A SolidWorks drawing of the bottom chip rail bracket.

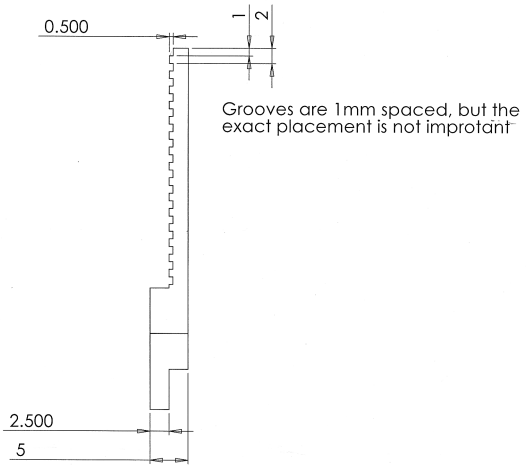

Figure D.14: A SolidWorks drawing of the bottom chip rail bracket.

Appendix E

Microwaves

E.1 Coupled slot line field components

In this appendix I will state both the **H** and **E** field components of a coplanar wave guide, where V_0 is the voltage directly across the slot, b is half the CPW width, $\delta = w/b$, where w is the gap width between the central conductor and ground planes, $\eta = 376.6\Omega$, λ is the wavelength, λ' is the slot mode wavelength and $F_n = \frac{b\gamma_n}{n\pi} = \sqrt{1 + (\frac{2bv}{n\lambda})^2}$ where $v = \sqrt{(\lambda/\lambda')^2 - 1}$. For further information on the derivation of the equations can be found in: Coupled slot line field components, IEEE Transactions on microwave theory and techniques. Vol MTT 30, no. 7 July 1982.

$$E_y = \frac{2V_0}{b} \sum_{n>0}^{\infty} \left[\frac{\sin n\pi\delta/2}{n\pi\delta/2} \sin n\pi\delta/2 \right] \sin \frac{n\pi y}{b} e^{-\gamma_n |z|} \tag{E.1}$$

$$E_z = -\frac{2V_0}{b} \sum_{n>0}^{\infty} \frac{1}{F_n} \left[\frac{\sin n\pi\delta/2}{n\pi\delta/2} \sin n\pi\delta/2 \right] \cos \frac{n\pi y}{b} e^{-\gamma_n |z|} \tag{E.2}$$

$$H_x = -j \frac{2V_0}{\eta b} \left(\frac{\lambda}{\lambda'} \right)^2 \frac{2b}{\lambda} \sum_{n>0}^{\infty} \frac{(1 - \lambda'/\lambda)^2}{nF_n} \left[\frac{\sin n\pi\delta/2}{n\pi\delta/2} \sin n\pi\delta/2 \right] \sin \frac{n\pi y}{b} e^{-\gamma_n |z|} \tag{E.3}$$

$$H_y = \frac{2V_0}{\eta b} \frac{\lambda}{\lambda'} \sum_{n>0}^{\infty} \frac{1}{F_n} \left[\frac{\sin n\pi\delta/2}{n\pi\delta/2} \sin n\pi\delta/2 \right] \cos \frac{n\pi y}{b} e^{-\gamma_n |z|} \tag{E.4}$$

$$H_z = \frac{2V_0}{\eta b} \frac{\lambda}{\lambda'} \sum_{n>0}^{\infty} \left[\frac{\sin n\pi\delta/2}{n\pi\delta/2} \sin n\pi\delta/2 \right] \sin \frac{n\pi y}{b} e^{-\gamma_n |z|} \tag{E.5}$$

$$E_y = \frac{2V_0}{b} \sum_{n\geq 0}^{\infty} \left[\frac{\sin\left[(\frac{2n+1}{2}) \frac{\pi\delta}{2} \right]}{(\frac{2n+1}{2}) \frac{\pi\delta}{2}} \cos \left[\left(\frac{2n+1}{2} \right) \frac{\pi\delta}{2} \right] \right] cos \left[\left(\frac{2n+1}{2} \right) \frac{\pi y}{b} \right] e^{-\gamma_n |z|} \tag{E.6}$$

$$E_z = \frac{2V_0}{b}\sum_{n\geq 0}\frac{1}{F_n}\left[\frac{\sin\left[(\frac{2n+1}{2})\frac{\pi\delta}{2}\right]}{(\frac{2n+1}{2})\frac{\pi\delta}{2}}\cos\left[\left(\frac{2n+1}{2}\right)\frac{\pi\delta}{2}\right]\right]\sin\left[\left(\frac{2n+1}{2}\right)\frac{\pi y}{b}\right]e^{-\gamma_n|z|} \quad \text{(E.7)}$$

$$H_x = -j\frac{2V_0}{\eta b}\left(\frac{\lambda}{\lambda'}\right)^2\frac{2b}{\lambda}\sum_{n\geq 0}\frac{1-(\lambda'/\lambda)^2}{(\frac{2n+1}{2})F_n}\left[\frac{\sin\left[(\frac{2n+1}{2})\frac{\pi\delta}{2}\right]}{(\frac{2n+1}{2})\frac{\pi\delta}{2}}\cos\left[\left(\frac{2n+1}{2}\right)\frac{\pi\delta}{2}\right]\right]\cos\left[\left(\frac{2n+1}{2}\right)\frac{\pi y}{b}\right]e^{-\gamma_n|z|} \quad \text{(E.8)}$$

$$H_y = -\frac{2V_0}{\eta b}\frac{\lambda}{\lambda'}\sum_{n\geq 0}\frac{1}{F_n}\left[\frac{\sin\left[(\frac{2n+1}{2})\frac{\pi\delta}{2}\right]}{(\frac{2n+1}{2})\frac{\pi\delta}{2}}\cos\left[\left(\frac{2n+1}{2}\right)\frac{\pi\delta}{2}\right]\right]\sin\left[\left(\frac{2n+1}{2}\right)\frac{\pi y}{b}\right]e^{-\gamma_n|z|} \quad \text{(E.9)}$$

$$H_z = \frac{2V_0}{\eta b}\frac{\lambda}{\lambda'}\sum_{n\geq 0}\left[\frac{\sin\left[(\frac{2n+1}{2})\frac{\pi\delta}{2}\right]}{(\frac{2n+1}{2})\frac{\pi\delta}{2}}\cos\left[\left(\frac{2n+1}{2}\right)\frac{\pi\delta}{2}\right]\right]\cos\left[\left(\frac{2n+1}{2}\right)\frac{\pi y}{b}\right]e^{-\gamma_n|z|} \quad \text{(E.10)}$$